Influence of Structure and Surface Chemistry of Porous Carbon Electrodes

on Supercapacitor Performance

A Thesis

Submitted to the Faculty

of

Drexel University

by

Boris Dyatkin

in partial fulfillment of the

requirements for the degree

of

Doctor of Philosophy

January 2016

DEDICATIONS

I dedicate this thesis to my family. My father and mother, Dr. Alexey B. Dyatkin and Dr. Katherine M. Ivanovsky; my grandparents, Prof. Natalia Y. Minina and Dr. Michael A. Ivanovsky; and to the memory of my grandparents, Prof. Maria N. Preobrazhenskaya (1931 – 2014) and Prof. Boris L. Dyatkin (1931 – 1975).

ACKNOWLEDGEMENTS

First and foremost, I am thankful to my advisor, Professor Yury Gogotsi. I first met him in December 2008, and I have had the honor of working with him, learning from him, and being guided by him during the most important part of my professional life. He gave me an opportunity that became an extraordinarily rewarding experience. Yury's intellect, work ethic, mentorship, and scientific vision will serve as an exemplary role model during my entire career. I will be eternally grateful for my experience in his research group.

I want to thank my thesis examination committee: Prof. Steve May (MSE), Prof. Michel Barsoum (MSE), Prof. Maureen Tang (CBE), and Dr. Oleg Borodin (Army Research Laboratory). I also wish to thank Prof. Youngmoo Kim (ECE) for reviewing my thesis proposal, and Prof. Vibha Kalra (CBE) and Prof. Michael Schrlau (Rochester Institute of Technology) for serving on my candidacy examination committee.

I wish to thank my mentor, Prof. Volker Presser (now at Saarland University). During his time as a post-doctoral researcher in our group, he taught me numerous techniques and got me my start on very rewarding projects. He provided constant encouragement and guidance and remained a valued colleague even after starting his group at INM. His data analysis approach, experimental setup, and attention to detail guided many of my studies throughout my entire PhD study.

I am extremely thankful for my colleagues in the Drexel Nanomaterials Institute (DNI) research group. Throughout almost 5 years, they acted as mentors, students, collaborators, conference partners, running buddies, and friends both inside and outside

Various staff members and organizations provided constant support during my time at Drexel University and helped me feel at home here. In the DNI office, Danielle Kopicko, Wendy Thurman, Jill Buckley, and Michelle Sipics helped me with financial issues and fellowship applications. In the MSE office, Sarit Kunz, Keiko Nakazawa, Yenneeka West, Dorilona Rose, and Leslie Champion patiently resolved various administrative issues. The International Studies Office and the Office of Graduate Studies provided me with travel funding. I want to thank the Graduate Student Association and everyone who served on the MAGNET executive board during my 3 terms as president. Outside of Drexel, the Materials Research Society, especially the Government Affairs Committee, helped me discover my passion for science policy. Researchers at NWPU (Xi'an, China), ECUST (Shanghai, China), Naval Research Laboratory, and National Reconnaissance Office allowed me to give invited technical seminars that were highly rewarding.

My PhD study was funded by the NSF project MRI-R2 CNS-0960061 and by the Fluid Interface Reactions, Structures and Transport (FIRST) Center, an Energy Frontier Research Center funded by the U.S. Department of Energy, Office of Science, Office of Basic Energy Sciences. My research visit to ARL was funded by the CQL Apprenticeship program funded by ASEE. My research stay at Dalian University of Technology was funded by the ICMR International Research Fellowship. My research stay at ORNL was funded by the DOE Office of Science Graduate Student Research Program (SCGSR).

Most importantly, I wish to acknowledge my parents, grandparents, my girlfriend Christine Buzzard, and her family for their patience, love, support, understanding, encouragement, advice, gifts of food, and occasional reality checks that got me through my PhD study. I could not have done it without them.

TABLE OF CONTENTS

LIST OF TABLES

LIST OF FIGURES

LIST OF EQUATIONS

ABSTRACT

Influence of Structure and Surface Chemistry of Porous Carbon Electrodes on
Supercapacitor Performance
Boris Dyatkin
Advisor: Professor Yury Gogotsi

Electrochemical double layer capacitors, which rely on electrosorption of ions in nanostructured carbon electrodes, can supplement or even replace traditional batteries in energy harvesting and storage applications. While supercapacitors offer > 10 kW/kg power densities, their ~5 Wh/kg energy densities are insufficient for many automotive and grid storage applications. Most prior efforts have focused on novel high-performing ionic liquid electrolytes and porous carbons with tunable pore diameters and high specific surface areas. However, existing research lacks fundamental understanding of the influence of surface heterogeneity and disorder, such as graphitic defects and functional groups, on key electrosorption properties at electrode-electrolyte interfaces. These interactions significantly impact charge accumulation densities, ion transport mechanisms, and electrolyte breakdown processes. Subsequently, they must be investigated to optimize ion screening, charge mobilities, and operating voltage windows of the devices.

The research in this dissertation examined the influence of surface functional groups and structural ordering on capacitance, electrosorption dynamics, and electrochemical stability of external and internal surface of carbon electrodes. High-temperature vacuum annealing, air oxidation, hydrogenation, and amination were used to tune pore surface compositions and decouple key structural and chemical properties of carbide-derived carbons. The approach combined materials characterization by a variety of techniques, neutron scattering studies of ion dynamics, electrochemical testing, and MD simulations

to investigate the fundamental intermolecular interactions and dynamics of ions electrosorption in different pore architectures and on planar graphene surfaces. Contrary to expected results and existing theories, defect removal *via* defunctionalization and graphitization decreased capacitance. Hydrogenated surfaces benefitted electrosorption, while oxygen-containing groups, which increased the wettability and ionophilicity of electrodes, positively impacted capacitance by decreasing ion densities in confined pores and improving electrolyte diffusion. The influence of surface defects strongly depended on ion properties, carbon particle size and internal-to-external surface ratio, porosity, and ion confinement. These fundamental concepts were applied to several energy storage systems, including high-performance coarse-grained and core-shell carbide derived carbon electrodes, a novel *in situ* spectroelectrochemical analysis method, and design of an environmentally benign "green" supercapacitor.

CHAPTER 1: BACKGROUND AND LITERATURE SURVEY

1.1 Introduction to Electrical Energy Storage

As the Earth's population approaches 8 billion habitants, our society exponentially demands increased energy sources to fit our needs. Consumption has risen from 7 to 30 quadrillion watt-hours in the United States over the last 70 years.[1] A large percentage of this energy is now needed to power remote, off-the-grid devices. These vary greatly in scale and function: from microelectronics and nanoscale sensors to mobile phones to automobiles and large aircraft, consumers demand greater functionality, reliability, and operating capabilities. As soon as a new electric car or laptop enters the market, performance differentiators typically include: how long can it operate without recharging? How much does it cost? How heavy is it? How quickly can it accelerate or perform complex functions? These considerations include hand-held devices, transportation networks, industrial applications, and military systems. Subsequently, energy storage technology must improve in the interest of economic growth, improved information exchange, higher quality of life, and stronger national security.

Improved energy storage devices are an important component of our pathway to improved sustainability. The key metrics are summarized in **Fig. 1.1**. The United States currently derives most of its energy from non-renewable sources, such as hydrocarbons (39% coal, 27% natural gas, and 1% oil) and nuclear materials (19%).[1] These resources are finite, and many economic indicators and market analysts predict fierce competition for them in the near future. Population increase (and corresponding energy use) is closely tied to CO_2 release into the atmosphere – a greenhouse gas and contributor to global climate change. Although this provides a strong incentive for efficient use of generated

energy, demands vary (by as much as 400%) during regular operation and pose undue strain on our aging power distribution grid.
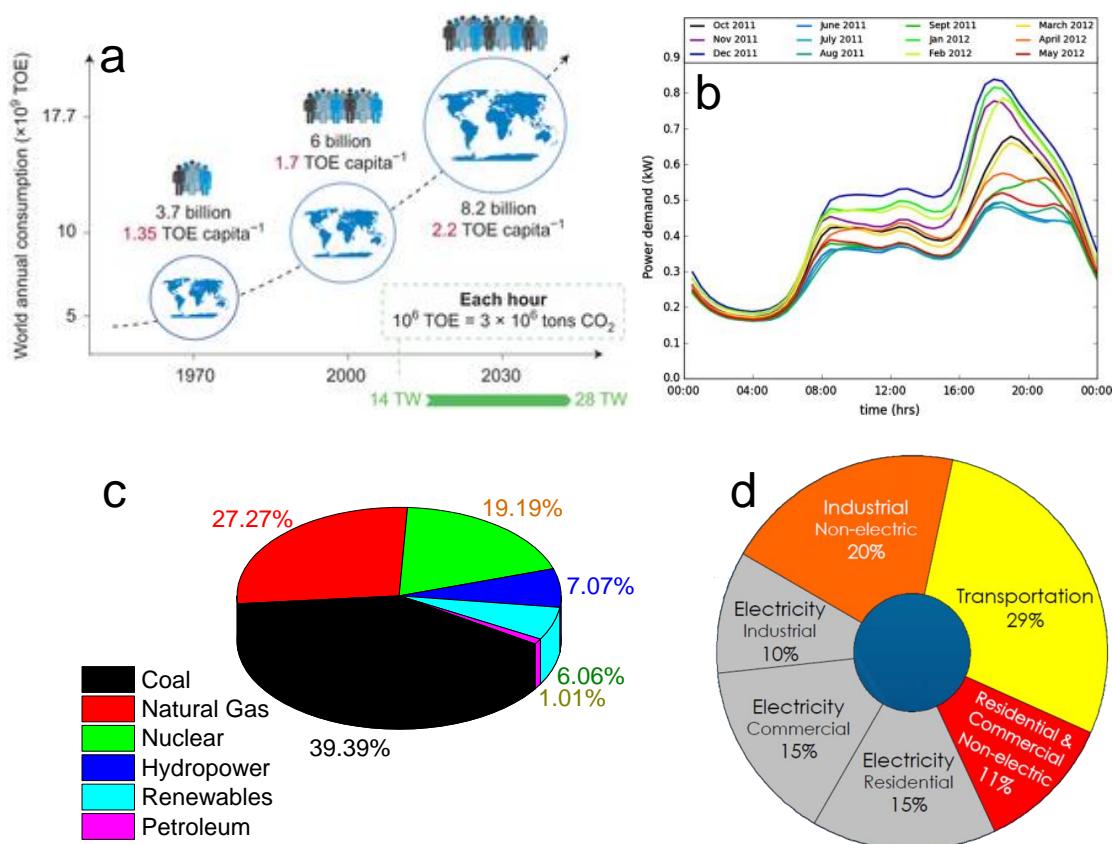
Figure 2.1. a) Correlation between energy consumption and CO_2 emission for a rising world population.[2][1] b) Energy loads on a power grid of a typical modernized town during different years.[2] c) Breakdown of electricity generation sources for the United States for 2014, adapted from Ref. [1]. d) Breakdown of consumption of energy by technology sector for the United States in 2009, from Ref. [1].

One of the key elements to national energy independence includes greater use of renewable energy resources, including wind turbines and photovoltaic cells. It is a widely recognized goal; even the Department of Defense includes environmentally sustainable approaches in its operations plan.[3] Although these "green" alternatives allow better off-the-grid operations and reduce overall demand, they introduce greater day-to-day variability and require reserve storage banks. Those only hold 2.5% of energy produced

---

[1] Reprinted by permission from Macmillan Publishers Ltd: *Nature Chemistry (*Ref. [2]), copyright 2015.

annually in the U.S., primarily in the form of pumped water for hydroelectric generation.[4] Although a number of other solutions, such as flywheels, thermoelectric generators, and electrolyzers are being considered, electrochemical energy storage devices offer an optimal combination of scalability, cost, and energy and power density. These include batteries (both solid state and flow systems), fuel cells, electrolytic capacitors, and electrochemical capacitors. Although they only provide a solution to the energy storage problem (and not energy generation), they improve operating efficiencies of devices at all scales and allow a smarter, more nimble nationwide electric grid design.

Novel materials will improve operating capabilities of these devices. The most common metrics are energy (measured in Wh kg^{-1}) and power densities (measured in kW kg^{-1}), which, respectively, measure the total amount of stored energy and the maximum rate at which it can be effectively stored or released.[5] They are normalized by mass (gravimetric) or volume (volumetric) of the electrodes or total systems. **Fig. 1.2** shows the Ragone plot that compares the power and energy tradeoffs.
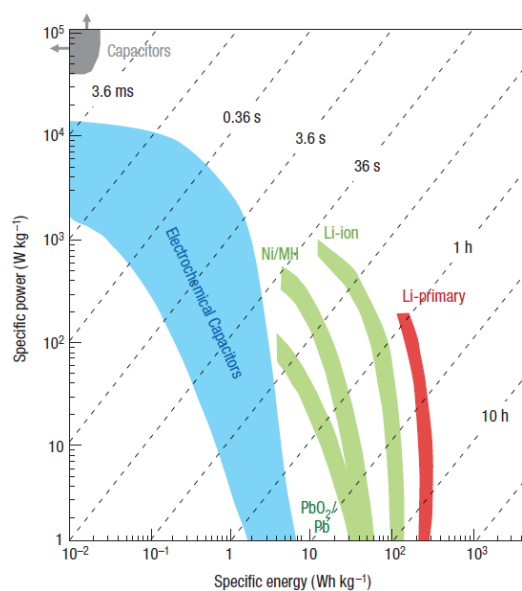
Figure 1.2. Specific power and energy comparisons.[5]²

---

² Reprinted by permission from Macmillan Publishers Ltd: *Nature Materials* (Ref. [5]), copyright 2008.

In addition to maximizing specific energy and power capabilities of energy storage materials, research efforts aim to improve their cyclabilities and reliabilities. Energy storage systems must accommodate the full life of devices, which have very divergent demands, in which they are implemented. They must operate efficiently and pose minimal flammability and explosion hazards. Certain applications require extreme temperature ranges (-100 ºC $\leftrightarrow$ 200 ºC) and, in certain military applications, minimal heat generation signatures. Energy storage materials must implement environmentally benign alternatives that minimize the impact of the entire energy generation cycle. Component synthesis, use, and disposal must minimize electronic waste and greenhouse gas emissions. Most importantly, novel energy storage materials must reduce cost of precursors and synthesis to improve their accessibility and widespread implementation.

Electrical energy storage alternatives are typically grouped by charge transfer systems, including most batteries and pseudocapacitive systems, and charge accumulation systems, which involve charge or ion electrosorption on electrode surfaces of capacitors. **Table 1.1** summarizes cost and performance comparisons of common Faradaic and non-Faradaic systems. This dissertation primarily focuses on a fundamental investigation of electrochemical capacitors, but the concepts that it discusses are applicable in development efforts for energy storage systems in a broad range of energy storage applications, including hybrid utility vehicles, grid storage banks, public transportation, and standalone street lighting systems.

Table 1.1. Comparison of performance metrics and costs of electrical energy storage technologies. Adapted from Ref. [6].

Technology	Energy density (Wh/kg)	Recovery Efficiency (%)	Development	Capital cost (€/kW)	Advantages	Disadvantages
Supercapacitors	0.1 – 5	85-98	Developing	200-1000	Long cycle life, efficiency	Low energy density, toxic compounds
Nickel batteries	20-120	60-91	Available	200-750	High power and energy density, efficiency	Highly toxic
Lithium batteries	80-150	60-95	Available	150-250	High power and energy density, efficiency	High cost, difficult production, recycling issues
Lead-acid batteries	24-45	75	Available	50-150	Low cost	Environmental concerns
Zn-Br flow battery	37	50	Early commercialization	900	High capacity	Low energy density
Metal air battery	110-420	> 86	Developing	-	High energy density, low cost, environmentally benign	Poor recharge ability, short lifetime
Na-S battery	150-240		Available	170	High energy density, efficiency	High cost, recycling difficulties

1.2 Electrochemical Capacitors: Fundamental Theory and Key Advantages

General Electric was the first entity to patent a concept for an electrochemical capacitor, which is also referred to as an electric double layer capacitor (EDLC) and supercapacitor (Becker *et. al.,* U.S. Patent 2 800 616), in 1957.[7] It covered a simple design of a crude porous charcoal electrode and an aqueous electrolyte. The specific charge mechanism was unclear at the time, and only a 1966 SOHIO patent established the electrical double layer (at the electrode-electrolyte interface) as the primary charge mechanism. NEC licensed the technology in 1971, and companies such as Maxwell, Dynacap, Nesscap, and Skeleton Tech have also commercialized supercapacitors,[8] and the entire market is expected to exceed $382 million in 2015.[9] They continue to attract scientific interest: since 2000, over 7100 publications have explored this technology.

The classical view of the charge storage mechanism of EDLCs resembles that of the traditional capacitor. In the latter, charge accumulates at two parallel plates with vacuum or a strong dielectric in the middle. Charge is driven by an applied voltage (V) through an electric circuit. The total capacitance is determined using (**Eq. 1.1**) below:

$$C = \frac{\varepsilon_r \varepsilon_0 A}{d} \qquad (1.1)$$

The capacitance (C) is dependent on the permittivity of free space and the dielectric (ε_r and ε_0) and the cross-sectional area of the parallel plates (A), and it is inversely dependent on the separation distance between the plates (d). The total capacitance, as measured in Farads (F), correlates charge (Q) with applied voltage (**Eq. 1.2**):

$$C = \frac{Q}{V} \qquad (1.2)$$

To maximize C, capacitors may maximize the area of the parallel plates, increase dielectric strength, and minimize plate separation. Since the device rapidly accumulates electrons under an applied electric field, its charge/discharge time is in the $10^{-6} - 10^{-3}$ second range. However, even in concentric tubular arrangements, parallel plates cannot reach high surface areas (not even 1 m^2), and even high-k dielectrics typically do not exceed the permittivity of vacuum by more than a factor of ~25-50.[10] Subsequently, although traditional capacitors may offer high power densities ($\gg$ 10,000 W kg^{-1}), most devices can store 10^{-6} F $- 10^{-12}$ F and have a 0.1 Wh kg^{-1} threshold.[8] Although traditional capacitors are usable in many power management systems, especially those that require rapid current bursts, they cannot function as standalone energy sources.

Electric double layer capacitors similarly rely on charge accumulation at electrodes under applied potentials. However, electrodes are typically highly porous with high specific surface areas (SSAs): $100 - 3,000$ m^2 g^{-1}. Furthermore, instead of vacuum or a dielectric, an electrolyte with cations (+) and anions (−) occupies the space between the electrodes. When voltage is applied across the EDLC, electrons travel across the circuit to accumulate at the negative electrode and give each electrode a surface potential (Ψ). To balance them out and maintain overall device charge neutrality, ions and counterions

assemble into organized layers at electrode surfaces. Subsequently, the separation thickness more appropriately describes the distance between the electrode surface and the electrostatically adsorbed (electrosorbed) ions. It is typically in the range of 1-50 picometers, and, along with greater SSA, substantially increases the capacitance of EDLCs as compared to traditional capacitors.[11] However, **Eq. 1.1** does not directly translate to properties of the ionic double layer and is not practically used to evaluate its key properties.

The most conventional ion double layer model involves the Stern model, which combines a dense monolayer of ions (the Helmholtz layer) at the fluid-solid interface (FSI) and a diffuse layer of ions and counterions (the Gouy-Chapman layer). The outer layer acts to screen the inner, dense layer and is more mobile under the influence of self-diffusion and electrostatic forces between ions and counterions. Different, oscillating gradations of co-ions and counterions screen preceding layers and reach the electrochemically neutral point between two electrodes. Since the strength and charge concentration of each layer is different, the electrical double layer does not preserve electroneutrality. The total capacitance (C_T) of an EDLC is, therefore, the series sum of Helmholtz layer (C_H) and the diffuse layer (C_{dl}) contributions (**Eq. 1.3**):

$$\frac{1}{C_T} = \frac{1}{C_H} + \frac{1}{C_{dl}} \quad\quad\quad (\mathbf{1.3})$$

Although initial double layer models simplified ions as point charges, recent efforts have incorporated ion finite sizes into mean-field approximations to correlate ion densities with applied potentials. The modified Poisson-Boltzmann (MPB) model, which assumes a binary and symmetric electrolyte, is described in the simplest form by Bikerman's equation (**Eq. 1.4)** for the diffuse layer:

$$\nabla \cdot \left(\epsilon_0 \epsilon_r \nabla_\psi\right) = \frac{2zeN_Ac_\infty \sinh(\frac{ze\psi}{k_BT})}{1+4N_Aa^3c_\infty \sinh^2(\frac{ze\psi}{k_BT})} \tag{1.4}$$

The equation denotes ϵ_0 and ϵ_r as the permittivities of the free space ($8.854 \cdot 10^{-12}$ F m^{-1}) and the electrolyte solution, k_B as the Boltzmann constant ($1.38 \cdot 10^{-23}$ J K^{-1}), e as the elementary charge ($1.602 \cdot 10^{-19}$ C), N_A as the Avogadro number ($6.02 \cdot 10^{23}$ mol^{-1}), T as the temperature, and c_∞ as the bulk ion concentration.[12] The specific ion concentration as a function of at a given distance (r) from the electrode is governed by **Eq. 1.5**:

$$c_i(r) = \frac{c_\infty \exp(\frac{-z_ie\psi(r)}{k_BT})}{1+4N_Aa^3c_\infty \sinh^2(\frac{z_ie\psi(r)}{k_BT})} \quad \text{for ion (i = 1) and counterion (i = 2)} \tag{1.5}$$

For a porous electrode (with pore radius R_0), the boundary condition at the Stern/diffuse layer interface (C_s^{St}) assumes a Helmholtz layer with a thickness H and is expressed as a function of local electric field (E_H) in **Eq. 1.6**:

$$\epsilon_0 \epsilon_r(E_H) \nabla_\psi \frac{r_H}{R_0+H} = C_s^{St}(\frac{R_0}{R_0+H})^p[\psi_s - \psi(r_H)] \tag{1.6}$$

The planar electrode capacitance assumes a thickness that is approximately equal to the Debye length of $\lambda_D = \sqrt{(\epsilon_0\epsilon_r)k_BT/2e^2z^2N_Ac_\infty}$ with ion packing parameter defined as $v_p = 2a^3N_Ac_\infty$. The areal (normalized by SSA) capacitance for planar electrodes (C_s) is defined by **Eq. 1.7**:

$$\frac{1}{C_s} = \frac{a}{2\epsilon_0\epsilon_r} + \frac{\psi_D}{2zeN_Ac_\infty\lambda_D} \times \left\{\frac{2}{v_p}\ln(1 + 2v_p \sinh^2(\frac{ze\psi_D}{2k_BT}))\right\}^{-1/2} \tag{1.7}$$

The structure of the double layer and its implementation in a symmetrical EDLC is shown in **Fig. 1.3**. Classical calculations and novel molecular dynamics show that both ions and counterions contribute to the charge screening layer at each electrode.[13] Subsequently, accurate simulations and experimental results must consider the sizes of

ions, presence and properties of solvent molecules, and their localized electrostatic interactions with both the electrode surfaces and with corresponding electrolyte species.
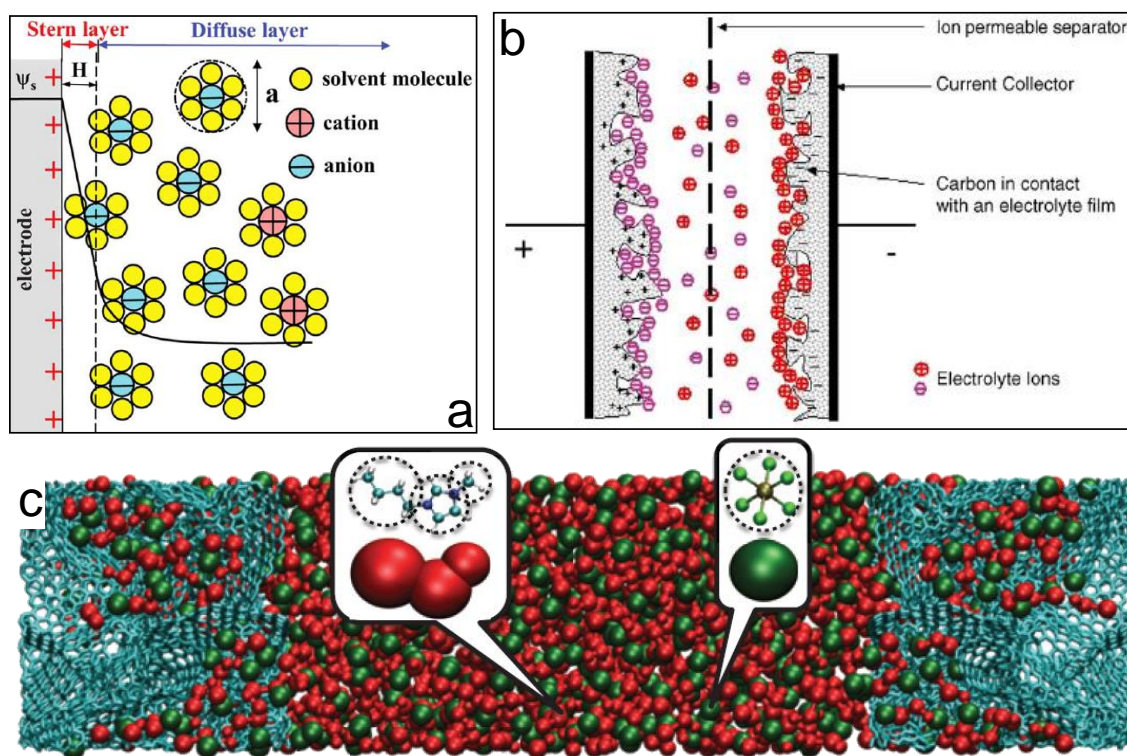
Figure 3.3. a) The model representation of electrical double layer at a positively charged electrode.[12][3] b) Schematic of a symmetrical EDLC in a charged state.[8][4] c) Molecular Dynamics (MD) simulation of a charged cell between two carbon electrodes (blue) with positive cations (red) and negative anions (green).[13][5]

In a two-electrode configuration, each electrode acts as a capacitor in series, so that the total capacitance of the system (C_T) is defined as the sum of the working electrode (C_{WE}, typically measured using electrochemical techniques) and the counter electrode (C_{CE}, acts to balance charge) with **Eq. 1.8**:[14]

$$\frac{1}{C_T} = \frac{1}{C_{WE}} + \frac{1}{C_{CE}} \tag{1.8}$$

The EDLC's total stored energy (E) depends on the capacitance of the system (C) and the applied voltage (V) across the system (**Eq. 1.9**):

$$E = \frac{1}{2}CV^2 \tag{1.9}$$

The specific power density of the system (P) depends on the applied voltage and electrical resistance of the EDLC (R), as defined using **Eq. 1.10**:

$$P = \frac{1}{4R}V^2 \tag{1.10}$$

These relationships further underscore the importance of applied electric potential across the device, as increases in operating voltage windows exponentially increase both energy and power densities. At the same time, EDLC energy and power densities benefit from greater charge storage densities (higher capacitance) and lower resistance contributions from electrodes and electrolytes.

The porous electrode structure adds some complexity to the assumed model of capacitance and charge dynamics in a typical EDLC. This pore network system is typically approximated as a transmission line model;[15] each pore "capacitor" acts as a resistor and in parallel with a capacitor.[16] Subsequently, EDLCs feature an RC constant (τ = time constant) that is calculated using **Eq. 1.11:**

$$\tau = R \cdot C = \frac{\lambda_D L}{(D_1 + D_2)/2} \tag{1.11}$$

The constant approximates the time to charge or discharge a capacitor to 68% of its total density given equilibrium conditions and is affected by diffusion constants (D_1: across the EDL; D_2: from one electrode to the other) and mobility lengths (L) of the individual ions.[12] To produce a desired high surface area, various forms of carbon allotropes are typically implemented as electrodes. These materials are very lightweight,

electrically conductive, and customizable for different electrolytes and geometric EDLC configurations. They are discussed in section **1.3**.

The conventional structure of an EDLC is shown in **Fig. 1.4**. The supercapacitor typically features a porous, electrically insulating separator between the two electrodes.[17] This system compresses into a smaller volume and reduces bulk diffusion limitations. The separator is often composed of PTFE, polypropylene, a surfactant-coated polymer, or cellulose-based fibers.[18] Each electrode is attached to an electrically conductive current collector (typically a metal), which transfers charge from the positive electrode to the negative one through the electric circuit.[19]
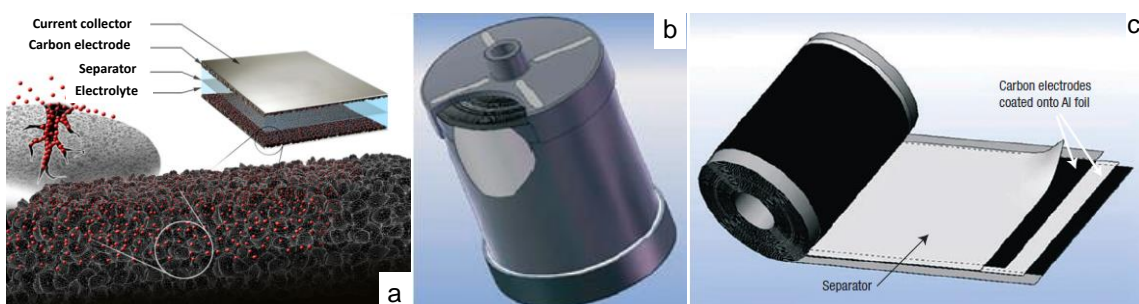
Figure 1.4. a) Cross-sectional diagram of a typical porous carbon supercapacitor. b) Cylindrical cell that is the conventional commercial configuration for most EDLCs.[5] c) Schematic of assembly of a porous carbon electrode film, with a current collector and separator, which is rolled into the cylindrical cell.[5][6]

Traditional, basic supercapacitor electrolytes had implemented a binary salt dissolved in a solvent. Recent advances have also reported gel and solid electrolytes in unique EDLC configurations.[20,21] Most prior studies have used aqueous (solvated in H_2O) electrolytes: $[H^+][HSO_4^-]$ (sulfuric acid), $[Na^+][Cl^-]$ (sodium chloride), $2[Na^+][SO_4^{2-}]$ (sodium sulfate), and $[K^+][OH^-]$ (potassium hydroxide) were most prevalent in measurements and computational simulations. All of these have different ionic diameters ($[Na^+] < [K^+] < [SO_4^{2-}]$), and different solvation shells: hydrated sodium cations are 3.59

---

[6] Reprinted by permission from Macmillan Publishers Ltd: *Nature Materials* (Ref. [5]), copyright 2008.

Å in diameter, potassium cations have a 3.34 Å diameter, and sulfate anions are 7.33 Å in diameter.[22] The size of the individual ion radii and their intermolecular interactions with water determine the hydration number and solvation shell(s) of H_2O around each ion. Although they provide high capacitance and rate handling abilities, their operating electrochemical window is limited by 1.23 V: H_2O begins to split into H_2 (g) and O_2 (g) and irreversibly degrade electrosorption at that threshold.[23] Nevertheless, aqueous electrolytes remain inexpensive and non-toxic electrolyte alternatives, and companies such as Aquion Energy implement them in commercial products.

More recent designs have shifted to organic salts and solvents with larger electrochemical stability windows. The most common salts use quaternary ammonium cations, such as tetraethylammonium ($[C_8H_{20}N^+]$ or $[NEt_4^+]$), and $[BF_4^-]$ or $[PF_6^-]$ anions. They dissolve in acetonitrile (CH_3CN) or propylene carbonate ($C_4H_6O_3$). The desolvated $[NEt_4^+]$'s diameter is 6.7 Å (13 Å solvated), and $[BF_4^-]$'s diameter is 4.8 Å (11.6 Å solvated).[24] These electrolytes offer a stable operating voltage window up to ~2.5-2.7 V. At higher potentials, ethane elimination (of the alkylammonium cation *via* Hoffman pathway), hydrolysis of $[BF_4^-]$ to HF and boric acid derivatives, and other reactions all perpetuate electrochemical breakdown.[25] Furthermore, as with aqueous electrolytes, organic solvents set a relatively narrow operating range: neither electrolyte can operate below ~ −10 ºC ↔ 0 ºC and above +85 ºC ↔ +120 ºC or under vacuum conditions.[26]

In the past few decades, research has increasingly explored organic salts with poor coordination at room temperature that remain liquid at room temperature without any solvent. They are commonly known as ionic liquids (ILs) or room-temperature ionic liquids (RTILs). Numerous ionic liquids have been successfully developed for different

industrial processes. Cations in electrochemical electrolytes often include imidazolium, pyridinium, or pyrrolidinum rings with attached alkyl groups; typical anions include $[BF_4^-]$, $[PF_6^-]$, and $[TFSI^-]$($[NS_2O_4C_2F_6^-]$). Although most prior work assumed a coarse-grained approach and simplified their structures to point charges or spherical molecules, RTIL charges have complex molecular structures and ellipsoid shapes (**Fig. 1.5**). The size of 1-ethyl-3-methylimidazolium ([EMIm$^+$], one of the most common cations, is 8.5 Å x 5.5 Å x 2.8 Å (158 Å^3 volume),[27] and bis(trifluoromethylsulfonyl)imide ([TFSI$^-$]) is 10.9 Å x 5.1 Å x 4.7 Å (224 Å^3 volume).[28] Although the neat (solvent-free) RTILs have greater theoretical electrochemical stability (~ 4.0 – 5.2 V)[23] and operating temperature range (–80 ºC ↔ +120 ºC)[29,30] than organic or aqueous solvated systems, they are denser and more viscous.[31] Even without a solvent, they still have solvation shells of co-ions and counterions around each ion. For [EMIm$^+$][TFSI$^-$], the first solvation shell around a cation is 13 Å and the second solvation shell is 17 Å in diameter.

The parabolic dependence of energy densities on electrochemical stability windows is shown in **Fig. 1.5**. All electrolytes and solvents have unique dimensions, molecular structures, and local dipole moments. These interactions are sufficiently strong to interact with electrode surfaces and influence charge accumulation and stability at the solid-electrolyte interface. Furthermore, organic molecules feature long tails, such as sulfone groups and alkyl chains (n = 2, 4, 6, 8, etc.) that influence steric limitations of their mobilities in confined pores.
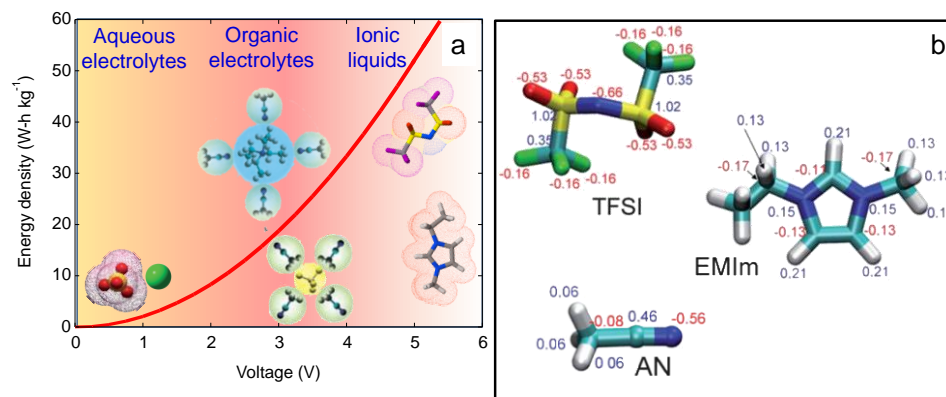
Figure 1.5. a) Voltage vs. energy density relationship and schematics of aqueous (Na_2SO_4), organic ($[NEt_4^+][BF_4^-]$ in CH_3CN), and $[EMIm^+][TFSI^-]$ ionic liquid electrolytes. b) Atomic partial charges around $[EMIm^+]$, $[TFSI^-]$, and CH_3CN.[28][7]

The ion electrosorption charge mechanism of supercapacitors gives them several performance advantages over conventional batteries with Faradaic storage mechanisms. The latter, as in the sample case of Li-ion batteries (LIBs), implement graphite anodes and metal oxide cathodes (such as $LiCoO_2$), along with lithium salts (typically $LiPF_6$, LiTFSI, or $LiBF_4$) electrolytes.[32] Single cells typically operate at 3.6 V and can store 700 to 2400 mAh per cell. The $LiCoO_2$ cathode has a theoretical gravimetric capacity of 274 mAh g^{-1} (140 mAh g^{-1} practical), while the anode is capable of storing up to 372 mAh g^{-1} (300-320 mAh g^{-1} practical).[33] However, the $[Li^+]$ shutting and anode intercalation process is much slower than electrostatic ion exchange in EDLCs. Consequently, while power densities of batteries do not exceed 1 kW kg^{-1}, supercapacitors offer 0.5 – 10 kW kg^{-1}. EDLCs can recharge in 0.5 – 60 seconds, whereas batteries typically require 1-5 hours. Battery modules are typically overloaded (more batteries than needed are connected in a network) to compensate for low output rates and add unnecessary weight and cost.[8] The cycle life of LIBs is limited by electrode stability and the solid-electrolyte interface (SEI) layer, which are both prone to

---

[7] Reproduced from Ref. [28] with permission of The Royal Society of Chemistry.

exfoliation, degradation, short-circuiting, and breakdown after 1,000 cycles. On the other hand, supercapacitors can charge/discharge over 1,000,000 times and typically exceed the lifetimes of the devices that they power. Electrosorption efficiency is not limited by thermodynamics and kinetics of phase reactions of ion intercalation, and EDLCs operate without swelling or generating heat. [8,34,35]

Despite these key advantages, electrochemical capacitors suffer a critical setback: they offer 90% smaller energy densities than their Faradaic energy storage systems. From a thermodynamic perspective, charge transfer is more energy-dense than electrostatic accumulation. Capacitance strongly depends on the accessible surface area; the highest theoretical SSA is 2,630 m^2 g^{-1} of graphene (discussed in section **1.3**), and its highest attainable capacitance (C_{sp}) is ~46 μF cm^{-2}.[36] No commercial devices currently operate above 2.7 V; this limits the energy density of EDLCs to ~8 Wh kg^{-1}.[34] Modules daisy-chain multiple supercapacitors in series and, subsequently, downgrade their power and energy densities. Electrodes with high surface areas and optimal pore structures typically implement expensive nanostructured carbons. Finally, many electrolytes, separators, and other device components are inherently toxic and unsafe to dispose or incinerate at the end of their usable life.[2,37,38] Future research efforts must holistically address these drawbacks, from fundamental electrosorption mechanisms to macroscale environmental sustainability, to facilitate broader implementation of electrochemical capacitors.

1.3 Porous Carbon Material Electrodes

Carbon electrodes are grouped into two main categories: porous (internal surface) and non-porous (external surface) materials. The most basic form of a non-porous, planar

electrode is graphene, which was first reported in 2004.[39] The structure is a sheet of sp^2-bonded carbon benzene rings and is mostly flat (with slight wrinkling). The π-π bonding nature of the material aligns its k-space Dirac cones to make the material a zero-bandgap semiconductor. Subsequently, it showcases near-metallic conductivity under an applied potential and a sufficiently high carrier density.[40] In addition to offering exceptionally high mechanical, electrochemical, and thermal stabilities, the single-sheet material offers a high theoretical SSA: 2,630 m^2 g^{-1}.[41] Owing to its idealized structure and high conductivity, graphene often acts the model electrode for molecular dynamics (MD) and density functional theory (DFT) simulations of charge accumulation and dynamics on its surface.[42] Single-layer graphene is produced via various mechanical or chemical exfoliation methods or *via* chemical vapor deposition. These approaches are expensive and difficult to scale up for commercialization. Furthermore, although single-layer graphene offers a C_{sp} of > 80 μF cm^{-2} (> 200 F g^{-1}),[43] it does not have sufficient areal capacitance to power any practical device. Other, scalable graphene synthesis approaches typically use thermal or chemical reduction of graphite oxide and further increase SSA with KOH activation.[44-46] The resulting electrodes, while still planar, feature few stacked layers (2-50) and an SSA in the 200 – 3,100 m^2 g^{-1} range. Although most models have, to date, overlooked the differences between edge and planar sites, the former are more reactive; this 1) makes them more susceptible to chemical modifications and 2) influences the dynamics and electrosorption densities of ions in supercapacitors.

In addition to graphene, other external surface allotropes of carbon offer high capacitance and power densities as supercapacitor electrodes. Carbon nanotubes (CNTs), especially as vertically aligned arrays on metallic current collector substrates, are highly

conductive electrodes with 100-200 m^2 g^{-1} SSA.[29,47] They are also often used in MD simulations as models of cylindrical pores, and various computational approaches have calculated ion[48] and molecule[49] adsorption both inside and outside of these structures. In actuality, there is no current clear consensus of whether charges actually enter nanotubes or just use the external surface; inner diameter dimensions (~1-10 nm), end caps, and any defects alongside the length[50] are important factors.[51] Other external surface carbon allotropes include carbon black (CB) powders, which are polycrystalline nanoparticles (~30 nm diameter) with 75-200 m^2 g^{-1} SSAs.[52] Spherical onion-like carbons (OLCs),[53] which are concentric fullerene structures (5-10 nm diameter), are produced *via* thermal treatments (vacuum annealing or laser heating) from nanodiamond precursors, offer 200-500 m^2 g^{-1}.[54] External surface carbons offer highly graphitized, electrically conductive electrodes that may be used as either standalone electrodes or conductive additives in conjunction with larger, disordered porous carbons (described below). Although external surface carbons exhibit inherently smaller SSAs (and smaller C_{sp}) than their porous counterparts, they do not confine ions in narrow pores. This critical difference minimizes ionic resistance (through bulk to electrode interface) and maximizes power densities of non-porous electrodes.

Internal surface carbons are a family of particles (20 nm – 100+ μm diameter) with nanostructured micropores ($d_{av} < 2$ nm), mesopores (2 nm $< d_{av} < 50$ nm), or macropores ($d_{av} > 50$ nm).[55] The pores are typically in the form of branched porous architectures inside of particles. Subsequently, internal pore systems offer greater specific surface areas (500 – 3,100 m^2 g^{-1}). Most of these carbons are semi-amorphous and feature heterogeneous mixtures of sp^2/sp^3 bonding and polycrystalline graphitic domains.[56]

The most common porous material is activated carbon (AC), which is produced *via* chemical (CO_2 or H_2O treatment at 800-900 ºC) or physical activation of carbonaceous materials (peat bog, phenolic resin, wood char, etc.).[57] Coconut shell precursors yield over 1,500 m^2 g^{-1} and nanostructured, well-ordered porosities ($d_{av} \approx 0.8$ nm). Other chemical processes, such as air,[58] acid (H_2SO4 or HNO_3),[59] and KOH activation[44] may further activate materials (including non-porous carbons described above) and maximize the prevalence of micropores. Templated mesoporous carbons, which are typically synthesized from silica templates and involve carbonization of various precursors, yield more monodisperse pores but are typically more expensive.[60] Carbide derived carbons (CDCs), which are synthesized *via* chemical etching of carbides, offer a highly tunable route to nanostructured internal surface electrodes with well-defined porosities and customizable graphitic structure.[61] Their structure, which is a key element of this dissertation, is described in greater detail in section **1.4** of this chapter.

Schematics of basic porous and non-porous electrodes and electrosorbed charges in each are shown in **Fig. 1.6**. Most internal and external surface materials are in the forms of powders. They mix with polymer binders, conductive additives (if needed), and assemble into freestanding electrode films (0.05 – 0.25 mm thick) using mechanical rolling and pressing. They can also be screen-printed or drop cast onto current collectors (like LIBs). Certain electrodes are synthesized as thin films (< 100 nm thick) or as bulk monoliths (> 1 mm) and can be directly transferred into cells. Suspension electrodes resemble redox flow batteries and rely on carbon-electrolyte slurries for grid-scale energy storage modules.[62] Finally, activated carbon fibers interweave, combine into elastic structures, and seamlessly integrate into textiles and flexible devices.[63] In practical

applications, total device capacitance strongly depends on areal capacitance (F cm^{-2} of electrode surface area), so high-density electrodes (typically with dense, porous materials) may be more advantageous than single-layer graphene structures.[64]
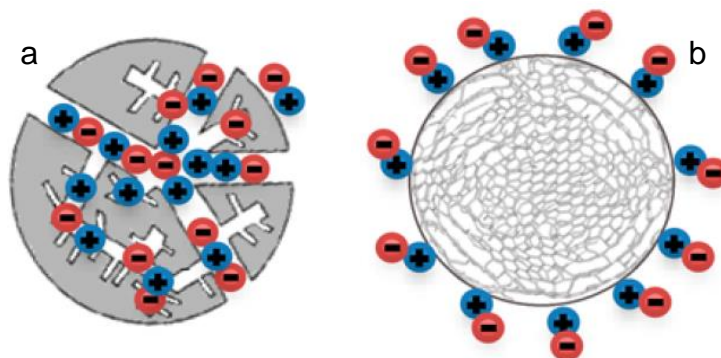
Figure 1.6. Ion electrosorption schematic for a) porous and b) non-porous electrodes.

Specific surface area and porosity are just a few of the numerous differences that influence capacitance and charge dynamics in external and internal surface electrodes. Non-porous carbons exhibit different surface curvatures. Based on MD simulations, smaller curvatures (narrower diameters of OLCs or CNTs) increase charge overscreening (counterions over co-ions) over a broad potential range and linearly increase differential capacitance ($\frac{dQ}{dV}$) with voltage.[65] On other hand, planar electrodes exhibit bell- and camel- shaped $\frac{dQ}{dV}$ curves (**Fig. 1.7**) and offer lower capacitance.[66] Since external surface carbons do not require ions to travel through narrow pores, bulk electrolyte limitations are lower for non-porous carbons. This advantage substantially decreases ionic resistance and increases the power densities and rate handling abilities of external surface electrodes.
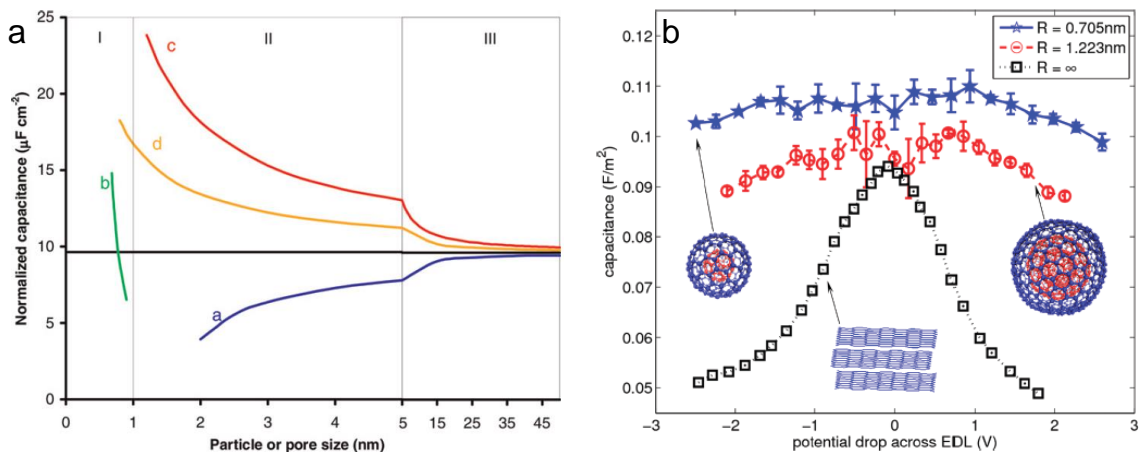
Figure 1.7. a) Influence of electrode surface curvature for internal surface (a = mesoporous and b = microporous carbons) and external surface (c = spheres and d = cylinders) electrodes.[48][8] b) Influence of curvature of non-porous carbons on differential capacitance (R_∞ = planar).[65][9]

On the other hand, C_{sp}, which inherently correlates with SSA, is inherently greater in porous electrodes. More importantly, the structure, ion exchange, overscreening, and packing density of the electrosorbed layer of ions in narrow pores (with matching ion-pore diameters) is fundamentally different from the diffuse double layer on external surfaces. While latter has more spatial degrees of freedom for ions and may be described, to a large extent, by classical models, confined ions require additional considerations of their behaviors and dynamics (described in section **1.5** of this chapter). From a geometrical perspective, ions in pores have greater contact with electrode surfaces. Subsequently, their chemical, electrical, and surface morphology properties are expected to have a significant (and different) influence on electrosorption behavior.

1.4 Carbide-Derived Carbons: Key Structures and Properties

CDC synthesis process was initially developed in 1918 for high-purity $SiCl_4$ production [67] and has since been optimized to maximize production of tunable

---

[8] From Ref. [48], copyright 2010, reproduced with permission.
[9] Reprinted with permission from Ref. [65]. Copyright 2011 American Chemical Society.

nanoporous carbon. The method chemically etches metals from metal carbides (MC) using Cl_2. The most common reaction is shown below in **Eq.1.12:**[68]

$$MC(s) + 2Cl_2(g) \rightarrow MCl_4(g) + C(s) \tag{1.12}$$
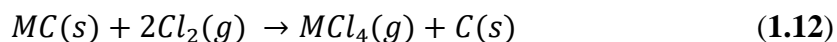
The reaction is thermodynamically favored to proceed above 200 °C. At that temperature, metal chloride products are in a gaseous state and can easily escape the particle structures, leaving the pure carbon behind.[67] As the metal is etched out the carbon retains the original material's volume and structure, self-reorganizes around new vacant sites, and bonds to local carbon atoms to form the corresponding pore structure. Resulting pore size distributions depend on the carbide precursor, factoring in both the initial lattice structure (NaCl,[67] orthorhombic,[68] trigonal (B_4C), hexagonal (MAX phase,[69]) etc.) and the diameter of the removed metal atoms to determine the resulting conformation to specific porous structures. Virtually any carbide may act as a precursor. Titanium carbide (TiC) and silicon carbide (SiC) yield most ordered porosities and are often used for synthesis of CDCs for supercapacitors, but molybdenum carbide (Mo_2C),[70,71] vanadium carbide (VC),[72] and many others have also been reported.

The chlorine treatment temperature is a key factor that influences pore size distribution. At higher temperatures, carbon atoms are more mobile and re-arrange themselves to increase the SSA and shift the pore size distribution from a predominantly microporous to a mesoporous range. CDC structure and the relationship between various carbide precursors, synthesis conditions, and the resulting pore sizes are shown in **Fig. 1.8**. Systematic studies of the various CDC synthesis parameters have produced SSA values between 500 $m^2 \, g^{-1}$ [68] and 2,000 $m^2 \, g^{-1}$ [73]. Average pore diameters range from 0.33 nm to over 5 nm [69] and are significantly more monodisperse than comparable

nanostructured activated carbons. Select systems, such as B_4C-CDC and Mo_2C-CDC, offer tunable bimodal pore size distributions (PSDs) at certain synthesis conditions.[74,75] In addition to offering high capacitance, these properties make CDC a useful model system for fundamental ion confinement and electrosorption studies.
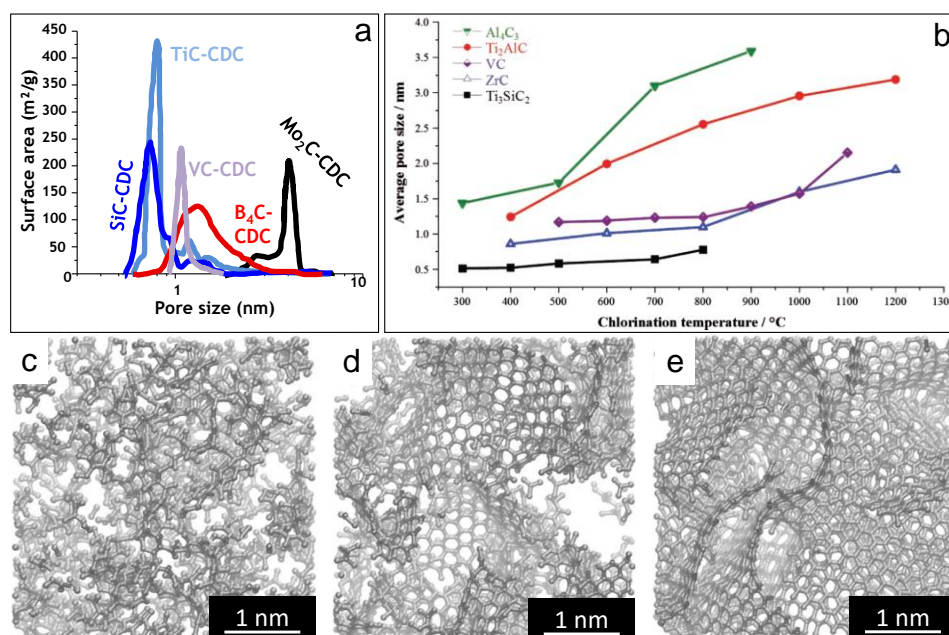
Figure 1.8. a) Influence of carbide precursor on resulting typical CDC pore size distributions. b) Influence of synthesis temperature on resulting average pore size.[67][10] Quenched Molecular Dynamics estimate the temperature-dependent graphitic structure of TiC-CDC synthesized at c) 600 ºC, d) 800 ºC, and e) 1,200 ºC.[76][11]

Graphitic structures of initial CDCs resemble typical internal surface carbons (**Fig.1.8 (c)-(e)**). They contain a mixture of graphitized and amorphous phases, have small heterogeneously distributed sp^2 and sp^3 bonding, and feature short-range correlations. Higher Cl_2 synthesis temperatures yield greater graphitization and sp^2 domain growth along the [100] direction, as evidenced by narrower Raman G band peaks [77]. At chlorination temperatures above 1,000 °C, grain growth along both [100] and [002]

---

[10] Reprinted by permission from WILEY-VCH Verlag GmbH: *Adv. Functional Materials*, Ref. [67] copyright 2011.
[11] Reprinted from Ref. [76], Copyright 2010, with permission from Elsevier.

directions become more pronounced, along with thermodynamically-favored rehybridization of remaining sp^3 bonding into sp^2.[78] Transitions from amorphous carbon to turbostratic graphite increase prevalence of graphitic ribbons, barrels, and fullerene-type allotropes.[67] Magnetotransport and electrode conductivity measurements [79] showed that, at the same 1000 °C temperature threshold, the electron transport network through CDCs shifts from a semiconducting to a metallic one. Conductivity modeling [80] determined that the percolation threshold (transition to metallic conductivity) accompanied emergence of long-range networks of ordered graphitic domains. Most prior computational models of capacitance and charge dynamics in CDCs had assumed universal metallic conductivity for all carbons (disregarding structured that had actually corresponded to the simulated PSDs), and no studies have addressed the implications of this discrepancy.

Immediately after chlorination, porous carbons contain many dangling and chlorine-terminated bonds, which are likely to react with air or electrolytes. To stabilize the surfaces, CDCs are typically annealed with H$_2$ (g) or NH$_3$ (g) at 600 °C to remove any residual Cl$_2$.[81] Since the newly synthesized carbon structure has a chemically unstable surface, these annealing steps selectively deposit functional groups and graft treatment-specific chemical species onto pore walls. Typically, hydrogenation yields the C–H functional group, while amination yields a heterogeneous mixture of C–N groups (C=NH, C–NH$_2$, quaternary nitrogen, etc.). [82] The resulting CDC surface chemistry is very robust and significantly influences interactions with electrosorbed ions.

Since carbides undergo a conformal transformation during synthesis,[83] their diameters remain unchanged (1-5 μm diameters, typically produced *via* ball milling of

coarser TiC powders). Although most commercial devices use micrometer-sized carbon particles, a recent study [84] had shown greater capacitance for 30 nm sized particles. These nanoparticles [85] require high-energy plasma synthesis of 20 nm TiC precursor nanopowders.[86] Nanosized CDC powders are significantly more expensive and are, at present, at an economic disadvantage compared to most cheap activated carbons.

Beyond economic costs, the fundamental advantage of fine-grained electrode particles is still ambiguous. There is some debate about thermodynamics and phase transitions of ion filling and defilling.[87] Behaviors of ions in bulk and in confined states may be inherently different.[88] In that case, the FSI will significantly influence ion exchange during cycling and resulting capacitance of charges in confined pores.

CDCs have a broad range of potential promising applications beyond electrochemical energy storage. Their pores have demonstrated high capabilities of cytokine sorption, and are, subsequently, useful in dialysis medical devices to treat sepsis and inflammation.[89,90] Much like activated carbons, CDCs can filter water and convert seawater brine to potable water *via* capacitive deionization.[91] CDCs with larger pores have shown promising performance as substrates for high-SSA catalytic supports and mechanically strong tribological coatings.[92] These applications require finely-tuned deposition of materials (Au, Pt, Cu, etc.) into pores and favorable pore wall substrates. Therefore, insights into chemical and structural properties of CDCs are applicable to diverse applications and will expand the use of these unique porous carbons.

1.5 Influence of Ion Confinement on Capacitance and Charge Dynamics

Most prior efforts have focused on the charge: pore size ratio and have noticeably optimized porous carbon structures to accommodate ions. Conventional wisdom had predicted that larger pores, which yielded higher specific surface areas, would linearly correlate with higher capacitance. However, a 2006 study by Chmiola *et. al.* discovered anomalous capacitance increases for CDCs with 0.6 – 0.8 nm pore diameters (**Fig. 1.9(a)**).[77] These dimensions matched the sizes of desolvated $[NEt_4^+]$ and $[BF_4^-]$ ions. Subsequent work has repeatedly shown that a tailored pore structure, which matches its diameter with the ion that it confines, desolvates ions and maximizes capacitance.[35] ±0.05 nm diameter deviations have drastically (±40%+) influenced C_{sp} (**Fig. 1.9(b)**).[93]

Confined ions, especially in such narrow pores, are expected to exhibit fundamentally different double layer configurations dynamics that deviate from prior classical understanding. To that end, recent Molecular Dynamics (MD) and Density Functional Theory (DFT) simulations have evaluated the behaviors of individual ions in pores and discovered an oscillatory relationship between ion size and pore size.[94] Depending on the number of ions that can fit across the diameter of the pores, the resulting layers of co-ions and counterions may form constructive or destructive interferences (shown in **Fig. 1.9(c-d)**).[95] However, most of these models have simplified ions to coarse-grained spheres with no remarkable interactions between the surfaces of ions and pores.
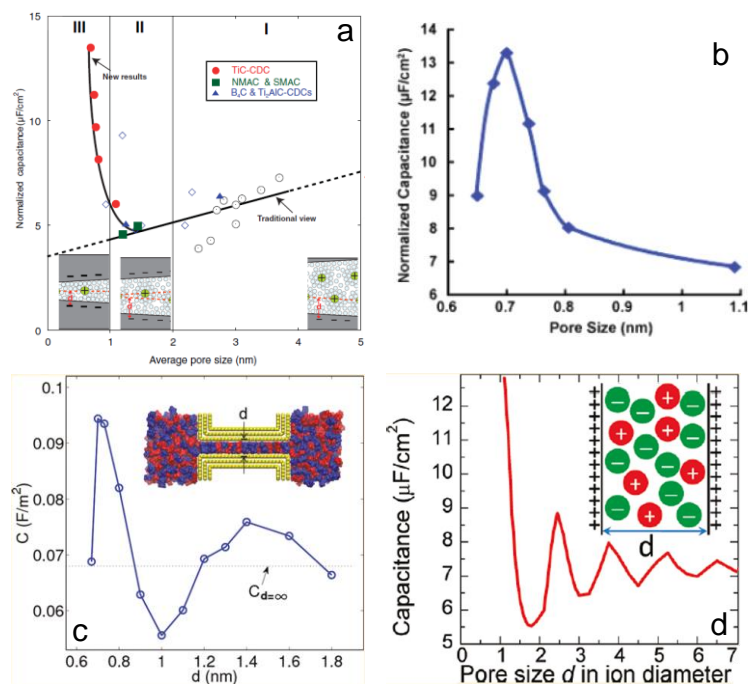
Figure 1.9. a) Relationship between ion size and resulting capacitance. Region I corresponds to larger pores and less confinement. Region II corresponds to slight ion desolvation, and Region III corresponds to total ion desolvation and highest capacitance.[77][12] b) Experimentally derived relationship between CDC pore diameter and capacitance of acetonitrile-solvated $[NEt_4^+][BF_4^-]$.[96][13] c) MD-derived [14] and d) DFT-derived [15] oscillation curves that demonstrate the constructive and destructive interference between double layers from confined ions in differently sized pores.[94,95]

Since narrow pores must allow tight packing of similarly charged ions, a considerable amount of electrostatic repulsion must drive co-ions further apart and establish minimal separating distances (in part, governed by the Lennard-Jones potential). However, a superionic state model, which was proposed in 2011, described a mechanism by which counterions are expelled from pores (and replaced by even more co-ions) at sufficiently high potentials.[97] This process maximizes charge packing densities.[98] Conductive metallic pore walls generate sufficient point charges to screen identically charged co-ion neighbors and allow them to achieve maximum proximity and packing in pores (**Fig.**

---

[12] From Ref. [75]. Reprinted with permission from AAAS.
[13] Reprinted with permission from Ref. [77]. Copyright 2008 American Chemical Society.
[14] Reprinted with permission from Ref. [96]. Copyright 2011 American Chemical Society.
[15] Reprinted with permission from Ref. [95]. Copyright 2011 American Chemical Society.

1.10.(a)).[99] Recent Nuclear Magnetic Resonance (NMR) measurements of CDCs partially corroborated this behavior: graphitized carbons, with larger ordered sp^2 domain sizes, exhibited stronger ring currents and more effectively shielded electrosorbed ions.[100] Smaller pores exhibited overlapping ring current effects from carbon structures on both sides of pores and further amplified this effect. *In situ* small-angle neutron scattering (SANS) measurements showed that smallest pores can, in fact, be only filled ("electrowetted") under sufficiently high applied potentials.[101] However, most porous carbons (including CDCs) exhibit very diverse graphitic structures with corresponding electronic properties. As described in section **1.4**, this behavior depends on CDC synthesis temperature and ranges from semi-conductive to conductive. Furthermore, pore diameters are positively correlated with graphitization: narrow pores are typically present in amorphous CDCs. Existing research does not present a specific electrode conductivity threshold at which image forces in the carbon structure become sufficiently strong to screen co-ions and facilitate the superionic state in pores.

The superionic state of carbon electrode likely strongly correlates with the electronic densities of state (DOS) of the material. Since graphene is a zero-bandgap semiconductor, increased applied voltages inject additional charge carriers into higher electronic DOS near the Fermi level.[102] This voltage-dependent capacitance increases charge screening of electrosorbed ions and boosts C_{sp} at higher potentials.[103] From a measurement perspective, it is described by a "butterfly"-shaped current-voltage relationship,[104] which contrasts with the idealized rectangular shape of ideal, classic supercapacitors (**Fig. 1.10(b)**). Physical distortion of the carbon structure, such as mechanical bending or crumpling, may press π–π delocalized bonding regions closer and achieve the same

effect.[105] However, all studies that have demonstrated this effect have implemented external surface carbons (nanotubes, OLC, etc.) and have not considered confined ion systems, which specifically applies to the superionic state model.
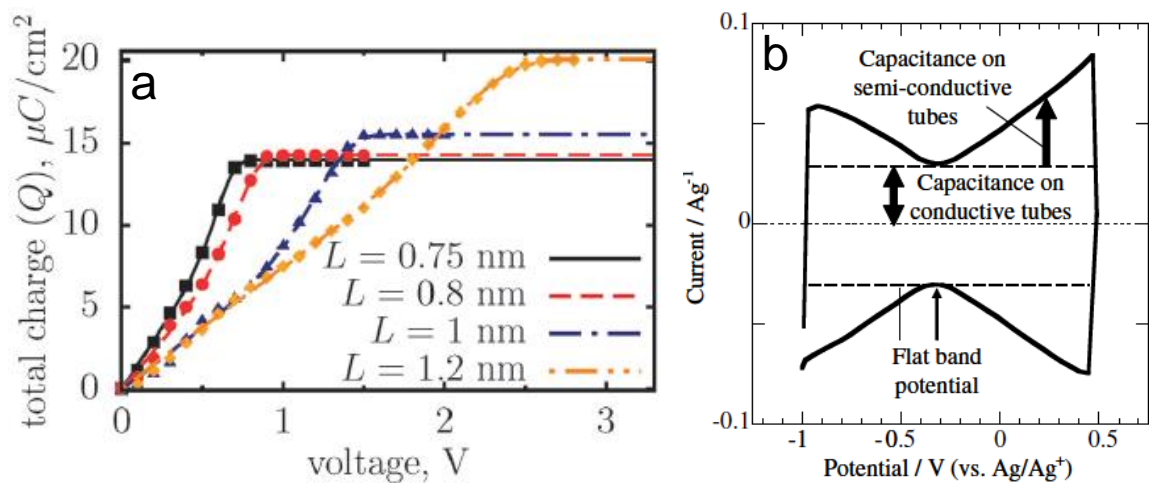
Figure 1.10. a) Saturation of the total charge accumulated in a pore. The charge vs. voltage relationship differs for each pore diameter (L).[97][16] b) Cyclic voltammogram behaviors for conductive and semi-conductive non-porous carbon electrodes.[103][17]

Although pore diameter has been the focus of most studies of electrosorption and capacitance, pore shape also significantly influences capacitance. Calculations of interaction potentials for ions in cylindrical pores (*i.e.,* nanotube-shaped) showed greater co-ion screening than in similarly sized slit (*i.e.*, peapod-shaped) pores. Cylindrical pores surround ions with "metallic" surfaces from more directions than slits, and the screening length is $0.21 \cdot d_{av}$ (as opposed to $0.32 \cdot d_{av}$ in slit pores).[106] CDC synthesis temperatures, along with precursor carbides, likely influence resulting pore shapes. Small-angle neutron scattering (SANS) measurements had shown that microporous, low-temperature TiC-CDCs ($Cl_2 < 600$ °C) predominantly feature spherical pores, whereas higher-temperature CDC pores are mostly slit-shaped.[107] Previous studies, which had analyzed influence

---

[16] Reproduced from Ref. [97] with permission of The Royal Society of Chemistry.
[17] Reprinted from Ref [103], Copyright 2008, with permission from Elsevier.

of Cl_2 synthesis temperature on capacitance, had ignored pore shape differences. On the other hand, SANS-derived conclusions regarding pore shape were primarily based on comparison of neutron scattering and gas sorption data, and the accuracy of "fits" of scattering with Density Functional Theory (DFT) modeling of N_2 adsorption isotherms. It is a fairly imprecise process and limited by the predetermined software data kernels. Other methods, such as Transmission Electron Microscopy, cannot accurately assess pore dimensions in internal surface carbons, and no existing studies provide more definitive analyses of the impact of pore shape on charge densities and dynamics in supercapacitors.

The work described above has universally overlooked specific interactions of ions with surface groups or evaluated the structural arrangement and interactions of electrosorbed charges in pores. However, recent efforts have partially considered the significance of the ion and pore dimensions and correlated them with resulting ion dynamics and capacitance. Densities of electrolytes typically decrease upon entering narrow pores, as charges assemble into complex clusters and attempt to establish configurations with minimal Gibbs free energies. Although confined ions typically exhibit lower mobilities than their bulk counterparts, lower electrolyte densities ($\rho \approx 0.8 \cdot \rho_{bulk}$) maximize ion transport rates.[108] Furthermore, lower pore loading results in localized clustering of ions and heterogeneous pore filling in terms of local densities.[109] Surface functional groups, which may attract (or repel) such charge agglomerations, influence densities and resulting electrolyte dynamics.[110,111] Although structural lattice gas models (for electrodes) have correlated diffusion-driven mobilities with electrosorption dynamics,[112] this coarse-grained approach cannot be directly applied to heterogeneous, semi-disordered carbon-electrolyte interfaces.

The density of electrolyte filling in porous systems depends on the intrinsic properties of electrosorbed electrolytes. Although RTILs require no solvents, they demonstrate a certain degree of ion-ion correlation in the bulk state and weak solvation radii of cations and anions around each other.[31,113] The molecules typically feature functional groups with strong dipole moments (C–F, S=O, –S–N–S–, etc.) and interact with surface charges and functional groups. Depending on the matching electrode-electrolyte surface chemistries, the FSI may be either ionophilic or ionophobic, which, in turn, may align the ions in parallel or perpendicular configurations with respect to pore walls.[28,114,115] Although prior research has demonstrated greater ion mobilities in functionalized pores,[116] differences in ion dynamics between oxidized and defunctionalized pore systems are not yet certain. Since the cations and anions of RTILs typically feature different sizes and functional groups (with different dipole moments),[28] simulations[108] and initial experimental data[116] predict different dynamics for each; cations are expected to be more mobile than anions. MD simulations predict that alkyl chains (on imidazolium-based cations) take advantage of lower pore fillings and occupy leftover void space in the pores.[117] Such configurations, which are affected by pore wall surface chemistry and hydrophobicity of the FSI, change the viscosity of confined ionic liquids and facilitate formation and swelling of macrophase ion aggregates. These arrangements significantly change the ion-ion correlation and layering in the confined diffuse ion/counterion layer. Simulations predict a 15-20 Å limit[118] to long-range charge ordering in pores (2-3 layers) and negligible contributions of ions outside of this threshold to the overall capacitance of the system.[118,119] Although this finding closely

correlates with the oscillatory behavior of MD/DFT simulations, it requires proper understanding of the significance of heterogeneity and disorder at the FSI.

1.6 Impact of Functional Groups and Graphitic Defects

The structure and surface composition of most experimental carbon electrodes is far from ideal. CDCs often include C–Cl, C-–H, and C–NH$_2$ groups that stem from halogen treatment and subsequent H$_2$/NH$_3$ annealing.[81] Various hydroxyl (–OH), acid/carboxyl (–HCOO), and carbonyl (–O–C=O, =O) groups originate from exposure of the material to air.[85] Structural defects and lattice strain points are often present[120] in carbons. The predominantly amorphous carbon structure is composed of short-range sp^2 bonding,[76] heterogeneous sp^3 (and even sp) bonding phases, and grain boundaries. Planar graphite structures contain monovacancies and divacancies, Stone-Wales transformations, and 5–, 6– and 7– member rings (with 108º, 120º, and 129º, respectively, as internal angles). Graphite edges, which are present around planar graphene and may randomly protrude on pore surfaces, influence surface heterogeneity and texture.[121] These defects alter surface charge concentrations, Fermi energy levels of distinct domains, surface morphology (roughness) of interfaces, electrode-electrolyte intermolecular interactions, and steric limitations of ion mobilities. These heterogeneous surface features have diverse, and, in certain cases, contradictory influences on capacitance, electrolyte dynamics, and electrochemical stability under higher applied potentials.

Surface defects (both functionalities and structural deformations) disrupts sp^2-inherent π-π bonding symmetry, magnify the p$_z$-controlled density of states, and drive extra charge carriers into defective graphene's conduction band under sufficiently high applied

potentials. This charge accumulation, which acts as a quantum capacitance (C_Q) contribution, may increase by over 300% due to electrode surface defects.[122] Recent fundamental investigations[122,123] simplified the total supercapacitor charge storage calculation to a 2-capacitors circuit, in which the contributions act in in series as follows:

$$\frac{1}{C_{total}} = \frac{1}{C_Q} + \frac{1}{C_{dl}}$$

(**1.13**)

This relationship dictates that the smallest capacitor in series has the greatest impact on total capacitance. When considering electrode systems with several stacked graphene layers, the quantum capacitance contribution (governed by electron density of states, E_F level, and Brilloin zone boundaries[123-125]) dominates until sheet stacking number reaches 4. When those conditions are exceeded, C_Q becomes exceedingly large and the C_{dl} ("standard capacitance" from ions) becomes the rate limiting, dominant factor.[126]

Previous modeling work calculated a 0.0 V Dirac point for ideal graphene that correspons to a thermally-governed value of 0.8 $\mu F\ cm^{-2}$. The capactiance increases nearly linearly from that position in the positive and negative applied voltage directions,[123] at an approximate rate of 23 $\mu F\ cm^{-2}\ V^{-1}$. Although single-layer graphene includes structural imperfections (Stone-Wales defects, monovacancies, curvature, chemical species, etc.), it operates under a linear C_Q vs. V relationship.[127]

As shown in **Fig. 1.11**, all defects independently contribute different magnitudes to total C_q. However, all computaiton analyses and experimental results concern steady-state charge accumulation and do not account for ion dynamics during charge/discharge processes. All prior C_Q studies have focused on few-layer graphene. None have successfully evaluated this effect for porous electrodes with ions in confined pores. Furthermore, since C_{dl} becomes the limiting capacitor in thick electrodes, the magnitude

of C_Q contribution strongly depends on the interpore thickness (the number of graphene sheets in the pore walls between each electrolyte-occupied pore). This is, in all likelihood, a heterogeneous value that varies throughout electrode particles; there is no reported consensus on its magnitude or distribution in CDCs. Furthermore, since prior WAXS results have indentified greater sheet stacking in the [002] direction for CDCs that had been synthesized at higher temperatures,[128] this parameter (and the resulting C_Q contribution) is unique to each electrode system.
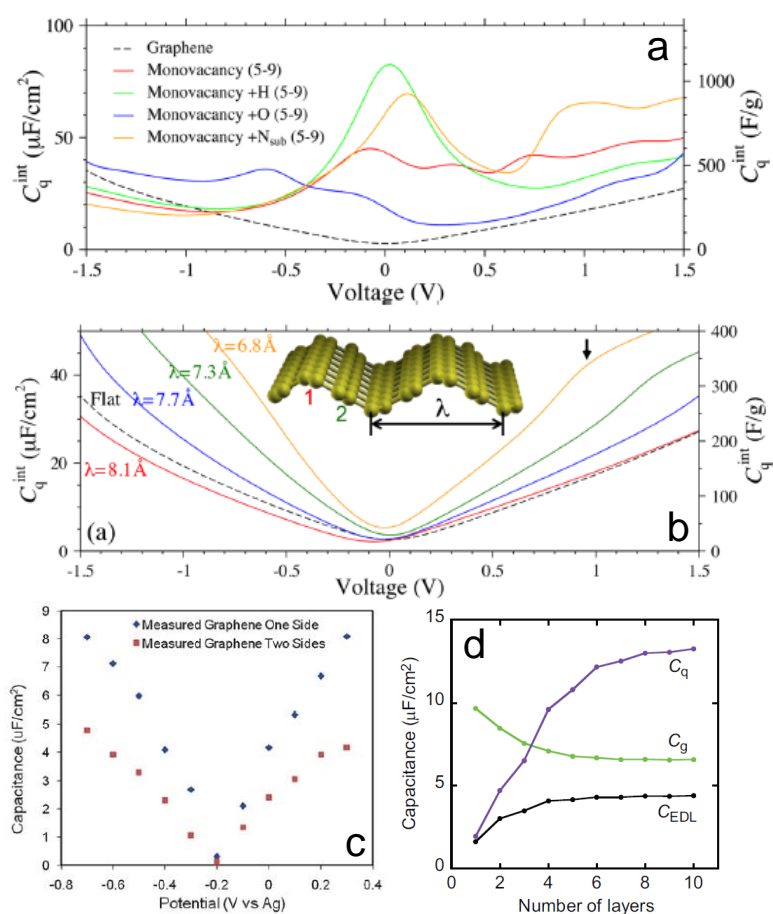
Figure 1.11. Voltage-dependent C_Q contributions from a) vacancies and surface chemical species and b) ripples and corrugation of graphene.[122][18] c) Measured C_Q contribution from single-sided graphene and double sided graphene (the latter resembling a wall between adjacent pores).[41][19] d) Relative influence of C_Q and C_{dl} on total capacitance (Cg). Transition at the 4-layer thickness is clearly visible.[126][20]

---

[18] Reprinted with permission from Ref. [122]. Copyright 2013 American Chemical Society.
[19] Reproduced from Ref. [41] with permission of The Royal Society of Chemistry.
[20] Reproduced with permission from Ref. [126] from the Nature Publishing Group.

Structural defects on pore surfaces also likely influence the packing and arrangement of ions at charged electrode-electrolyte interfaces. Recent MD simulations suggested that voltage-dependent differential capacitance (DC) exhibits a camel (U)-shape on atomically smooth basal planes and a bell-shape on atomically corrugated, prismatic surfaces (**Fig. 1.12**). The latter case yields greater DC values, primarily because the rough surface reconstruction inhibits dense ion packing and improves ion mobility under applied potentials.[129] Furthermore, structural defects do not noticeably slow down ions that fill pores.[130] However, this assessment somewhat contradicts prior conventional wisdom, which had correlated denser charge packing in the Helmholtz layer with greater capacitance. Other computational analyses have also shown that uneven electrodes interfere with double layer oscillations on planar surfaces, and charging/discharging processes disturb ion arrangement on surfaces and result in less dense, disordered co-ion and counterion layers.[131] This property has been universally overlooked, and few experimental techniques can properly assess atomic-level corrugation on pore walls, which originate from microcrystalline grain boundaries or protruding functional groups.
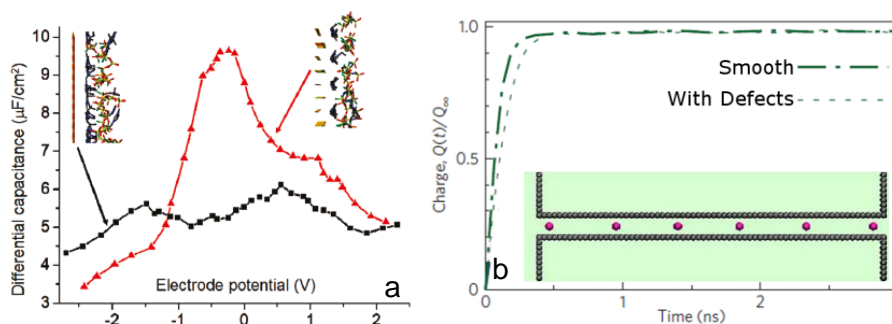
Figure 1.12. a) Differential capacitance for atomically smooth (camel-shaped) and corrugated (bell-shaped) electrode surfaces.[129][21] b) Charging dynamics of ions into pores with smooth surfaces and protruding defects (inset shows top view of pore).[130][22]

Porous carbons, including CDCs, typically become exposed to reactive synthesis conditions and air-filled environments. As a result, their surfaces rapidly obtain different chemical groups. The most common ones include hydroxyls,[132] quinones,[81] lactones,[133] carboxyls,[52] and nitrogenous groups, all of which either chemisorb during post-chlorination treatment or subsequent air exposure (**Fig. 1.13(a)**). They transform carbon surfaces, which are initially hydrophobic,[134] into more hydrophilic ones that decrease interfacial energies between electrodes and electrolytes. Per the combined Dubinin-Serpinsky-Do water adsorption model, maximum H_2O intake by porous carbon surfaces depends on the presence of adsorption sites (mesopores or functional groups), capillary action, and subsequent saturation.[134] The dynamics of pore wetting with solvent-free neat ionic liquids are still being developed, and the effects of surface functionalization and subsequent hydrophobicity [135] in the nanoporous regime are not yet completely clear.[52] Furthermore, since the functional group tails and dipole moments of electrolytes and solvents may be either hydrophilic or hydrophobic, each (functionalized) FSI is inherently unique. Subsequently, modifications of the carbon structure must account for changes to surface functionality and liquid adsorption sites to accurately predict ion dynamics and capacitive behavior.
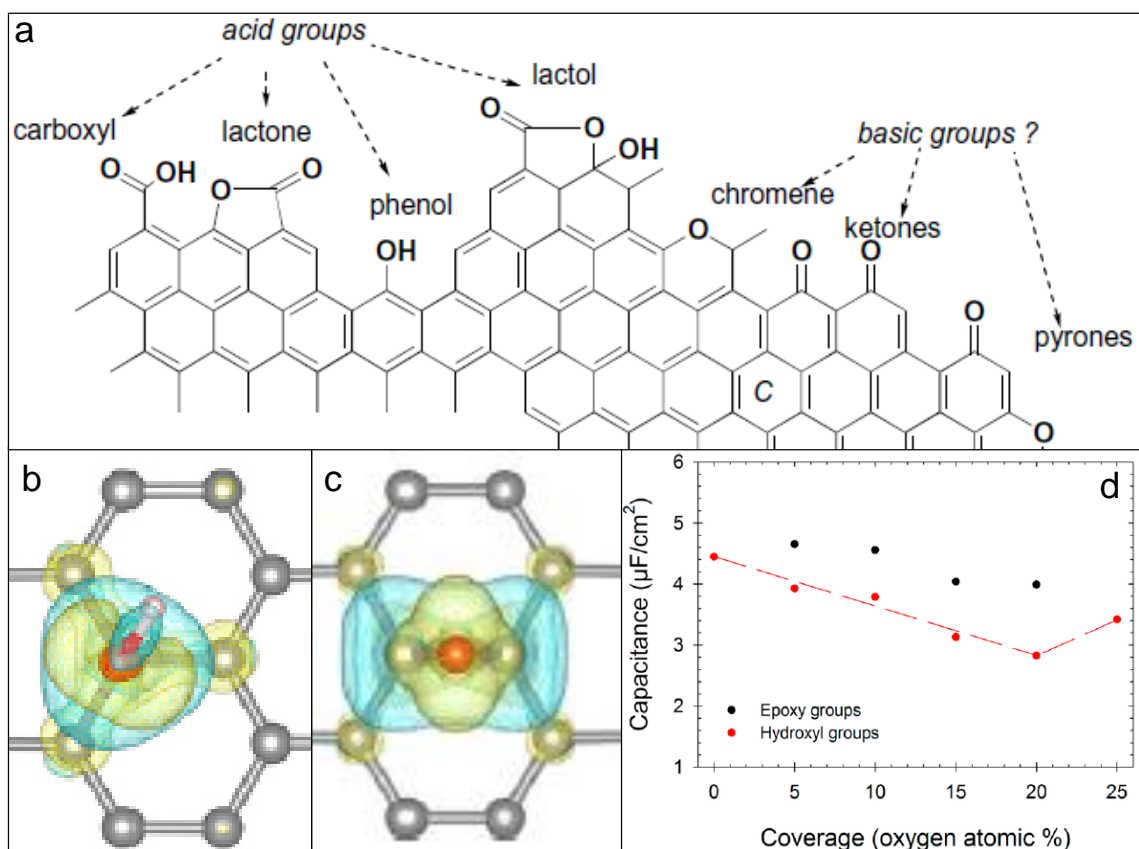
Figure 1.13. a) Summary of acidic and basic oxygen functionalities on carbon surface.[136][23] Top view of orientation of H_2O molecule on graphene surface with b) –OH groups and c) =O groups.[137][24] d) MD simulation results that compare capacitance of differently functionalized graphene in [BMIm$^+$][OTf$^-$] ionic liquid electrolyte.[138][25]

Specific chemical species (–OH, –R–O–R–, etc.) may interact with ions and selectively influence their orientation on the functionalized pore wall, impeding their mobility and depressing C_{sp} by 2-3 µF cm^{-2}.[138,139] Certain chemical groups (–HCOO, –O–C=O, etc.) may sterically hinder ion movement by pinning ions at narrow pore openings and blocking rapid electrolyte transport (**Fig. 1.13**).[113,140] Orientations of polar molecules (such as H_2O) on functionalized surfaces depend both on the dipole moments of the molecules and their unique interactions with selective functional groups

[23] Reprinted from Ref. [136]. Copyright 2003, with permission from Elsevier.
[24] Reprinted from Ref. [137], Copyright 2015, with permission from Elsevier.
[25] Reprinted with permission from Ref. [138]. Copyright 2014 American Chemical Society.

on surfaces.[141] Certain groups, such as carboxyls or complex amines, are larger than elemental hydrogen or oxygen adatoms on surfaces. Subsequently, selective surface chemistry compositions may promote or impede ion and solvent molecule mobilities.[113] However, the influence of pore chemistry on ion permeability has been calculated mostly for aqueous electrolytes. Those studies had driven ion and solvent motion by osmotic pressure (and not applied potential), and observed behaviors may not directly translate to identical electrosorption trends. Furthermore, pore shape, length, and termination (*i.e.*, whether the channel is open on one or both ends) are unique for each system and affect ion transport. Existing characterization methods cannot trace each pore from start to finish and assess every bulk electrolyte-pore opening interface.

There is no clear consensus regarding the benefits or drawbacks of ionophilic pore surfaces. Although they may improve ion mobility, they reduce ion filling density, and the net effect on capacitance is unique to each electrode-electrolyte interface. Recent work by Kondrat and Kornyshev holistically examined the entire pore, including both the interface and confined ions, and compared it to a mechanical spring.[87] A tight spring is harder to compress, but stores more energy. Recent Monte Carlo simulations applied mean-field theory and determined that ionophobic pores, which repel ions, charge quicker than ionophilic pores (**Fig. 1.14**). This approach moves beyond the classic free energy density functional and integrates it into a lattice gas model to derive a continuum kinetic equation for an interacting 2-component system.[112] The resulting model for charge dynamics resembles the Poisson equation and assumes coarse graining, with ion dynamics closely dependent on charge densities in pores. Ionophobic pores are initially empty (vacuum-filled) and do not require counterion de-filling; the ionic liquid moves

through the empty channels in a front-like manner.[142] On the other hand, ionophilic pores incur diffusion limitations and decrease overall energy and power densities.[143]
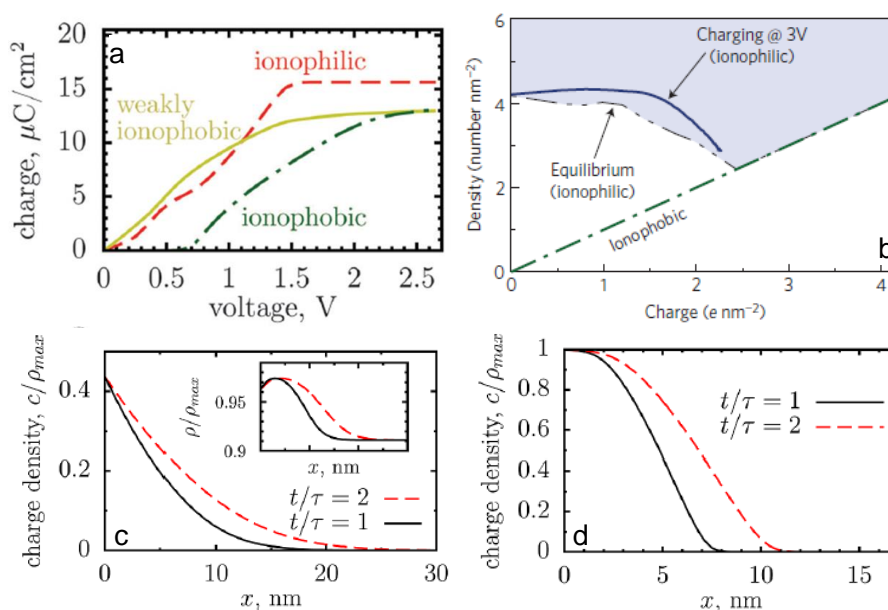
Figure 1.14. a) Charging energies for different pore systems under applied potentials.[87] b) Map showing average charge densities in ionophilic and ionophobic pores under neutral and applied potential regimes. Total charge is the shaded grey area.[130][26] Charging dynamics are shown for c) ionophilic pores (inset shows "congestion" of ions at pore entrances) and d) for ionophobic pores.[142][27]

This approach requires ionophobic pores to be initially under vacuum,[144] which is impractical in any experimental condition: most pores either contain some electrolyte or ambient gas (Ar, N_2, O_2, etc.) from standard cell preparation. The model, which simplifies pores to identical metallic cylinders, does not explain the origin of ionophobicity or ionophilicity of different system; interfaces are identical in both cases. However, experimental systems with tuned surface chemistries composition could resemble ionophilic or phobic interfaces and yield different filling dynamics.

Although oxygen-containing groups are the most common surface functionalities on porous carbons, various studies have evaluated the presence of nitrogen-containing

---

groups on capacitive performance of carbon electrodes.[145-148] Nitrogen can be added using wet chemistry methods (such as reaction with nitric acid, urea, melamine, and other reagents [146]) or by reacting the carbon substrate with ammonia. The resulting nitrogenous groups are either N-6/N-5 pyridines in the graphitic lattice or quaternary nitrogens (with bonded hydrogen) on plane edges.[147] Depth profiling elemental analysis showed that 70% of the adsorbed nitrogen is on the outermost carbon layer, with 27% of the remaining N atoms contained in the first few graphitic layers.[145] The extra electrons from nitrogen's valence shell add to the delocalized π-bonding of the material and enhance conductivity.[149] Potentiometric titration measurements showed strongly charged surface sites enriched with nitrogen that could attract polar molecules.[146]

Incorporation of nitrogen in carbon electrodes has attracted some interest due to possible pseudocapacitive reactions that maximize the material's charge storage. A possible reversible pseudocapacitive reaction is described in **Eq. 1.14** below [150]:

$$C^* = NH + 2e^- + 2H^+ \leftrightarrow C * H - NH_2 \qquad (1.14)$$
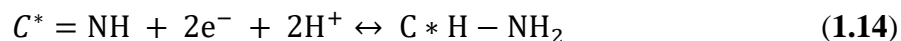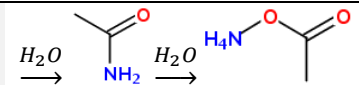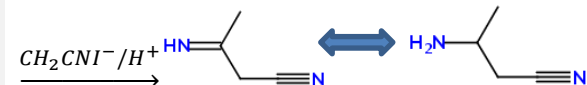
Although most redox-active pseudocapacitors exhibit distinct charge transfer cyclic voltammogram peaks, charge/discharge processes of aminated carbons are generally rectangular and more characteristic of classic supercapacitors.[150] To date, no specific redox peak has been identified for the reaction in **Eq. 1.14**, and nitrogen-enhanced capacitance remains open to interpretation.[145,146,149] This behavior occurs in both aqueous and organic electrolytes (which are less likely to protonate electrodes).[150]

Surface defects likely significantly influence the electrochemical stability of electrolytes. Aqueous-based electrolytes (such as H_2SO_4 and Na_2SO_4) suffer from the dielectric breakdown of water.[23] While the loss of solvent will, over time, result in the

solid deposition of salts and device failure, irreversible reactions protonate surface functional groups and produce various pore-blocking organic compounds.[151] Therefore, most aqueous supercapacitors may only operate in the 0.5-1.0 V window.

While ionic salts (such as $[NEt_4^+][BF_4^-]$ dispersed in organic solvents, such as acetonitrile, are thermodynamically stable up to 4.0 V applied potentials (the $[BF_4^-]$ ion itself is stable up to 5.1 V),[23] functional groups react with both the solvent and the dissolved ions to similarly degrade cyclability. Spectroscopy and chromatography studies have revealed CH_4 and HF byproducts and suggest several breakdown processes at positive and negative potentials (**Table 1.2).**[25] Breakdown-induced pore blockage can reduce electrodes' SSA by as much as 49% [151] and effectively negate all advantages microporous, internal surface carbons. Ionic liquid ions ($[BF_4^-]$, $[PF_6^-]$, $[TFSI^-]$, etc.) decrease electrochemical stability of organic solvents, such as CH_3CN and various carbonates, *via* proton transfer and H– and F– abstraction reactions.[152] Spectroscopy studies have suggested possible formation of solid-electrolyte interfaces (SEI), which are common for batteries but not expected for supercapacitors, on carbon surfaces after $[TFSI^-]$ and $[PF_6^-]$ electrochemical cycling.[153] Reactions with –OH and –COOH groups may promote breakdown of $[EMIm^+]$ (releasing H_2 that blocks pores and degrades charge storage).[154] Analysis of decomposition materials had previously identified breakdown byproducts (such as HBO_3) that only form at high temperatures [25]. These findings suggest that functional groups, which increase electrical resistance of electrodes, may amplify Joule heating and accelerate electrochemical breakdown.

Table 1.2. Summary of selected electrochemistry breakdown processes of organic solvents and ionic liquid anions. All shown reactions incorporate H^+ ions or H_2O functionalities that are chemisorbed on electrode surfaces. Adapted from Ref. [25].

Reaction Type	Starting Species	Reaction Pathways
Hydrolysis	$H_3C-C\equiv N$	
Dimerization	$H_3C-C\equiv N$	
Hydrolysis	$[BF_4^-]$	$[BF_4^-] \rightarrow BF_3 + F^-$ $BF_3 + HF \rightarrow HBF_4$ $HBF_4 + H_2O \rightarrow HBF_3(OH) + HF$ $4BF_3 + 3H_2O \rightarrow B(OH)_3 + 3HBF_4$

Although proton transfer reactions may significantly depress electrolyte voltage windows in supercapacitor electrodes, even defect-free surfaces cannot prevent irreversible breakdown reactions. Recent experiment results and MD simulations suggested that ions may undergo catalyzed dimerization under high applied potentials (shown in **Fig. 1.15.a**). Several simulations predict a potential-induced breakdown of the S-C bonds and, subsequently, the C-H bonds (both of which are present in the [TFSI⁻] anion) under applied potentials.[152] Conductive, accessible surface (*i.e.*, graphene or OLCs) may rapidly overcome activation energy barriers, accelerate these processes, and increase their contribution to electrolyte decomposition.
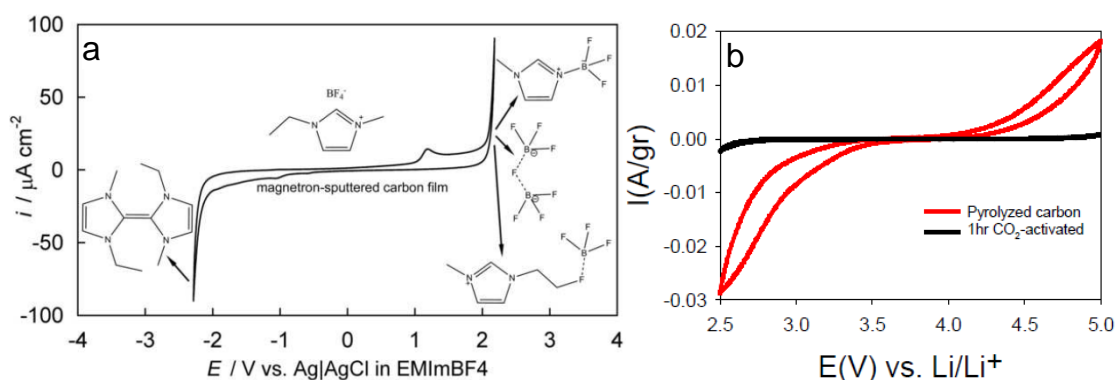
Figure 1.15. a) Catalyzed dimerization reactions of $[EMIm^+][BF_4^-]$, which forms $[B_2F_7^-]$ and insoluble imidazolium salts under high applied potentials.[154][28] b) Lithiation

---

cycling of defunctionalized and oxidized carbon black in $[Li^+][PF_6^-]$/carbonate electrolyte (unpublished results by R. Kostecki, Freedon Car Fuel Partnership 2011 presentation).

These processes likely depend on ion confinement, pore wall conductivity (derived from graphitization), and chemical species present at the ion-carbon interface. Experiments by Kostecki *et. al.* demonstrated improved electrochemical stability of oxidized external surface (carbon black) electrodes and suggested that surface chemistry groups may act as protective passivation layers (**Fig. 1.6.5.b**).[155] This (somewhat contradictory) behavior demonstrates that ion behavior in confined states, and resulting interactions with surface defects, are unique for each electrode-electrolyte interface and are strongly convoluted with porosity.

Multiple chemical functionalization pathways allow different functional groups to be selectively grafted onto carbon surfaces (illustrated in **Fig. 1.16**).[82,156] As described in section **1.4**, CDCs are typically treated with NH_3 and H_2 gas (300-600 ºC) after Cl_2 etching and, respectively, contain amine and hydrogen groups on surfaces. Previously reported surface chemistry studies of differently treated CDCs have been convoluted with Cl_2 synthesis conditions and cannot yield clear comparisons. Although NH_3 treatment has enhanced graphitic ordering (narrower D and G bands) compared to Ar treatment,[81] no comprehensive studies have decoupled the influence of resulting surface compositions on capacitive behavior. These annealing approaches have been used arbitrarily and interchangeably in prior studies. Multiple wet chemistry (acid treatments with $H_2SO_4/HNO_3/HCl$, Piranha etch with H_2SO_4/H_2O_2),[58,157] plasma (C_2F_6 or NH_3), hydrothermal (autoclave treatments with $KMnO_4$/melamine/urea),[158] high-temperature

fluidized bed furnace treatments (NH_3, H_2, O_2, CO_2, air),[58] and organic synthesis ($SOCl_2$, $LiAlH_4$) approaches have also successfully functionalized carbon surfaces.[156]
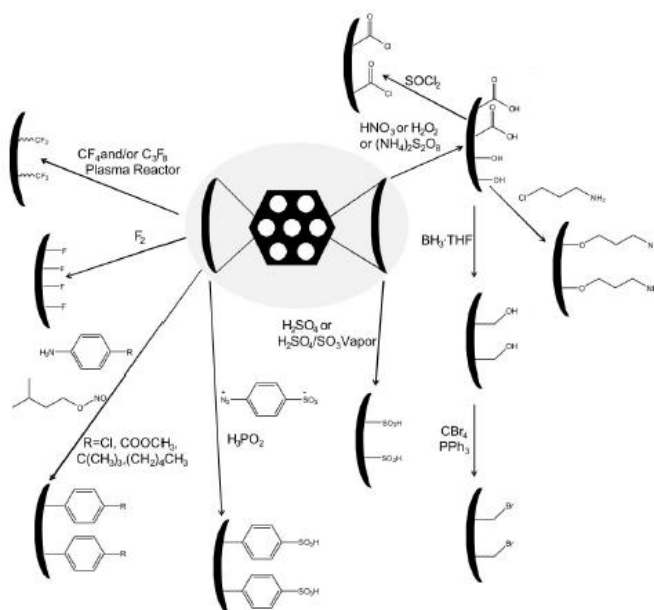
Figure 1.16. Pathways of common chemistry pathways for porous carbons.[82][29]

Some methods implement high-temperature treatments to remove surface chemistry groups and graphitize surfaces. Characterization studies have shown that most functional groups are completely removed from carbon substrates at 300-1,000°C.[159,160] However, per reaction equilibrium principles, high-vacuum treatments accelerate onset of removal of surface compounds. In addition to surface purification, thermal treatments facilitate mobilities of carbon atoms and allow them to graphitize above 800°C.[161] High-temperature vacuum annealing re-hybridizes sp^3 bonding into sp^2 structures.[162]

Although the treatments are highly tuneable, the final surface composition of each carbon structure also strongly depends on the initial pore composition of each material. Its initial chemical makeup, pore size, sp^2/sp^3 bonding ratio, and degree of graphitization all significantly influence the surface modification procedures. Since

porous carbons exhibit extremely heterogeneous surface chemistries, and external carbons include equally unpredictable edge sites, findings may not directly translate from one carbon-electrolyte system to other electrodes. Furthermore, most chemical treatments also activate carbons and modify their porosities. Although many studies often implement these approaches to maximize accessible surface areas for greater C_{sp}, pore restructuring has involved multiple variables and inhibited proper fundamental comparisons of specific surface effects and their influences on the FSI.

1.7 Summary of State of the Art

Through the last few decades, numerous studies have yielded important fundamental insights into the mechanisms of electrochemical capacitors and improved their energies and power densities. However, comparatively, few studies have investigated the influence of surface functional groups and graphitic structure on capacitance. The majority of fundamental work is limited to computational modeling of systems, which only partially resemble real-life supercapacitor systems. Almost every simulation that addresses the effects of pore wall composition delivers its results with multiple caveats and parameter restrictions, such as neutral-potential systems and coarse-grained models, which may not apply to practical electrochemistry measurements. Although multiple experimental studies have successfully introduced functional groups onto electrode surfaces and changed graphitization of porous and non-porous carbons, they pursued higher capacitance at the expense of fundamental analyses. Successful efforts activated electrodes and reported increased surface areas with larger pores, or grafted groups that yielded redox-active surfaces and improved energy densities *via* pseudocapacitive

contributions. As such, most prior efforts did not investigate FSI interaction mechanisms or deconvolute specific influences of surface defects from pore size and ion confinement.

Modeling and experimental results have highlighted significance of surface groups and graphitic defects. Furthermore, their relative influence on measured capacitance, rate handling abilities, and electrolyte voltage windows greatly depend on pore diameter or external surface curvature. Conclusions regarding influence of surface chemistry and ordering inherently depend on the understanding of long-range and short-range interactions at the FSI. Research efforts must determine the mechanics and limitations of ion exchange during charge/discharge processes and how those dynamics change on external and in internal surfaces. Subsequently, this thesis aims to decouple each of those parameters and examine the fundamental mechanisms.

Many efforts that had described electrode-electrolyte interactions and influences of surface defects contradicted each other. They evaluated inherently different model systems (slit pores vs. cylindrical nanotubes vs. graphene, static capacitance vs. dynamic charging, etc.) and could not incorporate comparable simulations. As such, the existing body of research cannot compare the relative magnitudes of different effects and assign their relevance to specific, real-life systems. Parameters of empirical findings and computational simulations must converge, and this thesis implements this approach.

Divergence of computational and experimental findings also stems from the fact that specific surface-ion interactions strongly depend on individual properties of both electrodes and electrolytes. Charge densities and dynamics strongly depend on a large range of variables – dipole moments of ions, sizes of molecules, solvation shells, ionic conductivities, temperature-dependent viscosities, solvent effects – that all influence

charge interactions at the fluid-solid interface. Steric limitations, intermolecular forces, and electrochemical breakdown pathways are unique for each FSI. Results from well-described electrode-electrolyte systems may apply to similar FSIs, and this thesis aims to provide findings that may be incorporated in such predictive chemistry.

Existing research also underscores the complexity and heterogeneity of each experimental electrode-electrolyte system. Certain surface chemistry groups and graphitic defects are difficult to detect and quantify using conventional techniques, especially in porous CDCs with robust surface chemistries and complex 3D pore architectures. Surface defects and corresponding ion dynamics require advanced in-depth techniques that specifically probe surface defects and ion dynamics in the double layer. Neutron scattering has proven to be an important complementary tool to gain novel insights, and this thesis uses them for in-depth explanations of previously undetected processes.

Research efforts, which properly investigate the influence of surface chemical groups and graphitic defects on electrosorption, will find use in practical systems that employ tailored pore structures and surface compositions. Novel *in situ* materials characterization techniques will help tailor electrosorption mechanisms for specific applications and operating standards (temperature range, rate handling ability, and voltage window). These findings will extend beyond just electrode surface structure and pore size and will facilitate the design of properly sized electrode particles with maximized power and energy densities. This holistic approach is beneficial beyond limited electrode design: research efforts must subject all supercapacitor components to strict scrutiny and overhaul its materials to maximize capacitance, minimize cost, and improve the environmental sustainability of these important energy storage devices.

CHAPTER 2 – DISSERTATION OBJECTIVES

The main objective of this dissertation is to investigate the influence of surface heterogeneity, composition, and disorder on electrochemical capacitance.

The dissertation aims to fundamentally address the following important, unresolved scientific questions:

1. Are surface defects beneficial or harmful to capacitance, rate handling abilities, and electrochemical stability of supercapacitors?

2. What is the influence of specific chemical groups on capacitance and ion dynamics?

3. What are the correlations between the electrode-electrolyte interfaces, ion densities in pores, and resulting specific energy and power of supercapacitors?

4. How significant is the contribution of quantum capacitance in porous carbons?

5. What structural ordering properties in porous carbons have the highest influence on charge storage?

6. How are ion confinement and pore length convoluted with individual, decoupled influences of pore wall defects?

Four specific tasks, which are discussed in chapter **4** of this dissertation, address these questions and the main objective:

1. Investigate the influence of pore surface defunctionalization and graphitization on capacitance, rate handling, and voltage window (section **4.1**)

2. Decouple the influence of surface functional groups on ion dynamics (section **4.2**)

3. Decouple the influence of ion confinement and pore length on capacitance, electrochemical stability, and charge/discharge rates (section **4.3**)

4. Implement findings in specific practical applications (section **4.4**)

CHAPTER 3: EXPERIMENTAL APPROACH

This chapter describes the precursor materials, synthesis and structural/chemical modification pathways, materials characterization, and electrochemical testing (including the properties of tested electrolytes and key derivations from experimental techniques). Unless stated otherwise, all experiments were conducted at Drexel University in Philadelphia, PA, USA. Application of fundamental discoveries in specific materials measurements and device applications (chapter **4.4**) include different experimental approaches that are explained in specific, relevant sections.

3.1 Materials

3.1.1 Porous Model System: Carbide-Derived Carbons

Carbide-derived carbons (CDCs) were selected as internal surface carbon model systems for these studies. As discussed in section 1.4, they offer a well-tuned, narrow, ordered porosity and high SSAs.[83] All CDCs were synthesized from granular metal carbide powders. Several different precursors, which were converted to CDCs at different temperatures, were used to obtain distinct porous systems that were suitable for different electrolytes. Nanosized (20 nm diameter) and coarse-grained (75-300 µm diameter) particles were included to deconvolute surface composition properties from pore length and particle aspect ratios. **Table 3.1** summarizes four distinct binary carbides that had been implemented for different approaches.

Table 3.1. Summary of metal carbide precursor particles used in this dissertation

Precursor	Medial Particle Size	Manufacturer	Material Notes
SiC[163]	20 – 30 nm	MTI Crystal, USA	99% purity
SiC	1.0 – 5.0 μm	Alfa Aesar, USA	99.5% purity
TiC[164]	2.0 – 5.0 μm	AEE, USA	99+% purity
TiC	75 – 250 μm	"Reaktiv," Ukraine	Ball-milled for 0-20 hours from 300 μm precursor
Mo_2C[71]	0.8 – 1.0 μm	Alfa Aesar, USA	99.5% purity

All CDC materials were synthesized in horizontal quartz tube furnaces (**Fig. 3.1**). Small batches of carbide powders (0.8 grams or lower per synthesis run, to minimize powder compaction and maximize sample yield and uniformity) were loaded into quartz boats. Sacrificial carbon black was placed upstream from the sample boat to react and absorb any oxygen impurities in the gas flow. All reagent gasses used during synthesis were purchased from Airgas Co. and were of ultra-high purity (UHP) grade or higher.
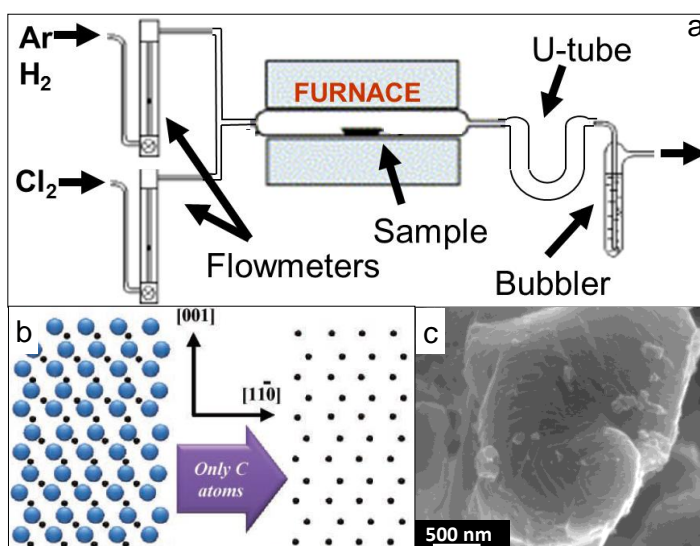
Figure 3.1. a) Schematic of tube furnace used for synthesis of CDC particles *via* Cl_2 etching. Gas flow is from left to right.[61] b) Conformal transformation of SiC cubic lattice to carbon-only CDC system.[67][30] c) SEM image of micron-sized TiC-CDC.

The loaded and sealed furnace was purged with Ar gas for 2 hours at room temperature (200 cm^3 min^{-1} flow rate). The furnace was ramped-up to the desired synthesis temperature (600 – 1,000 ℃) under flowing Ar gas. Upon reaching it, Ar was shut off and pure Cl_2 gas flowed over the material (400 cm^3 min^{-1} flow rate) for 6 hours. This procedure removed metal carbide products (in the form of $TiCl_4$ (g) or $SiCl_4$ (g)) along with excess Cl_2.[70] Byproducts accumulated in condensation bulbs and neutralization flasks (filled with KOH solution) downstream of the reactor. Following the Cl_2 etching step, the furnace was purged with pure Ar for 30 minutes while it was brought to a 600 ℃ temperature. The sample was, subsequently, exposed to flowing H_2 gas (500 cm^3 min^{-1} flow rate) for 3 hours to stabilize surfaces and remove any trapped Cl_2 (*via* HCl (g)) or residual metal chlorides from pores. CDCs then cooled to room temperature (typically overnight) under flowing Ar gas. For select samples, NH_3 (g) was used in place of H_2 with identical synthesis steps. Unless explicitly noted otherwise in text, all described CDCs were annealed with H_2 after chlorination. The samples were removed from the furnace and dried under low vacuum (0.1 torr, 100 ℃). Additional samples (75-250 μm TiC-CDC particles and Mo_2C-CDC) were synthesized at, respectively, Y-Carbon (Bristol, PA, USA) and Materials Research Centre (Kiev, Ukraine) using identical procedures. Coarse-grained, large CDC particles were pelletized with polyvinyl acetate (PVA) to minimize powder compaction and preserve high yields.

In addition to various CDCs, commercially available activated carbon (AC) was used in most studies for electrochemical cell troubleshooting, baseline performance comparisons with CDCs, and implementation in environmentally benign supercapacitors

(section **4.4**). The material, which carries a commercial name of YP-50, is a coconut shell-derived AC (Kuraray, Japan), with a 1,500 m^2 g^{-1} SSA and d_{av}=0.79 nm.[20]

3.1.2 Non-porous Model System: Graphene Nanoplatelets and Carbon Black

To decouple the influence of surface chemistry groups and graphitic defects from ion confinement, non-porous carbon materials were used as external surface model systems. Onion-like carbons (OLCs), which are graphite spheres (~5-10 nm diameter) that resemble multi-layered concentric fullerenes, were synthesized *via* vacuum annealing (10^{-6} torr) of UD-90 nanocrystalline diamonds (Nanoblox, Inc.) at 1,800 ℃ for 8 hours (described in section **3.1.3**). Commercially available Graphene Nanoplatelets (GNP, XG Sciences), which are multilayer (10-100 layers) graphene flakes with a 1-5 μm cross-sectional diameter,[165] served as planar electrodes. Commercially available carbon black (CB, Alfa Aesar) nanoparticles were used as semi-spherical, graphitized (polycrystalline) electrodes. Finally, commercially available graphite foil (Toya Tanso, 0.380 mm thick) acted as a non-porous flat carbon substrate. **Fig. 3.2** shows different external surface model systems. Although porosimetry analysis (details in section **3.2.1**) assesses porosities of both internal and external systems, external surface "pores" are more accurately described as interparticle slits, which are formed by particle-to-particle contact in the bulk phase, and do not suggest ion confinement.
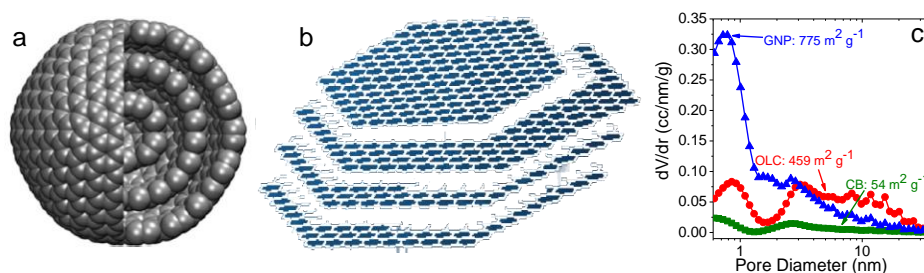
Figure 3.2. Schematic a) OLC [54][31] and b) GNP.[166][32] c) External system porosities.

---

[31] Reprinted from Ref. [54]. Copyright 2012, with permission from Elsevier.
[32] Reprinted from Ref. [166]. Copyright 2010, with permission from Elsevier.

3.1.3. Vacuum Annealing and Chemical Functionalization

Carbon powders were loaded into graphite crucibles and placed in a graphite vacuum furnace (Solar Atmospheres). The furnace was outgassed for 24 hours at room temperature, during which time the pressure decreased to approximately 10^{-6} torr. Samples were heated at a rate of 10 °C min^{-1} to specific peak temperatures. Most samples were treated at 700 °C – 1800 °C temperatures.[167] Low-temperature annealing primarily removed surface functional groups (**Table 3.2**), and higher-temperature treatment (> 1,100 °C) both defunctionalized and graphitized the surfaces. High vacuum accelerated surface defunctionalization kinetics: process byproducts were gases, which were rapidly removed from surfaces and drove the equilibrium towards chemical decomposition of weakly bonded groups. Samples were held at set isothermal conditions for 8 hours each and, subsequently, cooled to room temperatures under the same low pressure.

Table 3.2. Thermal treatment removal of specific groups from porous carbons.[168]

Treatment Temperature	Functional group removed (gas product decomposition)
150 °C	Physisorbed water (H_2O)
230 °C	Anhydrides (H_2O)
> 300 °C	Phenols (H_2O)
300 °C	Carboxylic acids (CO_2)
500 °C	Carboxylic anhydrides (CO_2)
600 °C	Phenols, carbonyls, quinones, ethers (CO)
> 750 °C	Lactones (CO_2)

Various chemical functionalization and defunctionalization pathways are shown in **Fig. 3.3**. The starting CDC structure (**Fig. 3.3(b)**) results from standard Cl$_2$ synthesis,

short H_2 annealing (2 hours), and exposure to ambient air. To maximize the presence of H– rich groups on surfaces, selected CDC materials were annealed with H_2 at 600 ℃ for 4 hours (**Fig. 3.3(a)**). Aminated CDCs relied on the same strategy and used 4 hours of 600 ℃ NH_3 annealing following Cl_2 treatment (**Fig. 3.3(c)**). Vacuum annealing described above (shown in **Fig. 3.3(d)**) was used to remove surfaces and graphitize structures. Flowing dry air (<0.01 ppm H_2O) oxidized surfaces (at 425-570 °C) using the same quartz boat and tube furnace as $Cl_2/H_2/NH_3$ treatments (**Fig. 3.3(e)**). To determine the appropriate air treatment temperature, which oxidized surfaces without activating or restructuring pores, thermogravimetric analysis (TGA) identified oxidation onset temperatures (99.5% remaining mass); this technique is described in section **3.4.2**.
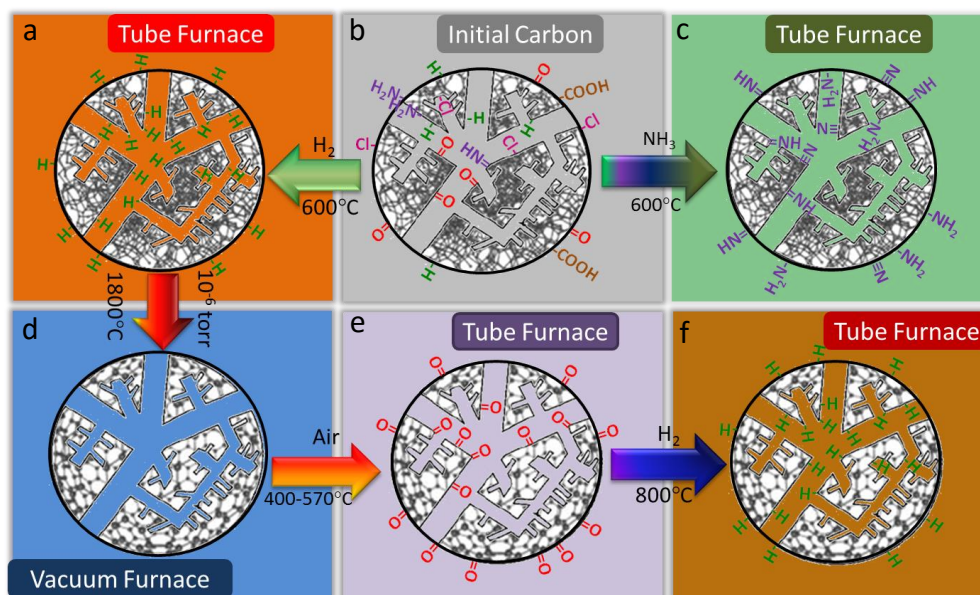
Figure 4.3. Chemical functionalization pathways for a) Hydrogenated, b) Initial (starting), c) Aminated, d) Defunctionalized, e) Oxidized, and f) Hydrogenated surfaces.

3.2 Characterization of Pore Structure

3.2.1 Gas Sorption and Porosimetry

Gas sorption measurements were carried out using the Autosorb-1 or Quadrasorb (Quantachrome Instruments, USA) sorption analyzers. Samples (0.01 – 1.0 g) were

loaded into glass cells and outgassed at 120 ℃ for 24 hours prior to analysis. The instruments collected gas adsorption and desorption isotherms (adsorbed volume vs. relative pressure) using the following gases and relative pressures (P/P_0):

1. N_2 gas: $7.5 \cdot 10^{-4}$ – 0.9995 P/P_0 range, 77 K isotherms (liquid N_2 coolant), $P_0 = 760$ torr

2. Ar gas: $7.5 \cdot 10^{-4}$ – 0.999 P/P_0 range, 77 K isotherms (liquid N_2 coolant), $P_0 = 240$ torr

3. CO_2 gas: $2 \cdot 10^{-5}$ – 0.03 P/P_0 range, 273 K isotherms (ice water bath), $P_0 = 26,100$ torr

The shape of the isotherms provided qualitative comparisons of typical pore structure and distinguished microporous from mesoporous carbons (**Fig. 3.4**).
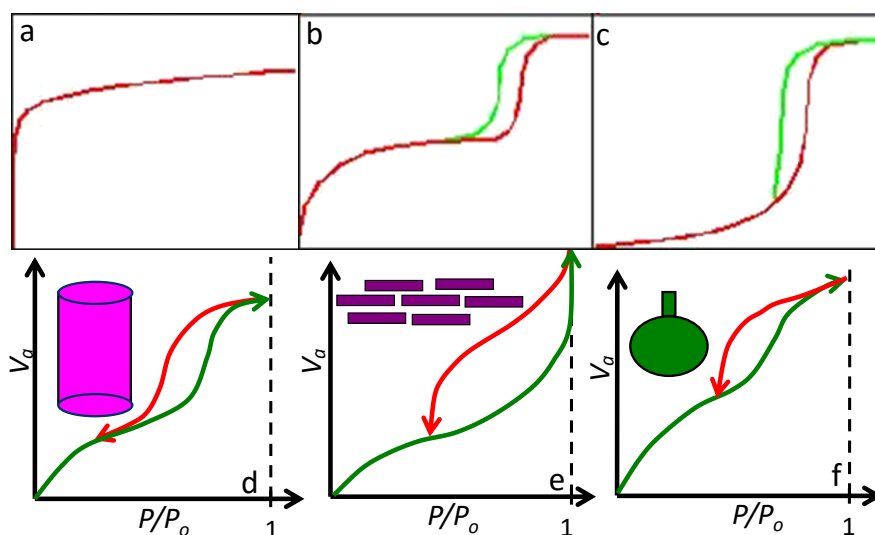
Figure 3.4. Gas sorption a) Type I (microporous), b) Type IV, and c) Type V (both mesoporous) adsorption isotherms that are characteristics for porous carbons. Mesopores exhibit hysteresis in their desorption behavior. Respective isotherm shapes are characteristic of d) cylindrical-shaped, e) slit-shaped, and f) bottleneck-shaped pores.[169]

The Brunauer-Emmett-Teller equation (BET, **Eq. 3.1**) was used to calculate the SSA (V_α is the adsorbed gas volume at pressure P, V_m is amount of gas required to form monolayer, C is the BET constant related to energy of adsorption of 1st monolayer):[170]

$$\frac{P}{V_\alpha(P - P_0)} = \frac{1}{V_m C} + \frac{(C-1)}{V_m C} \cdot \frac{P}{P_0}$$

(**3.1**)

The equation was calculated using a linear regression for 0.05 – 0.30 P/P_0 values and normalized by the sample mass to obtain m^2 g^{-1} values. For N_2 sorption, a Quenched Solid Density Functional Theory (QSDFT) data reduction analysis provided information on a secondary SSA value, cumulative pore volume (cm^3 g^{-1} values), and pore size distributions (PSDs, pore diameter vs. dV dr^{-1} plots).[171] DFT data reduction used only the adsorption isotherms and assumed slit pore configurations.[172] PSDs were provided from CO_2 data using Non Local Density Functional Theory (NLDFT) models. Quantachrome's Quadrawin software provided all BET calculations and DFT data modeling kernels and computational analysis.

3.2.2 Small-Angle Scattering

Small-angle neutron scattering (SANS) experiments on pure CDCs and on electrolytes confined in CDCs were carried out in EQ-SANS instrument at Oak Ridge National Laboratory (ORNL) (BL-6 beamline).[173] The data were collected covering the Q, a momentum transfer vector, range between 0.003 $Å^{-1}$ and 1.4^{-1} $Å^{-1}$ at 300 K and 353 K. The data was reduced using Mantid software, and expressed in terms of scattering intensity (I) versus Q from integration over 2D detector counts.[174] The scattering intensity is the function of the neutron contrast, *i.e.* the scattering length density differences between the carbon matrix and the ionic liquid used and the volume fraction of the filled liquid. Measurements combined a 1.3 m sample to detector (SDD) distance (1.13 – 4.65 Å) and a 4.0 m SDD (2.61 – 5.61 Å and 9.51 – 12.91 Å) to obtain a broad Q range (radius of gyration: $Rg \approx \frac{2\pi}{Q}$).[110]

Small-angle X-ray scattering (SAXS) experiments were performed using a Rigaku S-MAX 3000 setup. Samples were sealed in Kapton capillaries and placed under low vacuum in the sample chamber. The setup used a 3 pinhole collimation, a MicroMax 002+ CuKα (λ = 1.54 Å) radiation source, and a Gabriel 2D Multiwire X-ray detector.[175] Each SAXS measurement was collected for 300 seconds in the 0.01 – 0.15 Å^{-1} Q-range. Data was processed using the SAXS GUI (JJ X-ray Systems ApS).

Surface corrugation of pure CDC materials was evaluated by assuming surface fractals in the Porod scattering region (0.01 Å^{-1} < Q < Å^{-1} range). The scattering intensity was fitted to the following power law (**Eq. 3.2**) (K is a collection of measurement and sample-specific constants and c accounts for atomic-scale disorder)**:**[176]

$$I(Q) \approx KQ^{-n} + c \qquad\qquad (3.2)$$

Measurements assumed identical K and c values for sample sets and evaluated changes to the Porod constant (n). N approached 4 for smooth surfaces and decreased (approaching n = 3) in atomically rough surfaces.**[177]** The different scattering regimes from the entire Q range (from SANS and SAXS) are shown in **Fig. 3.5:**
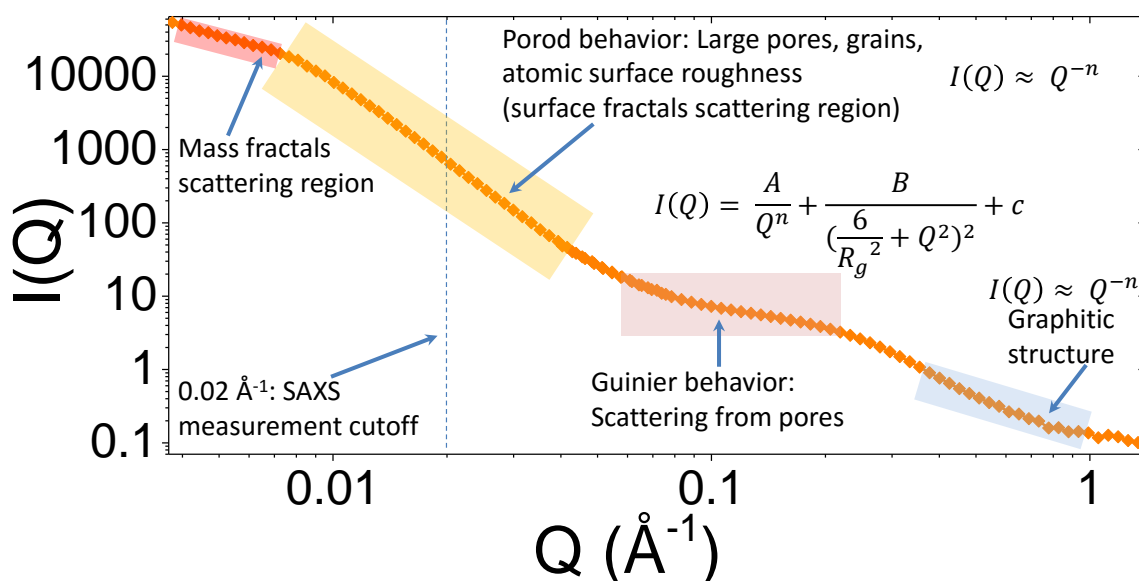
Figure 3.5. Different characteristic small-angle scattering regimes for porous carbons.

3.3 Characterization of the Graphitic Structure

3.3.1 Raman Spectroscopy

Raman Spectroscopy assessed changes in graphitic ordering and characterize ordering in CDCs. Measurements were collected using a Renishaw inVia Spectrometer with a 514 nm (green) Ar laser. Additional measurements used a 633 nm red (He-Ne) laser. Data was deconvoluted using an 1800 grooves mm^{-1} grating. Measurements typically involved 80-second collections and averaged measurements over 6 scans. The typical scan range was set between 1000 and 3500 cm^{-1} wavenumbers. WIRE 3.2 software (Renishaw Instruments, UK) analyzed the results and fit the vibration modes.
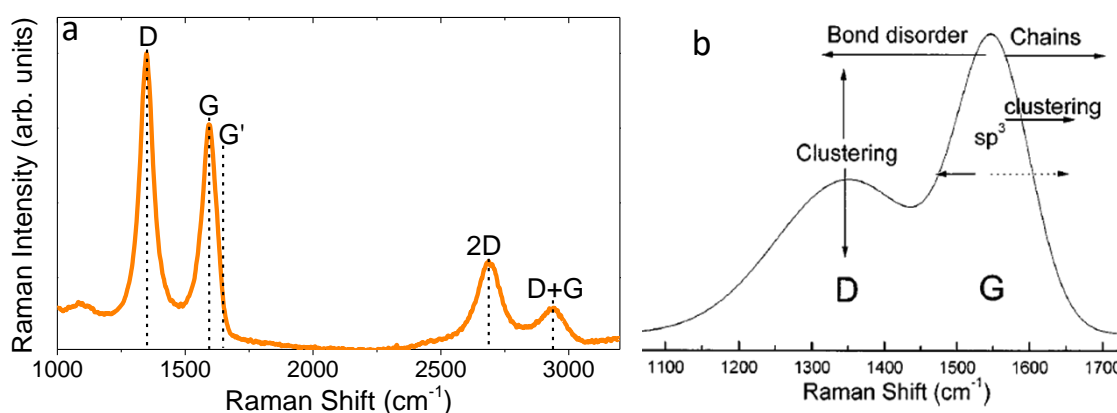
Figure 3.6. a) Characteristic vibration modes for porous, semi-graphitized carbon. b) Key influences of graphitic features on the Raman spectra and bonding in the carbon.[56][33]

Several distinct modes, which are characteristic of amorphous carbons, were the focus of most measurements (**Fig. 3.6**). The D band, which is centered at 1355 cm^{-1}, corresponds to a breathing mode of A_{1g} symmetry and is indicative of disorder in the carbon. Its intensity positively correlates with the relative prevalence of 6– membered rings in the structure.[178] The G band, which is centered at 1580 cm^{-1}, corresponds to E_{2g} symmetry and is correlated with perfect sp^2 ordering along the [100]/[101] direction

---

[33] Reprinted with permission from Ref. [56] Copyright 2000 by the American Physical Society.

in graphite. It does not require only benzene rings and can respond to 5– and 7– membered rings as well. Other resonance modes, such as the 2D band (centered at 2700 cm^{-1}) and the D+G band (centered at ~ 3100 cm^{-1}), are indicative of graphitic ordering in the carbon.[56] Some carbons also include a faint G' mode (at 1595 cm^{-1}). Peak information (intensities and full width at half maxima (FWHM) were derived using Lorentzian approximations with WIRE 3.2 software.

3.3.2 X-Ray Diffraction

X-ray diffraction (XRD) provided information about graphitic ordering and crystalline impurities (unreacted carbides, solid metal chlorides, etc.). Data was collected using an Empyrean Series 2 Diffractometer (PANalytical, Netherlands). Measurements were conducted in reflection mode using a flat stage in the 5-90° 2θ range (0.026° step size, 3.03° min^{-1} rate). Measurements were completed at ORNL.

3.3.3 Electron Microscopy Imaging

Transmission Electron Microscopy (TEM) provided qualitative information about key structural features and domain sizes. A JEM 2100 (JEOL Instruments) TEM with a 200 kV accelerating voltage generated images, which were subsequently processed using Digital Micrograph software. Samples were mounted on lacey copper grids.

Scanning Electron Microscopy (SEM) images provided additional information about microstructure of carbons and resulting electrode films, and the complementary energy dispersive X-ray spectroscopy (EDS) component provided elemental analysis comparison

of carbon surface chemistries. A Zeiss Supra 50VP SEM with built-in Oxford Energy-Dispersive X-ray Microanalysis was used for all micrographs in this dissertation.

3.3.4 X-Ray and Neutron Scattering and Pair Distribution Function Analysis

Although XRD and Raman spectroscopy provide useful characterization of carbons, they cannot comprehensively describe the structure of partially amorphous, disordered structures. Total elastic scattering provides a statistical analysis of the prevalence and distribution of bond lengths, structural defects, and vacancies. Pair distribution function (PDF) analysis, which is the Fourier transform of total scattering, provides relative intensities (denoted as G(r)) for different correlation distances (r).[179] The transformation of total scattering (S(Q) vs. Q) to PDF uses the following **Eq. 3.5:**

$$G(r) = \frac{2}{\pi} \int_0^\infty Q[S(Q) - 1] \sin(Qr) dQ \qquad (3.3)$$

X-rays and neutrons were used to collect scattering information for PDF. While the former is unaffected by neutron flux and is better suited for characterization of pure carbons, the latter is more sensitive to diverse elemental compositions and offers better resolutions for carbon + electrolyte systems. Total scattering was conducted using X-rays at the 11-1D-B beamline of the Advanced Photon Source (ANL). Samples were loaded into Kapton capillaries, and synchrotron X-ray total scattering measurements analyzed powders in transmission mode. Scattering measurements used 58.65 keV incident radiation (0.2114 Å wavelength) in the 0.01 Å^{-1} < Q < 22.2 Å^{-1} range at 298 K.[180] The Fit2D program was used to calibrate the measurement and PDFGetX2 to derive G(r) plots. Neutron scattering was conducted using the BL-1B NOMAD beamline at the Spallation Neutron Source (ORNL).[181] Materials were analyzed at 100 K and 300 K

temperatures. Neutron scattering was collected in the 0.1 – 3.0 Å incident wavelength range at 3º - 175º scattering angles, with a 108 neutrons cm^{-2} sec^{-1} flux on sample.

3.3.5 Four-point Probe Measurements

Electrical conductivity of carbons was measured by attaching evenly spaced gold wires to material surfaces using silver paste. A Keithley 4ZA4 current-voltage source or a JANDEL 4-point probe collected resistance values by applying a 20 mA current. Measurements used identical electrode films as the carbon-binder rolled films used for electrochemical tests; their preparation is described in section **3.7.1**. The film thickness (*t*) was significantly lower than separation between probes. The intrinsic conductivity was calculated using the 4-point probe method that measured voltage (*V*) as a function of applied current (*I*) derived from **Eq. 3.4**:

$$\sigma = \frac{I \ln 2}{(V \pi t)} \tag{3.4}$$

3.4 Characterization of Structural Bonding and Surface Chemistry

3.4.1. FTIR

Fourier-transform infrared spectroscopy (FTIR) is the most common method that is typically used to characterize surface functionalities on porous carbons. The chemistry groups are concentrated solely on the surfaces of the porous carbon materials. Therefore, although the relative amounts are small, they significantly alter the composition of carbon surfaces. Several measurements were attempted using an attenuated total reflectance (ATR) mode with an FTIR spectrometer (Nicolet 6700 Series, Thermo Electron Corporation). Samples were placed on the surface of a diamond attenuated total

reflectance ATR crystal with a surface area of 3.42 mm^2 using an anvil from the Golden Gate^{TM} accessory (Specac Inc.). However, the carbon materials are black and significantly absorb the FTIR signal. Even in grazing-angle mode, with attenuated total reflection, the functionalized materials showed very similar spectra with very low intensities for distinct vibrational modes. Subsequently, it was not used for surface chemistry characterization. The instrument was used, however, to conduct several *in situ* measurements on supercapacitors (discussed in section **4.4**).

3.4.2 X-Ray Photoelectron Spectroscopy

X-ray photoelectron spectroscopy (XPS) offers the most reliable surface-sensitive spectroscopy information. XPS analysis was performed on a VersaProbe 5000 instrument employing a 100 μm monochromatic Al-Kα X-ray beam to irradiate the sample surface. Photoelectrons were collected by a 180° hemispherical electron energy analyzer. Samples were analyzed at a 45° takeoff angle between the sample surface and the path to the analyzer. Survey spectra were taken at a pass energy of 117.4 eV and with a step size of 0.500 eV. High-resolution spectra in the C 1s, O 1s, and N 1s regions were taken at a pass energy of 23.5 eV and with a step size of 0.050 eV. Spectra were taken before and after sputtering with an Ar beam operating at 2 kV for 5 minutes. All binding energies were referenced to that of graphitic carbon at 284.4 eV. The quantification and peak fitting of the core-level spectra was performed using CasaXPS Version 2.3.16 RP 1.6. Prior to both the quantification and peak fitting the background contributions were subtracted using a Shirley function. Although this technique can provide elemental analysis and prevalence

of different surface functional groups, it cannot detect hydrogen and, subsequently, relies complementary methods for complete surface chemistry characterization.

3.4.3 Thermogravimetric Analysis

Thermogravimetric analysis (TGA) provided important information about the thermal stability of carbons, functional groups, and electrolytes. The technique heated samples and measured mass changes during the process. All samples were loaded into small alumina crucibles and placed onto Pt balance pans. This setup prevented any catalytic contributions from the sample pan to sample oxidation/decomposition. Measurements were conducted using an upright furnace of a Q50 Thermal Analyzer (Thermal Instruments, Inc.). Thermal Analysis software provided calculations of temperature-dependent remaining mass (%) and derivative changes (dM dT^{-1} or dTG) of mass at dynamic temperatures. TGA used 2 distinct modes: air oxidation (hereafter referred to as "Air TGA") and thermal decomposition in Ar (hereafter referred to as "Inert TGA").

Air TGA was conducted with a 10 ml min^{-1} air flow rate parallel to the sample (flowing over it to oxidize the carbons). Samples (typically 5-10 mg) equilibrated at 100 ºC and, subsequently, were ramped up to 850 ºC at a 5 ºC min^{-1} ramp rate. Disordered, amorphous carbons were expected to burn off in air at lower temperatures.[44]

Inert TGA procedures involved a similar procedure, except that UHP-grade Ar gas flowed over the sample (at 30 ml min^{-1} flow rate). This approach did not oxidize the carbon surface, but allowed thermally unstable functional groups (and organic molecules from electrolytes) to desorb and be removed with the flowing inert gas; bulk carbon remained intact.[160] The samples initially equilibrated under flowing Ar for 2 hours at

110 ℃ and desorbed H_2O water. The slower 2 ℃ min^{-1} heating rate for these samples allowed functional groups sufficient time to escape the porous structures.[182]

3.4.4 Dynamic Water Vapor Sorption

One of the most important surface properties of carbons includes the interfacial energy at the electrode-electrolyte interface. Pristine and hydrogenated graphene is expected to be hydrophobic, and oxygen- or nitrogen- rich surfaces are expected to favor water contact and become more hydrophilic. Pore wettability (and, thus, hydrophilicity), can be assessed with H_2O vapor uptake isotherms. Dynamic Water Vapor Sorption (DVS) was performed using a Q5000 SA Analyzer (TA Instruments). Samples were placed in Pt-coated pans. The relative humidity of the chamber increased from 0% to 90% using 90-minute equilibration steps, while the temperature was held at a 298 K isotherm. The sample mass changes correlated with H_2O uptake.

3.4.5 Electron Energy Loss Spectroscopy

Initially synthesized CDCs are typically composed of mixtures of sp^2 and sp^3 hybridized carbon bonding. Highly graphitized carbons exhibit greater sp^2 bonding throughout their structures. Furthermore, bond energies, bond polarization, and reactivities are likely different for materials with different sp^2/sp^3 bonding ratios.[183] These factors all underscore the significance of quantifying bonding ratios for carbon electrodes to properly assess their surface compositions and interfaces.
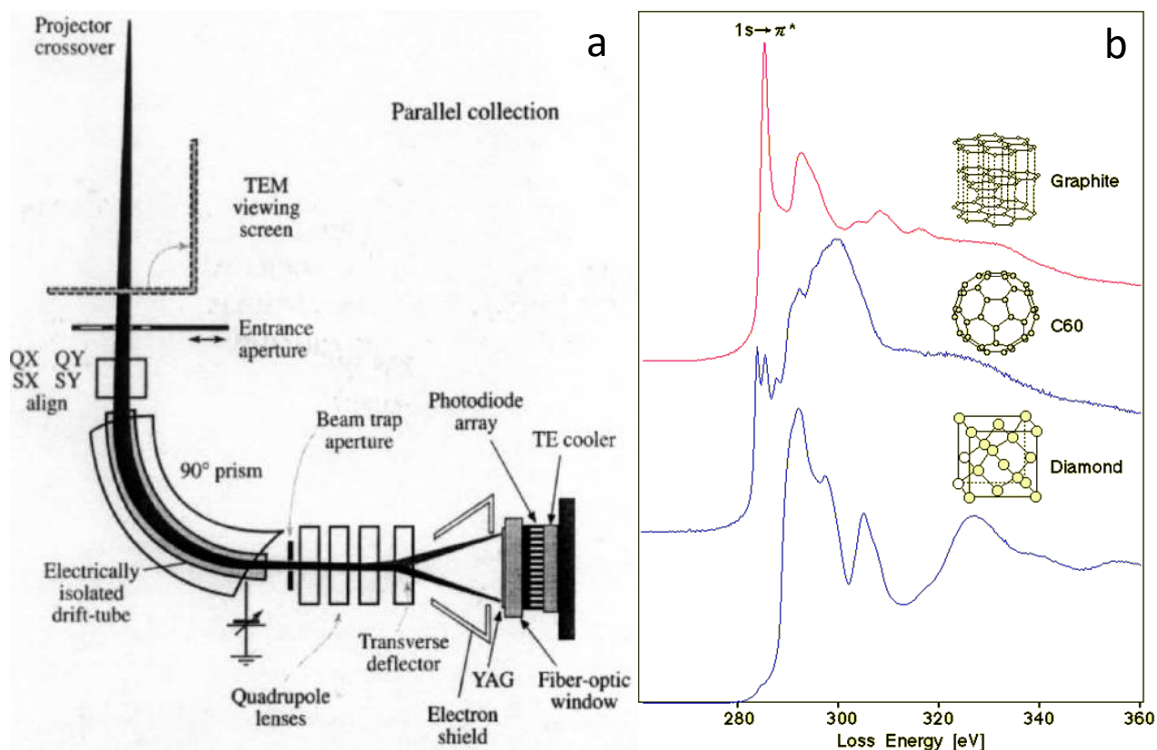
Figure 3.7. a) Schematic of the EELS data collection instrument. b) Typical EELS spectra for structures composed of solely sp^2 bonding (graphite and fullerenes), which exhibit K-shell excitation peaks at 284 eV and 291 eV, and sp^3-bonded carbon (diamond), which does not have a π bonding orbital and cannot exhibit a 284 eV peak.[34]

Electron Energy Loss Spectroscopy (EELS) was used to probe the sp^2/sp^3 bonding character (**Fig. 3.7**).[184] Measurements were conducted at Oak Ridge National Laboratory. This method relied on the carbon K ionization edge to describe the bonding properties through intensity of the $\pi*$ and $\sigma*$ peaks. A 60 kV Nion UltraSTEM was used to avoid laser heating and re-graphitization. This microscope was equipped with a cold-field emission gun and was aberration-corrected for atomic resolution imaging spectroscopy. EELS analysis focused on two K-shell excitation peaks.[185] The first peak, centered at ~291 eV, corresponded to the $1s \rightarrow \sigma*$ transition that is ubiquitous to both sp^2 and sp3 bonding. The ~284 eV peak, which corresponded to the $1s \rightarrow \pi*$, was

---

[34] Image obtained from http://eels.kuicr.kyoto-u.ac.jp/eels.en.html. Retrieved September 10, 2015.

only present in sp^2 (double) bonding. To calculate the relative sp^2/sp^3 ratios, the peak deconvolution data was fit to the following **Eq. 3.5**:

$$\frac{sp^2}{sp^2+s3} = \frac{\frac{I_{\pi^*}^u}{I_{\pi^*}^u+I_{\sigma^*}^u}}{\frac{I_{\pi^*}^g}{I_{\pi^*}^g+I_{\sigma^*}^g}}$$

(**3.5**)

The equation used I^u (intensity of carbon sample) and I^g (intensity of baseline reference HOPG reference). Measurements were collected in the $200 - 374$ eV range. Digital Micrograph software deconvoluted the peaks with a built-in processing script.

3.5 Characterization of Ion-Surface Interactions and Confinement Effects

3.5.1 Contact Angle and Ellipsometry Measurements

Differently functionalized surfaces are expected to exhibit different interfacial energies between electrodes and electrolytes. Surfaces with unfavorable with H$_2$O or electrolyte contact interfaces are, respectively, hydrophobic and ionophilic. The favorable counterparts are, respectively, hydrophilic and ionophilic. Repulsive surfaces tend to minimize liquid contacts with the surface, and contact angle ellipsometry calculations, which assess the liquid-solid interfacial energy (γ_{sl}) as a function of the liquid-vapor interface (γ_{lv}) and solid-vapor interface (γ_{sv}) by measuring the angle (θ_γ) between a liquid droplet and the surface (**Fig. 3.8**):
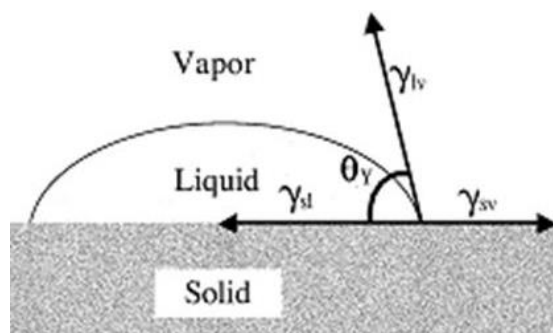
Figure 3.8. Schematic of a standard contact angle measurement.[186]

Contact angle measurements used a 2-axis goniometer. Defunctionalized or oxidized surfaces were set up on the adjustable flat sample stage. To avoid result convolution with capillary action effects (liquid drawn into pores or between small particles in electrode films), flat graphite foil films (with no microscale porosity or macroscale crevasses; SEM image shown in **Fig. 4.69(b)**) replicated identical surface chemistries. 10 µl droplets of H_2O or electrolyte were deposited on the surface. A digital camera took photographs of the surface; each set examined 5-6 individual droplets. ImageJ software provided ellipsometry analysis and contact angle calculations. The results report the average calculated contact angle; standard deviations did not exceed ±4° for each surface.[135]

3.5.2 Vacuum Infiltration of Ions into Pores

Novel, fundamental characterization of the FSI and ion dynamics required in-depth analyses of ions in direct contact with differently structured pore walls. Furthermore, although most electrochemical measurements allow a substantial bulk ("flooded") electrolyte phase that exceeds the pore volume, certain measurement techniques may become overwhelmed by the bulk phase and fail to capture interactions at the interface.

For proper characterization, electrolytes were confined fully inside of particles of porous CDCs using vacuum infiltration. Small amounts (~0.5 g of RTIL electrolytes, p_{bulk} ≈ 1.5 g cm^{-3}) were dispersed in CH_3CN (HPLC grade, Fisher Scientific) at room temperatures. CDC powders were added in an appropriate ratio for the neat RTIL in the solution to occupy 80%–100% of the pore volume. The solvent evaporated at room temperature for 24 hours while the solution stirred. Subsequently, the samples were dried at 100 °C under low vacuum (0.01 torr) for another 24 hours and ground with a mortar

and pestle for uniformity. Visual observations confirmed that no bulk electrolyte droplets remained on the surfaces. The material retained a powder consistency in its final dry form.[110] These samples were used for neutron scattering experiments (described in sections **3.3.4**, **3.5.3**, and **3.5.4**) and select Inert TGA measurements (section **3.4.3**).

3.5.3 Quasi-Elastic Neutron Scattering

Dynamics of ions in confined pores cannot be properly captured using conventional techniques described above, and electrochemical cycling may not account for all processes that occur at the electrode-electrolyte interface. Quasi-elastic neutron scattering (QENS) involves very small energy transfers (< 350 μeV) from incident neutrons to samples (**Fig. 3.9a**). These energy transfers, in turn, induce vibrations in molecules along similar time frequencies ($10^{-12} - 10^{-9}$ seconds) and length scales ($1 - 10$ Å) as their self-diffusion relaxation times and random walk distances. Subsequently, this technique was used to assess the mobilities of electrolyte ions in confined pores.[187]

QENS measurements were conducted using the Backscattering Spectrometer (BASIS) BL-2 beamline of the Spallation Neutron Source at Oak Ridge National Laboratory (**Fig. 3.9b**).[188] Empty CDCs and CDCs filled with electrolytes were loaded (and sealed with In wire) into aluminum cans inside of an Ar-filled glovebox (to prevent air contamination); setup is shown in **Fig. 3.9c-d**. Measurements were conducted in the 0.2 Å$^{-1} < Q < 1.6$ Å^{-1} range of scattering momentum transfer. The spectrometer operated at 60 Hz frequency of the SNS. Quasi-elastic spectra was analyzed from the ± 100 μeV energy transfer region.[27] The instrument analyzed empty CDCs and RTIL-filled CDCs for different surface chemistry configurations. Furthermore, since incoherent scattering from hydrogen dominates quasi-elastic scattering intensity, data reduction also calculated

the percentage of elastically scattering (i.e. "immobilized" on the energy scale and time scale of our measurement) species in each sample. Measurements were conducted under neutral electrochemical potentials. For each sample, data was collected and analyzed at 300 K, and, subsequently, from samples cooled down to the baseline temperature of 10 K to measure the sample-specific resolution spectrum used in the data fitting procedure. For IL-filled samples, the instrument also recorded the temperature dependence of the energy-resolved elastic scattering intensity from 10 K to 300 K at 5 K increments. This approach ruled out the presence of any bulk-like (10 nm or larger) droplets, which could potentially exhibit freezing-thawing behavior outside of CDC particles, and validated both the sample preparation approach and QENS measurements from confined ions.
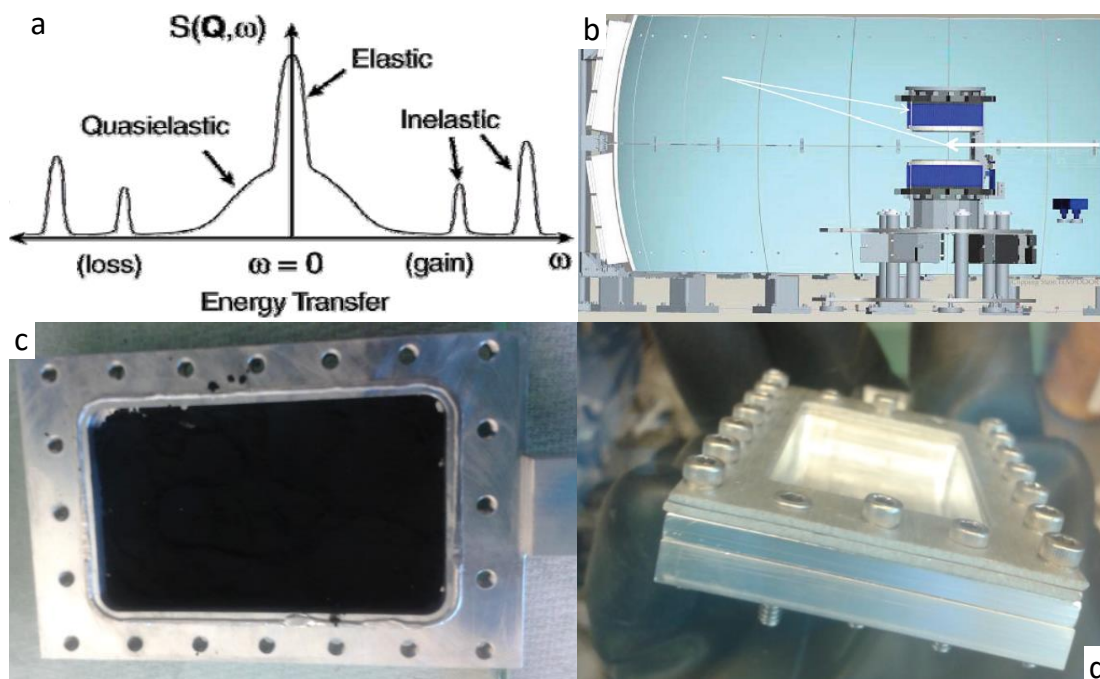
Figure 3.9. a) Energy transfer (ω) vs. the structure factor ($S(Q,\omega)$) for neutron scattering. b) Schematic of the BASIS instrument, with the arrows showing directions of neutron pathways toward sample and, subsequently, backscattered particles Bragg reflected by Si crystals and intercepted by a detector array.[189][35] c) Powder-filled QENS cell (average mass = 0.4 grams) and d) Sealed cell for measurement.

---

[35] Reprinted with permission from Ref. [189]. Copyright 2011, AIP Publishing LLC.

Several approaches were implemented to fit the scattering intensity vs. momentum transfer coefficient (Q). The most common one was a double-Lorentzian model scattering function (**Eq. 3.6**), which successfully fit the scattering data to a Q vs. Γ relationship (R(E) is the resolution function, (B(E)+C) is the linear background, δ(E) is the elastic scattering delta function centered at zero energy transfer, and x is the fraction of elastic scattering in the signal):

$$I(E) = \left[x\delta(E) + (1-x)S_{QENS}(E) + (B(E)+C)\right] \otimes R(E), \qquad (3.6)$$

$$\text{where } S_{QENS}(E) = \left[p\frac{\Gamma}{\pi(E^2+\Gamma_1^2)} + (1-p)\frac{\Gamma}{\pi(E^2+\Gamma_2^2)}\right]$$

For systems with coherent translational Lorentzian components, self-diffusion coefficients were obtained from the Q^2 dependence of relaxation times. The Cole-Cole distribution function,[190] which behaves as a stretched exponential function (half width at half maximum (HWHM) is independent of the stretched exponent), was used to calculate diffusion coefficients and jump lengths. The HWHM was obtained by fitting the $S(Q,E)$ using Cole-Cole distribution function as shown in **Eq.3.7**:

$$S(Q,E) = \frac{\cos\frac{1}{2}\pi\alpha(\frac{1}{\Gamma(Q)})^{-\alpha}}{1 + 2\sin\frac{1}{2}\pi\alpha(\frac{1}{\Gamma(Q)})^{1-\alpha} + (\frac{1}{\Gamma(Q)})^{2(1-\alpha)}} \qquad (3.7)$$

Γ(Q) is the HWHM of a Lorentzian peak and α is an exponent such that $0 \leq \alpha \geq 1$. If α = 0, equation 2 represents a Lorentzian function. Value other than zero gives the distribution of relaxation time. The jump diffusion equation (**Eq. 3.8**) was used to calculate self-diffusion coefficients (D_t) and jump lengths (L):

$$\Gamma(Q) = \frac{D_t Q^2}{1+D_t Q^2 \tau_0}, \qquad (3.8)$$

$$\text{where } D_t = \frac{L^2}{6\tau_0}$$

3.5.4 Inelastic Neutron Scattering

In addition to self-diffusion through narrow pores, confined electrolyte ions also exhibit intermolecular interactions with nearby co-ions, counterions, and adjacent surface functional groups. These interactions shed important insight into the dynamic processes at the FSI and help correlate surface heterogeneity and disorder with ion arrangement and charge dynamics. Since confined ion interactions have very low energies, they are difficult to probe with traditional spectroscopy techniques. Inelastic neutron scattering (INS) relies on the same spectroscopy principles as Raman, XPS, etc., but divergent neutron cross-sections of different atoms (**Fig. 3.10b**) significantly improve its resolution.
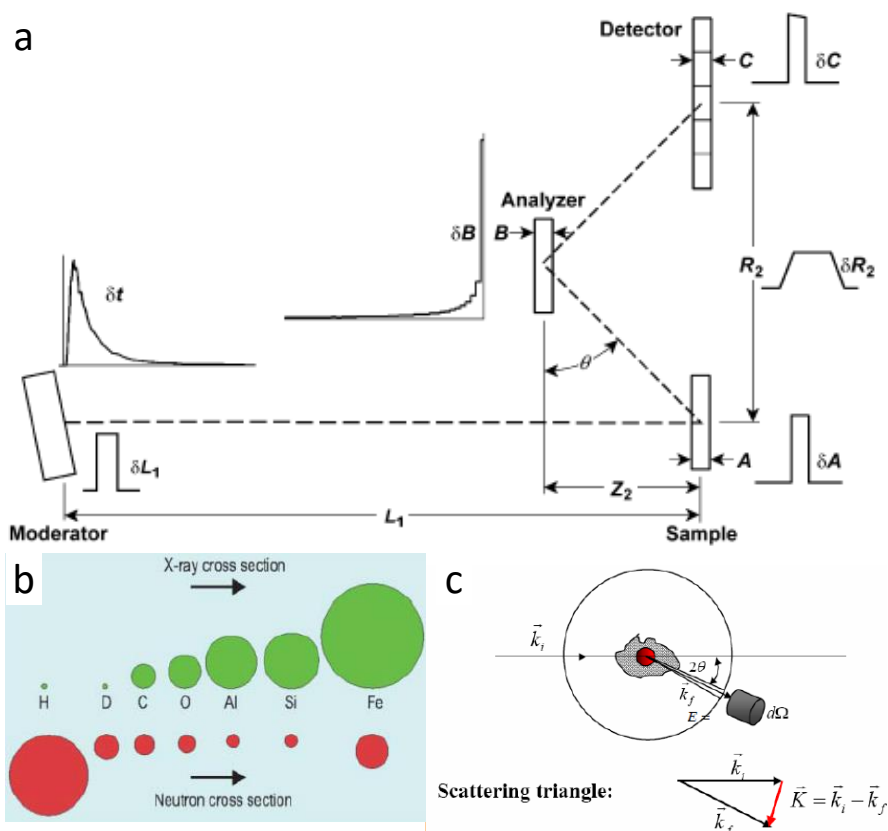
Figure 3.10. a) Layout of a crystal-analyzer spectrometer that is used in the VISION instrument.[36] b) Relative neutron cross-sections of common atoms and their comparisons to relative X-ray cross sections. c) Schematic of the energy transfer in the inelastic neutron scattering experiment.[191]

---

[36] Reprinted from Ref. [191], Copyright 2009, with permission from Elsevier.

Empty CDC and filled CDC materials, along with bulk ionic liquid, were loaded into similar aluminum cans for inelastic neutron scattering (INS) measurements at the Vibrational Spectrometer (VISION) 16B beamline of SNS at ORNL (**Fig. 3.10a**).[191] The samples were cooled down to 5 K to freeze all thermal motion in the sample, and vibrational mode intensity measurements were carried out in the 1 – 1000 meV energy transfer range. The background from the instrument and sample holder was subtracted to obtain the INS spectra from the empty CDC as well as the filled CDC cells. The empty CDC spectra were then scaled (by mass) and subtracted from the filled CDC spectra to compare solely the structure of bulk [EMIm⁺][TFSI⁻] and its confined states.

Since the intensities of the vibrational density of states (VDOS) in bulk and confined IL at high energies were very similar, the low-energy spectrum (≤ 60 meV) provided the most information and remained the focus of most measurements. The dynamical structure factor, *S(Q,E)*, measured by INS, can be expressed in one-phonon approximation as:

$$S(Q, E) = \frac{\hbar^2 Q^2 [n(E,T)+1]}{6 m_H E} \sum_i e^{-\langle u_i^2 \rangle Q^2} G_i^H(E),\qquad (3.9),$$

$$\text{where } G_i^H(E) = \sum_j \left| e_i^H(j, E_j) \right|^2 \delta(E - E_j),$$

$$\text{and } \langle u_i^2 \rangle = \frac{\hbar^2}{3 m_H} \int \frac{G_i^H}{E} \left[n(E,T) + \frac{1}{2} \right] dE$$

$G_i^H(E)$ and $\langle u_i^2 \rangle$ are the generalized density of vibrational states and mean squared displacement of *i* hydrogen atom in the sample, *n(E,T)* is Bose population factor, $e_i^H(j, E_j)$ and E_j are eigenvector and eigenenergy of normal vibration *j*, and the sum goes over all normal vibrations.[191] The squared neutron momentum transfer Q^2 is almost proportional to the neutron energy transfer *E* in INS measurements. Therefore, Q^2 is

relatively small at small energies, and Debye-Waller factor $exp(-\langle u_i^2 \rangle Q^2)$ is close to 1, and INS spectra from ionic liquid is sufficiently intense. Total neutron scattering cross-section of hydrogen (σ_H=82.02 barns) is much larger than all other constituent atoms (5.551, 4.018, 11.51, 4.232 and 1.026 barns for C, F, N, O and S, respectively).[192] In addition, the atomic contribution to the intensity of optical modes in the INS spectra is inversely proportional to the atomic mass. Subsequently, hydrogen-rich species in the carbon-electrolyte systems contributed the most to total scattering intensities.

3.5.5 Nuclear Magnetic Resonance

Nuclear Magnetic Resonance (NMR) analysis of carbons and electrolyte systems has proven to be a very useful tool for characterizing both pure carbons and adsorbed electrolytes.[193] The technique is sensitive to different elements, such as hydrogen, and can use differences in chemical shifts to discern ion configurations from pore wall structures. These results collected at the University of Cambridge (Cambridge, UK).

NMR measurements used electrode films composed of CDC materials (described in section **3.7.1**). Samples were measured in empty states (pure carbons) and after becoming saturated with electrolytes. NMR experiments were performed using a Bruker Avance spectrometer operating at a magnetic field strength of 7.1 T, (300.2 MHz ^{1}H Larmor frequency). The instrument used Bruker 2.5 mm double resonance MAS probe. All NMR experiments used spin–echo sequences with 5 kHz MAS Two specific NMR spectra focused on the chemical shifts ($\Delta\delta$) of 2 specific peaks: ^{19}F and ^{1}H. They were referenced relative to, respectively, neat hexafluorobenzene (C_6F_6) at -164.9 ppm, and

tetramethylsilane (Si(CH$_3$)$_4$) and CH$_3$ resonance of liquid C$_2$H$_5$OH at 1.2 ppm. [1]H and

[19]F experiments, respectively, used 100 and 109 kHz radiofrequency strengths.[194]

3.6. Molecular Dynamics Simulations

Molecular Dynamics (MD) provide computational analyses of different experimental systems and can provide simulations of structural models, ion arrangements inside of pores, and electrochemical measurements and capacitance.

MD computational analyses of ionic liquid electrolytes inside of CDC pores were performed at Vanderbilt University (Nashville, TN, USA). Simulations were performed using the molecular dynamics package GROMACS.[195] The force field for the ionic liquid was derived from previously derived MD all-atom force fields,[196,197] and the AMBER force field described the electrode atoms.[198] The configuration of the hydroxyl group on the surface was taken from the DFT work of Yan *et al.*[199] The temperature was kept constant via the Nóse-Hoover thermostat.[200] To generate different applied potentials, net charges were uniformly added to the atoms of the innermost layers. The surface charge density on electrode was equal but with opposite sign to keep the neutrality of the whole system. The slab-PME method was used to compute the electrostatic interaction in the two-dimensionally periodic geometry.[201] The box length in the dimension vertical to the electrode surface was set to five times the electrode separation distance to ensure that the accuracy of electrostatic force calculation is comparable to that calculated from two-dimensional Ewald method.[202] Each simulation initialized 800 K and was subsequently annealed to 298 K in 8 ns. After 8 ns

of equilibration at 298 K, it carried out a 10 ns production run. The 26 ns total simulation time corresponded to 30 CPU hours in NERSC (using 48 cores).
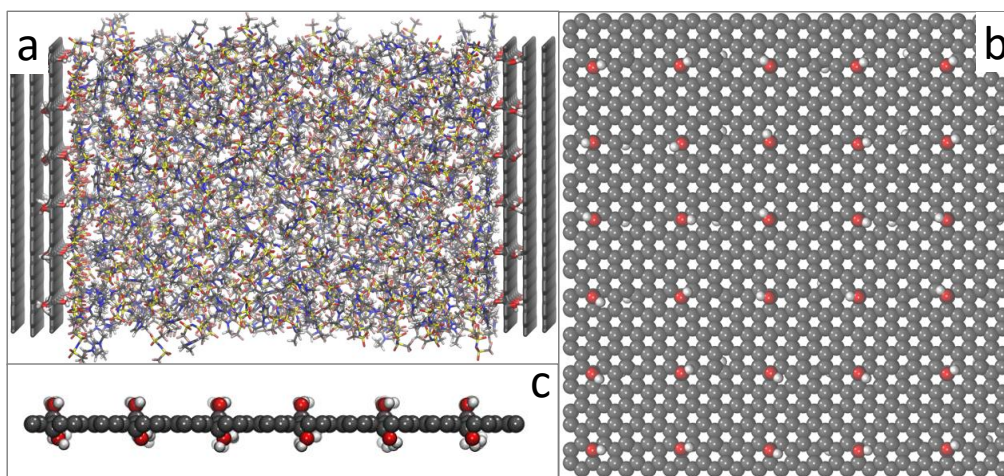
Figure 3.11. a) Simulation snapshot of the IL-filled pore. Functionalized graphene is shown in a b) top view and c) side view. Simulations correspond to section **4.2.3** results.

Fig. 3.11 shows the MD simulation system of [EMIm$^+$][TFSI$^-$] near oxidized graphene electrode surfaces. The electrolyte was enclosed between 2 parallel electrodes, with a separation distance of 8 nm to guarantee a bulk-like behavior of the electrolyte was found in the channel center. The pristine graphene electrode was modeled as 3 stacked graphene sheet layers with a 0.34 nm gap between each 2 neighboring sheets. All atoms maintained fixed positions during the simulation. Oxidized graphene electrodes added –OH groups to the innermost layers of the pristine graphene electrodes. All sp^2 carbon atoms remained rigid, while sp^3 bonded atoms and –OH groups were flexible.

3.7 Electrochemical Testing Setup

3.7.1 Electrode Film Preparation

Since tests of individual powder particles are impractical, carbon electrode powders were compressed into thin electrode films for electrochemistry experiments and

conductivity measurements. Carbon powders were mixed with polytetrafluoroethylene (PTFE). A 60 wt. % dispersion of PTFE in H_2O (Sigma-Aldrich) was mixed with excess ethanol and carbon to create a 95 wt. % carbon / 5 wt. % binder slurry. The solution stirred for 12-24 hours with low or no heating. After ethanol evaporated, the resulting slurry was ground with an agate mortar and pestle to homogenize the mixture and stretch the polymer fibers around the particles (**Fig. 3.12**). The materials were rolled to desired thicknesses using a mechanical rolling mill (Durston Mills, UK). This procedure yielded films that closely resembled commercially prepared supercapacitor electrodes. Rolled films were 85 – 110 µm thick, with 3 – 6 mg cm^{-2} mass loading densities. Coarse-grained powders (75 – 250 um diameter CDC) were rolled to minimal allowable thicknesses and yielded films with single carbon particles across an entire electrode. Although the binder was an electrically resistive, non-porous material, it did not significantly decrease total SSA of materials or block micropores. Counter electrodes (described in section **3.7.2**) were rolled into 250 um thick films. Electrodes were excised from bulk sheets into circular electrodes using high-precision hole punches. Symmetrical cells used 12 mm diameter disks (1.13 cm^2 cross-sectional areas); working electrodes used 9 mm diameter disks (0.636 cm^2 areas); counter electrodes used 15 mm disks (1.77 cm^2 areas).
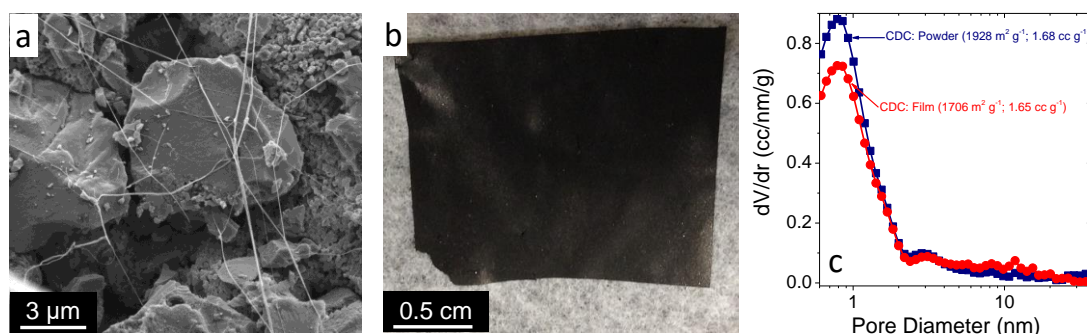
Figure 3.12. a) SEM image of PTFE-bound carbon electrode particles. b) Photographic image of a typical electrode sheet. c) Pore size distribution comparison of a typical bulk carbon powder and the resulting electrode film.

3.7.2 Electrochemical Test Cell Assembly

All electrodes were tested in "pouch"/"sandwich" cells, which had been described in literature (**Fig. 3.13**).[203] Electrodes dried in a low-vacuum oven (0.01 torr, 100 ℃) for 24 hours prior to testing. Aqueous electrolyte cells were assembled and tested in ambient air atmospheres; tests involving organic electrolytes and ionic liquids were carried out inside of an Ar-filled glovebox (Vacuum Atmospheres, < 1 ppm content of H_2O and O_2).

Electrodes were pressed against conductive current collectors, which transferred electrons from electrode films to the electronic circuit. Commercially available carbon-coated Al current collectors (Exopak, Inc.) were effective in organic electrolytes and ionic liquids. They were 50 µm thick, electrically conductive, and featured a stable carbon black coating that improved electron transport across the electrode film-current collector interface. Graphite foil (same as in section **3.5.1**) was used for aqueous electrolytes. Two layers of porous, hydrophilic polymer separator sheets (Celgard® 3501, ~150 µm thick films) were inserted between each electrode as (electrolyte-permeable) dielectric barriers. The electrolyte was poured into the cells (in excess quantity) after the supercapacitor components had been assembled. All cells were placed in polyethylene pouches and sealed with a heat sealer.
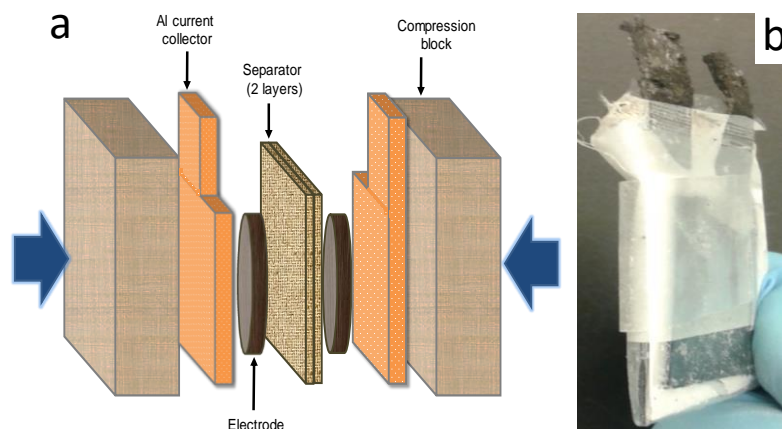
Figure 3.13. a) Schematic and b) photograph of a typical sandwich cell assembly.

Three different cell configurations were used during the course of experiments: two-electrode (symmetrical) cells, three-electrode/quasi-reference electrode (symmetrical cells), and three-electrode/reference electrode (asymmetrical cells):

1. Symmetrical cells implemented identical masses of both working (m_{WE}) and counter (m_{CE}) electrodes. Subsequently, the potential was set between the two electrodes, and each electrode obtained a certain potential (+ or -) with respect to a certain initial potential (open circuit potential (OCV) or point of zero charge (pzc); there is no clear consensus regarding the electrochemical state at initial equilibrium). The measurement that the potentiostat recorded included current that traversed through both the working and counter electrodes, which, in a symmetrical cell, acted as 2 capacitors in a series:

$$\frac{1}{C_{total}} = \frac{1}{C_{WE}} + \frac{1}{C_{CE}}$$
(**3.10**)

Since $C_{WE} = C_{CE}$, the capacitance of a single electrode, C_{WE}, equated to $2 \cdot C_{total}$.

2. A quasi-reference three-electrode setup included an Ag/AgCl wire as a pseudo-reference sensor. The silver wire was chlorinated in bleach for 10 minutes and inserted between the separator layers. The electrochemical measurement recorded the potential difference between the WE and the wire and the CE and the wire, but did not set the given potential between the WE and the wire; each electrode was allowed to accumulate charge and voltage according to its intrinsic properties. This approach allowed a proper examination of the symmetry of cation and anion accumulation.[204]

3. A classical three-electrode setup used the Ag/AgCl wire in a similar configuration; the potential of the WE was set against the reference wire. The mass of the CEs significantly exceeded (10+ tenfold) that of the WE. Subsequently, C_{CE} became much larger than the C_{WE}, and the $C_{total} \approx C_{WE}$.[205]

3.7.3 Electrolytes

Two different salts were dispersed in water for different aqueous electrolytes. 1.0 M H_2SO_4 (sulfuric acid) and 1.0 M Na_2SO_4 (sodium sulfate) were prepared from, respectively, diluting stock solution of acid (Alfa Aesar) and solid salt crystals (Sigma-Aldrich) in deionized H_2O (18.3+ MΩ rated resistivity). 1.5 M Organic electrolytes were prepared by dispersing tetraethylammonium tetrafluoroborate ($[NEt_4^+][BF_4^-]$, Fluka) in acetonitrile (CH_3CN, Alfa Aesar, HPLC grade). Ionic liquid electrolytes (all purchased from IoLiTec) included 1-ethyl-3-methylimidazolium ($[EMIm^+]$) bis-(trifluoromethylsulfonyl)imide ($[TFSI^-]$) and 1-ethyl-3-octylimidazolium ($[OMIm^+]$)$[TFSI^-]$). **Fig. 3.14** shows schematics and dimensions of different ions.

$[NEt_4^+]$: 0.68 nm x 0.68 nm

$[BF_4^-]$: 0.33 nm x 0.33 nm

CH_3CN: V_{av} = 0.077 nm³

$[EMIm^+]$: 0.85 nm x 0.55 nm x 0.28 nm
(V_{av} = 0.15 nm³)

$[TFSI^-]$: 1.09 nm x 0.51 nm x 0.47 nm
(V_{av} = 0.22 nm³)

$[OMIm^+]$: V_{av} = 0.32 nm³
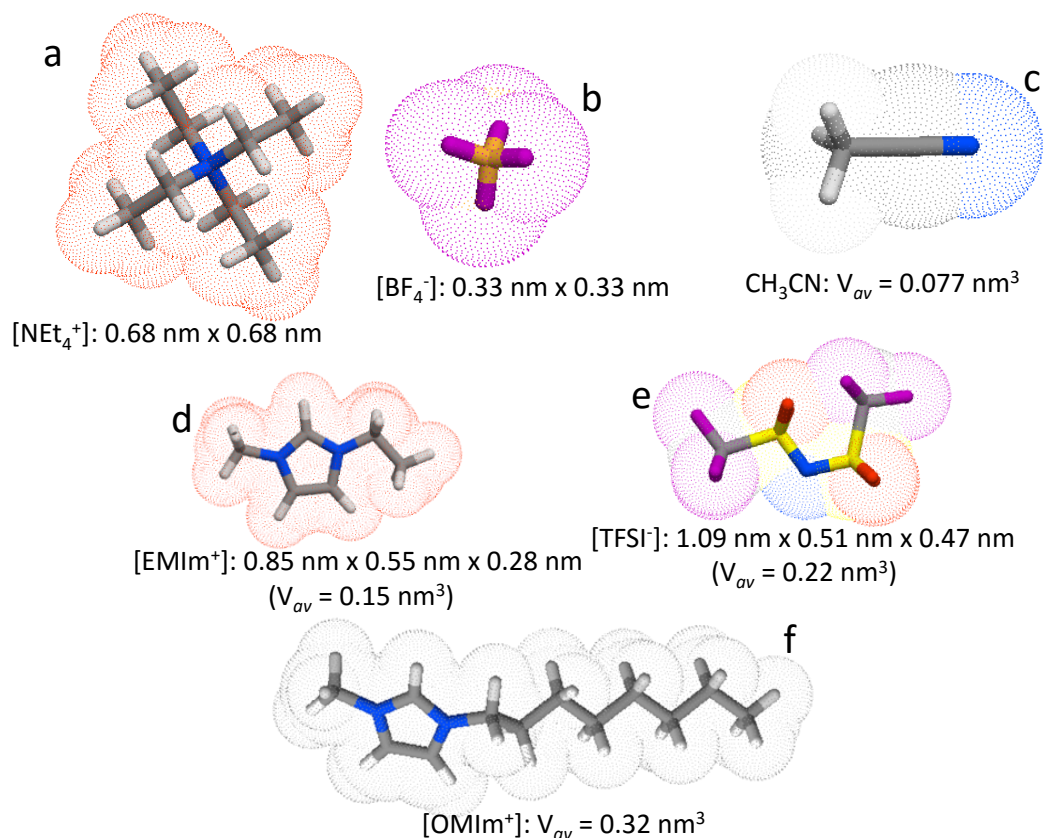
Figure 3.14. Schematics and dimensions of a) $[NEt_4^+]$, b) $[BF_4^-]$, c) CH_3CN, d) $[EMIm^+]$, e) $[TFSI^-]$, and f) $[OMIm^+]$.[37] Sizes derived from Ref. [28] and [27].

---

[37] Molecule structures generated using http://www.molinspiration.com built-in software.

3.8 Electrochemical Testing

All electrochemical tests were carried out with a VMP-3 Potentiostat (Bio-Logic, Inc., France) at room temperature (294 – 298 K). EC-Lab software (Bio-Logic) collected the data and converted it to an ASCII format, following which MATLAB and MS Excel were used to calculate key electrochemical parameters.

3.8.1 Cyclic Voltammetry

Cells were cycled between vertex potentials (V_0 and V_f) at certain dynamic potential (sweep) rates (dV dt^{-1}). Cells were cycled between 0.5 mV s^{-1} and 1 V s^{-1}; 10 mV s^{-1} was the 1st cycle sweep range. Cells were pre-cycled at each sweep rate for 10 cycles to attain steady-state, repeatable performance. The final cycle was used for all calculations.

Cyclic voltammograms (CVs) yielded gravimetric (normalized by electrode mass) or SSA-normalized (normalized by electrode mass (m_{WE}) and the gas sorption-derived SSA (A_{sp}) of the material) capacitance (C_{sp}) using the discharge segment of the CVs with the following current integration (V_w is the voltage window between V_0 and V_f vertices):

$$C_{sp} = \frac{2}{A_{sp}} \int_{V_o}^{V_f} \frac{I}{\frac{dV}{dt} m_{WE} V_W} dV \tag{3.11}$$

The typical CV shape is shown in **Fig. 3.15**. The classic electrochemical capacitor, which involves only electrosorption and charge accumulation in pores, typically exhibited a rectangular shape. Deviations from the shape, such as distorted or rounded edges of the CV rectangle, qualitatively signified electrical and ionic resistance contributions from various system components. Ion sieving, ionic impedance (through narrow pores or across ionophobic surfaces), and poor electrical transport through

electrode films all could contribute to this CV distortion. Butterfly-shaped CVs (described in section **1.5**) were indicative of voltage-dependent capacitance behavior.

Charge transfer processes (redox reactions and pseudocapacitive contributions) exhibited unique inflection points and reaction peaks at certain potentials and identified Faradaic processes. Upward inflection of the CV plot at vertex potentials qualitatively signified irreversible electrochemical breakdown and inferred voltage window stability limits. The coulombic efficiency (Q_{eff}) parameter quantitatively evaluated electrochemical breakdown by dividing the integrated discharge current (*i.e.,* total output charge) by the integrated charge current (*i.e.*, total input charge).

The Randles-Sevcik coefficient (*RS*) was calculated from CVs techniques using the following equation relating peak current (*I*), charge transfer coefficient (*n*), Faraday constant (F), SSA (*A*), molar IL concentration (*c*), diffusion constant (*D*), temperature (T), gas constant (R), and the scan rate (*v*):[206]

$$I = 0.4463 \ (n \ F)^{1.5} A \ c \ (\frac{D}{RT})^{0.5} v^{RS} \tag{3.12}$$

The equation was used to fit data from different sweep rates to derive values of x for each system. RS values that approached 1.0 suggested ideal capacitor behaviors, whereas values of *x* near 0.5 indicated diffusion-limited systems.
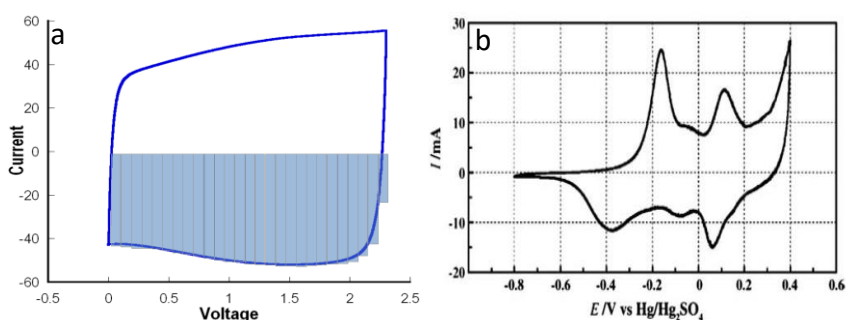
Figure 3.15. a) Ideal rectangular CV shape. The highlighted discharge portion is integrated for C_{sp} calculations. b) Irregularly shaped CV with redox processes.[207][38]

---

[38] Reproduced with permission from *J. Electrochem. Soc.* (Ref. [207]). Copyright 1999, The Electrochemical Society.

3.8.2. Galvanostatic Cycling

Cells were cycled at constant current (galvanostatic cycling with potential limitation, a.k.a. GC/GCPL) between vertex potentials. The current values were normalized by mass and fell in the 0.1 – 5.0 A g^{-1} range. Capacitance was extracted by dividing the current density by the slope of the discharge curve (Voltage vs. time). Ohmic drop resistance was calculated from the vertex potential by dividing the magnitude of the ohmic drop (volts) by current (amps) using Ohm's Law.[205] Life cyclabilities of electrodes were also calculated using this technique by ageing cells: they were cycled 10,000 times using high current densities (1.0 – 5.0 A g^{-1}).[151]

3.8.3. Electrochemical Impedance Spectroscopy

Unlike CV and GC techniques, which relied on direct (linear) current and voltage sweeps, electrochemical impedance spectroscopy (EIS) relies on alternating voltage (V) and current (*I*) with an initial frequency that dampens to a lower value. V and *I* follow sinusoidal relationships that, with Eulers relationship (exp(jφ) = cos(φ) + jsin(jφ)), are expressed as follows:

$$V_t = V_0 \cdot \exp(j\omega t); \quad I_t = I_0 \cdot \exp(j\omega t - \varphi) \tag{3.13}$$

Impedance Z, as a function of oscillating frequency $\omega = 2\pi f$, is expressed as:

$$Z(\omega) = Z_0 \left(\cos(\varphi) + j\sin(\varphi)\right) \tag{3.14}$$

As shown in **Fig. 3.16**, current and voltage oscillations exhibit a phase offset that provides insights into the nature of impedance in the supercapacitor system. Under the application of the transmission line model (described in **1.2**), and assuming that each pore

in the carbon is an RC circuit, small phase angle offsets ($0 < \varphi < -45°$) are dominated by electrical resistivity, and larger phase angle offsets ($-45° < \varphi < -90°$) are dominated by capacitive charging processes.

EIS measurements were conducted using a 200 kHz – 10 mHz dampening frequency range. The potential centered at 0.0 V and oscillated with ±0.2 mV amplitude. Parametric Nyquist plots (shown in Fig. **3.16**) compared the real (Re(Z)) and imaginary (-Im(Z)) components of the impedance. Equivalent series resistance (ESR) was derived from values of Re(Z) at which –Im(Z)=0 and accounted for all electron transport limitations in the system.[208] The high-frequency semi-circular region accounted for contact and charge transfer resistance in the electrodes.[19] The mid-frequency Nyquist plot region between the semicircle and the -45° "knee" frequency accounted for ionic impedance and bulk transport limits in the supercapacitors. The oscillation period at the -45° impedance point corresponded to the RC time constant (τ). The phase angle at the lowest oscillation frequency (10 mHz) approached -90° for ideal capacitors and -45 for resistive, diffusion-limited systems.[209]
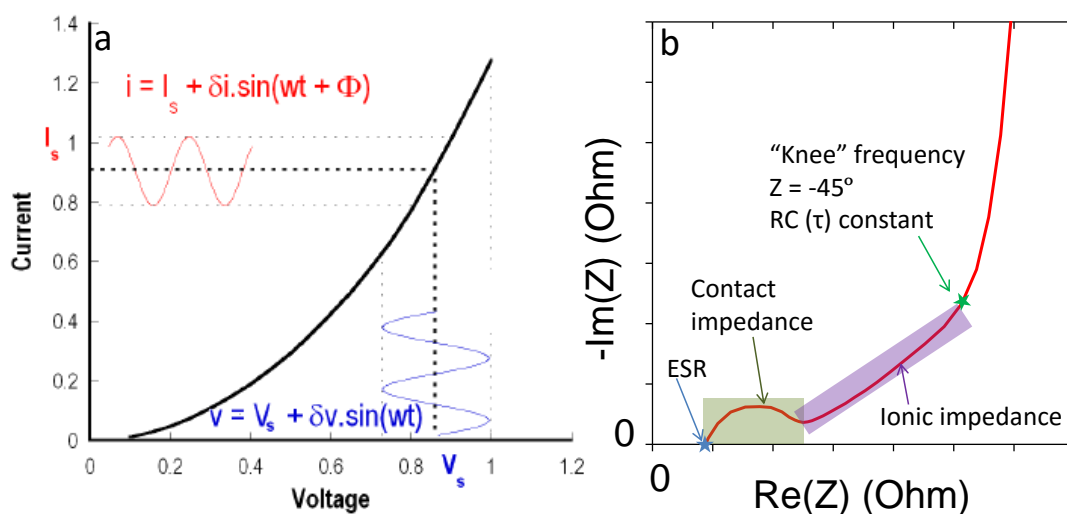
Figure 3.16. a) Sinusoidal current response in a linear system. b) Typical Nyquist parametric plot and the specific regions that are analyzed to determine key capacitive and resistive contributions.

Impedance included both real (C') and imaginary (C") components that were calculated using the following equations:

$$C'(\omega) = \frac{-Z''(\omega)}{\omega|Z(\omega)|^2} \tag{3.15}$$

$$C"(\omega) = \frac{Z'(\omega)}{\omega|Z(\omega)|^2} \tag{3.16}$$

These relationships were analyzed with Bode Impedance plots of C vs. frequency. The value of $C'(\omega)$ at f = 10 mHz provided a separate measure of C_{sp}; the frequency value at which $C"(\omega)$ demonstrated a maximum provided the time constant.

3.8.4. Chronoamperometry

Square wave chronoamperometry (CA) involved instantaneous potential jumps from 0.0 V to vertex potentials and measuring current (and total accumulated charge) vs. time. Measurements were collected every 0.5 µA fluctuation or 0.1 s (whichever occurred more frequently). Cells were held at given voltages for 1 hour to reach steady-state conditions and were fully discharged between each step charge accumulation. In addition to measuring the rate of charge accumulation vs. time and static C_{sp} values for different supercapacitors, the technique provided parasitic current measurements and quantified electrochemical breakdown reactions in different potential windows.

CHAPTER 4 – RESULTS AND DISCUSSION

The results of this research, including strategic approaches and resulting key findings, cover four main objectives. Subsequently, the discussion in this chapter is split up into four mains sections. Section **4.1** describes the efforts that removed surface defects from CDC pore walls, *via* both defunctionalization and graphitization, and their resulting influence on capacitance. Section **4.2** describes follow-up efforts that deposited specific chemical groups on porous carbons and evaluated the resulting electrode-electrolyte interface changes. Section **4.3** compares differently functionalized porous and non-porous surfaces, as well as CDCs with different pore lengths, to deconvolute the influence of defect pore surface composition from ion confinement. Section **4.4** implements those fundamental concepts in optimized nanostructured electrodes, novel *in situ* spectroelectrochemistry, and environmentally benign device designs.

4.1 Surface Defunctionalization and Annealing

The initial question that required an answer was fairly intuitive: are surface defects beneficial or detrimental to supercapacitor performance? The initial approach in this dissertation was inspired, in part, by Chmiola and Osswald's prior efforts,[167] which had controlled the porosity and graphitization of CDCs with high-temperature vacuum annealing. Although their approach had demonstrated expected structural evolution of porous carbons, the results could not explain observed capacitance changes in graphitized electrodes. Furthermore, basic characterization, which had been limited to gas sorption,

Raman spectroscopy, and X-ray diffraction, could not quantify detailed surface composition parameters and specific defects on pore surfaces of annealed CDCs.

The objective of this approach was to compare the capacitance, rate dynamics, and electrochemical stability of porous electrodes with different degrees of surface functionalization and graphitic ordering.[210] The approach focused on TiC-CDC and SiC-CDC microparticles (1-5 μm diameter), along with SiC-CDC nanoparticles (20-30 nm diameter), as model systems. Their initial pore structures (after 300 – 1,000 ℃ Cl_2 and H_2 treatment) were saturated with (heterogeneous chemical and structural) defects and ranged from amorphous to partially graphitized carbons. They were, subsequently, annealed to remove defects and increase carbon ordering. Their structure was studied in greater detail than previous attempts; such analysis more appropriately correlated surface chemical group compositions and graphitic features with electrosorption changes.

During the initial design of this study, vacuum annealing of CDCs was expected to retain a high SSA and well-ordered porosity, maximize electrical conductivity (*via* graphitization), and reduce/eliminate functional groups from (now-passivated) surfaces. Subsequently, the operating hypothesis for this approach predicted: 1) higher capacitance in graphitized, electrically conductive CDCs, 2) improved rate handling abilities of ions through smoother, defect-free surfaces; and, 3) expanded voltage windows in carbons with no functional groups and, subsequently, no irreversible breakdown reactions.

4.1.1 Annealing-Induced Structural Transformations

4.1.1.1 Particle Changes

The main processes that occurred during vacuum annealing were, in order of

prevalence, removal of functional groups from pore surfaces, graphitic reorganization and increase in size of ordered sp^2 domains, and limited pore restructuring. The procedure removed 10-15% of the mass of annealed CDC, with the amount of lost material proportional to the annealing temperature (**Fig. 4.1**). This mass loss included chemical groups, weakly attached carbons on surfaces, and all eternal liquid or gas species chemisorbed or trapped in tight pores.
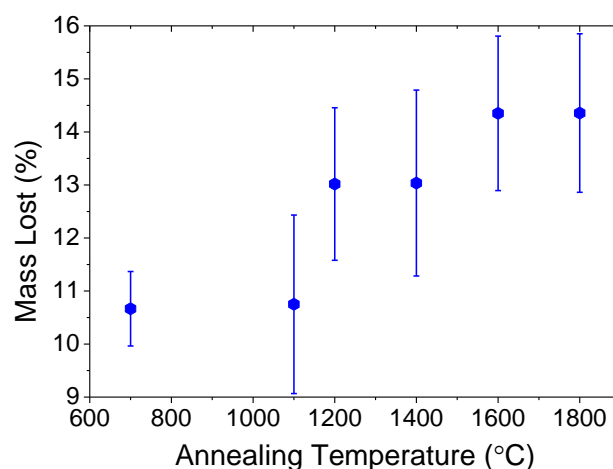
Figure 4.1. Mass changes of TiC-CDC micropowders after annealing the initial CDC at different temperatures under high (10^{-6} torr) vacuum.

4.1.1.2 Pore Structure Changes

TiC-CDC microparticles and SiC-CDC nanoparticles underwent very similar pore structure transformation under the influence of vacuum annealing. The initial materials had SSA values of 1682 m^2 g^{-1} and 2001 m^2 g^{-1}, respectively, and pore distributions demonstrate a 0.61 nm pore diameter for TiC-CDCs and 0.85 nm for SiC-CDCs. When annealed at 700 °C, the SSA of the microparticles increased by 15%, while the pore diameter increased slightly to 0.67 nm. Higher annealing temperatures decreased SSA by 19% (1371 m^2 g^{-1} after a 1400 °C anneal), with the micropore distribution remaining relatively unchanged and an increase in

mesoporosity. **Fig. 4.2** shows the pore size distributions and changes in accessible SSA and pore volume.
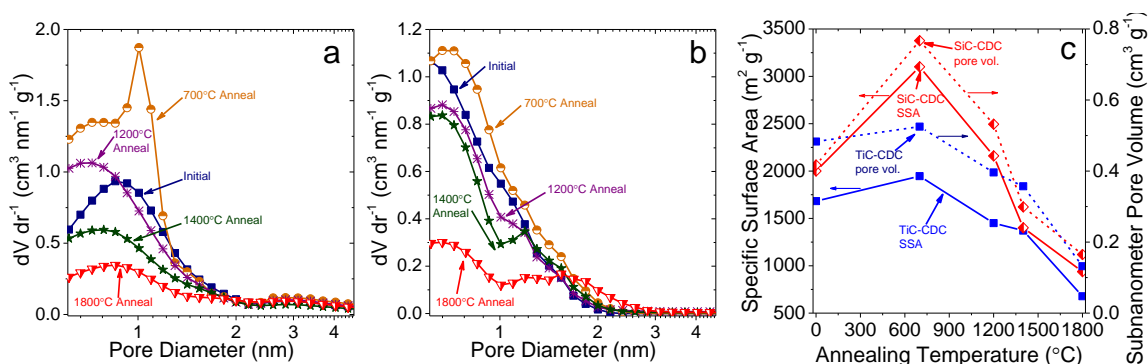
Figure 4.2. a) Pore size distributions for TiC-CDC microparticles in their initial state and annealed at 700 °C, 1,200 °C, 1,400 °C, and 1,800 °C. b) Pore size distributions for SiC-CDC nanoparticles annealed using the same conditions. Similar trends are observed. c) Changes in surface area and cumulative pore volume for the two systems.

The SiC-CDC nanoparticles reported similar responses to annealing temperatures: the SSA increased by 55% to 3100 $m^2 g^{-1}$ (1.01 nm pores) after 700 °C treatment and decreased by 30% to 1401 $m^2 g^{-1}$ (0.79 nm pores) after a 1400 °C anneal (**Table 4.1**). While the systems (synthesized at 800 °C) in their initial, non-annealed states exhibited similar structural and chemical properties, the effects of high temperature vacuum treatment differed for materials with divergent initial structures.[167]

Table 4.1. Surface area, pore volume, and pore size distribution values derived from N_2 gas sorption for initial and annealed microparticles and nanoparticles.

	TiC-CDC Microparticles			SiC-CDC Nanoparticles		
	Initial CDC	700 °C Annealed	1400 °C Annealed	Initial CDC	700 °C Annealed	1400 °C Annealed
BET SSA, $m^2 g^{-1}$	1682	1946	1371	2001	3101	1401
DFT SSA, $m^2 g^{-1}$	1699	1870	1337	1762	2899	1290
Cumulative pore volume, $cm^3 g^{-1}$	0.65	0.77	0.58	1.44	2.04	1.21
Subnanometer pore volume, $cm^3 g^{-1}$	0.48	0.53	0.36	0.42	0.77	0.30
Pore diameter mode, nm	0.61	0.67	0.67	0.85	1.01	0.79

Fig. 4.3 compares the influence of different vacuum annealing temperatures on the porosity and SSA of TiC-CDCs synthesized at 600 and 1,000 ℃. For all annealed materials, the micropore structure remained generally intact. The increase in mesoporosity for materials annealed at high temperatures was expected to enhance the mobility of ions during charging and discharging.[211]
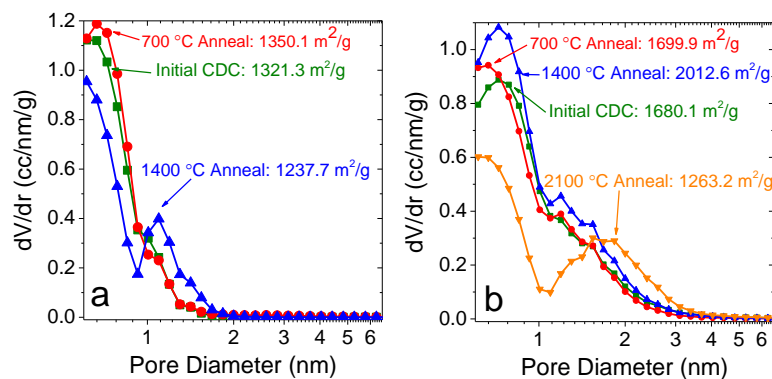
Figure 4.3. Pore size distribution for TiC-CDCs originally synthesized at a) 600 ℃ Cl_2 and b) 1,000 ℃ Cl_2, which show the influence of vacuum annealing on SSA and porosity.

Low-temperature annealing removed functional groups and attached carbon atoms from outer pore walls, opened closed channels (possibly removed functional groups or few-carbon layers blockages), and increased SSA. On the other hand, annealing above a 1,100 – 1,200 ℃ threshold restructured and merged micropores into mesopores, collapsed small branches, and decreased the cumulative surface area. The general schematics of these transformation mechanisms are shown in **Fig. 4.4**.
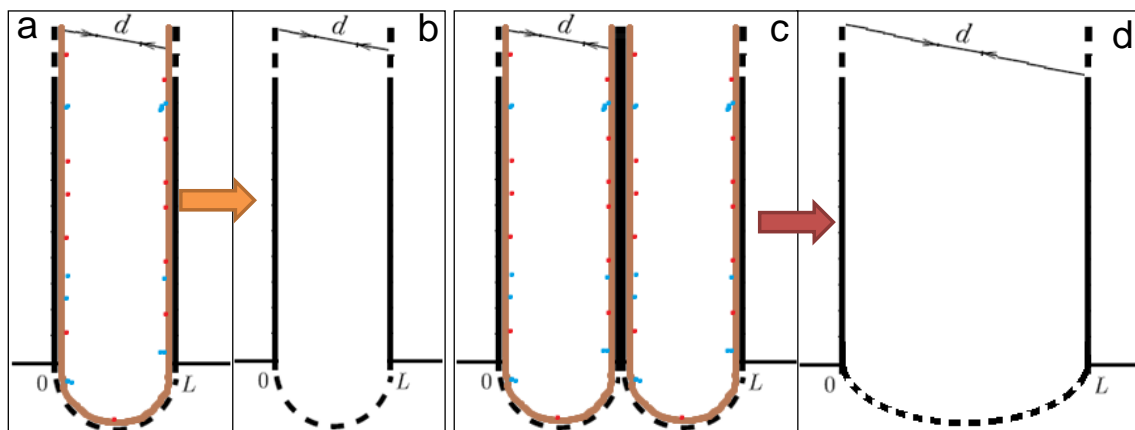
Figure 4.4. Low-temperature functional group removal and increase in accessible SSA from a) defect-rich to b) defunctionalized (but non-restructured) pores. At high temperatures, carbon restructuring merges c) adjacent small pores into d) larger pores and loses the surface area of the pore walls shared between two adjacent channels.

4.1.1.3 Changes in Graphitic Structure

The high-temperature annealing resulted in increased graphitization, as sp^2 domains became larger and more ordered. However, this was only observed for materials annealed at 1100 °C and above. Thermal treatment at 700 °C removed surface functional groups, yet did not provide sufficient energy for the carbon atoms to induce significant graphitization. Raman spectroscopy (**Fig. 4.5**) shows a temperature-dependent narrowing of both D and G bands, as well as the emergence of the resonant 2D and D+G bands.
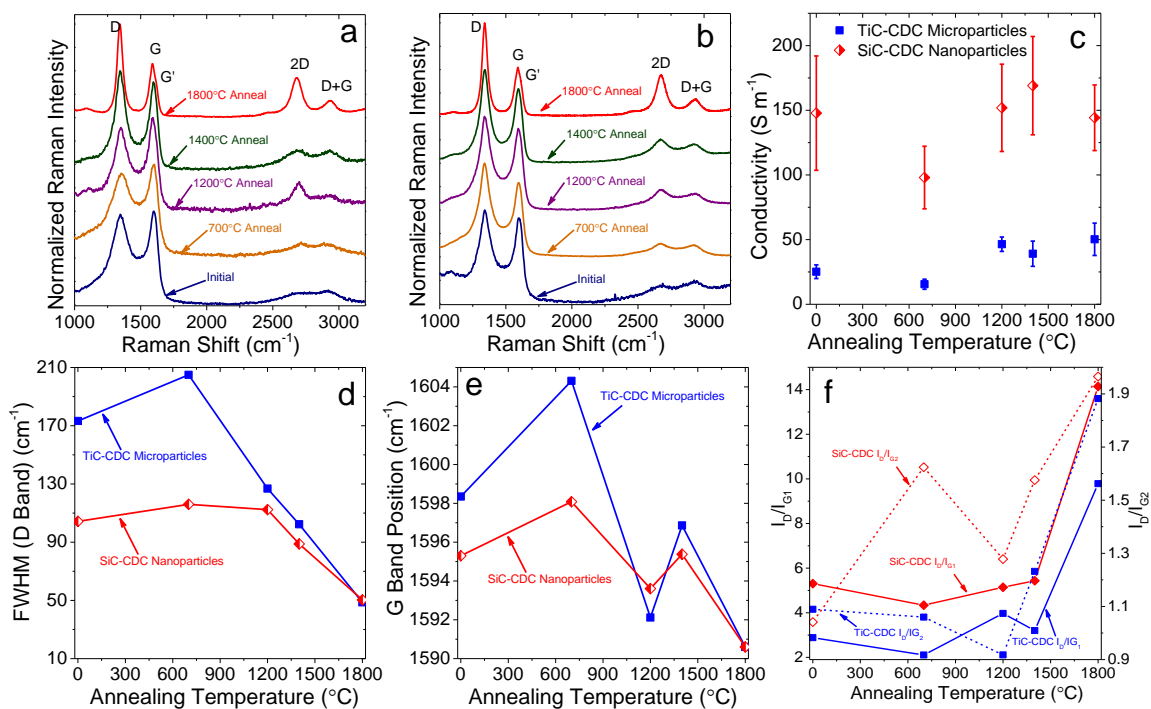
Figure 4.5. Raman spectroscopy offset spectra for a) TiC-CDC microparticles and b) SiC-CDC nanoparticles. Resonant modes became more prominent in graphitized structures. c) Effects of annealing on electric conductivity of PTFE-bound electrode films. d) FWHM of the main bands became narrower, indicating increases in ordering. Low-temperature annealing (700 °C) slightly decreased ordering, as surface carbons were removed without re-arranging the bulk carbon into sp^2 domains. e) Shifts of the center of the G band peak position, which gradually migrated from larger wavenumbers towards its intrinsic 1580 cm^{-1} value as a result of defect removal. f) Changes in the intensity ratios of the D-band (I_D) and the split G-band (I_{G1}, 1580 cm^{-1} and I_{G2}, 1595 cm^{-1}) peaks.

These observations confirmed expected increases in graphitic ordering.[56] The material retains a generally amorphous carbon structure before and after annealing, and its three-dimensional architecture (featuring small interlocked sp^2 domains) impedes the formation of long-range, defect-free graphene sheets on pore wall surfaces. As a result, the FWHMs of the D band are more appropriate than I_D/I_G ratios to describe graphitization.[78] The appearance of the G' band at the ~1610 cm^{-1} for both materials after 1800 °C annealing suggests the eventual collapse of the CDC particles into non-porous, polycrystalline structures; this is described well by the porosimetry data.

While Raman spectroscopy also provided some initial insights into specific structural transformations of CDCs during graphitization, the process is complex and encompasses a wide range of effects. Although the I_D/I_G ratios increased after annealing, the D bands did not disappear. The resulting carbon structures did not resemble ideal (HOPG-like), monocrystalline graphite but maintained polycrystallinity and small graphitic domains. Subsequently, the growth in the relative intensity of the disorder vibrational mode could be more accurately attributed to the increased prevalence of 6-membered (benzene) rings in annealed CDCs.[56] Furthermore, the leftward shift of the G band peak could be attributed to annealing-induced changes in electronic dopant structures in the CDCs. Previous experiments had correlated charge carrier concentrations (n-doping), which had shifted the Fermi level of carbon electrodes above the Dirac point, with 10-20 cm^{-1} wavenumber rightward G band peak shifts. The G-band shifted to the left by 7 cm^{-1} (for microparticles) and 5 cm^{-1} (for nanoparticles) after an 1800 °C anneal. If these results, which had been obtained for carbon nanotube electrodes, could extrapolate onto porous CDCs, these findings could suggest that defunctionalization had led to the removal of n-dopants from the carbon structure. Although graphitized electrodes became more electrically conductive, the G band peak shifts could have signified structural transformations that decreased quantum capacitance of defect-free CDCs.

Fig 4.5(d) shows the effects of annealing and increased graphitization on intrinsic electric conductivities. Conductivity generally increased with annealing temperature for both CDC materials, with nanoparticles generally exhibiting greater electron transport due to improved interparticle connectivity.[212] Conductivities of both materials dropped by 33-38% after 700 °C annealing. They exhibited higher pore

volumes, which impeded electron transfer,[213] without becoming sufficiently graphitized. Annealing at 1400 °C increased conductivity of TiC-CDC by 14 S cm^{-1} and SiC-CDC by 21 S cm^{-1}. The 16-50 S m^{-1} microparticle conductivities and 98-168 S m^{-1} nanoparticle conductivities were smaller than the values reported for monolithic, chemically reduced graphene oxide with high sp^2 ordering.[214]

Air TGA analysis (**Fig. 4.6**) showed increased oxidation temperature for samples annealed at higher temperatures and corroborated surface graphitization with pore wall passivation and greater stability. FWHM analysis of the oxidation profiles (from dTG, i.e. dM dT^{-1}) showed the broadest oxidation profile for the 700 °C samples and demonstrated significant dispersity and a generally disordered structure of both microparticles and nanoparticles annealed at that temperature. Previous experiments correlated narrower dM dT^{-1} peaks with greater structural defect concentration in MWCNTs (inter-wall faults, broken walls, etc.).[215] However, the narrowing of the dTG peaks shown for CDCs, which have a more heterogeneous structure, more likely corresponded with increased homogeneity and uniformity in annealed carbons.
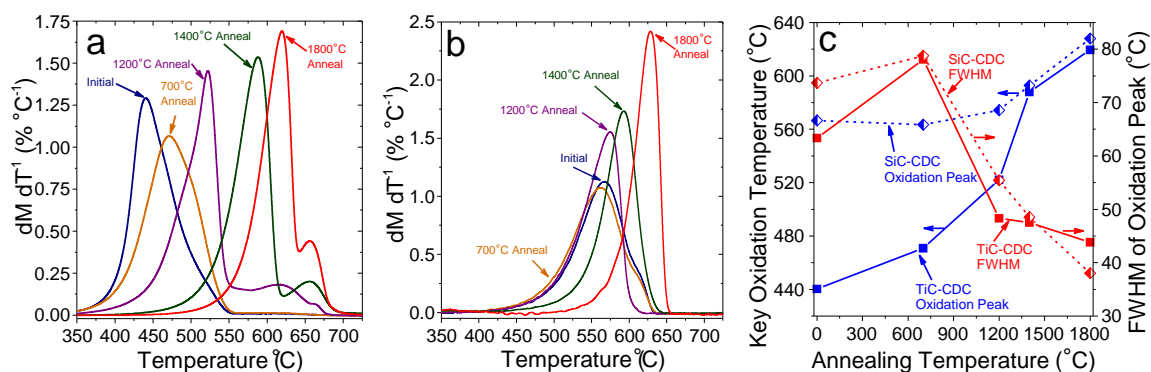
Figure 4.6. Oxidation peaks determined using TGA in air environment for a) TiC-CDC microparticles and b) SiC-CDC nanoparticles. c) These peaks show a shift to higher oxidation temperatures and suggest greater ordering/homogeneity in graphitized CDCs.

XRD analysis of annealed materials is shown in **Fig. 4.7**. The 26º 2θ peak grew and narrowed for CDCs annealed at higher temperatures. It corresponds to the 3.4 Å dense graphite phase (d-spacing). Therefore, annealed CDCs increased long-range ordering and stacking along the [002] direction. Since none of the CDCs exhibited bulk graphite phases, this transformation instead signified greater alignment/ordering of carbon sheets between pore walls.
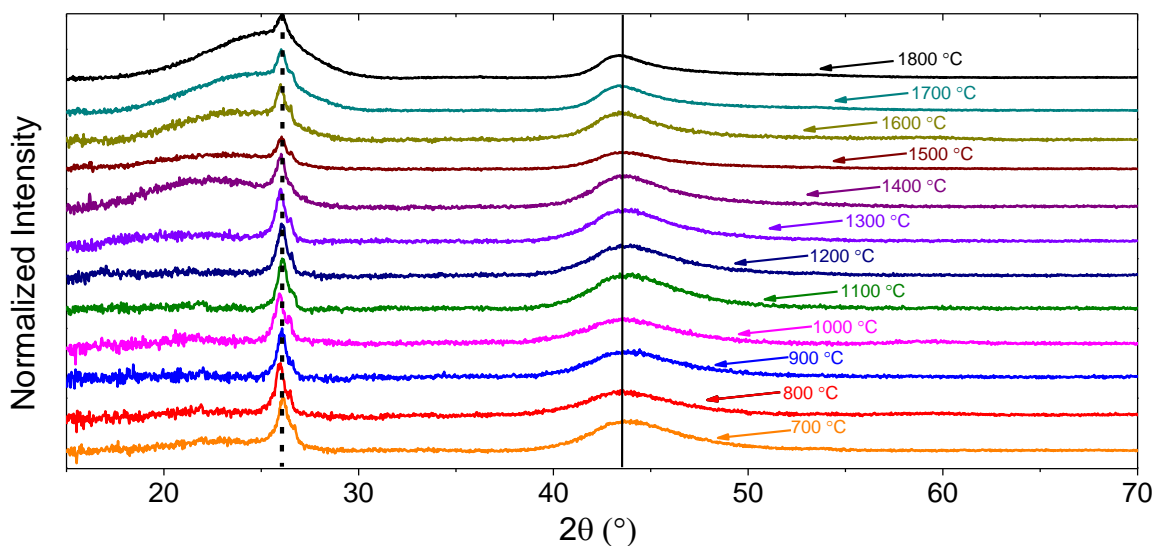
Figure 4.7. X-ray diffraction analysis of SiC-CDC microparticles annealed at 700 – 1800 ºC. The [002] peak and the [100]/[101] peaks are marked with dashed and solid lines.

4.1.1.4 Carbon Structure Transformation

Pair distribution function (PDF) analysis, which relied on neutron scattering and a synchrotron X-ray source for total diffraction analysis, provided a more in-depth look at the structural transformations. The Fourier-transformed intensity scattering data (S(Q) vs. Q) and the fitted and processed analysis data (in the form of G(r) vs. r) is shown in **Fig. 4.8**. Data fitting implemented **Eq. 3.3**.

As expected, the results indicated sharpening of all diffracted peaks and the appearance of graphite [002] peak (Q of 1.8 Å^{-1}), which suggested a monotonic

graphitization trend. The results have some carryover to wider-angle measurements (large Q values), so the S(Q) intensity change at 1.4 Å^{-1} could have signified porosity reduction or other long-length scale phenomena, such as pore network or pore surface texture changes.

The first three peaks (1.43 Å, 2.47 Å, and 2.85 Å) are C–C bonding distances that occur within the aromatic-type ring of graphene or graphite. Their changes in intensity suggest that the 6–member ring should be the dominated configuration over pentagons and heptagons. The intensity ratio of 1st vs 2nd and 2nd vs. 3rd peaks implied the relative populations of 5–, 6–, and 7–member carbon rings. Since the internal bonding angles of heptagons (108°), hexagons (120°), and heptagons (129 °) are all different, differently sp^2 π-π bonds could be expected to change the material's quantum capacitance or electrostatic/steric interaction with electrosorbed ions.
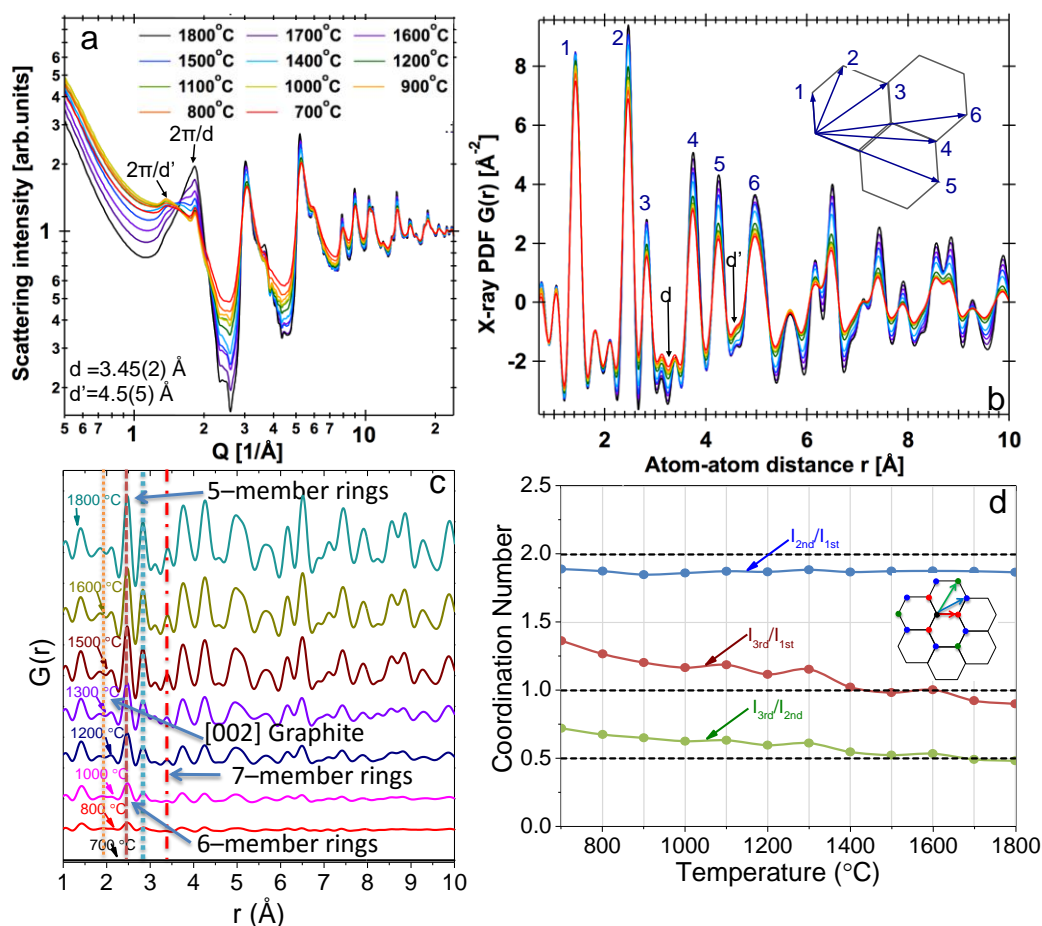
Figure 4.8. a) S(Q) structure factor data for SiC-CDC microparticles annealed at 700 – 1,800 ºC, obtained using neutron scattering. b) Fitted PDF data. The inset shows different correlation lengths marked on the graph. c) Low-Q (low-r) region of the PDF data, with the baseline peaks of 700 ºC annealed CDC subtracted from each of the other temperatures. d) Intensity ratios of correlation carbon bonding lengths. The inset marks a typical structure with 3 distinct lengths.

The PDF data was fitted to a simple 3-phase carbon model: 1) a bulk graphite phase (assuming infinite stacking of layers in the [002] direction with 3.4 Å d-spacing), 2) curved, freestanding graphene phase (standalone unique carbon sheets with no stacking or alignment), and 3) slit-pore morphologies that use layer-layer graphene correlations to mimic subnanometer porosities.[180] The results of the fits of the PDF findings to the model are shown in **Fig. 4.9**. The graphene structure (phase 2) assumed large thermal atomic displacements for carbon atoms moving normal to the [100] direction. The

thermal displacements, which were allowed by the model's absence of layer-layer correlation and structural confinement, indirectly accounted for curvature effects.
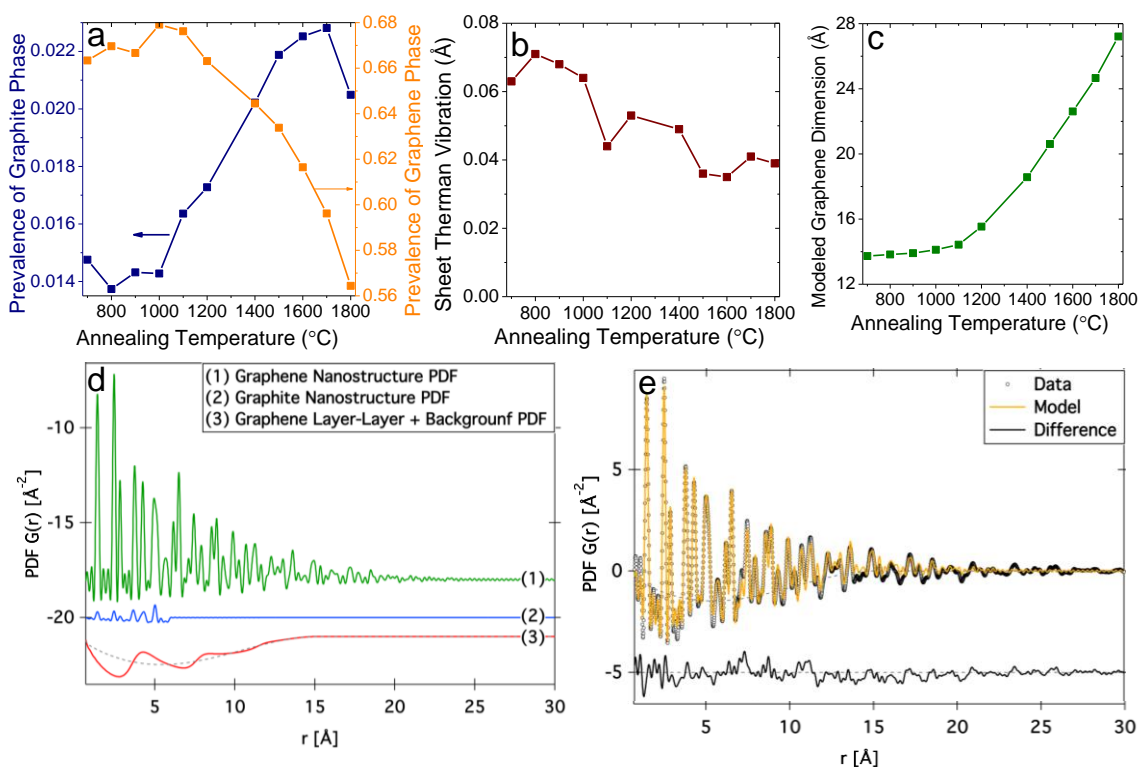
Figure 4.9. a) Comparison of prevalence of graphite (stacked) phase and graphene (freestanding sheet) phase as a function of graphitization. b) Modeled curvature-dependent thermal vibrations of the graphene sheets. c) Estimated planar dimension of graphene sheets as a function of annealing temperature. d) Initial model parameters and e) accuracy of its fit to the experimental X-ray PDF data.[39]

Although the model demonstrated planar growth of graphene domains, loose freestanding sheets became less prevalent at higher annealing temperatures. At the same time, the graphite phase became more dominant and further confirmed increases in stacking along the [002] direction. Structural transformations became significant in CDCs that were annealed above 1,100 ºC; this finding agreed with other measured structural changes. The curvature of layers slightly decreased with graphitization and suggested more prevalent 6-membered carbon rings in resulting CDCs. Finally, graphene layer-

---

[39] Model calculations were conducted at Oak Ridge National Laboratory.

layer correlation distances deceased and suggested that layer restacking narrowed certain pores and, eventually, collapsed internal porosities (in line with porosimetry).

Structural characterization of the material suggested that primary pore surface composition changes were limited to chemical group removal and defunctionalization at low annealing temperatures (700 – 1,100 ℃) and included significant carbon ordering transformations only at higher annealing temperatures (1,200 – 1,800 ℃). Defect concentrations and pore wall thicknesses transformed during graphitization. These structural differences were predicted to influence both charge screening in confined pores and relative quantum capacitance contributions to total C_{sp}.

4.1.1.5 ReaxFF Modeling of Porous Carbons

Although Raman spectroscopy and X-ray scattering provided qualitative comparisons between differently graphitized CDCs and assessed thermally-driven structural evolution trends, these empirical techniques could not comprehensively quantify precise concentrations of defects on pore walls. Quenched Molecular Dynamics (QMD) simulations of CDCs could provide more accurate comparisons of porous carbons and assign more specific values to certain structural features.[216] To accomplish this goal, PDF data was integrated into QMD simulations that used the reax/c implementation of ReaxFF in the LAMMPS simulation package.[217,218] The simulation used the most recent carbon-carbon interaction parameters.[219] The simulation quenched the system from 3,500 K to 3,000 K from 1.25 to 500 picoseconds. To equilibrate charge in ReaxFF,[220,221] a 500 ps simulation took 48 hours using two nodes (48 cores) on NERSC's Edison cluster. The findings are shown in **Fig. 4.10**.
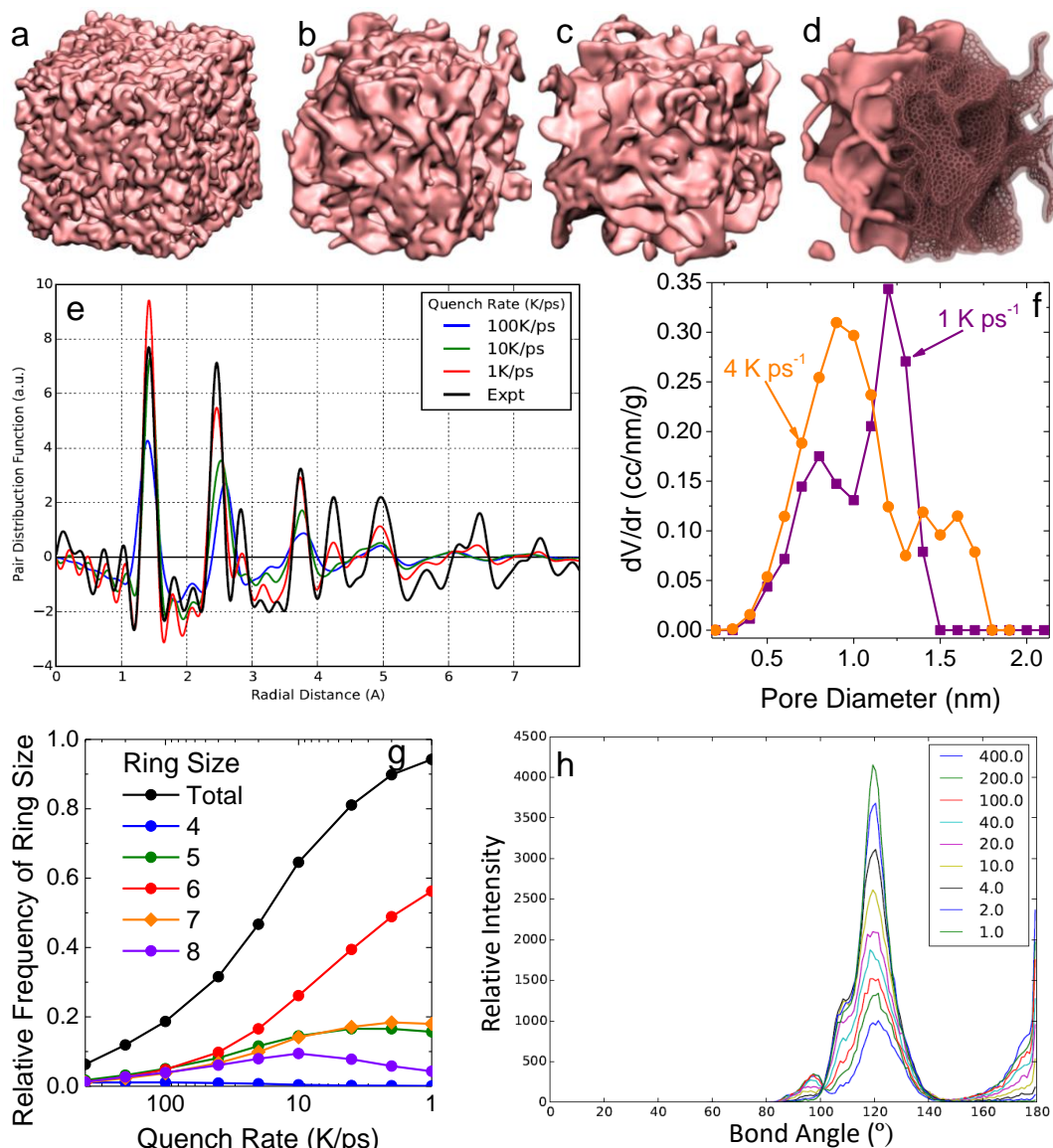
Figure 4.10. Snapshots of the MD simulation of CDC after a) 1.25 ps, b) 50 ps, c) 125 ps, and d) 500 ps quench rates. e) Comparison of simulations of PDFs for different quench rates and its comparison against experimentally-derived CDC annealed at 1,800 C. f) Simulated pore size distribution. g) Comparison of ring prevalence and its transformation for different quench rates. h) Distribution of calculated bond angles for $1.0 - 400.0$ K ps^{-1} quench rates.

Results drew on prior QMD simulations of CDCs[76] and nanoporous graphene ribbons.[222] Slower quench rates yielded more ordered simulated structures, which primarily influenced the relative prevalence and distributions of carbon-carbon bonding rings. Trend analysis showed greater prevalence of benzene rings in graphitized

structures and matched the conclusions from experimentally-derived PDF. Separation distances between ordered graphene structures were attributed to slit pores, and additional MD simulations compared predicted and measured N_2 adsorption to derive porosities.

The model has not, to date, been able to accurately reflect the graphitization of experimentally-measured CDCs. Even the slowest quench rates did not predict the level of ordering that X-ray or neutron PDF had recorded for 1,800 ℃ SiC-CDCs. The most up-to-date simulations could not control porosity as accurately as Cl_2 and vacuum annealing treatments. The inherent strategy behind this computational approach likely led to this divergence: while Cl_2 etching removed metal atoms from the carbide lattice, the QMD approach condensed carbon from a liquid to a solid state. Although the simulation results parametrically correlated with annealed porous carbon structures, they could not capture all relevant surface defects. However, the findings demonstrated graphitization-dependent changes in ring prevalence distributions in annealed CDCs, and the resulting changes in bonding angles (and, subsequently, bond energies and chemical strain in structures) were expected to significantly influence ion electrosorption, capacitance, and electrochemical stability under high applied potentials.

4.1.1.6. Graphitization-Induced Morphology and Roughness Changes

Transmission Electron Microscopy (TEM) analysis revealed an increase in ordered graphite/graphene features in all annealed and graphitized CDCs. While the materials maintained a predominantly heterogeneous amorphous or turbostratic carbon structure, annealed TiC-CDCs showed greater prevalence of graphitic features such as barrels (**Fig. 4.11(c)**) and ribbons. Although nanoparticle-sized CDCs exhibited more structural

uniformity and lower annealed-induced visible transformations, their edges noticeably transformed to curved nanoribbons and featured that resembled single-layer graphene. Ordered domains of graphene sheets vertically stacked in different orientations throughout the particles. Subsequently, interpore thicknesses and carbon compositions in walls became very disperse for annealed, graphitized CDCs.
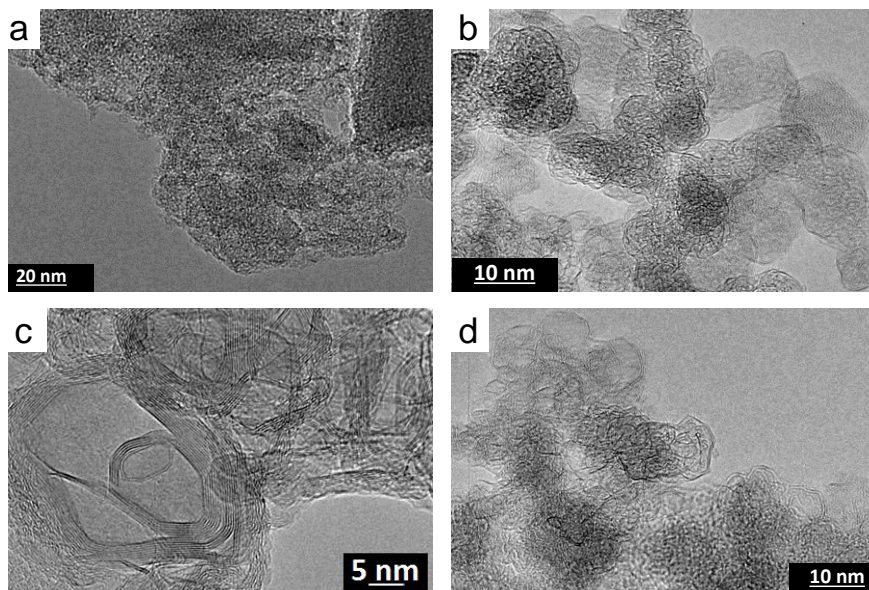
Figure 4.11. TEM micrographs that showed relative prominence of key morphological features as a result of 1,400 °C 8-hour vacuum annealing. a) Annealed TiC-CDC microparticles produced c) a variety of graphitic ribbons and barrels more prevalent turbostratic graphite, and ordered, smooth particle termination edges. SiC-CDC nanoparticles shown in b) developed mostly graphitic ribbons shown in d).

In addition to bright-field TEM analysis of annealed TiC-CDC particles, a scanning TEM (STEM) provided dark-field images of 700 – 1,800 ℃ annealed SiC-CDCs. This approach improved the resolution of certain structural features and provided better contrast for side-by-side comparison of structural evolution effects. The images are shown in **Fig. 4.12**.
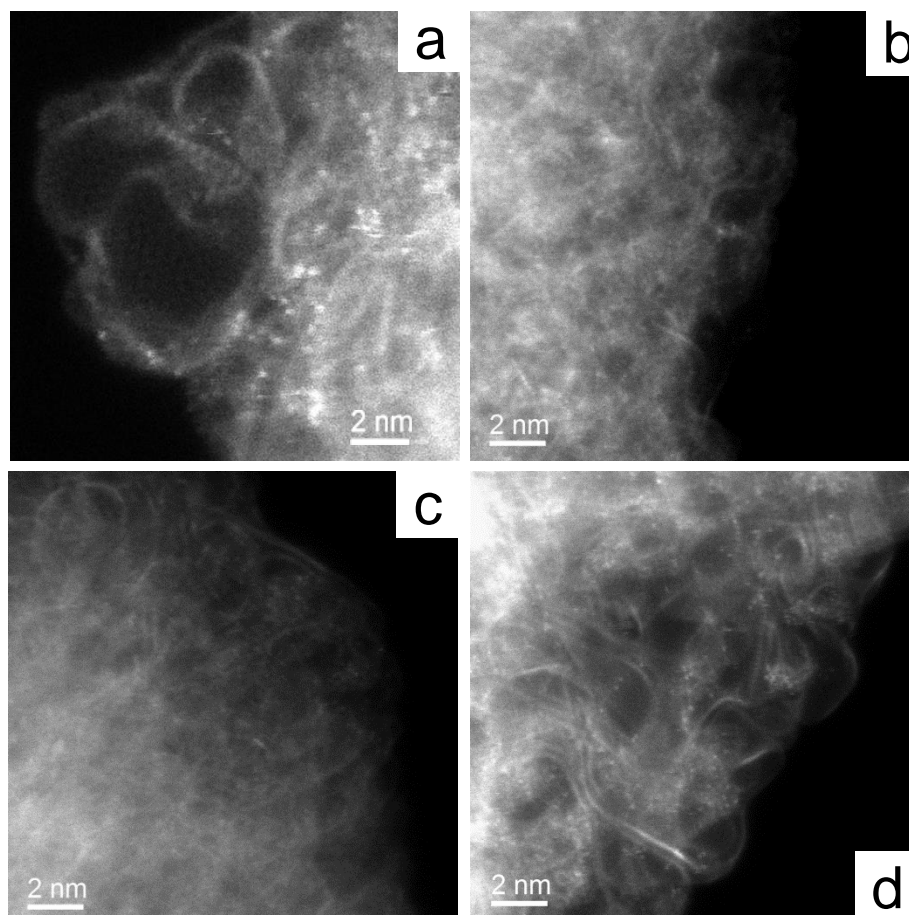
Figure 4.12. STEM images of SiC-CDC microparticles annealed at a) 700 ℃, b) 900 ℃, c) 1,100 ℃, and d) 1,600 ℃.

In agreement with structural findings, the images demonstrated periodic, graphitized structures that became more ordered at higher annealing temperatures. The biggest transition occurred above 1,100 – 1,200 ℃ thermal treatments. Images showed freestanding graphene sheets (at 700 ℃), which likely acted as single-layer walls between adjacent pores, that restacked into more compact monoliths at higher temperatures.

This imaging technique also discovered elemental silicon atoms (bright spots) that were prevalent in all analyzed CDCs. Their overall amount had been negligible in CDCs: none of the scattering techniques (PDF, XRD) noted any $Si/SiC/SiCl_4/SiO_2$ phases, and TGA analysis recorded negligible ash contents ($< 1\%$) for all materials. The elemental Si

impurities did not disappear after annealing and, therefore, were present in all analyzed CDCs. This particular defect has been overlooked in previous capacitance measurements that had relied on CDCs. Although previous research efforts have noticed different impurity levels for carbons synthesized at low temperatures, the most discussed effect, to date, has been solely the lower SSA of partially unconverted CDCs.[85] Elemental Si may alter quantum capacitance, intermolecular interactions of electrolyte ions with surfaces, and atomic surface roughness of pore walls. However, the relative low quantity of this phase could not be properly quantified with available techniques. Furthermore, despite greater resolutions of the UltraSTEM instrument, the images could not confidently discern whether the elemental defects were on pore surfaces or sandwiched by carbon layers between pores.

Small-angle scattering provided additional comparison of atomic pore surface roughness and corrugation that was influenced by structural evolution and vacuum annealing. **Fig. 4.13** demonstrates the small-angle neutron scattering (SANS)-derived I(Q) vs. Q relationship for SiC-CDCs annealed at 700 – 1,800 ℃. Deconvolution of results primarily focused on the Porod scattering region (0.08 Å^{-1} < Q < 0.01 Å^{-1}) and fit the results to the Porod power law equation (**Eq. 3.2**). Although the results did not demonstrate clear trends for lower annealing temperatures, significant graphitization onset (> 1,300 ℃) correlated with lower values of the negative Porod exponent (n). Subsequently, amorphous CDCs exhibited smoother pore surfaces, and their graphitized counterparts featured atomically rough, corrugated walls.[176] This approach assumed ideal surface fractals; although the regression fits exhibited good correlations (R-squared = 0.998), future characterization efforts must develop complementary analysis methods.
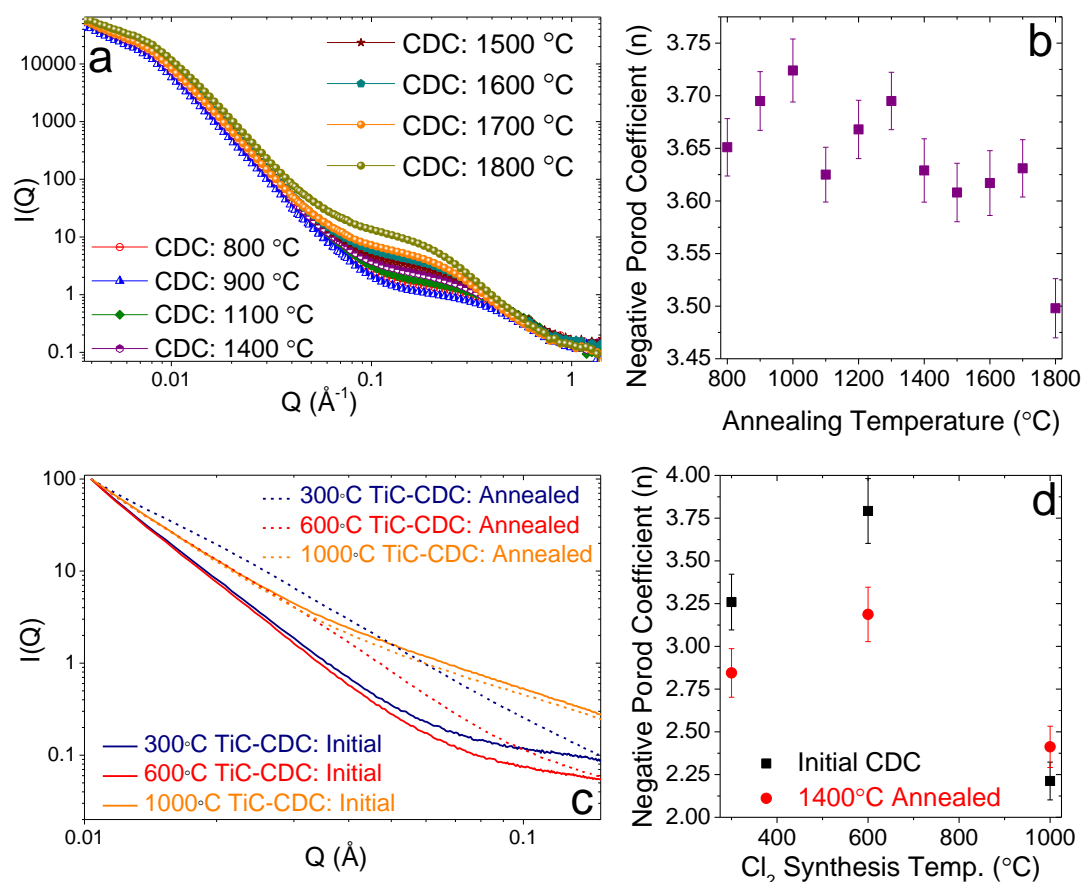
Figure 4.13. a) I(Q) vs. Q SANS data for SiC-CDC microparticles annealed at 700 – 1,800 °C. b) Corresponding Porod coefficient fits for the surface fractal region. SAXS data for TiC-CDCs synthesized at 300, 600, and 1,000 °C (before and after 1,400 °C vacuum annealing) is shown in c), with corresponding Porod coefficient fits in d).

Small-angle X-ray scattering (SAXS) provided a similar analysis of TiC-CDC microparticles synthesized at 300 °C, 600 °C, and 1,000 °C in their initial state and after 1,400 °C annealing. The finding demonstrated similar annealing-induced pore roughness increases for initially amorphous (300 °C and 600 °C Cl_2) CDCs. TiC-CDC that had been synthesized at 1,000 °C was already moderately graphitized, and additional annealing did not significantly reconstruct its pore wall surfaces (hence negligible changes in the Porod constant). However, both its initial and annealed surfaces were more corrugated than lower-temperature structures; this structural description corroborated the SANS-derived conclusions regarding atomic smoothness of annealed SiC-CDCs.

4.1.2 Annealing-Induced Bonding and Surface Chemistry Changes

4.1.2.1. Electron Energy Loss Spectroscopy Analysis

In addition to providing high-resolution TEM images, the UltraSTEM instrument collected electron spectroscopy data. In particular, it analyzed the carbon K edge.[223] Specific spectra and calculated relative sp^2/sp^3 bonding ratios are shown in **Fig. 4.14**. The calculations for sp^2/sp^3 bonding ratios relied on **Eq. 3.5**.
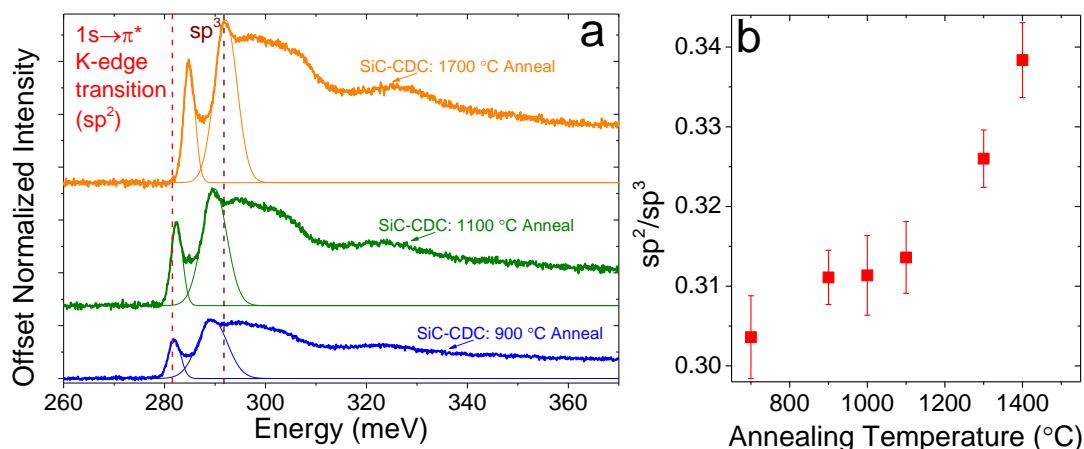
Figure 4.14. a) EELS core-loss spectra of SiC-CDC microparticles annealed at 900 ℃, 1,100 ℃, and 1,700 ℃. b) Integrated sp^2/sp^3 bonding ratios for annealed CDCs.

This approach provided bonding information that had not been detected by other techniques, such as X-ray PDF analysis. Carbon-carbon bonding has three characteristic types and several corresponding lengths: sp^3–sp^3 (1.54 Å); sp^3–sp^2 (1.50 Å); sp^2–sp^2 (1.47 Å); sp^2–sp (1.43 Å); and sp–sp (1.37Å). PDF analysis did not detect any shifting of the 1.43 Å peak (to higher r distances).[224] Subsequently, a more sensitive technique was needed to detect relatively uncommon sp^3 bonds. The bonding analysis provided by EELS primarily provided a relative comparison and could not derive absolute rations without incorporated sp^2 (HOPG) and sp^3 (crystalline diamond) references. Experimentally measured EELS measurements for similar CDCs derived sp^2/sp^3 ratios

that reached 0.88 – 0.90 (with sp^2 bonding accounting for up to 90% of total bonding in the structure).[183] The absolute values for annealed CDCs likely reached and exceeded these ratios.

EELS spectra analysis showed that overall bonding in the carbon structure was significantly influenced by thermal annealing. Graphitization increased sp^2 (ideal graphite bonding) prevalence throughout the carbon structure, although the dependence was not linear and featured an inflection point at 1,100 ºC. Although sp^3 bonding was likely dominated by (diamond-like) carbon-carbon bonding, some of those bonds could have accounted for carbon-hydrogen bonding, which exhibited similar hybridization. Since C=C and C–C bonds exhibit different energies and polarizations, their relative prevalence on pore surfaces also influenced intermolecular interactions with electrosorbed ions.

4.1.2.2. Functional Group Content

As expected, high-temperature vacuum annealing defunctionalized surfaces of the CDC materials. XPS-derived elemental analysis of the materials, which is shown in **Table 4.2**, showed that elements such as oxygen, nitrogen, and chlorine steadily decreased in atomic % after the 700 °C anneal and were almost completely eliminated after the 1400 °C treatment. SiC-CDC nanoparticles, which had lower relative initial amounts of surface chemical species, did not experience such drastic defunctionalization. This effect could be related to both their higher SSAs (increasing the prevalence of contaminants adsorbed from air) and particle aspect ratio, which could have facilitated re-functionalization (after exposure to air).

Table 4.2. XPS-derived atomic percentages of key chemical species identified for the two systems. Entries indicating a range of values signify amounts found outside of particles (before Ar sputtering) and inside (after sputtering away several nm).

	TiC-CDC Microparticles			SiC-CDC Nanoparticles		
	Initial CDC	700 °C Annealed	1400 °C Annealed	Initial CDC	700 °C Annealed	1400 °C Annealed
Carbon	92.3	96.1	99.7	97.9	98.1	97.4
Oxygen	4.1	1.4	0.0	1.7	1.4	1.7
Nitrogen	2.3	2.1	0.0	0.0	0.0	0.0
Chlorine	1.3	0.0 – 0.3	0.0 – 0.3	0.0 – 0.4	0.0 – 0.5	0.0 – 0.9
Titanium/Silicon	0.0	0.0 – 0.7	0.0	0.0	0.0	0.0

TGA analysis in an Ar environment (**Fig. 4.15**) showed that the functional group content, which had constituted 7-9% of the total CDC mass in its initial state, decreased to < 3% after the high-temperature treatment. Analysis of dTG curves showed a few decomposition peaks at 300 °C (for 700 °C anneal), 175 °C and 650 °C (for 1,100 °C anneal), and 300-330 °C and 460 °C (for 1,600 °C anneal). However, desorption was convoluted by porous CDCs (gas products required diffusion time through pores during steady temperature increase). Nevertheless, the approach provided a quantitative comparison of functional group content on pore walls.
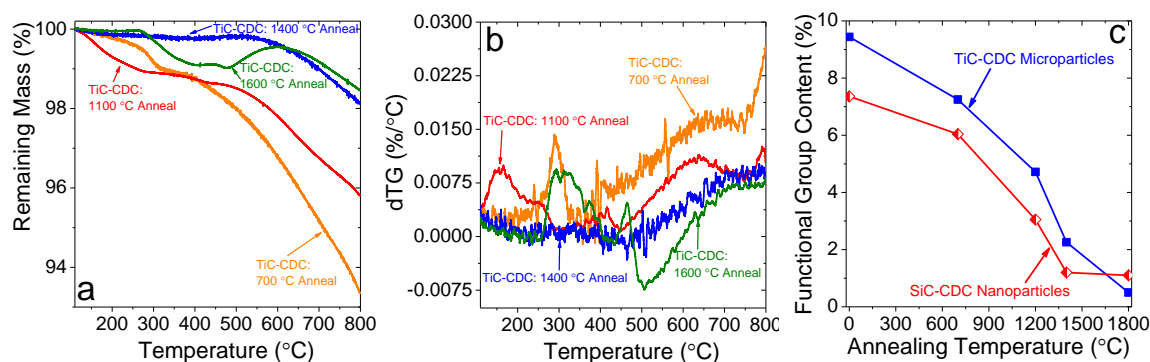
Figure 4.15. a) Inert TGA and b) dTG analysis of TiC-CDC microparticles annealed at different temperatures. c) Percentage of mass lost during heating of microparticles and nanoparticles, which corresponded to amounts of non-carbon functional groups that had been present on surfaces of annealed CDCs.

Neither analysis could accurately quantify the hydrogen content, which was

assumed to be present on surfaces of as-produced samples (H_2 annealing that followed Cl_2 etching). Functional group analysis revealed predominantly C–OH, C=O, and C–Cl bonds, with trace amounts of acid, ether, and C–O–Cl groups. Chlorine was found only on the insides of particles (after Ar sputtering), so its presence could be limited to the XPS-induced opening of previously closed channels. For both systems, annealed materials exhibited passivated, stable surfaces and did not become noticeably re-functionalized during post-treatment exposure to air.

The defunctionalization process influenced the hydrophobicity of the materials, as shown in **Fig. 4.16**. As the number of surface species decreased, adsorbance became dominated by capillary action at higher partial pressures and not attraction from chemical groups.[134] The water sorption profiles of defunctionalized CDCs were indicative of surfaces devoid of H_2O adsorption sites. This effect was more pronounced for microparticles than for nanoparticles. While the trend was still observed for the latter system, the low pore lengths diminished the energy limitation of water adsorption on CDC surfaces. Pore wetting was expected to significantly influence ion dynamics,[225] impedance, and rate handling .[226]
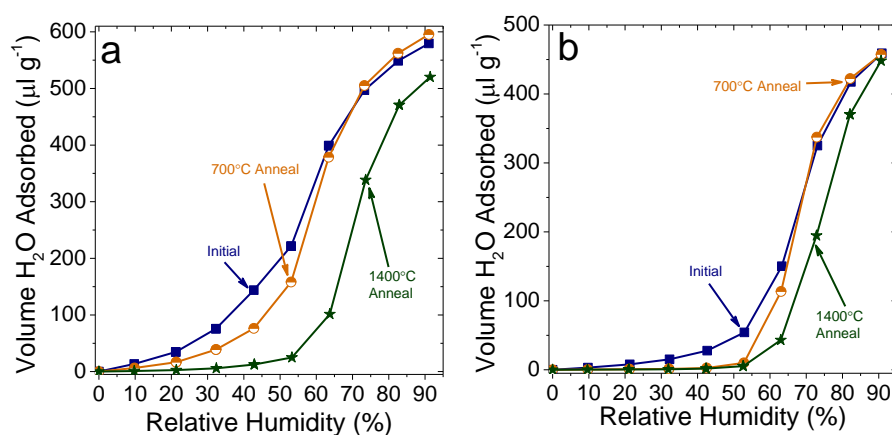
Figure 4.16. Dynamic H_2O vapor sorption on a) TiC-CDC microparticles and b) SiC-CDC nanoparticles.

4.1.3. Influence of Pore Defunctionalization on Capacitance

4.1.3.1. Capacitance and Rate Handling Abilities

Fig. 4.17 shows the **e**ffects of vacuum annealing on gravimetric capacitances of TiC-CDC microparticles and SiC-CDC nanoparticles with [EMIm$^+$][TFSI$^-$] ionic liquid electrolyte. The microparticle electrodes showed a 19% increase in capacitance after the 700 °C anneal. This was explained, in part, by the 16% increase in SSA and a slightly larger pore diameter, which minimized the ion-sieving effect that was somewhat present in the initial CDC material (based on the resistive nature of the discharge curve). Despite retaining 81% of its SSA, the capacitance of the 1,400 °C annealed microparticle material decreased by over 30%. SiC-CDC nanoparticle electrodes demonstrated an even clearer annealing-induced capacitance decrease trend: with no ion sieving limitations, C_{sp} decreased slightly for the 700 °C annealed material (despite gaining 1,000 m^2 g^{-1}) and by over 20 F g^{-1} for the 1,400 °C annealed material. While certain inflection points in the cyclic voltammograms suggested possible side reactions present in both initial CDCs, evidence of any side reactions noticeably diminished after a 700 °C anneal and completely disappeared in materials annealed at 1,400 °C. The nanoparticle samples also demonstrated "butterfly" -shapes of cyclic voltammograms for SiC-CDCs annealed at 1,400 °C. This behavior suggested improved electric conductivity of both materials and greater prevalence of voltage-dependent capacitance.[103]

Capacitance retention indicated that the microparticle CDCs best handled high sweep rates after undergoing 700 °C annealing; however, above a 250 mV s^{-1} scan rate, the 1,400 °C material outperformed the rest. Nanoparticles demonstrated

improved rate handling abilities at low and high sweep rates after 1,400 °C annealing. Analysis of capacitance derived from galvanostatic cycling showed the best performance for materials that had been annealed at 700 °C. This result underscored the importance of high SSA and accessible pore sizes for high rate handling. [60]
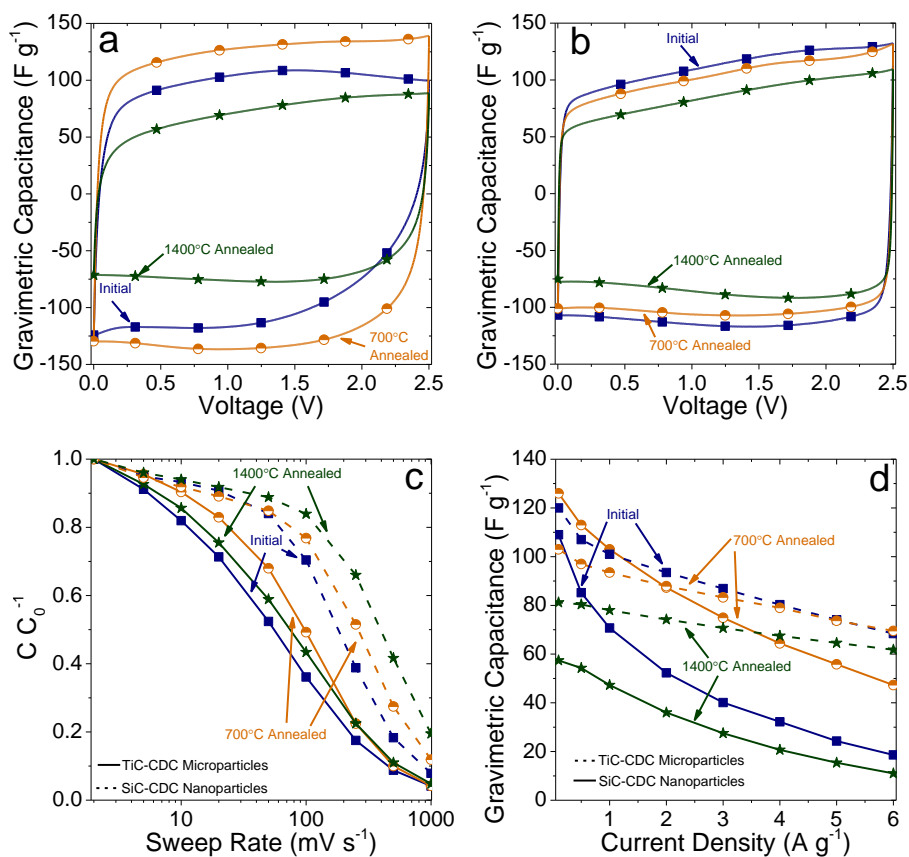
Figure 4.17. Cyclic voltammograms of a) TiC-CDC microparticles and b) SiC-CDC nanoparticles in their initial, 700 °C annealed, and 1,400 °C annealed states, collected at 5 mV s^{-1} and normalized by m$_{WE}$ mass. c) Capacitance retention of the 2 systems and their defunctionalized and graphitized versions in the 2 mV s^{-1} – 1000 mV^{-1} range, normalized to the maximum capacitance recorded for each sample at 2 mV s^{-1} (C$_0$). d) Capacitance values derived from galvanostatic cycling at current densities (normalized by m$_{WE}$ mass) between 0.1 A g^{-1} ad 6.0 A g^{-1}. Tests used neat [EMIm$^+$][TFSI$^-$].

Considering that the amount of accessible surface area is different for each sample, effects of annealing were also re-normalized by BET-derived SSA; results are shown in **Fig. 4.18**. For the TiC-CDC microparticles, both sweep rate and current density

comparisons showed that the 700 °C annealed material performed best, although cyclic voltammograms indicated converging C_{sp} at 500 mV s^{-1} sweep rates. The SiC-CDC nanoparticle electrode performance indicated that the 1,400 °C material stored the largest amount of charge per unit of area. However, this finding was partially convoluted with rate handling, as current density comparisons showed that the initial material exceeded the annealed counterpart's capacitance per surface area at very low scan rates.

The convergent appearance of the rate handling response to increased sweep rates suggested that the initial material stored more charge per accessible electrode area than the 1,400 °C annealed CDC at sweep rates below 2 mV s^{-1}. Although the BET-derived SSA values were used for normalization of aerial capacitances, DFT-derived SSA values would produce very similar trends: the SSA differences between the two are insignificant. The BET equation consistently calculated slightly higher m^2 g^{-1} values than the DFT simulation (16-75 m^2 g^{-1} greater SSA for microparticles and 44-240 m^2 g^{-1} for nanoparticles). The corresponding 3-12% changes would slightly affect the absolute F m^{-2} numbers, but the trends would remain unchanged.
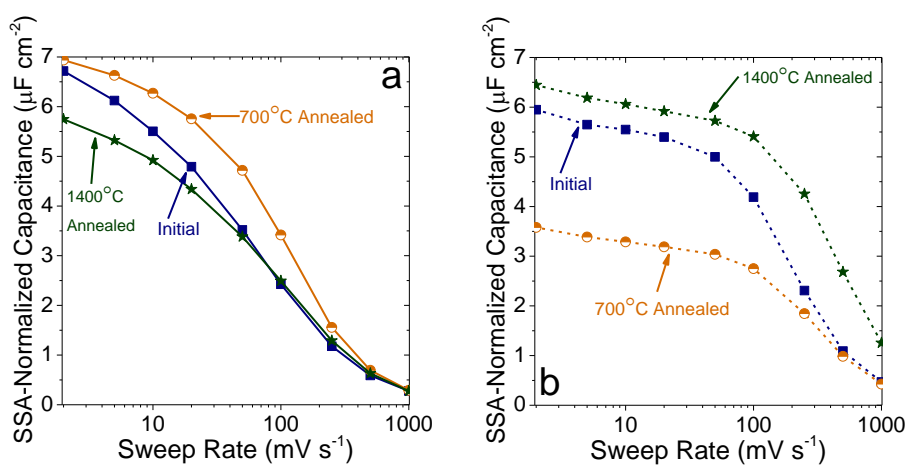
Figure 4.18. Capacitance changes with increasing sweep rates derived from cyclic voltammetry normalized by SSA (BET value) for a) TiC-CDC microparticles and b) SiC-CDC nanoparticles. Tests used neat [EMIm$^+$][TFSI$^-$] in a 2-electrode configuration.

Surface defunctionalization and graphitization likely changed relative contributions from quantum capacitance and charge confinement in the superionic state. C_{sp} was likely influenced by different types of pore morphologies for microparticles with longer pores and nanoparticles with shallow pores. The defects changed both charge screening screen lengths (controlling ion spacing) and ion-pore distances (*via* steric forces) and, subsequently, were beneficial to capacitance.[13] While nanoparticles are expected to have thinner pore walls, the number of graphitic layers separating each channel has not, to date, been accurately determined. However, the expected benefit of conductive pore walls and increased charge screening in defunctionalized CDCs did not translate into enhanced gravimetric capacitance.

It is unlikely that the decrease in gravimetric capacitance for the annealed materials (or, conversely, a higher C_{sp} for the initial CDCs) stemmed from significant Faradaic reactions of the electrolyte with surface functional groups.[227] A more direct observation is the positive correlation between increased surface defunctionalization and improved rate handling capabilities. Defect-free pores facilitated [EMIm$^+$] and [TFSI$^-$] movement, as previously reported for similar systems.[225] It should be noted that improved graphitic ordering and electrode conductivity are somewhat convoluted with this relationship: nanoparticles, although less defect-free, showed the greatest increases in capacitance retention.

4.1.3.2. Ion Dynamics and Impedance

Nyquist impedance plots for the TiC-CDC microparticles and SiC-CDC nanoparticles are shown in **Fig. 4.19**. Ionic impedance of RTIL showed biggest

differences between initial, defect-rich CDCs and their 700 °C annealed counterparts. This divergence stemmed primarily from sieving effects: the larger pore diameters of the annealed materials decreased ionic resistance and dominated impedance with ideal capacitance at low frequencies.[228] The 1,400 °C annealed material featured lager R_s and overall ionic resistance. While electrode assembly could affect the interfacial resistance between the electrode and current collector,[205] the absence of significant semi-circular regions at high frequencies suggested that ionic impedance through the intrinsic material structure was mostly responsible. Smaller ion diameters (0.05 nm larger than the initial material) and annealing-induced defects most likely increased ionic resistance.
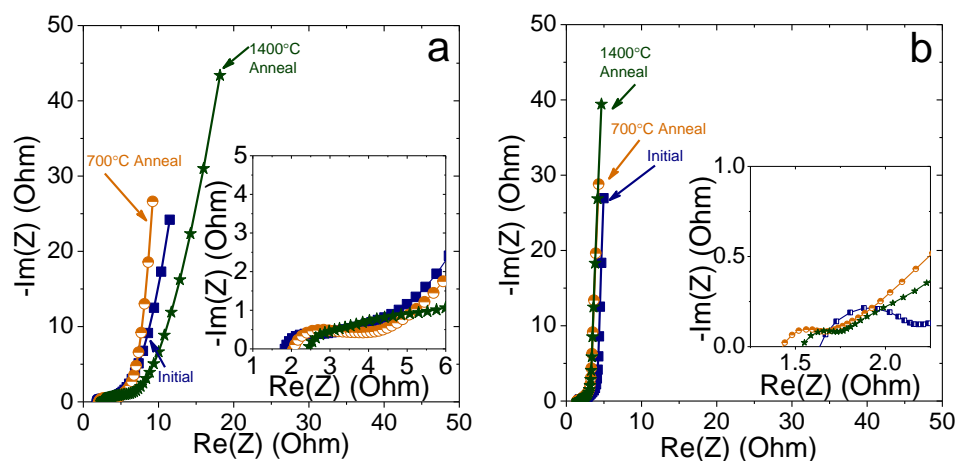
Figure 4.19. Nyquist impedance plots derived from EIS for the a) TiC-CDC microparticles and b) SiC-CDC nanoparticles. Insets in each plot zoom in on the high-frequency region to properly describe electrical resistance.

As the annealing temperature increased, the time constant decreased and impedance became more capacitance-dominated. Nanoparticles showcased lower ionic resistances, which corroborated the CV-derived improved rate handling abilities of these materials. The time constant monotonically decreased with higher annealing temperatures, as it did with the microscale system. The real capacitance (C')

normalized by SSA showcased the same trends that CV and GCPL had shown for aerial charge storage densities. **Table 4.3** includes the key parameters regarding the system's ionic resistance and capacitance derived from EIS.

Table 4.3. Electric and ionic resistance parameters derived from impedance spectroscopy. The time constant is derived from the frequency value at which impedance angle = -45.0°. Series resistance (R_s) is derived from the real impedance value at which – Im(Z) = 0 Ω. C' is calculated using the following equation: $C'(\omega) = -Z''(\omega) [w Z(\omega)^2]^{-1}$. Values are shown normalized by the materials' BET SSA.

	TiC-CDC Microparticles			SiC-CDC Nanoparticles		
	Initial CDC	700 °C Annealed	1400 °C Annealed	Initial CDC	700 °C Annealed	1400 °C Annealed
R_s, Ω	1.84	2.04	2.44	1.63	1.42	1.52
τ, seconds	26.5	23.2	19.3	13.3	10.1	7.4
Ionic Resistance, Ω	3.39	2.17	4.27	1.02	0.69	0.48
Z (0.01 Hz), °	-64.6	-70.9	-67.3	-79.6	-81.5	-83.2
C'_{sp} (0.01 Hz), F m^{-2}	0.24	0.27	0.18	0.25	0.15	0.28

The diffusion limitations of the systems that were calculated with the RS equation (**Eq. 3.12**) showed a correlation between annealing temperature and prevalence of capacitance-dominated behavior (**Table 4.4**). The maximum coefficient value for the microparticles was obtained on the 700 °C annealed CDC, mostly because of the larger pore diameter that facilitated ion mobility. The most annealed nanoparticles exhibited minimal diffusion-limited behavior despite having a smaller pore diameter. This further underscored possible differences in the structure and defects that were present on the surfaces of the two materials.

Table 4.4. RS coefficients derived from CVs and GPLs. R-squared fits were 0.98 – 0.99.

	TiC-CDC Microparticles			SiC-CDC Nanoparticles		
	Initial CDC	700 °C Annealed	1400 °C Annealed	Initial CDC	700 °C Annealed	1400 °C Annealed
CV-Derived	0.69	0.81	0.71	0.88	0.92	0.94
GCPL-Derived	0.71	0.77	0.77	0.86	0.89	0.92

While the ionic resistance decreased for nanoparticles from 1.02 Ω (initial CDC) to 0.48 Ω (1400 °C annealed), the same process increased this resistance from 3.39 Ω to 4.27 Ω for microparticles. It is possible that the annealing-induced morphology developed on the surface of large TiC-CDC particles increased ionic resistance and hindered ion diffusion at semi-infinite length scales.[229,230] These impediments could have included out-of-plane defects that impeded electrosorption, poorer packing of graphitized particles in films, and structural/steric bottlenecks at pore openings. Overall, annealed materials exhibited lower time constants, diffusion limitations, and ionic resistance. However, particle size and pore diameter had equally significant impacts and were, in part, coupled with these observations.

4.1.3.1. Charge Distribution and Symmetry

The quasi-reference 3-electrode configuration allowed CV measurements of both working and counter electrodes. Performances for the two systems (collected using a 5 mV s^{-1} sweep rate) showed the contribution of each electrode to total capacitance. The CVs in **Fig. 4.20** show this difference. Identical trends were observed for nanoparticles and microparticles: in their initial states, CDC materials stored greater charge in working electrodes, while the counter electrode extended to a significantly lower potential (vs. Ag/AgCl). This asymmetry emerged despite identical WE and CE masses and thicknesses of electrodes in each cell. This suggested that the initial materials' structure (both pore diameter and surface chemistry) facilitated [TFSI$^-$] anion's entry over the [EMIm$^+$] cation.
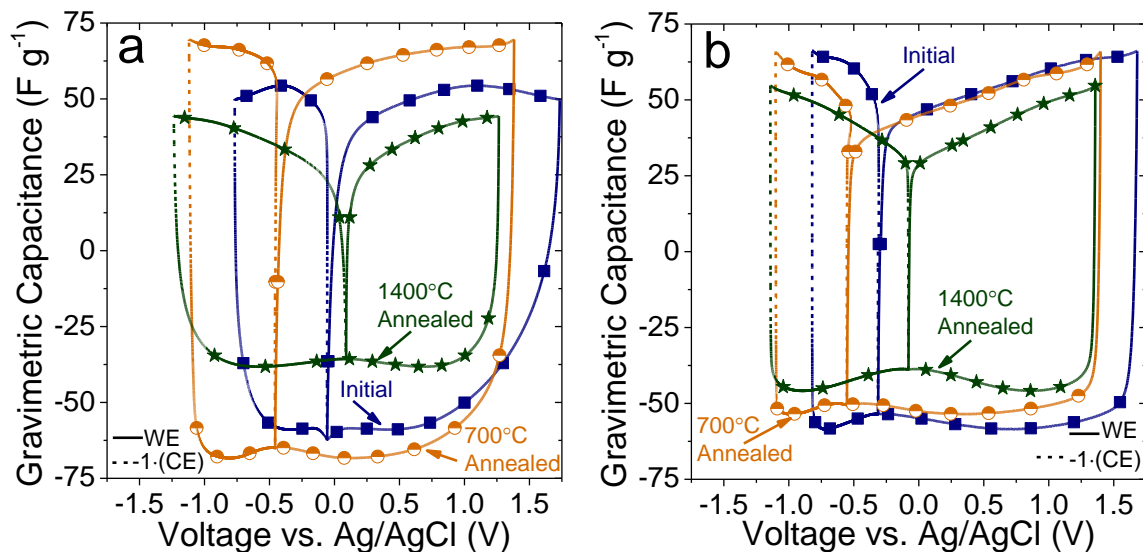
Figure 4.20. Comparison of operating potential distribution and capacitance contributions (normalized by mass) of the working and counter electrodes of a) microparticles and b) nanoparticles collected using cyclic voltammetry at 5 mV s^{-1}. For counter electrodes, the plots show the negative of the current to facilitate comparison of the symmetry. Quasi-reference electrode potential was identical for each case. Open circuit potentials fluctuated between 6 mV and 60 mV for each system.

After the 700 °C vacuum annealing treatment, both the microscale and nanoscale materials experience a negative shift in potential, with the samples' charge distribution becoming even more asymmetric. Nanoscale and microscale materials annealed at 1,400 °C show near-perfect charge distribution symmetry, with the equilibrium potential shifting closer towards 0.00 V vs. Ag/AgCl. The "butterfly" shape is evident for the working electrodes for both microscale and nanoscale powders annealed at this condition.

The changes in symmetry could not be attributed to porosity changes alone: while materials annealed at 700 °C had the largest pore diameters (expected optimal access to both ions), they responded most asymmetrically to [EMIm$^+$][TFSI$^-$] electrosorption. Therefore, surface chemistry and morphologically-induced structural defect transformations governed charge distribution. These changes also likely controlled ion sieving: the initial TiC-CDC microparticles and their 700 °C annealed

counterparts showed noticeable resistance-induced deviation from the ideal rectangular shape of the discharge voltammograms. Annealing transformations also influenced Faradaic processes, which were completely absent in WE and CE after 1,400 °C anneals. The 700 °C annealed micro- and nanoparticles exhibited inflection points during the charge cycle of the CE at -1.00 V; it is unclear whether this stemmed from voltage-dependent capacitance or electrochemical breakdown.

4.1.4. Performance of Various Electrolytes in Defunctionalized Pores

Surface defunctionalization and graphitization directly influences only half of FSI. Electrosorbed ions and solve molecules exhibit unique interactions with specific CDC pore wall defects. Subsequently, capacitance and ion dynamics in defunctionalized pores depended on sizes and properties of electrolytes. **Fig. 4.21** shows properties of TiC-CDC microparticles synthesized with Cl_2 at 1,000 °C and, subsequently, vacuum annealed at 1,400 °C. Although the defunctionalized material became more hydrophobic, it was already initially substantially graphitized, and vacuum annealing (at only 400 °C higher) did not collapse the pores.

Despite greater SSA, this structural evolution translated to capacitance-impeding resistance in Na_2SO_4 (in H_2O). The shape of 1,400 °C annealed CDC cyclic voltammograms was significantly less rectangular that that of untreated electrodes and underscored greater resistance of aqueous (polar solvent) electrolyte mobilities into hydrophobic pores. This effect became less evident for organic electrolyte tests (1.5 M $[NEt_4^+][BF_4^-]$ in CH_3CN). The latter is a more mobile electrolyte and entered/egressed larger TiC-CDC-1000 ºC pores without significant interference from

energetically unfavorable pore interfaces.
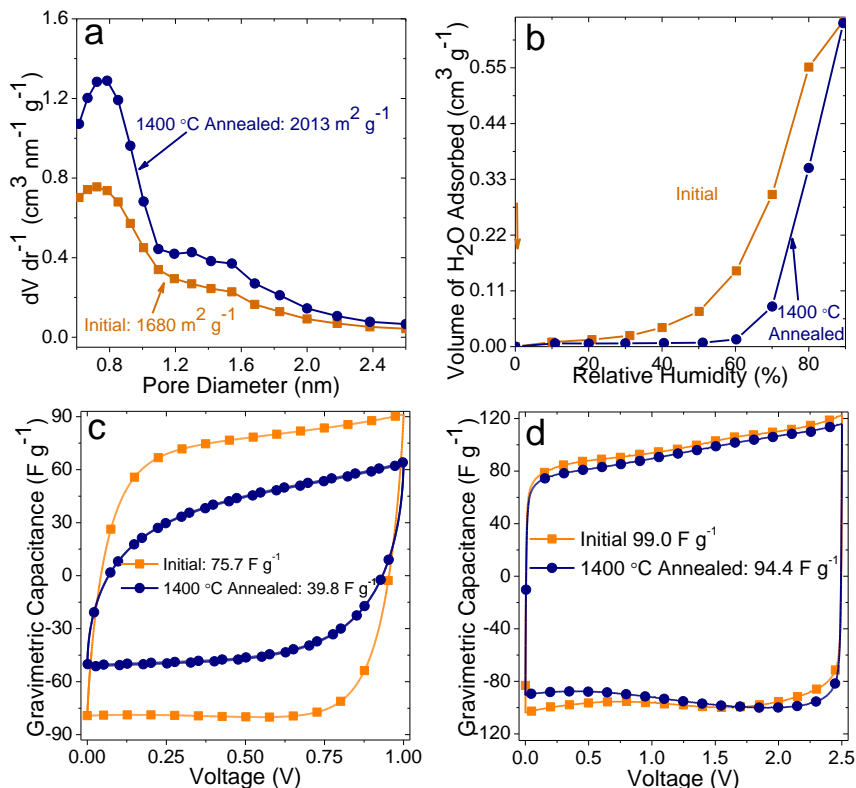
Figure 4.21. a) Pore size distributions and BET-derived specific surface area of TiC-CDC microparticles that were synthesized at 1,000 °C and annealed at 1,400 °C. Initial high degree of ordering minimized pore collapse and expanded pore volume through defunctionalization and some additional graphitization. b) Dynamic water vapor sorption of the initial and annealed materials. c) 10 mV s^{-1} performance of the materials in 1.0 M Na$_2$SO$_4$ aqueous electrolyte that indicated lower capacitance and greater resistance for the annealed material due to poor pore wetting. d) 10 mV s^{-1} electrochemical performance of these materials in organic electrolyte of [NEt$_4^+$][BF$_4^-$] in CH$_3$CN, exhibiting similar ionic resistance, fewer faradaic reactions, and no increases in capacitance of the 1,400 °C annealed material despite higher SSA and increased material conductivity.

This organic electrolyte was tested for narrower pores of TiC-CDC synthesized at 600 °C and annealed at 700 – 1,400 °C. For comparison, the tests also included a TiC-CDC sample that was treated with NH$_3$ instead of H$_2$ after Cl$_2$ (at 600 °C). Materials characterization and electrochemical testing (with the same 1.5 M [NEt$_4^+$][BF$_4^-$] in CH$_3$CN) are shown in **Fig. 4.22**.
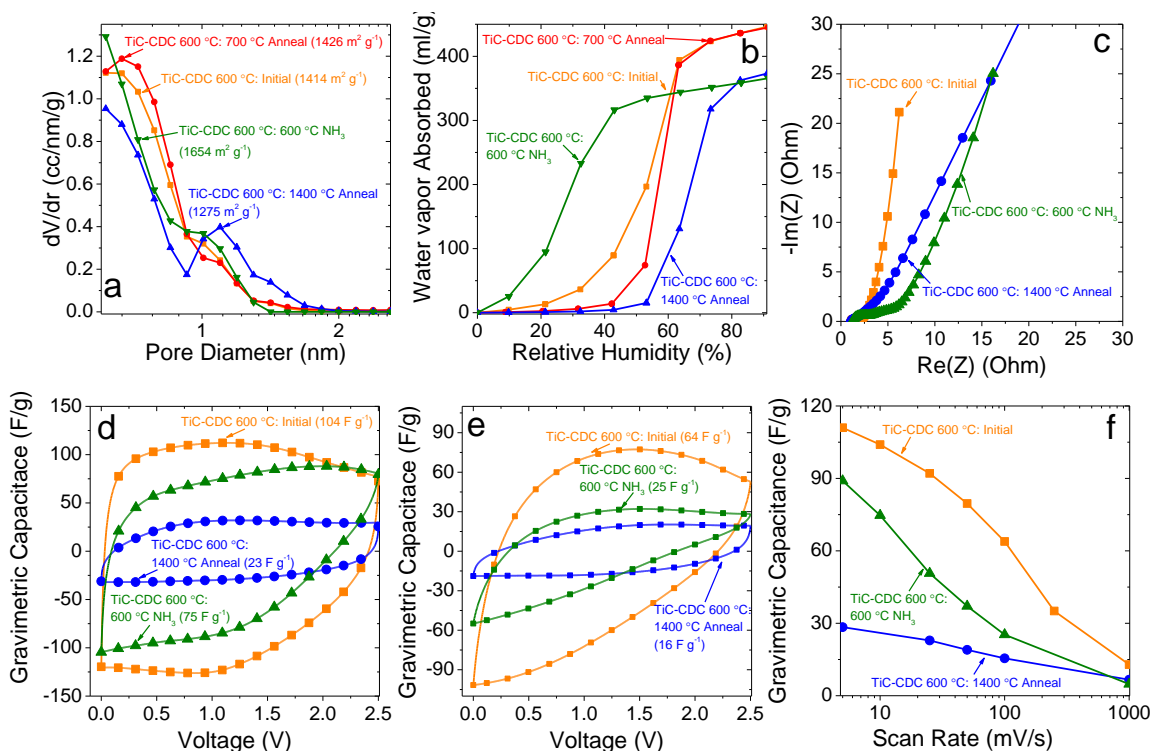
Figure 4.22. a) Pore size distributions of TiC-CDC synthesized at 600 ºC, annealed at 700 ºC, annealed at 1,400 ºC, and aminated at 600 ºC. b) Corresponding DVS isotherm. c) Nyquist impedance plots that compares performance of these electrodes with organic electrolyte. Cyclic voltammograms are shown for d) 10 mV s^{-1} and e) 100 mV s^{-1}. f) Rate handling abilities that cover the entire 5 mV s^{-1} – 1,000 mV s^{-1} sweep range.

The starting pore structure was very amorphous and exhibited robust surface chemistry, and resulting defunctionalization significantly reduced hydrophilicity. The pores (initial, 700 ºC annealed, and 1,400 ºC annealed) were very narrow and slightly smaller than electrolyte and solvent molecules. Cyclic voltammograms showed the significant benefits of surface defects, as capacitance of defunctionalized CDCs was lower at all sweep rates. Although the surface area decreased by only 150 m^2 g^{-1} after annealing, C_{sp} fell by 75% (23 – 16 F g^{-1} at 10-100 mV s^{-1}). NH$_3$-terminated surfaces became most hydrophilic (from dynamic H$_2$O vapor sorption) and showed significantly less capacitance (73-25 F g^{-1} at 10-100 mV s^{-1}) than initial (H$_2$-treated) TiC-CDCs that had been synthesized at 600 ºC (104 – 64 F g^{-1}). Therefore, surface

wettability was not the only important factor that governed capacitance, and other defects (such as graphitic features) significantly influenced both charge storage densities and rate handling abilities.

From the perspective of CV shape, defect-rich CDCs (hydrogenated and aminated) showed some evidence of charge saturation of accessible surfaces at higher voltages (decreasing current > 1.25 V).[231] However, these materials also exhibited resistive discharge curves. The 1,400 ℃ annealed CDCs did not demonstrate either effect, although greater ion transport resistance through hydrophobic (ionophobic) pores was likely convoluted with the charge/discharge profiles.

4.1.5. Comparative Influence of Annealing on Activated Carbon

Although defunctionalization and graphitization had detrimental effects on capacitance of CDC electrodes, they must be verified against other internal surface, porous carbon systems. Activated carbon (YP-50), which is a commercially available material with 1-5 μm particle size, was annealed at 650 ℃, 1,400 ℃, and 1,600 ℃. **Fig. 4.23** shows the corresponding structural and surface chemistry characterization. The YP-50 carbons underwent similar structural transformations as comparative CDC particles. The material was, initially, mostly free of functional groups. XPS analysis revealed the initial composition to be 95 wt.% carbon and 4.6 wt.% oxygen. 650 – 1,600 ℃ annealing drove the oxygen content down to 2.5 – 2.4 wt.%; no other elements were detected. Subsequently, thermally-induced structural evolution primarily yielded restructured pore surfaces and greater ordering/graphitization. Ordering transformations, and pore evolution, suggested similar trends for YP50 as for CDCs. The (initially amorphous)

porous carbon material graphitized most significantly above 1,400 ºC annealing, gained

greater mesoporosity, and collapsed smaller pores at high temperatures.
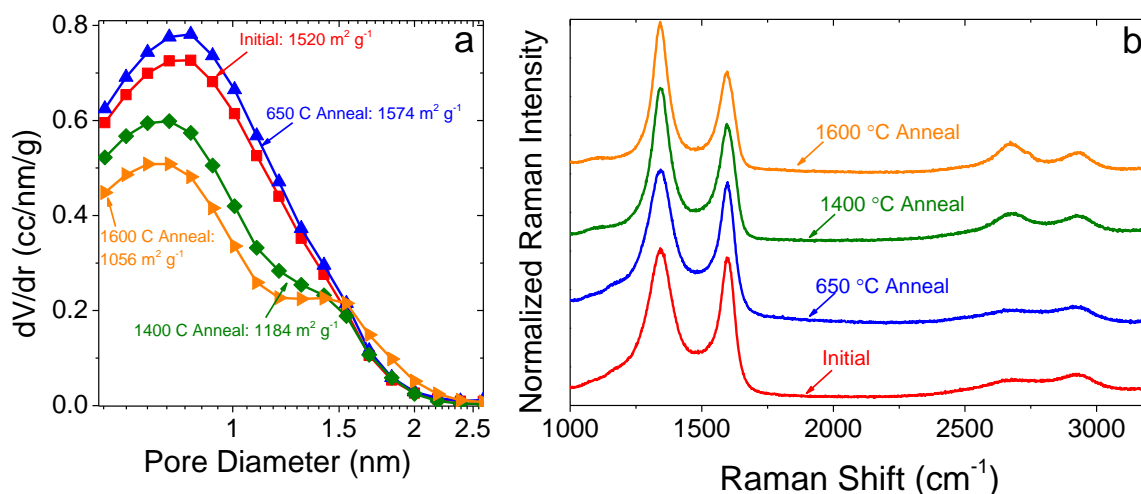
Figure 4.23. a) Pore size distribution and b) Raman spectroscopy analysis of YP50 activated carbon annealed at 650 ºC – 1,600 ºC.

The four electrode material variants were tested with 1.5 M [NEt$_4^+$][BF$_4^-$] in CH$_3$CN.

Fig. 4.24 shows the electrochemical results. For all annealing temperatures, including the

low-temperature 650 ºC anneal that had increased SSA, capacitance and rate handling

abilities decreased. The initial material was not significantly functionalized. Therefore,

most annealing-induced modifications primarily involved graphitic transformation and

structural re-ordering. Despite exhibiting larger pores, the most graphitized 1,600 ºC

annealed AC was too resistive (ionophobic) to allow ion mobility through pores and

yielded very low capacitance. These results corroborated CDC findings and confirmed

the important influence of graphitic defects on capacitance.
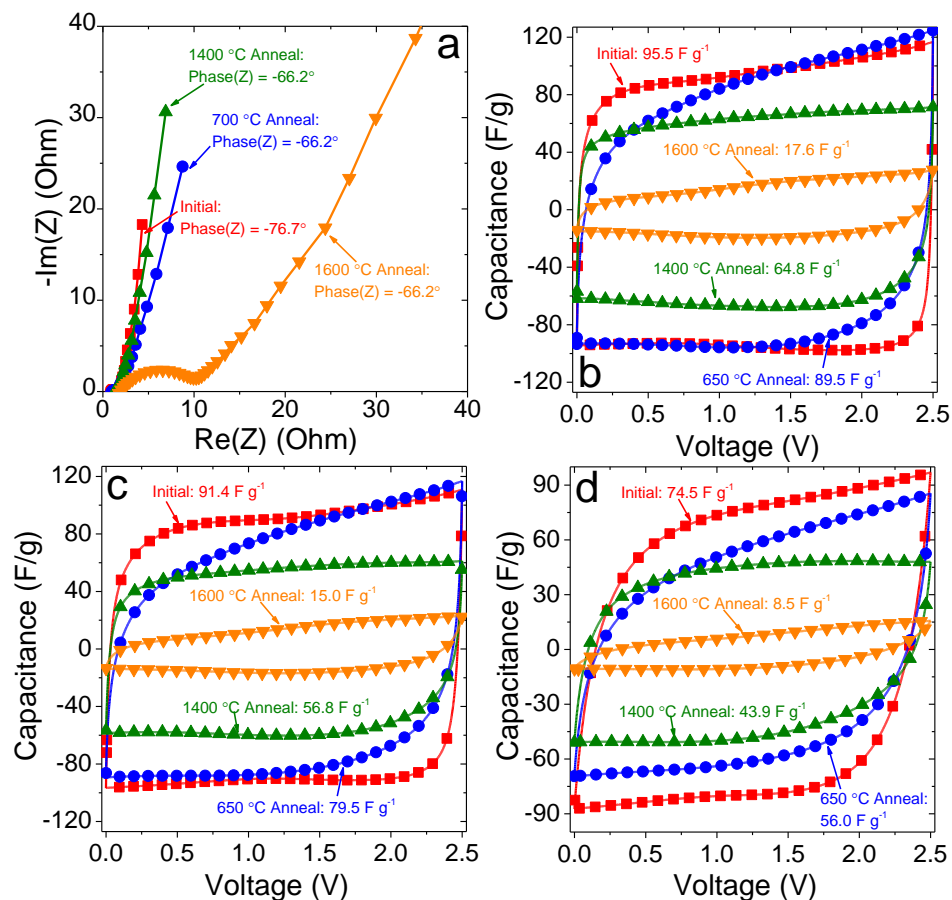
Figure 4.24. a) Nyquist plot for YP-50 activated carbon annealed at different temperatures in organic electrolytes. Captions indicate phase angles at 10 mHz oscillating frequencies. CVs are shown for b) 10 mV s^{-1}, c) 20 mV s^{-1}, and d) 100 mV s^{-1}.

4.1.6. NMR-derived Ion Adsorption in Defunctionalized Pores

Although structural characterization and electrochemical analysis demonstrated lower capacitance values in graphitized pores, the origin of this capacitance decrease had remained uncertain. Some evidence had pointed to ion repulsion by graphitized-defect free pore walls as the main culprit. To help narrow down the cause of lower capacitance, several SiC-CDC microparticles, which had been annealed at 700 – 1,800 °C, were soaked with 1.5 M [NEt$_4^+$][BF$_4^-$]/CN$_3$CN organic electrolyte and analyzed using Nuclear Magnetic Resonance (NMR). Initial CDCs used in this sample set had been totally defunctionalized, and, subsequently, narrowed the focus of these measurements squarely

on influences of graphic defects. To separate the signal from hydrogen-containing [NEt$_4^+$] and CH$_3$CN, deuterated acetonitrile (CD$_3$CN) was used for measurements.

The results of NMR measurements are shown in **Fig. 4.25**. Both cations and anions entered pores and soaked the porous electrodes in similar fashions. The electrolyte failed to properly enter the pores of SiC-CDCs annealed at 1,800 ºC, mostly due to their low SSAs (247 m^2 g^{-1}) and collapsed porosities. This finding was in line with electrochemistry results and highlighted a key detriment of high-temperature vacuum annealing. Chemical shifts ($\Delta\delta$) measurements noted large in-pore shifts for CDCs annealed above 1,000 ºC, which had corresponded to structures with more ordered carbon domains. On the other hand, NMR measurements noted very minute $\Delta\delta$ differences, which were nucleus-dependent, between samples annealed below this transition temperature. Subsequently, the in-pore $\Delta\delta$ signal was dominated more by the carbon structure than the adsorbed ions. The in-pore and ex-pore peaks for CD$_3$CN measurements were not readily resolved in all spectra (**Fig. 4.25(c)**), which suggested greater chemical exchange of ions (displacing solvent in pores) in confined environments.
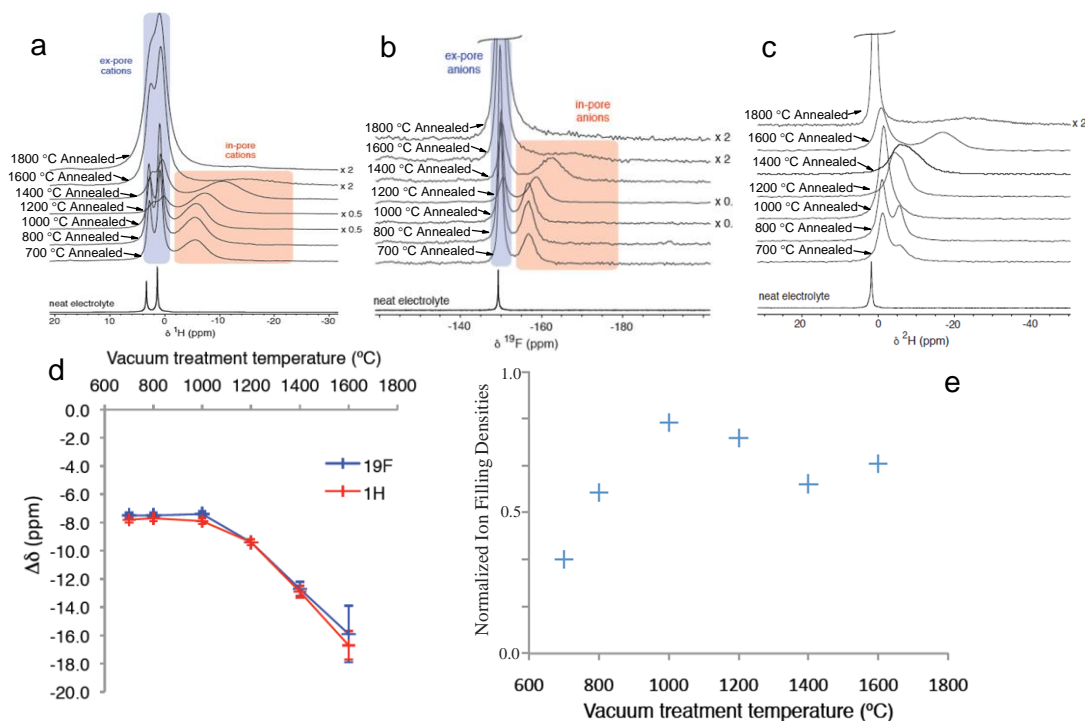
Figure 4.25. Chemical shift ($\Delta\delta$) values are shown for a) cation adsorption (tracking the ^{1}H chemical shift from $[NC_8H_{28}^+]$), b) anion adsorption (tracking the ^{19}F shift from $[BF_4^-]$), and c) solvent adsorption. d) Summary of the chemical shift values and previously simulated carbon structures. e) Relative prevalences of in-pore anions for samples annealed at different temperatures (from the ^{19}F intensities).

Vacuum annealing correlation with $\Delta\delta$ demonstrated that chemical shift values were very similar for ^{19}F and ^{1}H and confirmed nucleus independency of chemical shift. $\Delta\delta$ values depended on both degree of order in the carbon and the pore size distributions. Simple simulated carbon molecules, which had been derived in prior work from PDF and NMR measurements,[194] were compared to the experimentally-derived chemical shift values. The slightly different pore size distributions of the carbons suggested greater expected $\Delta\delta$ values for more graphitized SiC-CDCs.

Although the results provided more insights into the graphitic structure of CDCs than resulting ion adsorption, in-pore intensities in the NMR spectra, which were proportional to anion filling in pores, provided a comparative analysis of the relative packing densities

of electrolyte species in differently graphitized pores. The results (shown in **Fig. 4.25(d)**) did not demonstrate different filling densities in pores with different graphitic defect concentrations. Furthermore, results slowed very similar $\Delta\delta$ values upon adsorption for the anions and the cations and did not indicate any surface-specific, unique interactions between electrolytes and surface defects. This finding contradicted initial expectations, which had counted on larger ring currents from graphitized,[100] more electronically conductive carbons, to effectively screen charges and enhance closer packing of co-ions in pores. Since these results helped rule out lower ion densities in graphitized, defect-free pores as cause of lower C_{sp}, they (by process of elimination) further elevated the significance of defect-driven quantum capacitance on charge storage densities in CDCs.

4.1.7. Electrochemical Stability in Defunctionalized CDCs

Most TiC-CDC microparticle and SiC-CDC nanoparticle electrode tests with [EMIm$^+$][TFSI$^-$] were conducted in the 0.00 – 2.50 V potential range. Separate experiments assessed the systems' operations with vertex potentials of 2.75 V, 3.00 V, and 3.25 V. Voltammograms of these measurements performed at 2 mV s^{-1} are shown in **Fig. 4.26**. The behavior at vertex potentials suggested that electrochemical breakdown occurred above 2.50 V for all microscale and nanoscale samples, regardless of defunctionalization or ordering. The materials annealed at 700 °C showcased highest breakdown and the lowest overall coulombic efficiencies. However, this was partially convoluted with the large accessible surface areas, which had offered more ion reaction and decomposition sites, of these materials. Parasitic currents and voltammograms showed that the 1,400 °C annealed (most defunctionalized) CDCs became most stable under high potentials. However, they

were not immune from some electrolyte breakdown above 2.50 V.

Separate analysis of the working and counter electrodes (**Fig. 4.26(e-f)**) evidenced breakdown of both [EMIm$^+$] and [TFSI$^-$] ions. Excessive vertex potentials showed different charge distribution asymmetries than those shown in **Fig. 4.20** and likely indicated breakdown-driven irreversible pore structure and chemistry changes (such as gas evolution and pore blockage with solid breakdown products). Respective coulombic efficiencies of the microparticle electrodes consistently showed greater resistance and breakdown associated with the positive electrode (86%-89% Q_{eff}, compared to 92-97% Q_{eff} of CE) and, subsequently, more prevalent [TFSI$^-$] decomposition.
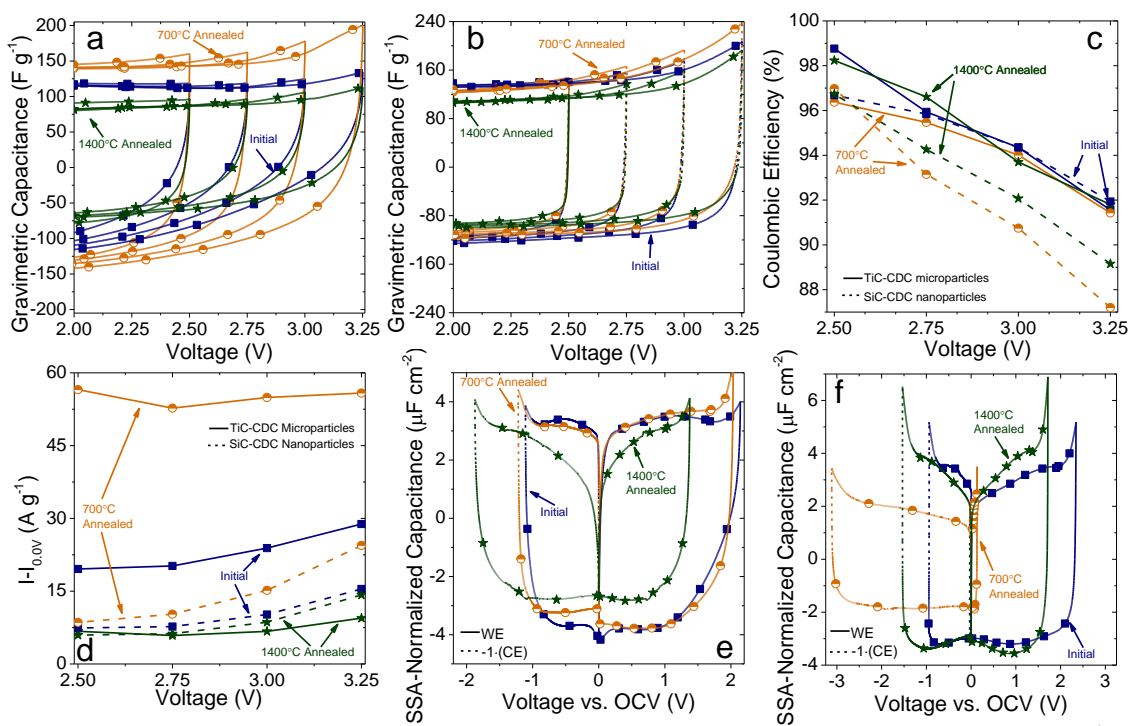
Figure 4.26. Vertex potentials shown for cyclic voltammograms collected at 2 mV s^{-1} for a) microparticles and b) nanoparticles. The first cycle is shown for each system. c) Coulombic efficiencies calculated from above CV results, showcasing increases in breakdown-related reactions increasing as the operating potential is increased from 2.50 V to 3.25 V. d) Net parasitic currents (currents measured at 0.0 V subtracted) normalized by mass for each system for square wave amperommetry conducted at 2.50 V, 2.75 V, 3.00 V, and 3.25 V. Performances of working and counter electrodes in a 3.25 V

operating window measured using cyclic voltammetry conducted at 2 mV s^{-1} for e) microparticles and f) nanoparticles. Data shown is the first cycle of this potential window. Voltammograms are plotted vs. open circuit voltage (OCV). The values for the initial, 700 °C annealed, and 1400 °C annealed samples were, respectively, -57.5 mV, -498.7 mV, and -16.8 mV for microparticles and -356.0 mV, 22.1 mV, and -120.9 mV for nanoparticles. Previously, each system was cycled multiple times in the 0.0 – 2.5 V window, and cycled twice to 2.75 V and 3.00 V. Narrowing of specific electrodes (such as the WE of the 700 °C annealed nanoparticle sample) was possibly attributed to selective decomposition of one ion (in this case, the [TFSI$^-$] ion in the working electrode) and its relative instability compared to the [EMIm$^+$] ion in the CE.

Significant contributions from impurities in the IL (trapped water, synthesis byproducts, etc.) were possible but unlikely: the characteristic ~1.23 V window showed no redox processes. Furthermore, the differences between materials annealed at different temperatures accounted for over 30% of breakdown-induced contributions to capacitance and suggested the overwhelming significance of surface chemistry effects. These differences were less significant for the annealed SiC-CDC nanoparticles than for TiC-CDC microparticles. The ratio of external particle (particle surface accessible to bulk electrolyte) surface to internal particle (inside of pores) surface was greater for the former, and, subsequently, became another important factor that had influenced electrochemical stability.

While high-temperature annealing slightly decreased electrolyte decomposition, pure defunctionalization was still insufficient for ILs to operate in their theoretical 4.0 V window.[207] The differences in magnitude of the breakdowns between materials annealed at different temperatures could be attributed to different reaction mechanisms. These processes likely depended on ion confinement (external surface: internal surface ratios), pore wall conductivity (derived from graphitization), and chemical species at the ion-carbon interface. Reactions with –OH and –COOH groups could have facilitated dimerization-induced breakdown of [EMIm$^+$] (released H$_2$ that

blocked pores and degraded charge storage).[154] Separate alternative simulations also suggested potential-induced S–C bonds breakdown and, subsequently, C–H bonds (both of which are present in the [TFSI⁻] anion) under applied potentials.[152] Although both breakdown processes required overcoming substantial activation energy barriers, conductive, accessible surface (i.e, the structure of annealed pores) may have catalyzed these processes and accelerated their contribution to electrolyte decomposition. Furthermore, the three-dimensional confinement of ions in pores likely distorted the ions' electron clouds and created unique environments that had diverged from previously simulated conditions.

4.1.8. Summary of Carbon Defunctionalization and Graphitization

The experimental approach relied on high-temperature vacuum annealing to selectively tune surface chemistry composition and graphitic features of porous CDCs. Vacuum annealing 1) mostly retained ordered pore size distributions, 2) removed functional groups after 700 – 1,100 ℃ annealing, and 3) re-ordered and graphitized carbon structures after 1,100 – 1,800 ℃ annealing. Vacuum annealing induced nearly identical structural and chemical transformations in microparticles and nanoparticles, CDCs derived from TiC and SiC, and similar active carbon electrodes. Annealed electrodes, which featured fewer surface defects, did not, as had been initially expected, yield greater gravimetric capacitances. Nanoparticles improved their rate handling abilities and charge dynamics after annealing. Pore surfaces with fewer chemical species demonstrated lower electrochemical breakdown at high potentials. However, the most important finding was the fact that electrically conductive porous carbons with nearly-

ideal, graphitized surfaces did not effectively screen charges and maximize energy densities of defunctionalized electrodes. **Fig. 4.27** summarizes the key structural effects and corresponding electrochemical performance changes.

The results raised several important issues and underscored the number of key structural parameters that influenced capacitance, charge dynamics, and electrochemical stability. Although a wide array of characterization techniques was used for this study, they have yet to quantify every pore surface feature that had influenced electrochemical performance. Vacuum annealing altered both structural and chemical surface properties, and the relative magnitude of each was extremely important. Graphitization transformed heterogeneous morphological properties that require advanced MD simulations and DFT analysis. Porous carbons are complex structures, and multiple parameters influence their pore surfaces. Since annealing-induced graphitization transformed graphene ring distributions, surface roughness, and sp^2/sp^3 bonding, the standalone influence of each on capacitance can only be determined once computational simulations catch up to experimental measurements and decouple absolute magnitudes of each parameter. Furthermore, although graphitization-induced surface composition changes likely significantly altered contributions from quantum capacitance, the latter cannot be quantified using conventional electrochemical techniques. Finally, defunctionalized pore surfaces reduced – but failed to eliminate – electrochemical breakdown. Although supercapacitors may eventually reach the theoretical 4.00+ V operating limit of ILs, pure defunctionalization will not accomplish this goal.

These measurements also underscored the influence of pore diameter and pore length. Annealing-induced restructuring slightly altered porosities. Although PSDs showcased minor transformations, their influence cannot be discounted altogether.
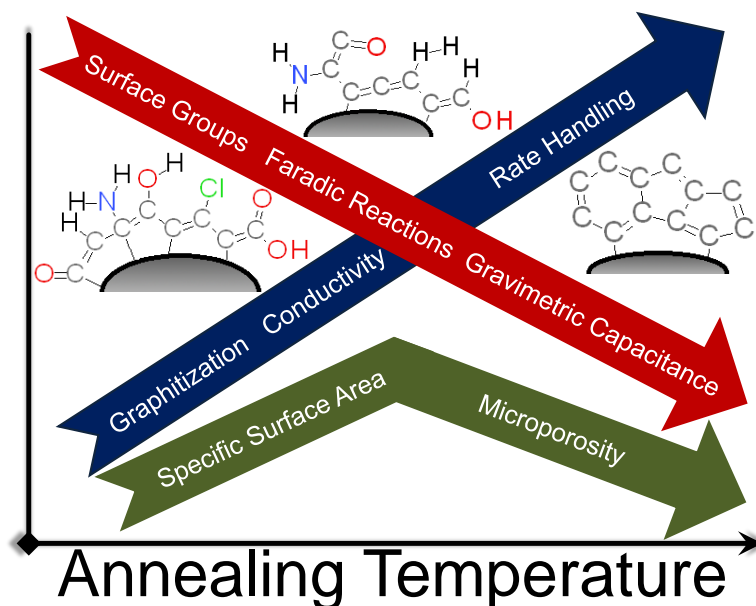
Figure 4.27. Summary of influence of pore defunctionalization and graphitization on the interfacial properties of CDCs and resulting electrochemical changes.

4.2. Deposition of Chemical Functional Groups

Since defunctionalization and defect removal decreased capacitance and left many unanswered questions regarding ion-electrode interactions at disordered interfaces, the logical follow-up approach focused on individual effects of specific pore surface features. The approach compared defect-free, vacuum annealed CDCs with chemically modified porous counterparts. Well-defined surface functional groups were grafted onto CDC pores using chemistry approaches described in section **3.1.3**. To decouple ion confinement from surface chemistry, functionalization pathways aimed to retain ordered porosities. Deposited chemical species were expected to be (sterically) small, electrochemically stable, and common in conventional carbon electrodes. To that end,

hydrogen, amine, and oxygen groups were tested. Based on the rate handling comparisons between defunctionalized and defect-rich CDCs (section **4.1.3**), and experiments with aminated CDCs in organic electrolytes (section **4.1.4**), the operating hypothesis predicted that 1) hydrogenated and aminated CDCs would demonstrate higher capacitance and 2) oxygen groups would slow down dynamics of ions in narrow pores.

4.2.1. Hydrogenated and Aminated Surfaces

TiC-CDCs microparticles were synthesized at 800 ℃ and, subsequently, defunctionalized at 1,200 ℃ in high vacuum for 8 h. To stabilize the surface and minimize pore re-oxidation during post-treatment air exposure, this process used 1-hour isothermal steps (at 400 ℃, 650 ℃, and 800 ℃) before reaching its peak temperature. The material is hereafter referred to as "annealed CDC." A separate, "hydrogenated CDC" counterpart maximized its surface hydrogen content by increasing the 600 ℃ H_2 annealing time to 6 hours. Finally, flowing NH_3 (g) (instead of H_2 (g)) was used to anneal the materials after Cl_2 etching for 6 hours at 600 ℃ and yielded nitrogen-rich CDC surfaces (referred to as "aminated CDC").[232]

4.2.1.1. Structural and Chemical Effects of Hydrogenation and Amination

The approach successfully yielded three porous carbon systems with divergent surface chemistries but nearly-identical porosities. As shown in **Fig. 4.28(a)**, each material featured a predominantly microporous structure, with most pores in the 0.61 – 0.66 nm range. Although the 1,200 ℃ annealed material was slightly more graphitized, structural ordering of all three materials was very similar.
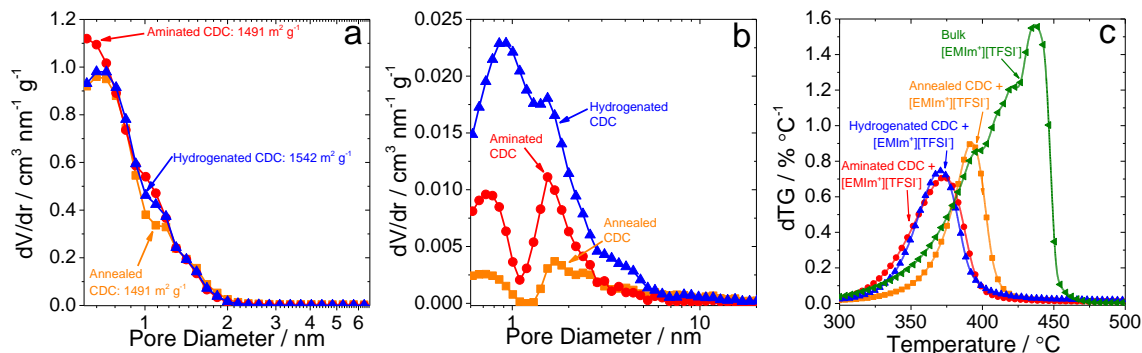
Figure 4.28. a) PSD for TiC-CDC-800 after 1200 ℃ vacuum annealing, H_2 annealing, and NH_3 annealing. b) Porosimetry data on CDC materials after 80% of the pore volume of each was filled with $[EMIm^+][TFSI^-]$. c) dTG comparison for bulk ionic liquid and differently functionalized CDCs filled with the IL in an inert (Ar gas) environment.

Using the procedure described in section **3.5.2**, 80% of the available pore volume for each sample was filled with $[EMIm^+][TFSI^-]$ ionic liquid. The pore size distribution of filled CDCs is shown in **Fig. 4.28(b)**. Although most of the volume was occupied by the IL, the pore loading left a small percentage of unoccupied micropores. Hydrogenated filled CDCs stood out the most and demonstrated most void space around confined ions. Given that pore filling was identical for each system, this surface exhibited the strongest intermolecular interactions between $[EMIm^+][TFSI^-]$ ions and the hydrogenated surfaces that had bound the ions closer to the walls (and left middle of pores empty).

These findings underscored the significance of intermolecular interactions between electrolyte ions and surface defects and functional groups on carbon electrodes. In addition to governing dynamics in confined pores, bonding forces also influence the thermal stability and degradation of these molecules. Inert TGA analyzed IL-filled CDCs and described thermal stabilities. As shown in **Fig. 4.28(c)**, $[EMIm^+][TFSI^-]$ confined in annealed pores decomposed (into gas products such as SO_2 and CO_2) at a significantly lower temperature (393 °C) than in its bulk state (437 °C).[233] Furthermore, hydrogen

and amine groups on surfaces, and their subsequent bonding interactions with the RTIL, decreased the thermal stability of the electrolyte even lower (371-373 °C).

Compositional analysis revealed a chemical makeup that we had anticipated and that agreed with prior characterization of differently annealed CDCs. Analysis of deconvoluted XPS spectra (**Fig. 4.29**) showed similar C 1s peaks for all three materials. Peaks were assigned to C–C (284.4 eV), C–H (285.2 eV), C–OH (286.3 eV), C=O (287.4 eV), and C–OOH (288.4 eV) species. Although there were likely C–NH and C–NH$_2$ species present in hydrogenated and aminated CDCs as well (see below), photoemission from those species overlapped with peaks from other species at 285 – 286 eV and, thus, could not be sufficiently deconvoluted. As expected, the combined content of C–C and C–H species was ~ 3.5% higher for the annealed CDC than for the aminated or hydrogenated CDCs. This was indicative of the removal of surface termination from this CDC. The annealed CDC contained no nitrogen, the hydrogenated sample contained 2 nitrogen species, and the aminated sample contained 3 nitrogen species. Both the hydrogenated and aminated CDCs contained N 1s peaks near 400.2 eV and 398.7 eV, which corresponded to NH and NH$_2$ groups, respectively. Hydrogenated CDC likely adsorbed N$_2$ from the air and acquired these species.[85,234].
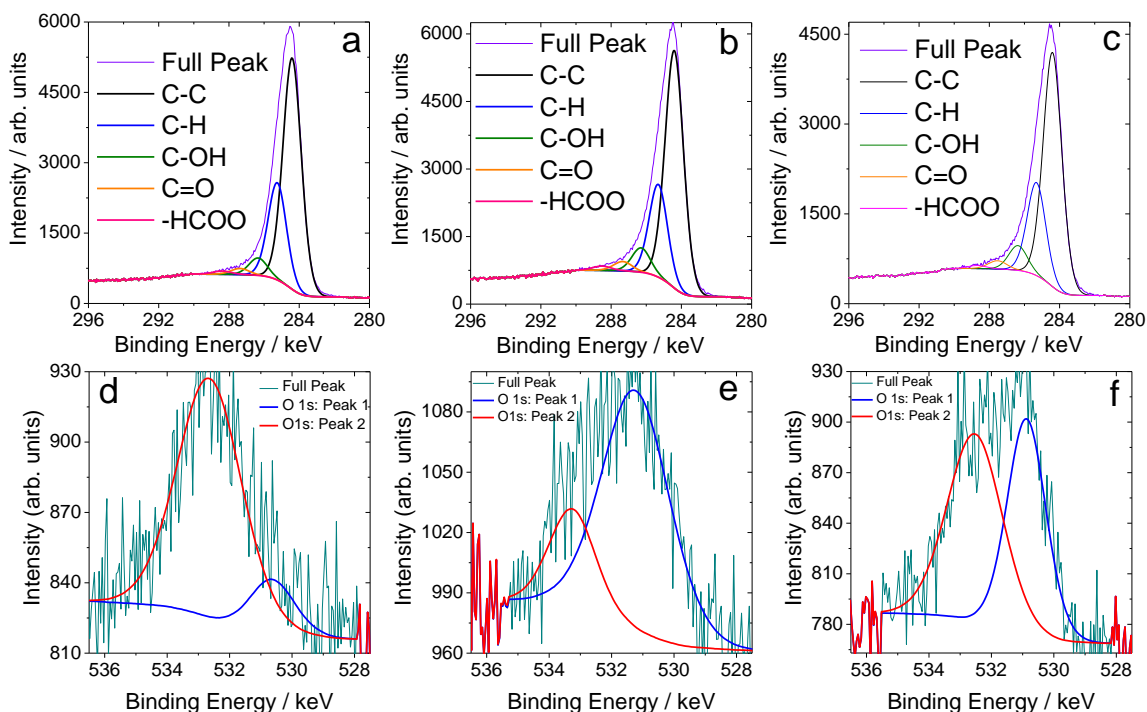
Figure 4.29. High-resolution XPS spectra in the C1s region for a) annealed CDC, b) aminated CDC, and c) hydrogenated CDC. Corresponding high-resolution XPS spectra in the O1s region are shown in d), e), and f).

The spectra in the O 1s region for the annealed and hydrogenated CDCs revealed peaks assigned to C–OH (~ 530.7 eV) and C=O/C–OOH (~ 532.6 eV) functional groups. Although oxygen was absent from this synthesis process, its presence stemmed from chemisorption of O_2 and H_2O from air.[235] Hydrogenated CDC contained more C-OH surface groups than C=O/C–OOH groups. The O 1s spectrum of the aminated sample also revealed two peaks, though they are shifted to 531.2 and 533.3 eV. The shift in these peaks was likely due to N–C–OH, and N–C=O/N–C–OOH functionalities, respectively, within these samples.

Table 4.5. XPS-derived elemental composition of differently functionalized CDCs. Trace impurities (Ti, Cl, and Fe) account for 0.0-0.1% of measured elemental compositions. The functional group content (column 4) was measured using inert TGA.

Material	C / wt. %	O / wt. %	N / wt. %	Functional Group Content / %
Annealed CDC	98.8	1.2	0	4.0
Aminated CDC	95.6	1.5	2.9	6.2
Hydrogenated CDC	95.2	2.1	2.6	10.9

To summarize (**Table 4.5**), annealed CDC contained no nitrogen, while aminated CDC contained (as expected) the greatest amount of nitrogen, and all three carbons contained small amounts of oxygen. Previous results have also detected noticeable oxygen (6.1 – 10.1 wt. %) quantities in aminated and hydrogenated porous carbons.[236] Chemical treatment (of any kind) of porous, semi-amorphous carbon has typically left behind some unterminated/dangling bonds that likely become saturated with reactive species from the environment. The conventional approach described above could not precisely quantify the amount of hydrogen on carbon surfaces; such analysis requires neutron activation spectroscopy or other similar techniques. Inert TGA analysis compared initial and final masses to quantify total surface chemistry compositions. This measurement (indirectly) deduced significant amounts of hydrogen in hydrogenated CDCs (**Table 4.5**): it included the greatest relative number of functional groups.

4.2.1.2. Influence of Hydrogenation and Amination on Electrolyte Dynamics

Quasi-elastic neutron scattering (QENS) assessed dynamics of ions in differently functionalized CDCs using the approach described in **3.5.3.** Based on the percentage of elastic scattering, as well as the lack of any observed transitions during heating of the sample from 10 K to 300 K, [EMIm$^+$][TFSI$^-$] was fully confined inside of micropores and left no bulk droplets on the surface. The confined hydrogen-containing [EMIm$^+$] cations (in Filled CDC samples) and hydrogen-containing surface functional groups (in Empty CDC samples) overwhelmingly contributed to neutron scattering signals.

For all samples, the width of the scattering signal was found to be Q-independent, indicating localized rather than long-range mobility of ions on the time scale of our quasi-elastic measurements (tens to hundreds of picoseconds) and allowing summation of the data over the entire Q range of the experiment for data analysis. The resulting scattering signal as a function of neutron energy transfer, $I(E)$, was subsequently Fourier-transformed from the energy to the time space. The resulting incoherent scattering function, $I(t)$, contains information about single-particle microscopic dynamics of [EMIm$^+$] cations. The decay of $I(t)$ as a function of time represented the loss of self-correlation in space with time, t, for a moving particle that was at the origin point at t=0.[237] Since time dependence for $I(t)$ cannot exist for a completely immobile particle, neutron scattering from such particle would be fully elastic. Unlike the vast majority of systems investigated by quasi-elastic neutron scattering, the $I(t)$ in this experiment could not be described satisfactorily by an exponential or a stretched exponential decay: [238]

$$I(t) = Ae^{-(t/\pi)^\beta} \tag{4.1}$$

Instead, the best regression function to fit the $I(t)$ was a logarithmic decay model, expressed by the equation below (τ is the characteristic relaxation time):

$$I(t) \ = \ A - B * \ln(^t/_\tau) \tag{4.2}$$

This relationship is shown in **Fig. 4.30(a)**. The logarithmic decay model for $I(t)$, which is highly unusual in quasi-elastic scattering, underscored the low mobility of ions in narrow pores. Such functional form for the I(t) had only been previously observed for hydrated biomolecules.[239] The low mobility of cations, epitomized by the very slow logarithmic decay of the $I(t)$, precluded quantitative determination of the diffusion constants on the time scale of the QENS measurement (using **Eq. 3.7** and **3.8**).
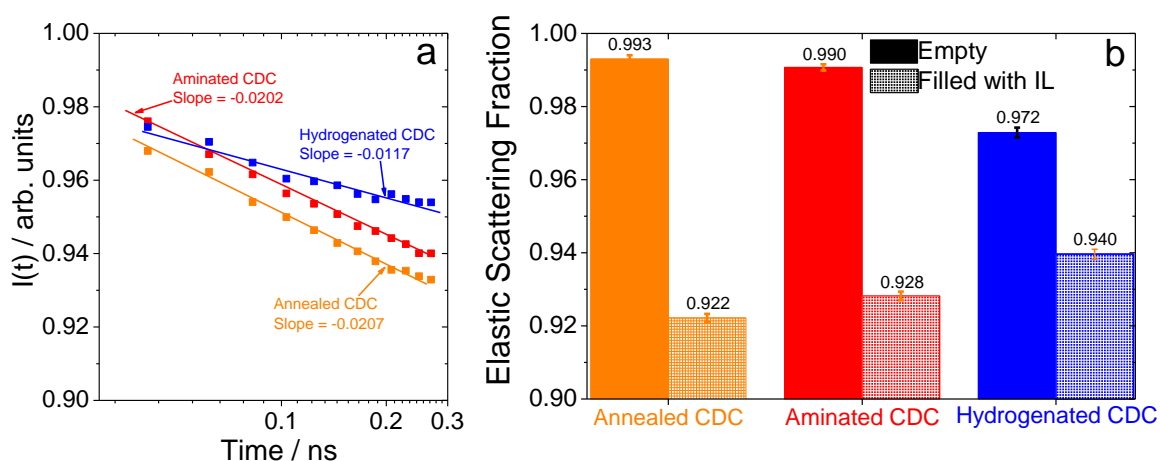
Figure 4.30. a) Logarithmic decay relationship between τ and the incoherent scattering function (representing self-correlation in space) of mobile cations. b) Fraction of elastic scattering for differently functionalized CDCs before and after IL loading. The fraction corresponds to the number of "immobilized" species in the sample that did not move appreciably on the QENS measurement time scale (10-100 picoseconds).

A linear regression analysis of the I vs. log(t) relationship derived the absolute value of the slope for hydrogenated CDC (0.0117) that was noticeably lower than for the aminated CDC (0.0207) or annealed CDC (0.0202). Among the self-correlation functions for [EMIm$^+$] cations in various environments, $I(t)$ for the hydrogenated CDC exhibited the slowest decay; therefore, ions inside of H-terminated pores were least mobile.

Given the narrow pore diameter (~0.61 nm), large molecular diameters of both [EMIm$^+$] and [TFSI$^-$], and the relatively low 80% pore volume loading, ions inside of

pores were likely in direct contact with the walls and absent from the "middle" of pores. Furthermore, strongest interactions between pore functionalities and electrolyte ions also drew the molecules closer to surfaces and left more void space around them. Therefore, the slowest dynamics for that system measured by QENS further singled out hydrogenated CDC pores interfaces as most favorable for [EMIm$^+$][TFSI$^-$] sorption.

The apparent fraction of the elastic signal in the total neutron scattering spectrum provided a complementary look at the relative interaction strength of cations with CDC pore walls. Stronger interactions with the pore walls lowered ion mobility, and, thus, increased coefficients of elastic scattering. Hydrogen surface species primarily determined this parameter in empty CDCs. The annealed and aminated samples showed nearly-perfect elastic scattering (0.99), whereas the lowest elastic scattering fraction for hydrogenated CDC (0.972) further confirmed the significantly greater amount of hydrogen on its pore walls.

For the elastic scattering fractions measured for filled CDCs (where the signal is now dominated by the H-containing cations, whereas contributions from pore surface groups become relatively small), the situation was reversed: hydrogenated CDC showed the most elastic scattering and, therefore, the most "immobilized" ions attached to pore surfaces. Both neutron scattering findings showed that hydrogenated pore surfaces were most favorable to [EMIm$^+$][TFSI$^-$] adsorption and attracted those ions the strongest.

4.2.1.3. Capacitance and Ion Dynamics of Hydrogenated and Aminated CDCs

Cyclic voltammetry measurements measured capacitance for the differently functionalized CDCs with neat [EMIm$^+$][TFSI$^-$] at room temperature. The results are shown in **Fig. 4.31**. Even at low sweep rates (2 mV s^{-1}), the hydrogenated electrode

surface demonstrated highest C_{sp}. Although some ionic resistance slightly distorted the rectangular (ideal) CV profile of each material, none of the materials exhibited distinguishable redox peaks at any sweep rates. Subsequently, neither hydrogen nor amine groups initiated any additional pseudocapacitive processes with [EMIm$^+$][TFSI$^-$].
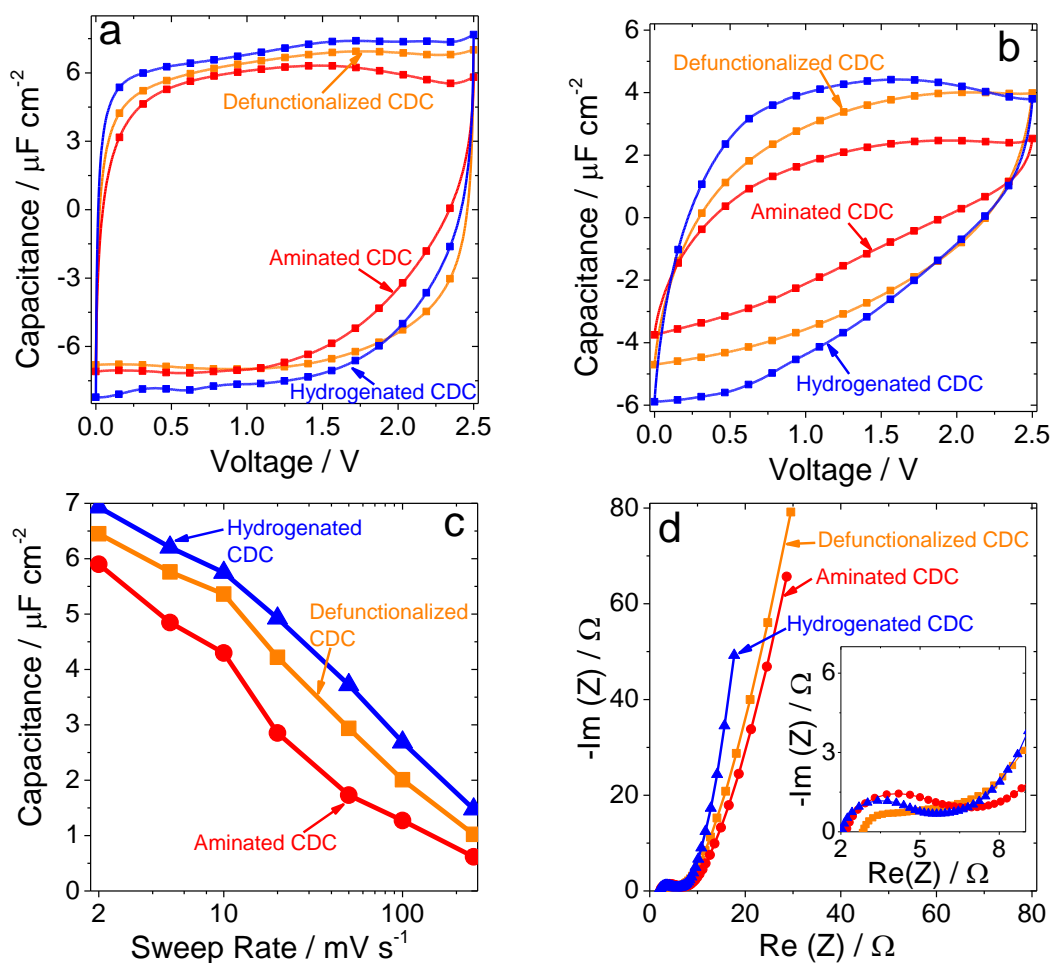
Figure 4.31. Cyclic voltammograms of differently functionalized CDCs conducted at a) 2 mV s^{-1} and b) 50 mV s^{-1}. c) Rate handling ability comparison for performance of CDCs in the 2.0 – 250 mV s^{-1} sweep rate range. d) Nyquist plot comparing electrochemical impedance for annealed, aminated, and hydrogenated CDC.

The influence of surface groups on capacitance and ion dynamics became more apparent at 50 mV s^{-1} sweep rate (**Fig. 4.31(b)**): hydrogenated CDCs stored 3.7 μF cm^{-2}, while annealed CDCs and aminated CDCs exhibited, respectively, 2.9 and 1.7 μF cm^{-2}.

Ionic resistance was especially apparent during the discharge segment of the CV sweep, which suggests that [TFSI⁻] anion was less mobile in narrow pores. Ion sieving followed a similar trend for all three surface chemistries. However, it was significantly more pronounced for aminated CDC surfaces and hurt its capacitance the most. Subsequently, its nitrogen-rich pore wall chemistry was least favorable for [EMIm⁺][TFSI⁻] electrosorption. This result contrasted with prior findings for aqueous electrolytes such as KOH, which had demonstrated higher capacitance (albeit, possibly due to redox processes) in nitrogen-enriched porous carbons.[158]

Table 4.6. Summary of electrochemical performance of differently functionalized CDCs with [EMIMm⁺][TFSI⁻] electrolyte at room temperature, as determined using cyclic voltammetry and impedance spectroscopy. Film resistance was determined using a 4-point probe.

CDC	ESR / Ω	C_{sp}, 10 mV s^{-1} / μF cm^{-2} (F g^{-1})	RS Coefficient	τ / s	Ionic Impedance / Ω	Film Resistivity / Ω cm
Annealed	2.82	5.36 (79.3)	0.793	11.74	9.56	2.10±0.3
Aminated	2.22	4.30 (74.2)	0.688	17.36	9.61	9.32±0.7
Hydrogenated	2.04	5.75 (87.1)	0.802	18.21	6.06	9.30±0.5

Hydrogenated CDC offered greater capacitance across the entire sweep range (Figure 4c). Its rate handling ability and capacitance decay at higher cycling rates parallels the behavior of defunctionalized CDCs. However, the capacitance of aminated CDC decayed at a somewhat faster rate above 10 mV s^{-1}. The RS coefficients, along with key electrochemical parameters of different electrode materials, are summarized in **Table 4.6**. The values were similar for hydrogenated and annealed CDCs (0.80 and 0.79, respectively), yet the aminated CDC (0.69) demonstrated greater diffusion limitations.

Electrosorption-induced mobility of confined ions featured a unique correlation with neutron scattering-induced mobility of [EMIm$^+$][TFSI$^-$]. Ion dynamics showed that CDC hydrogenation had improved ion mobility and minimized ionic resistance better than the other two surface treatments. Hydrogenated CDC exhibited lower ionic impedance, whereas annealed and aminated CDCs featured lower charge mobilities at low voltage oscillation frequencies.[209] QENS also highlighted a significant deviation of RTIL mobility in hydrogenated CDC, but neutron scattering showed primarily "immobilized" ions in that system. Therefore, slow neutron-measured dynamics of [EMIm$^+$][TFSI$^-$] primarily highlighted a favorable interface between the ionic liquid and the hydrogen-rich electrode surface. Under ambient conditions, the intermolecular interactions between hydrogenated surface groups and the RTIL drew ions closer to the surface. In effect, this allowed the ions to slide past the surface and past each other with less resistance during electrochemical cycling. Aminated CDCs exhibited opposite behavior: those functional groups repelled [EMIm$^+$][TFSI$^-$] ions and impeded their transport and exchange in narrow pores. These findings agreed with recent results that had highlighted distinct electrosorption dynamics for ionic liquids in nitrogen-rich carbon pores.[240]

Electrochemical behavior and measured ion dynamics agreed with the CV and EIS results for initial and annealed CDCs (section **4.1.3**). However, since the pore size for this sample set was slightly smaller than for the initial CDCs that were used for defunctionalization, ions were pressed closer to pore surfaces, and their rate handling was significantly more controlled by favorable/unfavorable surface chemistries. Furthermore, the advantage of hydrogenated CDC over its defunctionalized counterpart closely matched the performance of organic electrolytes in similarly sized pores (section **4.1.4**).

However, unlike $[EMIm^+][TFSI^-]$, 1.5 M $[NEt_4^+][BF_4^-]/CH_3CN$ demonstrated better capacitance and ion dynamics in aminated CDCs than in defunctionalized CDCs. This finding further reinforced an important result of this dissertation: the dynamics and resulting energy storage of differently functionalized supercapacitor electrodes depends on both sides of the electrode-electrolyte interface.

4.2.1.4. Cycle Life of Hydrogenated and Aminated CDCs

Annealed, hydrogenated, and aminated CDCs were cycled at a high current loading rate (5.0 A g^{-1}) for 10,000 cycles to discern any evidence of supercapacitor degradation. The changes in coulombic efficiency (shown in **Fig. 4.32**) demonstrated that hydrogenated CDCs were most reversible and stable throughout the entire cycling regime. Their Q_{eff} maintained 75% of its initial value, whereas the values for annealed CDCs and aminated CDCs declined to 65% and 57%, respectively, of their respective starting efficiencies. Hydrogenated CDC maintained relatively high capacitance: its C_{sp} slightly decreased from 102 to 93 F g^{-1}. Annealed CDCs also showed good capacitance retention and lost only 7 F g^{-1} (from 77 to 70 F g^{-1}) as a result of cycling. However, the aminated CDC material experienced a 13 F g^{-1} decrease as a result of cycling, which is in line with its coulombic efficiency drop.
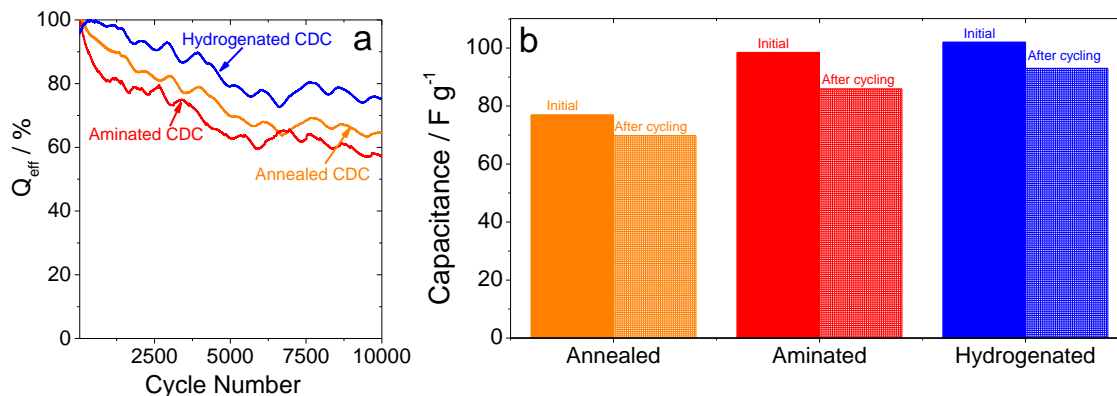
Figure 4.32. a) Coulombic efficiency comparison for annealed, aminated, and hydrogenated CDC after galvanostatic cycling at 5.0 A g^{-1} for 10,000 cycles. B) Gravimetric capacitance of different CDCs before and after long-duration cycling, measured using cyclic voltammetry at 10 mV s^{-1}.

Long-duration CDC cycling did not show any signs of pseudocapacitive behavior. No new charge transfer processes in the cyclic voltammograms emerged after 10,000 cycles. Electrochemical breakdown of confined electrolyte and blockage of narrow pores with resulting decomposition products likely contributed most to supercapacitor degradation rather than oxidation or reduction of pore walls. Poorly reversible insertion of ions into narrow pores may also be partially responsible for this effect.[241] As compared to typically reported supercapacitors,[242] narrow pore diameters significantly accelerated the cycling-induced device degradation. However, favorable surface chemistries that improved ion mobilities and FSI interactions also correlated with greater capacitance retention over prolonged cycling. Subsequently, ionic resistance during electrosorption may negatively impact the long-term stability of [EMIm$^+$][TFSI$^-$].

4.2.2. Oxidized CDC Surfaces

Although hydrogenated and aminated CDCs provided a very useful comparison of capacitance and electrosorption dynamics against defunctionalized porous electrodes,

they provided only a partial overview of the influence of chemical defects at interfaces. Both hydrogenated and aminated surfaces also included oxygen groups, and their standalone effect on IL dynamics has not yet been separated and investigated. Furthermore, in an effort to minimize sample-to-sample surface property variations, TiC-CDCs exhibited very small pores that could not facilitate sufficiently unrestricted ion diffusion. To broaden the understanding of specific defects on capacitance and ion mobilities, high-temperature flowing dry air treatment oxidized surfaces of (initially defunctionalized) SiC-CDCs, which had been synthesized at 900 ℃ and vacuum annealed at 1,400 ℃. TGA and porosimetry measurements tuned the air treatment temperature to 425 ℃. This air oxidation condition presented the best balance between sufficient chemical functionalization and retaining nanostructured porosities.

4.2.2.1. Structural and Chemical Properties of Oxidized CDCs

Treatment conditions negligibly increased the SSA and pore volume (**Fig. 4.33**) without altering the narrow pore size distributions (pore d_{av} ≈0.62 nm). This correlated with previous air oxidation results.[243] Oxygen-containing groups on carbon surfaces noticeably altered the wettability of the surface. As shown in ellipsometry measurements (**Fig. 4.33(b-c)**), the contact angle of [EMIm$^+$][TFSI$^-$] improved from 70.2° (on bare graphite) to 50.7° (on oxidized graphite), suggesting a more favorable interface and greater ionophilicity for the latter. The increase in wettability for the ionic liquid paralleled improved H_2O wettability of oxidized carbon.
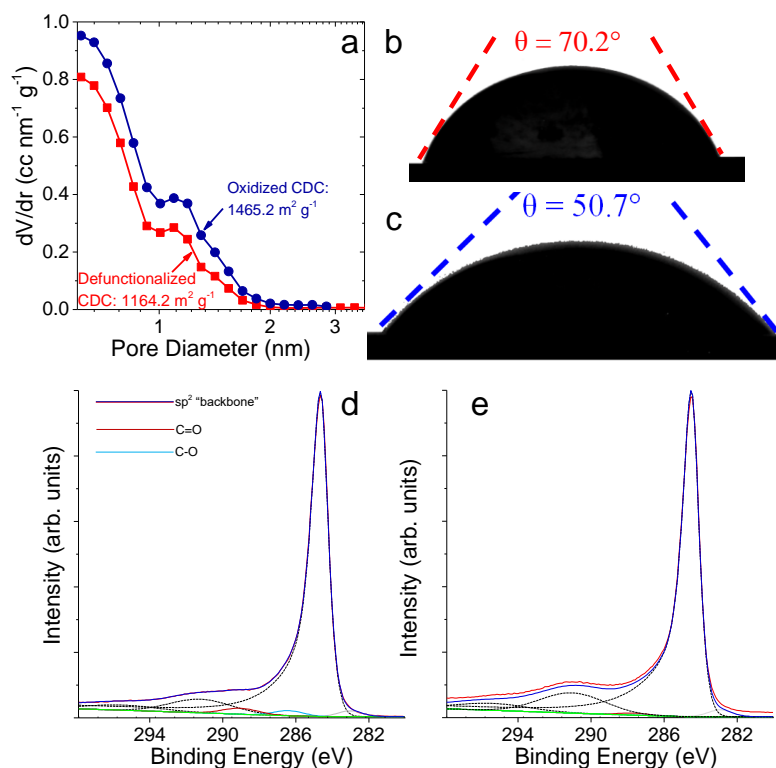
Figure 4.33. a) N_2 sorption derived pore size distribution of defunctionalized and oxidized porous CDC materials. The contact angle between [EMIm$^+$][TFSI$^-$] and a reference flat graphite substrate is shown for b) defunctionalized and c) oxidized surfaces that underwent identical annealing and oxidation procedures. XPS fitted the C1s peak for a) defunctionalized and b) oxidized carbons.

XPS analysis (**Fig. 4.33(d-e)**) identified a few distinct oxygen-rich species on oxidized CDC surfaces. Elemental oxygen content increased from 3.6 wt. % (defunctionalized CDC) to 5.9 % (for CDC) after air treatment. Deconvolution of C1s and O1s peaks identified carboxyl (–HCOO) and hydroxyl (H–O–C–) functional groups. Although 400-500 °C dry air oxidation was expected to primarily yield carbonyls (–C=O),[156] those groups were absent from all spectroscopy measurements. The carbonyl peak shifted from ~287 eV to 288.6 eV during oxidation and indicated that C=O became part of an O–C=O bonding configuration. Since the samples came into contact with ambient air after each treatment step, it is possible that some O_2/H_2O molecules reacted with leftover dangling bonds in the carbon structure.

4.2.2.2. Static and Dynamic Electrochemistry of Oxidized CDCs

Cyclic voltammetry recorded significantly greater capacitance of Oxidized CDC electrodes with [EMIm$^+$][TFSI$^-$]. As shown in **Fig. 4.34**, oxidized CDCs featured more rectangular CV curves that were indicative of more ideal capacitive behavior and could store 4.6 μF cm^{-2} at 50 mV s^{-1}. Conversely, the CV profile for defunctionalized CDCs was distorted due to ionic resistance, and its capacitance reached only 1.4 μF cm^{-2}. The defunctionalized CDC material exhibited drastic capacitance decay over the entire 0.5 and 250 mV s^{-1} CV sweep range.
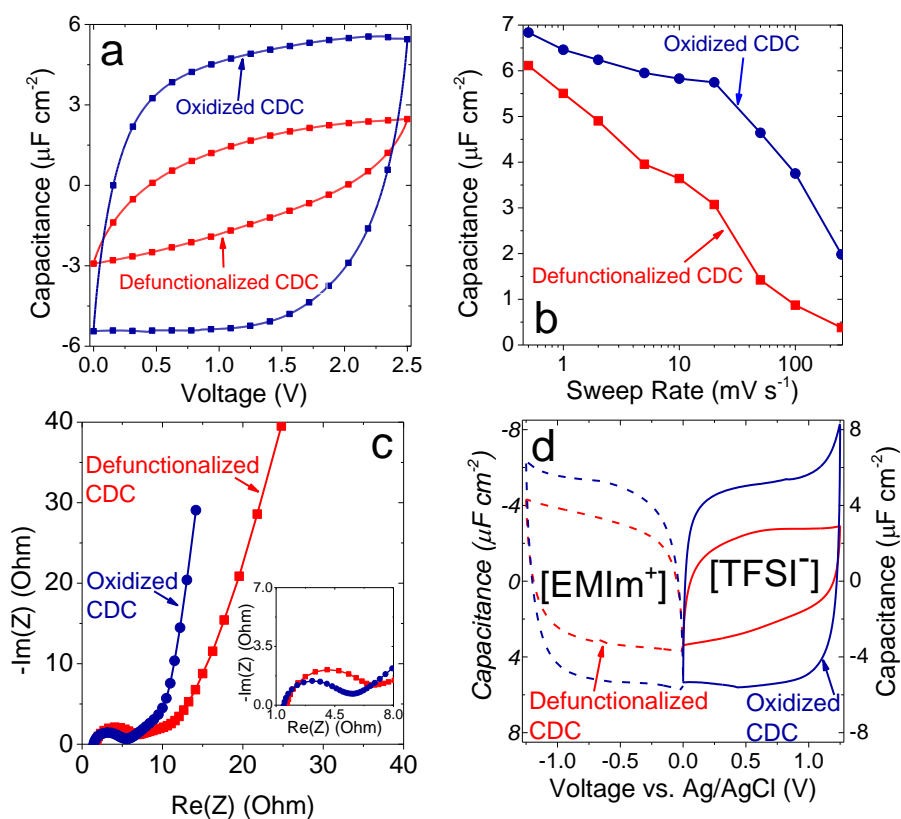
Figure 4.34. a) Cyclic voltammetry plot for [EMIm$^+$][TFSI$^-$] cycling in defunctionalized vs. oxidized CDCs at 50 mV s^{-1} sweep rate. b) Rate handling comparison of performance in oxidized and defunctionalized pores in the 0.5 – 250 mV s^{-1} sweep range. c) Nyquist plot that compared ionic resistance differences. The inset shows the high-frequency region with identical R$_s$~0.8 ohms for both materials. d) A 3-electrode sweep conducted at 1.00 mV s^{-1} showed differences in electrosorption of the cation and anions in annealed and oxidized pores. To compare symmetry, the negative electrode current was multiplied by -1 and the scale for it (italicized) is given on the left.

As shown in the Nyquist plot in **Fig. 4.34(c)**, ionic resistance significantly decreased in oxidized CDCs. The 4-point probe conductivity measurements showed that oxidized CDC (σ = 1.42±0.09 S cm^{-1}) was only slightly more resistive than the defunctionalized electrode (σ = 1.68±0.09 S cm^{-1}). Subsequently, ionic resistance of the defunctionalized, ionophobic surface was the primary limiting factor of the electrochemical capacitance of this material. 3-electrode measurements (**Fig. 4.34(d)**) investigated the standalone influences of cations and anions. While the trends are similar to two-electrode results, defunctionalized CDCs demonstrated significantly greater ionic resistance and ion sieving of the [TFSI$^-$] anion than the [EMIm$^+$] cation. Therefore, these findings showed that hydrophobic/ionophobic defunctionalized surfaces impeded larger, more polar anions. This conclusion agreed with prior results.[108,116]

Square wave amperommetry measurements derived charge accumulation at given steady-state voltages (static conditions); these results are shown in **Fig. 4.35**. While charge accumulated more rapidly in oxidized CDCs (in line with dynamic potential experiments above), total charge storage densities at different voltages reached near-identical magnitudes for the two materials. The voltage vs. charge relationship (**Fig. 4.35(c)**) showed that defunctionalized CDCs (5.6 µC cm^{-2}) matched or slightly exceeded equilibrium charge storage capacities of oxidized CDCs (5.3 µC cm^{-2}). Subsequently, the mobility-induced advantage of oxidized CDCs in dynamic charge/discharge systems disappears for steady-state capacitance with static conditions.
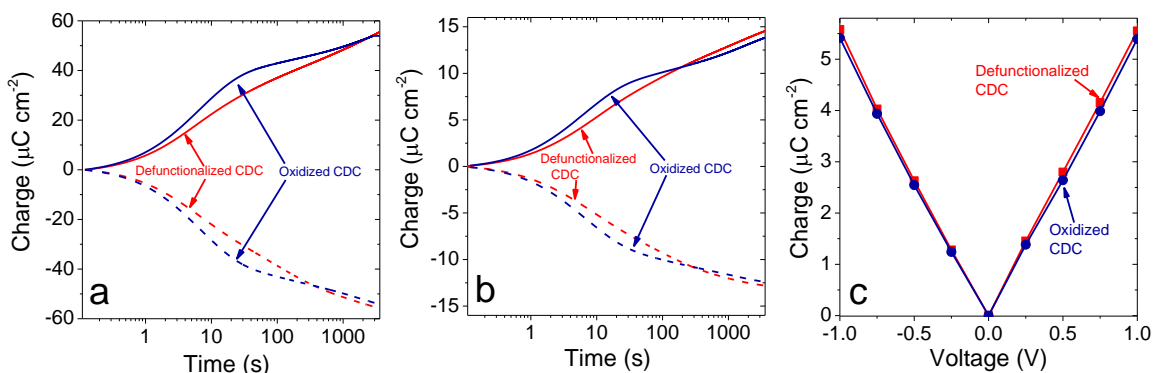
Figure 4.35. Charge accumulation vs. time during a square wave amperommetry step from a) 0.0 to ±0.25 V and b) 0.0 to ±1.0 V. c) Absolute amount of charge stored at each electrode during static 1 hour CA at different voltages in the -1.0 ↔ 1.0 V window.

The ionophilic CDC pores significantly improved the capacitance and rate handling ability. However, the benefit of oxygen-rich pores did not extend beyond improving mobility. Static state experiments in porous CDCs determined that, at equilibrium conditions, [EMIm$^+$][TFSI$^-$] is electrosorbed into defunctionalized pores with greater densities and no ionophobic drag. Electrode-electrolyte interactions in narrow pores mainly affected the packing density of ions with respect to pore walls and influenced the conditions for ions to move past each other.

4.2.2.3. Neutron Scattering of Ions in Monomodal Oxidized CDCs

QENS measurements provided insights into the relative mobilities of [EMIm$^+$][TFSI$^-$] ions inside of defunctionalized and oxidized CDC pores. The energy transfer vs. scattering intensity distributions (**Fig. 4.36(a)**; averaged for 0.4 Å^{-1} ≤ Q ≤ 1.6 Å^{-1}) demonstrated the small but sizable difference in the microscopic dynamics of cations confined in defunctionalized and oxidized CDCs. A double-Lorentzian model scattering function successfully fit the scattering data to a Q vs. Γ relationship (**Eq. 3.7**).

The narrow Lorentzian component was attributed to very slow localized ion dynamics. The extracted HWHM fits of component extracted from the fits are shown in

Fig. 4.36(b). As evidenced by the Q-dependent broadening for $Q > 1$ Å^{-1}, this component originated from translational cation mobilities. Broadening plateau at low Q values signified significant spatial constraints of ions. The long-range translational diffusion coefficients could not be determined for ions in these systems, due to significant confinement in narrow pores that precluded the ions from demonstrating long-range mobilities However, systematically larger Γ values for ions in oxidized pores indicated that the ions that were present in oxygen-containing pores had greater mobility and self-diffused with less resistance. The elastic scattering fraction in the QENS signal (**Fig. 4.36(c)**) suggested that oxidized pores had "tethered" a larger percentage of ions onto functionalized surfaces. Therefore, oxygen-rich ("ionophilic") pores had stronger attractive intermolecular interactions with electrolyte molecules. At the same time, the ions further from the pore walls, which exhibited appreciable localized diffusivity, were more mobile in the "ionophilic" pores of oxidized CDCs.
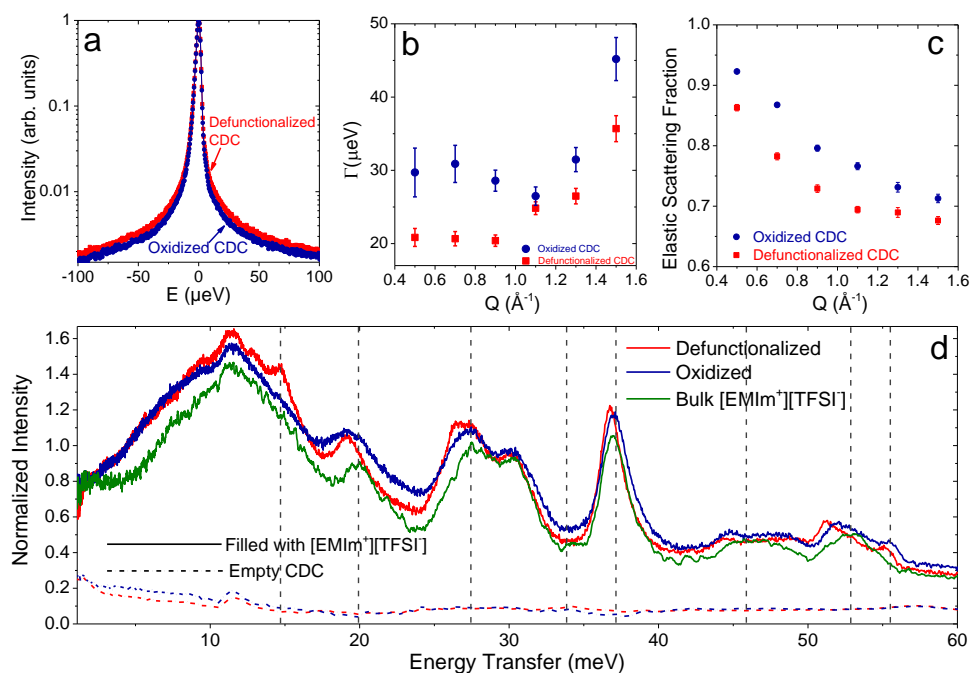
Figure 4.36. a) QENS signal averaged over the entire measured range of Q values for annealed and oxidized pores 100% filled with [EMIm$^+$][TFSI$^-$]. The maximum of intensity (at zero energy transfer) was normalized to unity for both samples, b) QENS signal broadening was determined using a double Lorentzian fit equation at different Q values. c) The fraction of elastic scattering in the QENS signal measured for the two

systems at different Q values. d) INS spectra obtained at 5K on the empty (dashed lines) and IL-filled (solid lines) defunctionalized and oxidized CDCs, with the empty CDC contributions subtracted from the CDC+IL systems. Distinct vibrational modes are marked with vertical black lines.

INS measurements at 5 K provided information on the relative vibrational densities of states (VDOS) of $[EMIm^+][TFSI^-]$ in the bulk and confined states as well as VDOS of the used empty CDCs samples. The intensities of the INS spectra for confined $[EMIm^+][TFSI^-]$ are much larger than those for empty CDCs, and the latter were subtracted from the former. Almost all RTIL vibrational modes underwent a ~1-3 meV shift as a result of confinement in CDC pores. Several peaks (19 meV and 27 meV) red-shifted for confined IL; others (46 meV) were slightly split in bulk IL but broadly split in confined IL. Extra peak appeared for confined IL at 55.3 meV (for both pore types) and at 14.5 meV (in defunctionalized pores). According to prior Raman measurements and vibrational spectra calculations for liquid and solid $[EMIm^+][TFSI^-]$,[244,245] the planar structure should have provided an extra peak at ~55 meV. This peak was absent in the INS spectrum of the bulk IL (having non-planar configuration) but present in the confined IL spectrum. Therefore, confined IL had planar $[EMIm^+]$ arrangement. All vibrational modes of RTIL confined in defunctionalized pores were significantly narrower than those in oxidized CDC. This suggested more uniform local bonding environment (less structural disorder) and/or lower mobility (less dynamical disorder) of ions confined in defunctionalized, ionophobic pores.
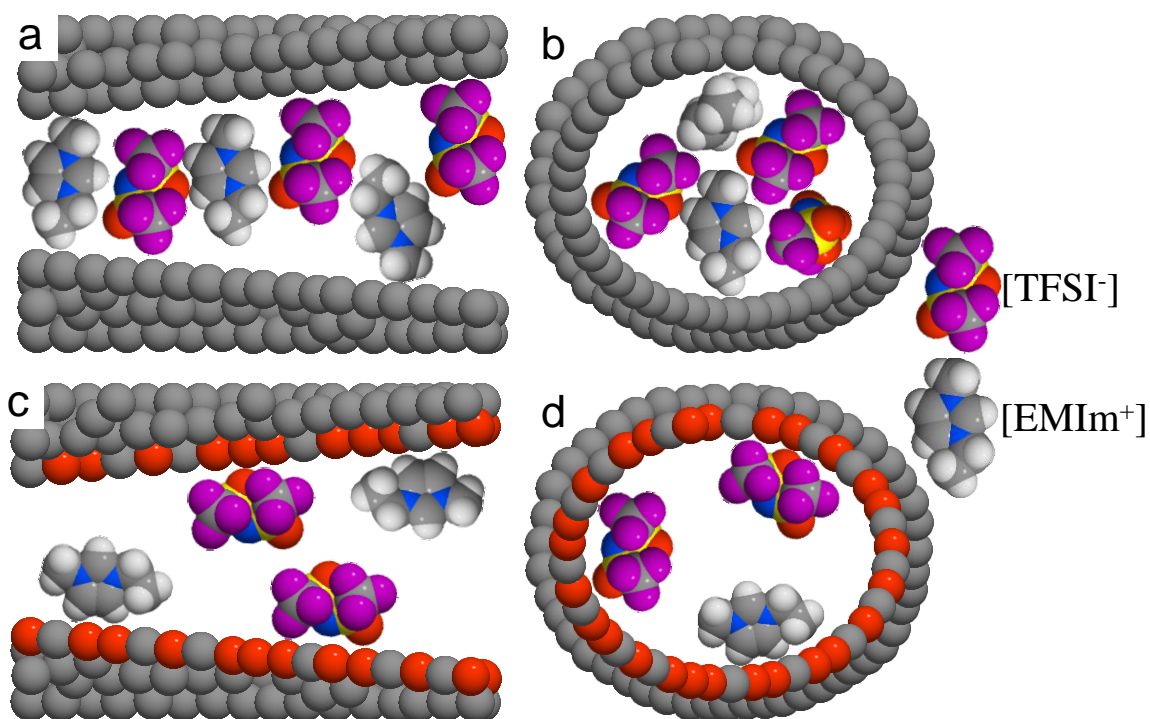
Figure 4.37. The a) cross-sectional and b) top view schematic of a defunctionalized CDC pore and confined [EMIm$^+$][TFSI$^-$]. Ion configuration on defunctionalized surfaces allowed greater packing of ions in pores, increased local IL densities in pores, but restricted ion motion. Oxidized pores in c) and d) arranged more ions in parallel directions with respect to surfaces; this decreased ion densities but allowed the electrolyte molecules to exchange positions and move past each other. Pore diameters of schematics are not to exact scale of the SiC-CDCs discussed in this section.

Ionophobic surfaces repelled ions that, in turn, migrated towards centers of pores. Conversely, favorable electrode-electrolyte interactions attracted ions from mid-pore voids and achieve minimal separation in the fluid-solid interface. The ions achieved near-parallel arrangements (in greater contact) on oxygenated interfaces and more random arrangements (fewest interactions possible) on defunctionalized, ionophobic surfaces. Although the perpendicular arrangement allowed greater ion packing into pores (and thus greater INS-measured vibrational energies), this configuration left longer, obtrusive paths through pores and impeded molecular motions through the confined spaces. In oxidized pores, ions stuck closer to surfaces and left the middle of the pores empty (thus reducing

overall density). This arrangement, which is shown in **Fig. 4.37(c-d)**, provided sufficient void space for cations and anions to shuffle past each other and increased mobility.

4.2.2.4. MD Simulations of Ions in Functionalized Pores

Based on similar ReaxFF computational principles that were used to describe porous carbon structures (section **4.1.1**), Molecular Dynamics simulated slit pores with 1.1 nm separation distances between 2 carbon basal planes. The effective pore size ($d_{av} = 0.7$ nm) closely resembled the experimental SiC-CDC electrodes. Hydroxyl groups were grafted onto pore surfaces and constituted a 7.7 wt. % (5.6 molar %) composition. MD simulated the ion accumulation and resulting charge densities under applied steady-state potentials and most closely resembled the square wave/chronoamperometry experiments from **Fig 4.35**. The simulation results and production snapshots are shown in **Fig. 4.38**. Each simulation used a box with approximately 10^4 atoms.
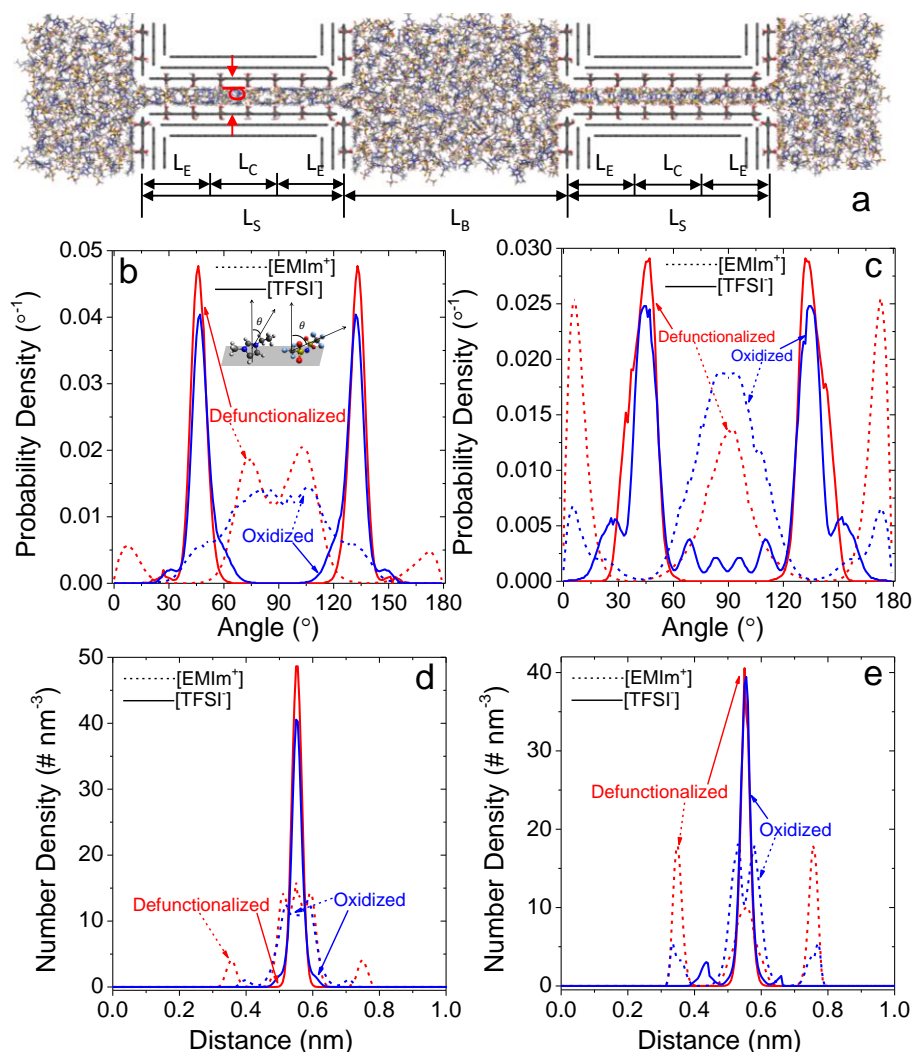
Figure 4.38. a) Snapshot of the MD simulation of the filled pore system. L_S: the length of the slit (6.3 nm); L_B: The length of the IL bath (7.0 nm); L_E: the length of slit entrance (2.1 nm); L_C: the length of center part of slit (2.1 nm). Ion orientations inside of oxidized or defunctionalized pores are shown under b) no applied charge and c) -5.0 μC cm^{-2}. Inset in (b) shows reference directions of [EMIm$^+$] (normal to the imidazolium rings) and [TFSI$^-$] (tail-to-tail) orientations. Corresponding ion accumulation densities in the pores are given in d) and e).

Charge accumulation densities of ions showed that the amount of [EMIm$^+$] cations inside slit pores decreased by more than 20% after oxidation, while [TFSI$^-$] anion densities decreased by approximately 5%. Under neutral potentials (conditions that matched QENS and INS measurements), oxygen functional groups repelled [EMIm$^+$] and attracted [TFSI$^-$]. Under positive applied potentials, the functional groups attracted more

counter-ions into pores. Under negative applied potentials, oxidized groups reoriented the ions and maximized their densities in confined states. Resulting ion densities in oxidized pores (3.70 ions nm^{-2}) exceeded those of defunctionalized pores (3.31 ions nm^{-2}).

The interactions between specific surface groups and individual IL ions influenced their orientations with respect to pore surfaces and, in turn, affected accumulation number densities and resulting capacitances. Oxygen groups were more favorable to the [TFSI$^-$] molecules, which exhibited several highly polar groups (S=O, N–S, C–F). On the other hand, defunctionalized surfaces were more favorable to the imidazolium ring and the –C$_2$H$_5$ alkyl chain on the [EMIm$^+$] cation. Subsequently, while the aligned perpendicularly with respect to oxidized pore surfaces (due to reduced π–π interaction), the anions prevalently aligned in parallel to the pore surfaces after functionalization.

The simulations provided an important analysis of the orientations of ions with respect to defunctionalized and oxidized pores. They verified the conclusions that had been obtained using neutron scattering and demonstrated that surface defects had influenced ion arrangement in pores and pore filling densities. However, the simulations showed that functionalization had unequal influence on the two ions; while [TFSI$^-$] anions favored oxidized surfaces, [EMIm$^+$] cations preferred to align closer to pristine graphene surfaces. Since the net effect on experimentally-measured capacitance positively correlated with oxygen functionalization, the anion could be assumed to be rate-limiting. Furthermore, although the simulation showed higher ion densities for oxidized surfaces (in line with cyclic voltammograms), the number density profiles could not take into account ion dynamics and factor in the benefit of enhanced electrolyte mobilities in oxidized pores. Ion exchange and swapping in confined pores, and the

confounding influence of nearby functional groups on ion orientations and transport processes, remains an important question for future investigations.

4.2.3. Electrolyte Dynamics in Bimodal Functionalized CDCs

The narrow pore structure of defunctionalized and oxidized SiC-CDCs provided an important overview of the influence of oxygen groups on electrochemical mobility and capacitance under static and dynamics applied potentials. However, a larger pore system, and a more complex electrolyte with dissimilar ion sizes, provided an additional fundamental overview of ion configurations and interactions in pores. Mo_2C-CDC, which had been synthesized at 800 ºC, exhibited a bimodal pore size distribution: approximately 50% of pores were 0.78-0.82 nm in diameter, and the rest were 1.9 – 2.8 nm in diameter. It was defunctionalized and oxidized using the same methods as SiC-CDC in section **4.2.2**. Furthermore, its electrochemical performance was tested with [OMIm$^+$][TFSI$^-$] electrolyte. As described in section **3.7.3**, [OMIm$^+$] had an 8-carbon alkyl chain (instead of [EMIm$^+$]'s 2-carbon chain). Since the cations became larger than the smaller pore diameters, some ion partitioning was expected. Finally, since the cation molecule became more hydrophobic, it was expected to poorly interact with oxygen groups on surfaces.

4.2.3.1. Porosity and Ion Dynamics in Bimodal Pores

The material retained its bimodal pore size distribution after vacuum annealing and subsequent air oxidation. As shown in **Fig. 4.39(a)**, air oxidation increased the SSA by 300 m^2 g^{-1}; however, since the total surface area was over 2,100 m^2 g^{-1}, this was a relatively slight oxidation that did not influence pore polydispersity. For defunctionalized

CDCs, small pores accounted for 1,028 m^2 g^{-1} (53%). After oxidation, small pores accounted for 1,174 m^2 g^{-1} (52%). XPS elemental analysis of the surface revealed that, after air treatment, oxygen content increased from 1.1 at. % to 2.2 at. %. As with the monomodal CDCs, most oxygen was in form of C=O and O–C=O bonding.
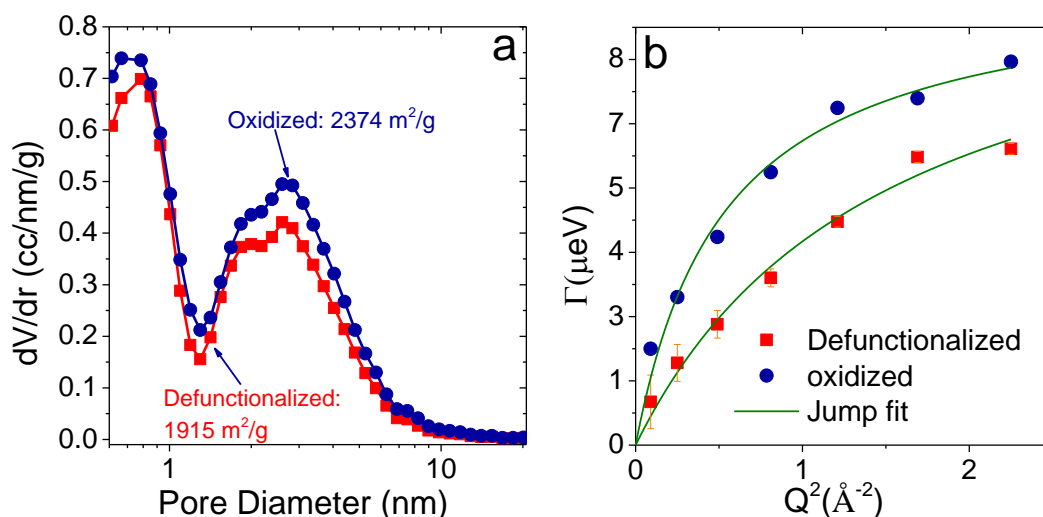
Figure 4.39. a) Pore size distribution of Mo$_2$C-CDC after annealing (defunctionalized) and air treatment (oxidized). b) Dependence of HWHM of QENS spectra of [OMIm$^+$][TFSI$^-$] confined in defunctionalized and oxidized Mo$_2$C-CDC extracted from the Cole-Cole model function as a function of Q-squared. Solid line shows the model fits.

QENS results were obtained from porous CDCs that had been filled with [OMIm$^+$][TFSI$^-$] using the same approach as in section **4.2.2.3.** Data was fitted to a two-Lorentzian equation (Eq. **3.6**). Since the characteristic relaxation time was coupled with the stretched exponent, calculation of average τ did not show any trend from which the diffusion coefficient could be extracted. Therefore, the Cole-Cole distribution function, [190] which behaves as a stretched exponential function with the half width at half maximum (HWHM) is independent of the stretched exponent (**Eq. 3.7**). HWHM increased at low Q's and flattened at higher Q's, which indicated translational jump diffusion behavior. Using **Eq. 3.8**, diffusion coefficients and jump diffusion lengths were calculated and are shown in **Table 4.7**.

Table 4.7. Diffusion of [OMIm$^+$][TFSI$^-$] in oxidized and defunctionalized Mo$_2$C-CDCs.

Pore Surface	Diffusion Coefficient	Jump Length
Oxidized	$2.71 \pm 0.32 \cdot 10^{-10} \, m^2 \, s^{-1}$	3.3 Å
Defunctionalized	$1.05 \pm 0.14 \cdot 10^{-10} \, m^2 \, s^{-1}$	1.9 Å

The D_{coeff} of the IL confined in oxidized Mo$_2$C-CDC was higher than the one extracted from defunctionalized CDCs. Subsequently, intrinsic mobility of [OMIm$^+$][TFSI$^-$] in oxidized pores was 2.6 times as large as its mobility in defunctionalized pores. This finding agreed with similar dynamics that had been described for oxidized monomodal CDs (section **4.2.2**). The bimodal CDC system featured somewhat larger pores, which allowed less restricted translational and rotational motion and sufficiently long random walk distances, for measurements of coherent diffusion behavior. As with previous QENS measurements, most of the measured dynamics concerned the hydrogen-rich [OMIm$^+$] cations. Although ions were expected to rely on electrostatic interactions to drag along the oppositely-charged counterions and interlink the mobility properties, it is unclear whether the large cations (with a long hydrophobic tail) or the smaller anions were the main drivers of this property.

Small-angle neutron scattering (SANS) measurements were collected on the IL-filled defunctionalized and oxidized pores, as well on the bulk [OMIm$^+$][TFSI$^-$], at 300 K and 350 K. The effects of surface chemistries on the scattering from the confined IL on bimodal CDC are shown in **Fig. 4.40**. The scattering profiles at the low Q regime overlapped with each other for both samples at both temperatures. Effects of surface chemistries become more apparent at the intermediate Q regime. The scattering intensities were higher from [OMIm$^+$][TFSI$^-$] confined in oxidized CDCs compared to

defunctionalized pores. Higher intensity corresponded to the higher scattering contrast. The scattering length density (SLD) of Mo_2C- CDC was ~ 6.66 x 10^{-10} $Å^{-2}$ (assuming ~2 g cm^{-3} density), whereas the SLD of the ionic liquid was 1.46 x 10^{-10} $Å^{-2}$.[246]
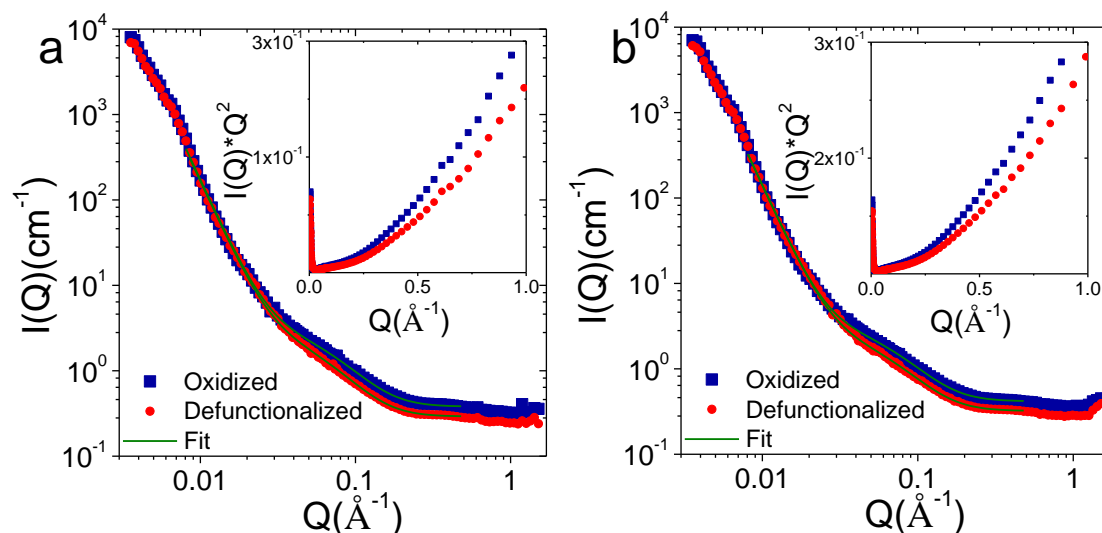
Figure 4.40. SANS profiles of [OMIm+][TFSI−] confined in oxidized and defunctionalized Mo_2C-CDC with Kratky plots shown in insert at (a) 300 K (b) 353 K.

Since the scattering from the low Q regime can originate from different sources, the final data fitting used only Q values up to ~ 0.01 $Å^{-1}$ on the low Q side. The data was fit to a modified Debye-Anderson-Brumberger (DAB) model:[247]

$$I(Q) = \frac{A}{Q^{\alpha}} + \frac{B\xi^3}{[1+(Q\xi)^2]^2} \qquad (4.3)$$

In this equation, α is the scattering exponent that scaled the intensity and provided information regarding the geometry of the scattering objects and ξ is a length scale that measured the spacing between the two phases. The correlation length extracted from the fit can be related to the radius of gyration (R_g) using Guinier approximation that gave an average pore size of $R_g = \xi\sqrt{6}$. Based on a previous approximation of carbon pores as

cylindrically-shaped,[107] the model calculated the average radius of the cylindrical pore

(R_{cyl}) using the relation: $R_g = R_{cyl}/\sqrt{2}$. Fitted parameters are presented in **Table 4.8**.

Table 4.8. Fitting parameters from the sum of power law and DAB model.

Sample	α	ξ (Å)	R_g (Å)	R_{cyl} (Å)
IL in defunctionalized pores: 300 K	3.94	11.53	28.24	39.93
IL in defunctionalized pores: 353 K	3.94	10.89	26.67	37.71
IL in oxidized pores: 300 K	3.95	10.64	26.06	36.85
IL in oxidized pores: 3530 K	4.00	10.58	25.91	36.64

Although value of α is roughly the same for both samples at all measured

temperatures, the R_g correlation length was lower in oxidized samples. This very subtle

change could originate from pore surface hydrophilicity. Furthermore, intensity

differences in the intermediate Q regime suggested that the reduction in contrast was less

significant from [OMIm$^+$][TFSI$^-$] confined in oxidized CDC. This indicated a lower

density of IL confined in oxygen-rich pores. From the scattering intensities, the density of

[OMIm$^+$][TFSI$^-$] in oxidized pores was ~ 20% lower than in the annealed samples. Since

the surface of the oxidized CDC was more hydrophilic, most of the electrolyte molecules,

especially the anions, attached to the pore surfaces and reduced the number of the RTILs

molecules in the center of the pores. This measurement agreed with neutron scattering

results (for both monomodal and bimodal CDCs), and the quantified density changes

closely matched the MD-derived (section **4.2.2.4**) simulations of ions in oxidized pores.

4.2.3.2. Electrochemical Behavior of [OMIm$^+$][TFSI$^-$] in Bimodal CDCs

The [OMIm$^+$][TFSI$^-$] electrolyte was tested with defunctionalized and oxidized

Mo$_2$C-CDC electrodes in two-electrode and three-electrode configurations. The results

are shown in **Fig. 4.41**. Electrochemical impedance measurements (**Fig. 4.41(a)**) showed

greater mobility of the electrolyte in oxidized pores at mid-to-low oscillation frequencies. The mid-range ionic impedance (between the charge-transfer resistance and the "knee" frequency) was 18.1 Ω for defunctionalized CDCs and 10.0 Ω for oxidized CDCs. Although impedance was almost identically capacitive-dominated at 10 mHz (-81.9º for oxidized CDCs and -80.9º for defunctionalized CDCs), oxidized CDCs were more predominantly capacitive at mid-to-high frequencies.
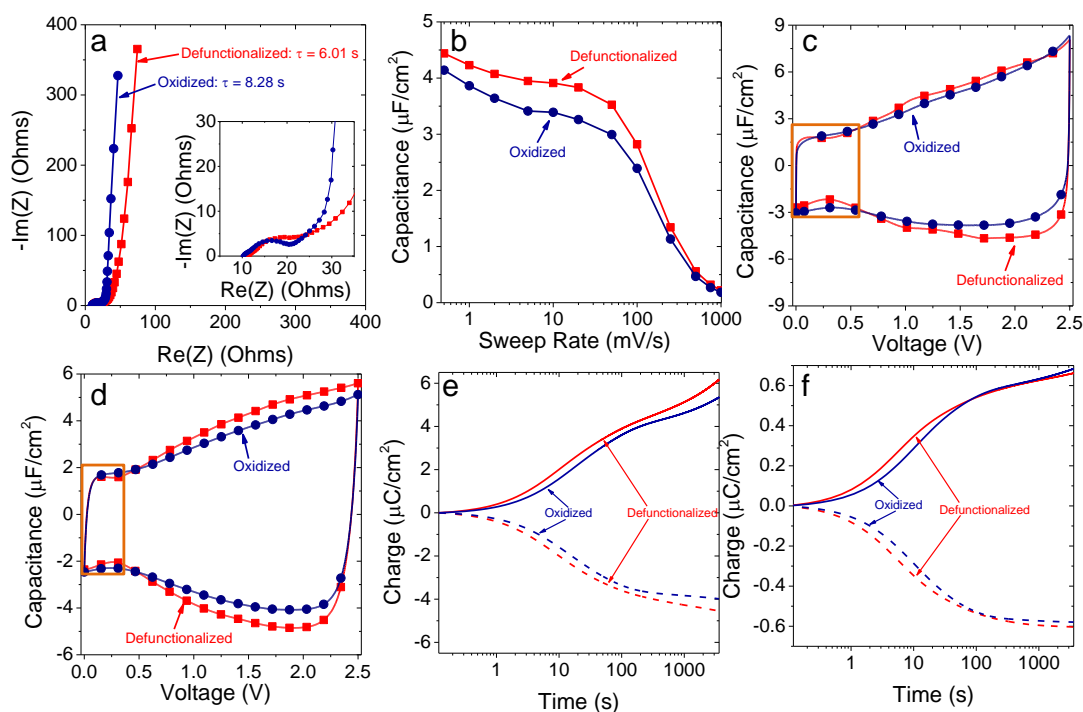
Figure 4.41. a) Nyquist plot that compared electrochemical impedance of [OMIm$^+$][TFSI$^-$] in defunctionalized and oxidized Mo$_2$C-CDC. b) Rate handling comparison of the two-electrode cells in the 0.5 – 1,000 mV s^{-1} range. Cyclic voltammograms are shown for c) 0.5 mV s^{-1} and d) 10 mV s^{-1}. Three-electrode charge accumulations are shown for square wave amperommetry measurements for e) 0 → ±1.25 V and f) 0 → ±0.25 V charge accumulations (1 hour each).

Although gravimetric capacitance for oxidized CDCs (76 F g^{-1} at 10 mV s^{-1}) exceeded the C_{sp} for defunctionalized CDCs (73 F g^{-1} at 10 mV s^{-1}), the SSA-normalized capacitance for defunctionalized CDCs was greater for this electrode-electrolyte system (**Fig. 4.41(b)**). This result differed from the similarly functionalized monomodal SiC-

CDCs (section **4.2.2**). Larger pores made available more bulk space that facilitated free ion mobility and exchange during electrosorption with fewer contacts with the surfaces. Subsequently, while [TFSI⁻] ions likely arranged themselves parallel to hydrophilic (ionophilic) pore walls, hydrophobic [OMIm⁺] ions positioned themselves as far away from surfaces as possible and minimized charge densities in pores. However, some narrow channels (the subnanometer pore components) impeded mobilities of defunctionalized ions.

Cyclic voltammograms at low sweep rates (**Fig. 4.41(c-d)**) showed inflection points during charge/discharge processes around +0.25 V (highlighted with orange square). Greater capacitance at lower potentials, followed by a dip at that voltage, and, subsequently, by an increase in capacitance at greater potentials likely signified charge saturation and partial ion defilling of the small pore component. The charge accumulation and integral capacitance of oxidized CDCs was greater for this segment of the CV. Furthermore, the defilling was more pronounced for the defunctionalized CDC and signified its more unfavorable, ionophilic pore-electrolyte interface.

Square wave static accumulation measurements further demonstrated differences in potential-dependent charge saturation of oxidized and defunctionalized CDCs. Under applied ±1.25 V (**Fig. 4.41(e)**), oxidized pores reached charge saturation earlier and demonstrated inflection points at ~200 seconds, whereas defunctionalized pores steadily accumulated charge. They accumulated 6.2 $\mu C\ cm^{-2}$, as opposed to oxidized pores' 5.4 $\mu C\ cm^{-2}$. However, $0 \rightarrow +0.25$ V charge accumulation in defunctionalized pores demonstrated an inflection point at ~70 seconds (**Fig. 4.41(f)**), and oxidized pores ended up storing 0.02 $\mu C\ cm^{-2}$ more than the defunctionalized Mo_2C-CDCs..

Surface oxidation yielded a net mixed effect on the electrochemical performance of [OMIm$^+$][TFSI$^-$] in bimodal CDCs. On the one hand, in agreement with neutron scattering and similar measurements with unimodal CDCs, surface oxidation improved the mobilities of the IL. On the other hand, this advantage did not translate into greater C_{sp} of oxidized pores. The larger pore contributions allowed many of the electrosorbed ions to move freely, and the overall porous system represented a transition condition between perfect ion confinement and a diffuse, bulk-like state. Furthermore, while oxygen groups improved the [TFSI$^-$]'s interface with pore surfaces, they repelled the alkyl chain on the [OMIm$^+$] cations, and the net effect may have further reduced the number density of ions electrosorbed on accessible surfaces.

4.2.4. Summary of Effects of Chemical Functionalization on Capacitance

Hydrogenated and oxidized surfaces of porous carbons with small pores, which matched the dimensions of ionic liquid electrolytes, improved capacitance and electrosorption dynamics. Most of the benefits stemmed from strong, favorable intermolecular interactions between functionalized surfaces and [TFSI$^-$] anions. Surface chemical groups drew ions closer to surfaces and allowed greater mobility of co-ions and counterions through resulting void spaces in pore centers. Although hydrogenated and oxidized surfaces yielded net positive effects on capacitance and dynamics, aminated surfaces reduced the capacitance and rate handling capabilities of [EMIm$^+$][TFSI$^-$]. In the cases of oxygen-rich interfaces, the favorable arrangement of anions parallel to the surfaces yielded lower areal densities of accumulated charges. As pore diameters

increased, enhanced mobility became less important for high capacitance, and defunctionalized pores outperformed oxidized CDCs.

Although neutron scattering primarily derived key ion dynamics and density comparisons based on hydrogen-rich cations, the mobilities of ions and counterions were inextricably linked. As shown in **Fig. 4.42(a-b)**, asymmetric cells (with oxidized CDCs as working electrodes and defunctionalized CDCs as counter electrodes, and vice versa) were limited by the weaker component (*i.e.*, the defunctionalized electrode).

Although different ion arrangements in oxidized and defunctionalized pores provided different pathways for ions in pores (**Fig. 4.42(c-d)**), their net effect on capacitance was contingent on: 1) pore size and 2) type of electrochemical measurement (static or dynamic applied potential). These caveats shed some insight into the wide divergence of results that had been previously reported in the literature, as previous results have interchangeably used microporous electrodes, non-porous surfaces, cyclic voltammograms, and voltage-dependent constant charge accumulation results to support their claims. The MD simulations in this study also accounted for steady-state charge accumulations and could not factor in transport limitations and net effects of mobilities on capacitance. Although surface functional groups and adatoms were expected to increase the quantum capacitance contribution to total C_{sp}, neither the experimental results nor computational analyses could account for it. Finally, although neutron scattering characterized ion densities and dynamics that exhibited good correlation with electrochemical measurements, they did not incorporate *in situ* measurements of ion mobilities during charge/discharge processes and their electrosorbed arrangements under applied potentials. Future research efforts must investigate these issues in greater detail.
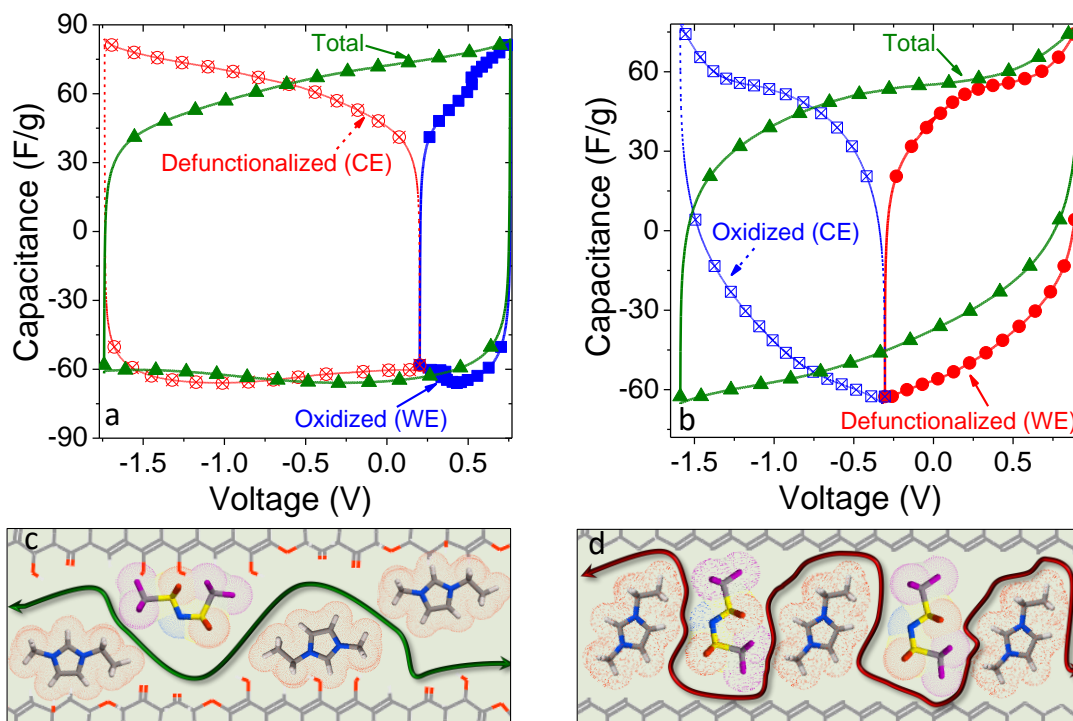
Figure 4.42. Cells with identical masses cycled at 1 mV s^{-1} in [EMIm$^+$][TFSI$^-$] with a) oxidized monomodal SiC-CDC as the working electrode and defunctionalized SiC-CDC as the counter electrode and in a b) reversed configuration. c) Improved ion pathway through oxidized pores with more ions stuck on ionophilic pore walls and lower ion densities in middle of pores. d) Greater ion densities in defunctionalized pores increase in densities in pores and complicate ion transport pathways during electrosorption.

4.3. Influence of Ion Confinement and Pore Length

The results from sections **4.1** and **4.2** demonstrated somewhat divergent conclusions regarding the influence of certain graphitic defects and functional groups on capacitance and ion dynamics. Although they all used internal surface particles with fairly similar initial structures, pore diameters slightly varied from one CDC set to another. Furthermore, similar defunctionalization and graphitization treatments yielded different rate handling changes for micron-sized particles (longer pores) and nanoparticles (pore diameter was comparable to pore length). Ion confinement was likely convoluted with standalone influence of surface defects. Similar fundamental FSI properties could translate into different capacitance and dynamics in internal and external surfaces.

To decouple the effects of pore size from surface defects, the approaches described in this section tested the same types of surface defects that had been investigated in sections **4.1** and **4.2** (graphitization and oxygen functional groups) in differently sized pores and on non-porous spherical and planar exohedral particles. The experiments also investigated CDCs with large particle diameters and near-infinite pore lengths. The operating hypotheses predicted that: 1) ionophilic pore defects would facilitate ion transport in longer pores and improve rate handling compared to defunctionalized pores; 2) defunctionalized external surfaces would benefit from greater number densities of charges on surfaces (and yield greater C_{sp}); and, 3) electrode-electrolyte interfaces would demonstrate identical voltage windows in porous and non-porous particles.

4.3.1. Oxidized Mesopores and Carbon Black

To explore the relative influence of oxygen groups on electrosorption in different pore sizes, micron-sized TiC-CDCs were annealed at 1,400 ℃ (identical material as one used in section **4.1**). This (hereafter labeled as "Initial") material was oxidized in air at 425 ℃ for 5 h ("Oxidized"), and, finally, some of the material (after oxidation) was annealed again at 1,400 ℃ ("Defunctionalized"). This condition used a stronger, longer air activation treatment that should have increased pore diameters. As a non-porous external surface particle, commercially available carbon black (CB, described in section **3.1.2**, hereafter labeled as "Initial") was annealed at 1,800 ℃ ("Defect-free") and, subsequently, oxidized at 570 ℃. Initial CB particles had no functional groups, and, while they were highly graphitized, they featured polycrystallinity, grain boundaries, and short-term sp^2 bonding. Annealing was expected to restructure them and reduce graphitic

defect concentration without reconstructing interparticle porosity or surface chemical composition.

4.3.1.1. Structural and Chemical Transformations of CDC and Carbon Black

Fig. 4.43 shows the porosity changes and oxidation-induced changes in surface chemistry and hydrophobicity. Air oxidation of CDCs (**Fig. 4.43(a)**) activated the microporosity of nanostructured CDCs, reduced the prevalence of micropores, and enhanced the growth of mesopores. The procedure increased the SSA of defunctionalized CDCs by over 600 m^2 g^{-1}. Since the surfaces of oxidized CDCs were covered by chemically unstable oxygen groups, secondary annealing simply removed them and did not restructure the pores. Annealing did not modify the SSA or porosity of CB particles, but oxidation lightly activated the particles and increased their surface area to 150 m^2 g^{-1}.
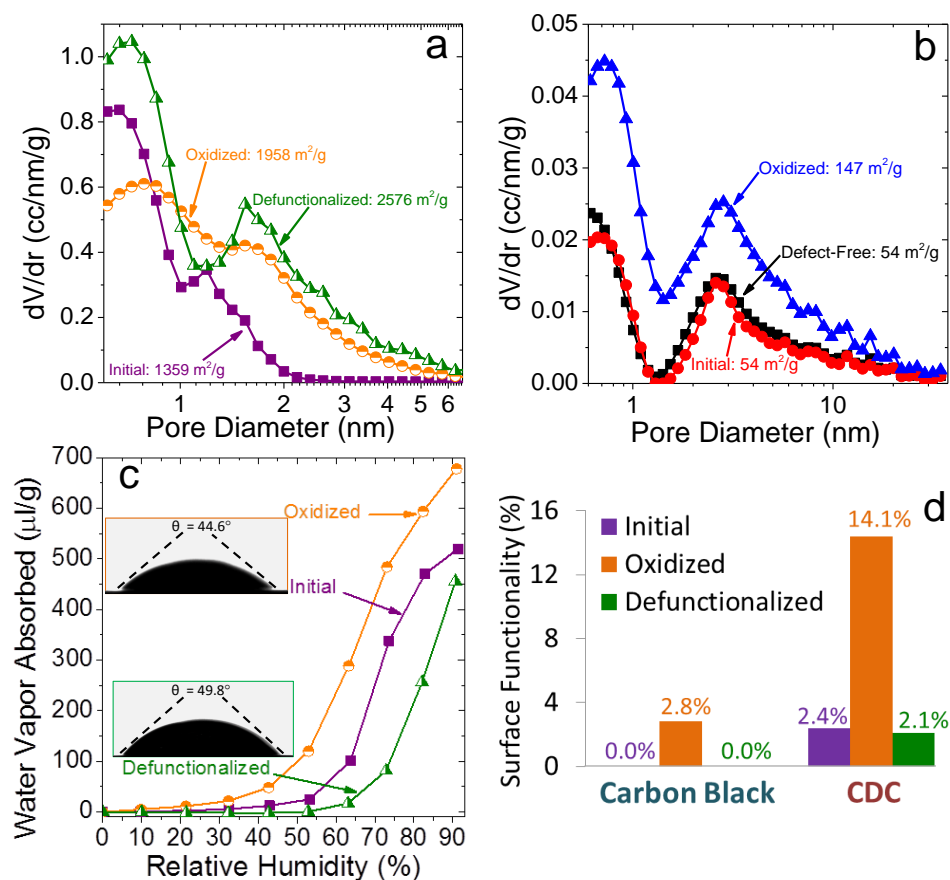
Figure 4.43. Pore size distributions of (a) TiC-CDC microparticles after 1,400 °C vacuum annealing (Initial), air oxidation of the annealed CDC at 425 °C (oxidized), and secondary 1,400 °C annealing of the oxidized material (defunctionalized). (b) Carbon black particles in their initial state, after 1800 °C annealing (defect-free), and after 570 °C air oxidation (oxidized). c) Dynamic H$_2$O vapor sorption on CDCs after different treatments. Insets show contact angle measurements of IL droplets on defunctionalized (green) and oxidized (orange) CDC films. d) Inert TGA-derived relative functional group compositions for CDC and CB particles.

Dynamic H$_2$O sorption (**Fig. 4.43(c)**) showed the significant influence of defunctionalized surface chemistry of annealed CDCs on hydrophobicity. Although defunctionalized CDCs exhibited the largest SSA and the greatest mesopores prevalence, oxidized surfaces most readily adsorbed water. As expected, functional group content (Fig. **4.43(d)**) was highest in oxidized CDCs and CBs.

Annealing-induced graphitization changes in CDC and CB particles are shown in **Fig. 4.44**. TEM images of CDC materials showed graphitic features and layered ribbons on

surfaces. Secondary annealing increased graphitization (more prominent G band and 2D band) and suggested that defunctionalized CDCs exhibited the fewest graphitic defects. Annealing of CBs increased size of ordered domains on particle surfaces, as shown by XRD and graphitic ribbons on edges of particles.
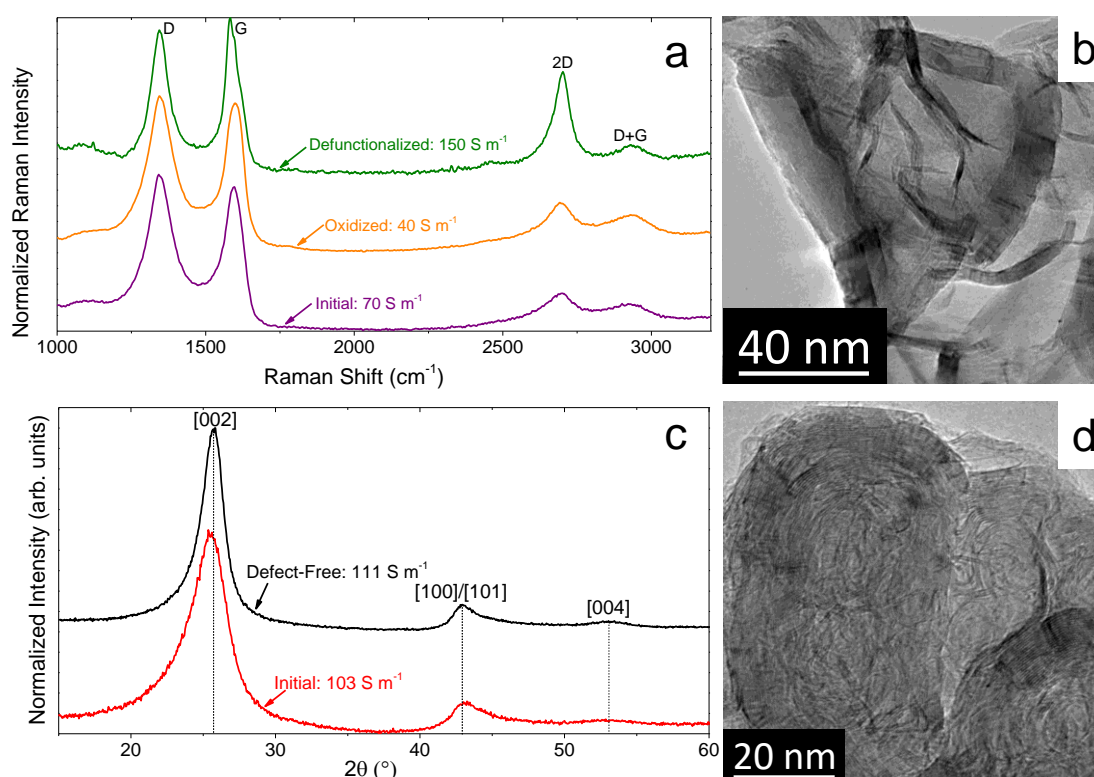
Figure 4.44. a) Raman spectroscopy analysis of TiC-CDCs with different surface compositions. b) TEM image of CDC after secondary annealing. c) XRD analysis of CB before and after annealing, with the annealed particle shown in d). Graphs all include 4-point probe measurements of electrical conductivities of electrode films.

4.3.1.2. Electrochemical Cycling of Functionalized CDCs and Carbon Black

CDC and CB electrode films with different surface defects were cycled with 1.0 M H_2SO_4 *(aq.)* and [EMIM$^+$][TFSI$^-$] IL at room temperatures. To minimize redox contributions, the electrochemical potential for aqueous electrolyte used an experimentally derived narrow range with no redox peaks: -0.30 V $\leftrightarrow$ 0.00 V for CB and 0.00 V $\leftrightarrow$ +0.60 V for CDCs. Cyclic voltammograms for intermediate sweep rates and

corresponding Nyquist plots are shown in **Fig. 4.45**. Oxidized CBs certainly benefitted the most from surface chemistry groups in an aqueous electrolyte and demonstrated significantly greater capacitances than their bare carbon counterparts. This advantage was not as apparent for porous CDCs after oxidation. However, after the oxygen groups were removed, capacitance of defunctionalized CDCs significantly decreased. The ions did not experience a significant amount of resistance in their effort to enter larger CDC pores, and the resulting drop in capacitance is likely attributed to a lower density of electrosorbed ions on surfaces of oxygen-free CDCs.
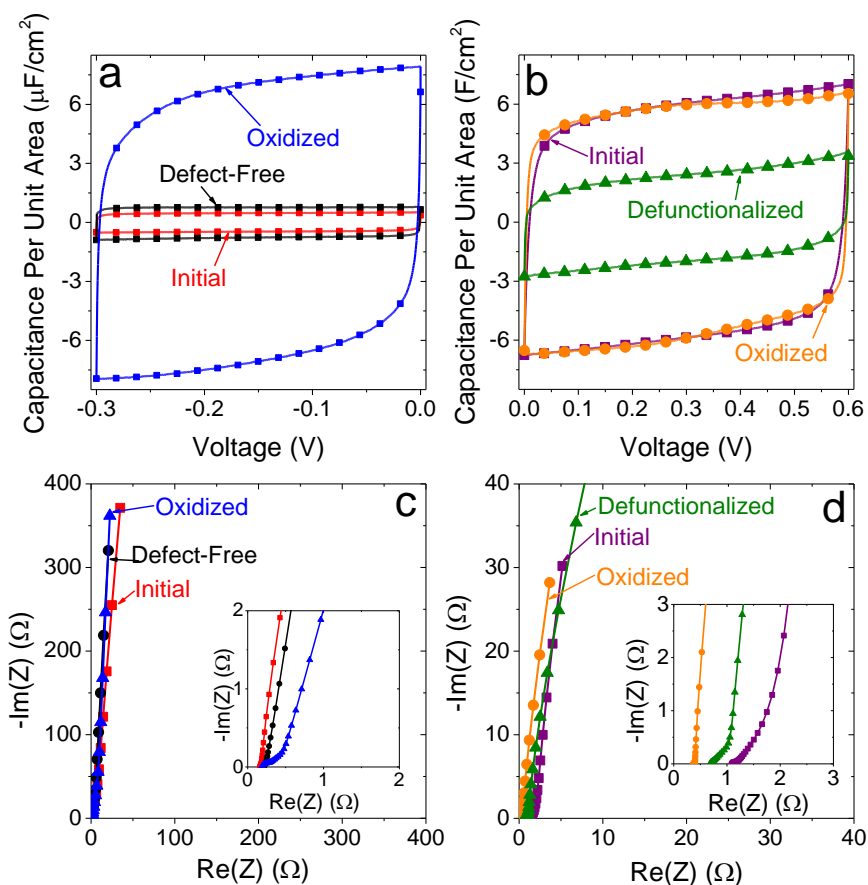
Figure 4.45. a) Cycling of CB in sulfuric acid at 100 mV s^{-1} and b) CDC in sulfuric acid at 10 mV s^{-1}. Corresponding Nyquist plots for CB is shown in c) and for CDC in d).

The materials showed distinctly different electrosorption behaviors and demonstrated different influences of oxygen and graphitic defects in porous and non-porous carbons in IL electrolyte (**Fig. 4.46**). CBs with fewer graphitic defects showcased greater capacitance. It was likely correlated with improved conductivity and resembled prior findings for onion-like carbons.[102] Oxidation substantially improved gravimetric C_{sp} but did not significantly alter the SSA-normalized capacitance, which differed from the behavior of this electrode material in aqueous electrolytes.
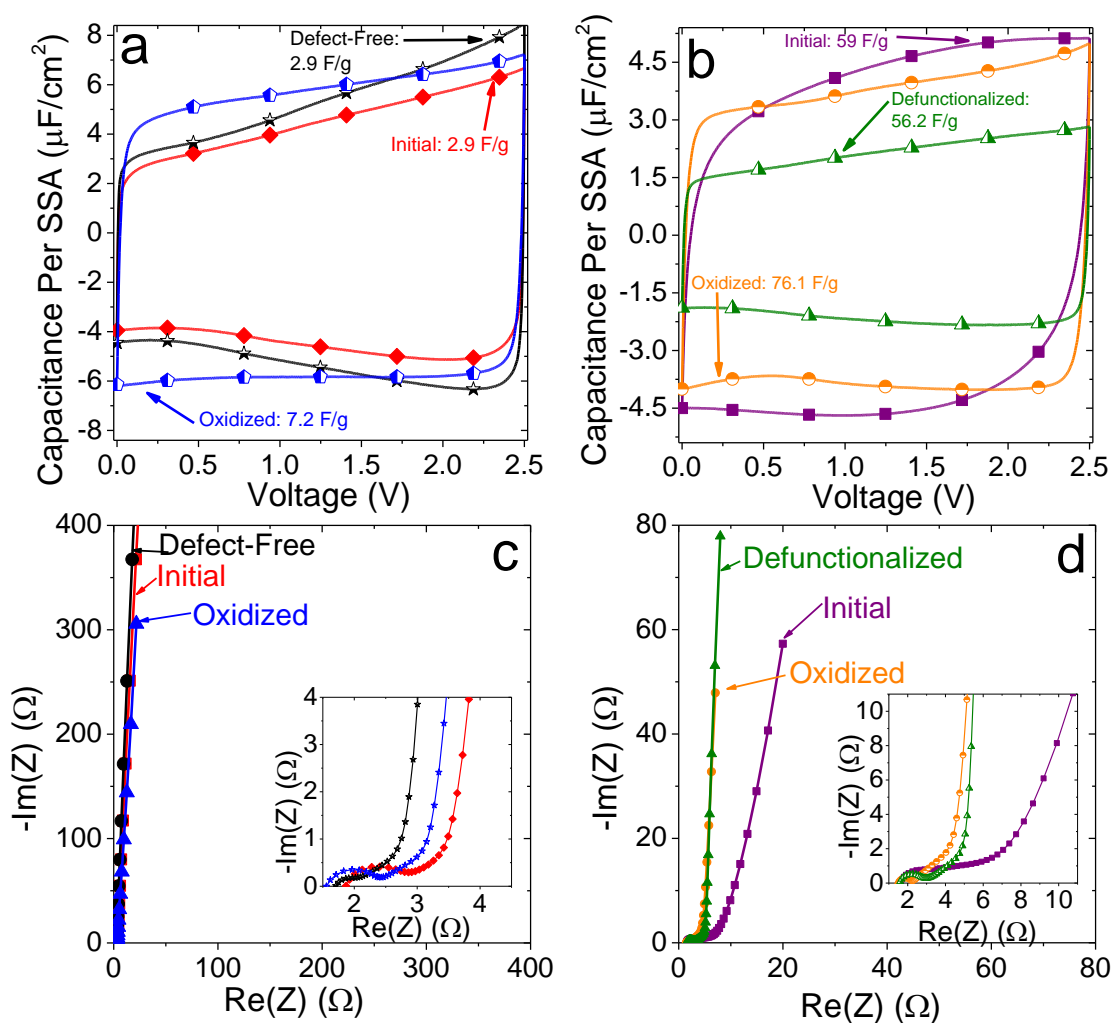
Figure 4.46. a) Cycling of CB in [EMIm$^+$][TFSI$^-$] at 100 mV s^{-1} and b) CDC in the IL at 10 mV s^{-1}. Corresponding Nyquist plots for CB is shown in c) and for CDC in d).

The CDC that had undergone secondary annealing (most defunctionalized and graphitized surface) exhibited the lowest C_{sp}. Since it exhibited the same surface chemistry as the initial CDC, but was more graphitized, fewer graphitic defects likely depressed its charge storage capability. On the other hand, ionic impedance (derived from Nyquist plots) was substantially lower for oxidized and defunctionalized CDCs, which featured larger pores than the initial CDC particles. With substantially large pores, oxidized CDCs did not demonstrate significant increases in SSA-normalized capacitance over their hydrophobic porous counterparts. This result paralleled the findings for IL electrosorption in bimodal Mo_2C-CDC (section **4.2.3**). The defect-free materials (both CDC and CBs) exhibited more pronounced butterfly shapes and hinted at more prevalent voltage-dependent capacitance characteristic, which had been expected for more conductive electrode materials.

The presence of defects was more pronounced for non-porous materials in aqueous electrolytes. Although C_{sp} was substantially enhanced in H_2SO_4 for oxidized CB electrodes, it decayed very rapidly at high charge/discharge rates (**Fig. 4.47(a)**). The corresponding EIS Nyquist plots (**Fig.46(c)**) confirmed rapid ion electrosorption from the bulk electrolyte onto defunctionalized, bare surfaces of non-porous carbons. Since both the $[H^+][HSO_4^-]$ ions and the H_2O solvent were very hydrophilic, they were likely tightly drawn to ionophilic oxidized CB surfaces and impeded high-rate ion exchange processes.
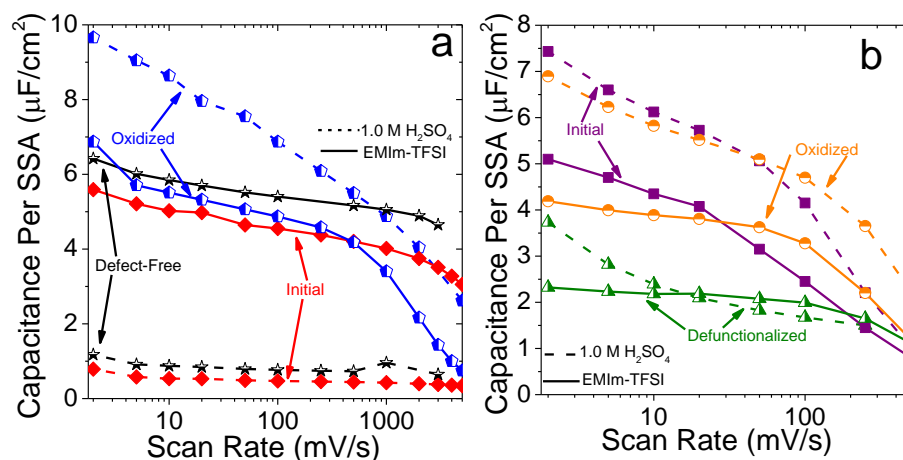
Figure 4.47. Rate handling comparisons for a) non-porous CBs and b) porous CDCs in aqueous electrolyte (dashed lines) and ionic liquid (solid lines).

CDCs showed similar capacitance decay for defunctionalized, graphitized surfaces, but the oxygen-induced enhancement of capacitance in sulfuric acid was not nearly as evident when ions were confined in narrow pores (**Fig. 4.47(b)**). Oxidized CDCs demonstrated the best rate handling abilities of both $H_2SO_4(aq.)$ and $[EMIm^+][TFSI^-]$ at high sweep rates (50 mV s^{-1} < dV dt^{-1} < 1 V s^{-1}). Since oxygen-rich pores yielded the most favorable interfaces for both electrolytes, ions were most mobile in oxidized CDCs. Although defunctionalized CDCs demonstrated better capacitance retention than initial CDCs, a combination of fewer graphitic defects on surface of defunctionalized CDC's pore walls and its larger porosity likely contributed this effect.

RS coefficient measurements did not demonstrate significant influences of surface defects on diffusion limitations of $[EMIm^+][TFSI^-]$ in non-porous CB electrodes (**Table 4.8**). However, in porous CDCs, the system with the smallest pore size (Initial CDC) was most-diffusion limited, regardless of its surface defect composition. Defunctionalized pores facilitated greater ion diffusivity than its oxidized counterpart, but they benefited from significantly larger pore volumes.

Table 4.8. RS Coefficients derived from cyclic voltammetry measurements of non-porous CBs and porous CDCs in [EMIm$^+$][TFSI$^-$] electrolyte.

External Surfaces: CB		Internal Surfaces: CDC	
Electrode Surface	Randles-Sevcik Coefficient	Pore Surface	Randles-Sevcik Coefficient
Initial	0.98	Initial	0.80
Defect-Free	0.96	Oxidized	0.89
Oxidized	0.96	Defunctionalized	0.93

4.3.1.3. Voltage Window of Porous and Non-porous Oxidized Carbons

As discussed in section **1.6**, oxygen groups on carbon surfaces were more prone to irreversible surface breakdown processes, undesired side reactions with electrolytes, gas evolution, etc. This drawback has typically shaped most electrode synthesis processes to "burn off" these unstable groups from commercial carbon powders.[248] Oxidation studies in this dissertation have, so far, avoided this issue and have relied on electrochemically stable electrolytes and safe operating voltage windows. However, this property must be investigated for porous and non-porous oxidized and defunctionalized pores.

Defect-free and oxidized CBs, as well as oxidized and defunctionalized CDCs, were tested in 2.50 V, 2.75 V, 3.00 V, and 3.25 V windows using static and dynamic techniques. The results are shown in **Fig. 4.48**. As expected, CDCs with defunctionalized pores exhibited lower parasitic currents (**Fig. 4.48(b)**) and greater coulombic efficiencies than oxidized pores at higher potentials. However, non-porous CBs exhibited a directly opposite behavior (**Fig. 4.48(a)**): oxidized surfaces demonstrated greater electrochemical stabilities than bare, defect-free carbon structures.
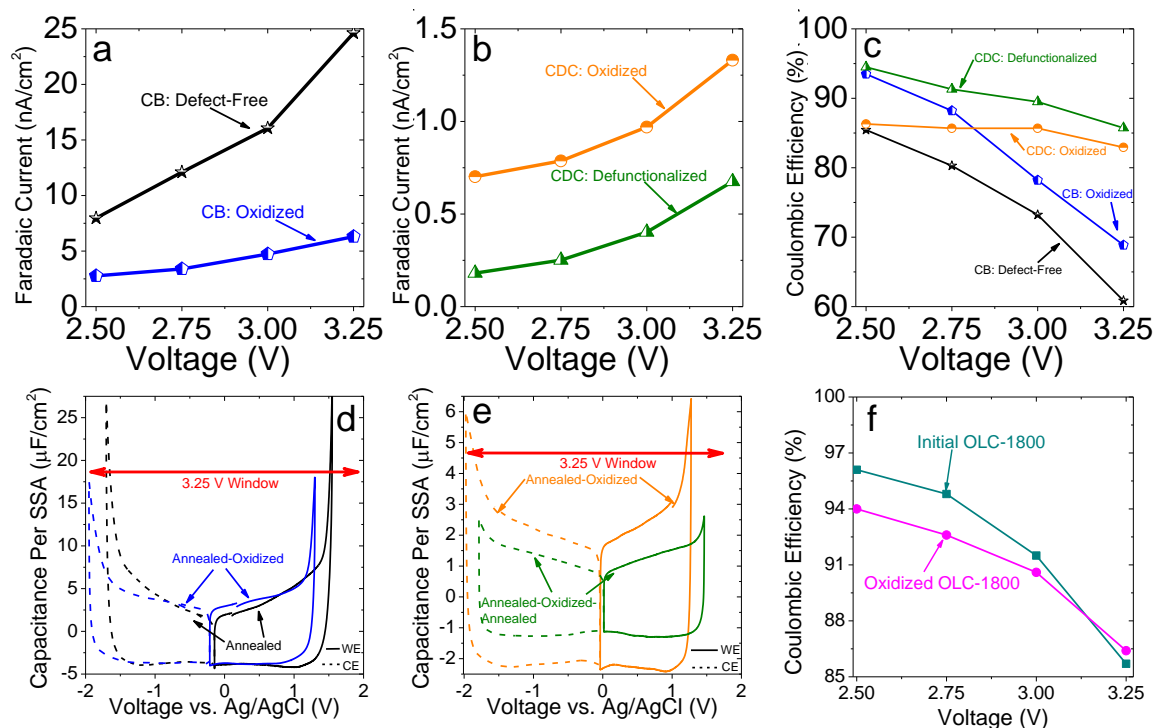
Fig. 4.48. Residual, steady-state (parasitic current) of defunctionalized and oxidized a) non-porous CB and b) porous CDC particles, derived from square wave amperommetry. c) First-cycle coulombic efficiencies derived from CVs in the 0 ↔ 2.50 V and 0 ↔ 3.25 V voltage windows. Three-electrode (symmetrical) 2 mV s^{-1} CVs in the 3.25 V window are shown for d) CBs and e) CDCs. f) Coulombic efficiency comparison for defunctionalized and oxidized carbon onions in the same extended voltage windows.

Although neither defunctionalized nor oxidized electrodes – porous or non-porous – could demonstrate sufficient electrochemical stability near the expected 4.0 V operating limit for [EMIm$^+$][TFSI$^-$], oxygen-rich electrode-electrolyte interfaces showed different stability limits in internal and external surface systems. To test the validity of these results, non-porous onion-like carbons (described in section **3.1.2**) were subjected to similar chemical functionalization with oxygen. Cyclic voltammograms showed similar Q_{eff} trends (shown in **Fig. 4.48(f)**): the oxidized non-porous materials exhibited less electrochemical breakdown at 3.25 V. This approach, which had been previously suggested for Li-ion carbon additives to cathodes,[249] underscored the advantage of

oxygen groups, which acted as protection layers that prevented continuous breakdown reactions, during electrochemical cycling in the positive voltage range.

The convolution of surface chemistry and pore size on electrochemical stability could be attributed to different breakdown mechanisms, which were likely to proceed at different relative rates. Ion confinement influenced several key properties: 1) net sum of chemical forces (from pore walls, functional groups, and nearby ions) that acted on the ions; 2) the molecules' steric configurations in pores; 3) densities of ions per units of electrode area or pore volume; and 4) access to the bulk electrolyte.

4.3.2. Surface Defects on Planar Electrode Surfaces

External surface CBs compared the relative influences of graphitic defects and surface functional groups on capacitance in electrodes with no ion confinement. Although CB particles were not perfectly spherical, they exhibited slight, heterogeneous curvatures. Planar graphene electrodes more properly matched computational simulations with experimentally-derived influence of functional groups on external surface capacitance. Non-porous graphene nanoplatelets (GNPs), which are described in section **3.1.2**) acted as appropriate model systems for this approach. The initial material, which resembled multilayer (10-20 sheets) graphene flakes, included a noticeable number of oxygen and sulfur groups on reactive surface sites. The flakes were annealed at 1,800 ℃ under a high vacuum to yield defunctionalized GNPs (0.7 at. % oxygen). It was, subsequently, oxidized in dry air at 475 ℃ and developed oxygen-rich surfaces (3.7 at. % oxygen). The pore size distributions, morphologies, and PDF-derived structure of nanoplatelets are

shown in **Fig. 4.49**. Aside from chemical functionalization, the air oxidation did not restructure the carbon ordering or surface morphologies of GNPs.
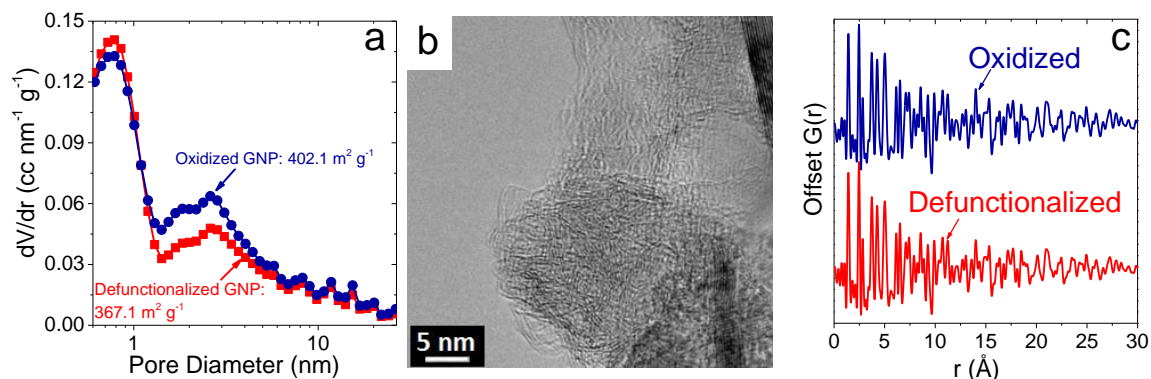
Figure 4.49. a) PSD for defunctionalized and oxidized non-porous GNPs that featured external, planar surfaces. b) TEM image of defunctionalized GNPs. c) X-ray PDF analysis of the graphitized carbon structure of defunctionalized and oxidized GNPs.

4.3.2.1. Electrochemical Behavior of Planar Functionalized Electrodes

Electrochemical tests of [EMIm$^+$][TFSI$^-$] with non-porous defunctionalized and oxidized GNPs decoupled the influence of oxygen groups from ion confinement. As shown in **Fig. 4.50**, oxidized GNP surfaces exhibited lower performance during both dynamic and static electrochemical cycling conditions. Defunctionalized GNP electrodes demonstrated greater capacitance and superior rate handing ability (over the entire 0.5 – 1,000 mV s^{-1}) than its oxidized counterparts. Contrary to similarly functionalized porous CDCs (section **4.2.2**), the CV sweeps (**Fig. 4.50(a)**) for planar carbons did not show any ion sieving for either material. EIS analysis (**Fig. 4.50(c)**) demonstrated similar ionic impedance during electrosorption onto defunctionalized and oxidized GNPs.
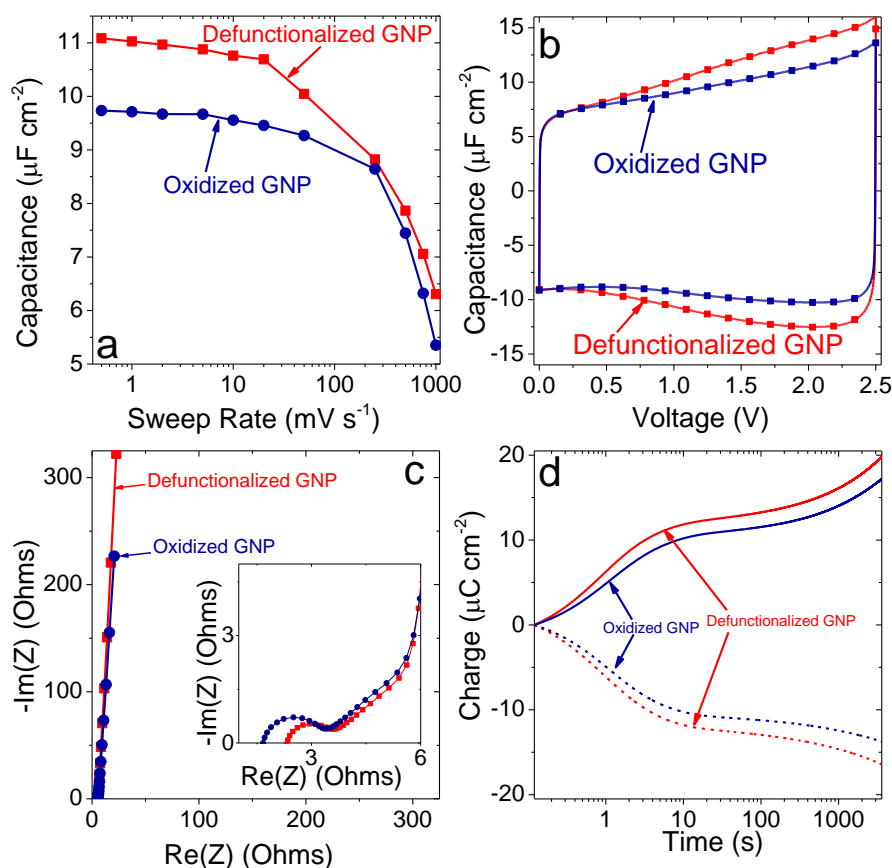
Figure 4.50. a) Rate handling comparison of performance of non-porous oxidized and defunctionalized GNPs in the $0.5 - 1000$ mV s^{-1} sweep range. b) Cyclic voltammetry plot showing differences in of [EMIm$^+$][TFSI$^-$] capacitance for defunctionalized vs. oxidized GNPs at a 5 mV/s sweep rate. c) Nyquist plot that compared electrochemical impedance of defunctionalized and oxidized GNPs. d) Charge accumulation vs. time during a square wave amperommetry $0 \rightarrow \pm 1.25$ V step.

Static experiments used CA to charge electrodes to specific voltages. Voltage-dependent C_{sp} densities for bare, defect-free graphene nanoplatelets exceeded those of their oxygen-containing counterparts. Furthermore, unlike CDCs, charge accumulated at the same rate for both electrode surface chemistries (**Fig. 4.50(d)**).

In addition to [EMIm$^+$][TFSI$^-$], oxidized and defunctionalized GNPs were tested in 1-ethyl-3-methyl tetrafluoroborate ([EMIm$^+$][BF$_4^-$]) and 1-methyl-1-propylpyrrolidinium bis(trifluoromethylsulfonyl)imide ([MPyr$^+$][TFSI$^-$]). The cells were tested in three-electrode asymmetric configurations. To avoid pseudocapacitive side reactions, which

have been occasionally observed in [EMIm$^+$][BF4$^-$]-filled cells, electrodes were cycled in the 0.0 ↔ -1.25 V window. The results are shown in **Fig. 4.51.** In both cases, the defunctionalized electrodes outperformed the oxidized nanoplatelets. However, the difference was much more pronounced for [EMIm$^+$][BF$_4^-$]. Ion mobility more strongly depended on the chemical composition of the non-porous electrode surfaces, and [EMIm$^+$][BF$_4^-$] ions electrosorbed much more quickly on defect-free GNPs.
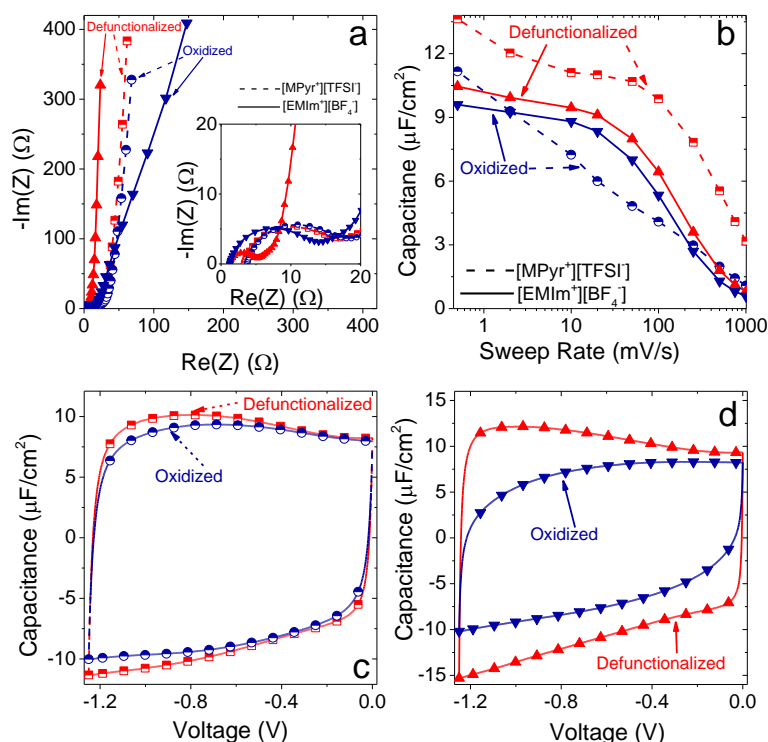
Figure 4.51. a) Nyquist impedance plot for [MPyr$^+$][TFSI$^-$] and [EMIm$^+$][BF$_4^-$] electrolytes with defunctionalized and oxidized GNPs. b) Rate handling comparison for the 2 electrolytes in the 0.0 ↔ 1.25 V window. c) [MPyr$^+$][TFSI$^-$] CVs at 10 mV s^{-1} and d) [EMIm$^+$][BF$_4^-$] CVs at 10 mV s^{-1}.

4.3.2.2. MD Simulations of Electrolytes on Functionalized Planar Electrodes

ReaxFF computational analysis used the same approach as in section **4.2.2.4** to simulate chemical functionalization on planar graphene surfaces. The simulation integrated gas sorption isotherms (from intrinsic GNP electrodes) and experimentally-

derived square-wave amperommetry charge accumulation results into a CMD-derived calculation of number densities and differential capacitance at different potentials. The results of the computational approach are shown in **Fig. 4.52**. In agreement with experimental results, calculations demonstrated higher capacitance for defunctionalized surfaces (**Fig. 4.52(a)**). The bell-shaped C_{sp} curves resembled simulations of [EMIm$^+$][BF$_4^-$] and [BMIm$^+$][PF$_6^-$] on planar graphite [250] and in nanopores.[251]
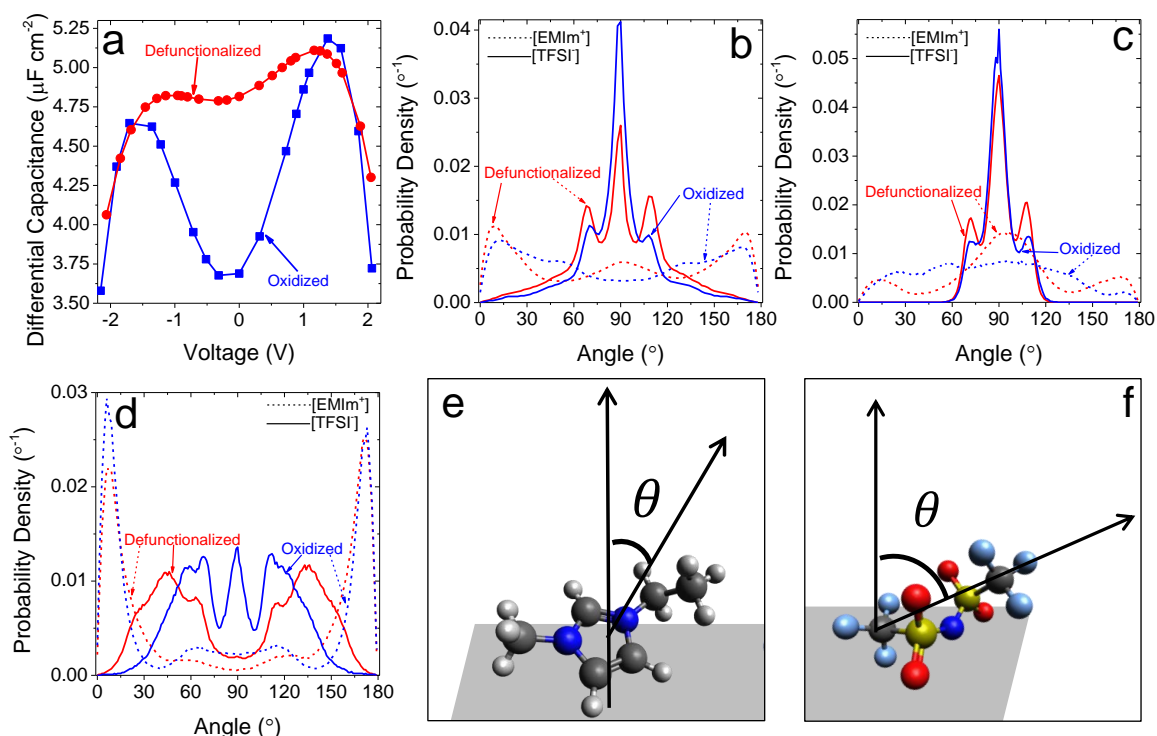
Figure 4.52. a) MD simulation of differential capacitance as a function of potential for defunctionalized/oxidized graphene. Integral C_{sp} = 4.89 µF cm^{-2} for defunctionalized graphene and C_{sp} = 4.31 µF cm^{-2} for oxidized surfaces. Simulations of orientation angles of cations and anions on planar graphene under b) 0.00 V, c) +1.00 V, and d) -1.00 V. Orientation angles of e) [EMIm$^+$] (normal vector of the electrode and the normal vector of the imidazolium ring) and f) [TFSI$^-$] (angle between the normal vector of the electrode and the vector connecting the 2 carbon atoms).

Under neutral conditions (**Fig. 4.52(b)**), the anions adopted a more ordered distribution and oriented themselves in parallel to the oxidized surfaces, whereas the cations were more randomly scattered. Under +1.0 V (**Fig. 4.52(c)**), the tail-to-tail

orientation of [TFSI⁻] demonstrated pronounced 90º orientation angles (parallel to the surface). Since the anions pushed [EMIm⁺] away from the electrode-electrolyte interface, ion arrangement became more disperse. Under applied -1.0 V (**Fig. 4.52(d)**), [TFSI⁻] drew much closer to oxidized surfaces; however, the 45º and 135º orientations of the anions on defunctionalized surfaces yielded greater charge densities. Experimental results did not demonstrate such hysteresis between positive and negative potential ranges.

Although this simulation recreated only –OH terminated surfaces, additional simulations also accounted for hydrogenated and epoxy-functionalized surfaces with [EMIm⁺][BF₄⁻] electrolyte. The results are shown in **Fig. 4.53**. Number density calculations underscored superior capacitance of defunctionalized graphene surfaces compared to all other surface chemistry configurations. The relative advantage of epoxy groups over –OH groups matched recently reported simulations for [BMIm⁺][OTf⁻].[138] The model suggested a relative advantage of hydrogenated surfaces over all other functionalities. MD-derived C_{sp} electrosorption depended on unique surface interactions of cations and anions with differently functionalized electrodes: [TFSI⁺] had the largest interaction energy, and [BF₄⁻] had the lowest interaction energy (**Fig 4.53(b)**.
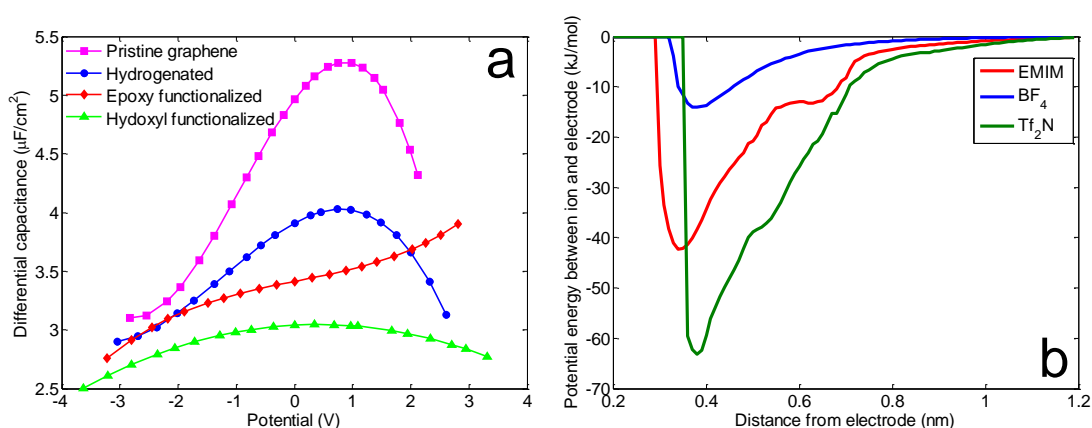
Figure 4.53. a) Differential capacitance for [EMIm⁺][BF₄⁻] on differently functionalized planar electrodes. b) Interaction energies for IL cations and anions with graphene.

The simulations demonstrated similar capacitance and ion orientation trends for porous (section **4.2.2.4**) and non-porous surfaces with different surface chemistries. Since the model could only account for equilibrium charge accumulation and favorable ion orientation under steady-state conditions, differences in interface-dependent ion mobilities did not play a significant role. In the case of the non-porous GNP electrode system, the experimental conditions more closely matched the model. Oxygenated surfaces could not enhance mobilities of ions in bulk-like spaces around flat electrodes. Subsequently, while oxygen groups lowered areal ion densities on electrodes, they decreased capacitance in static and dynamic charging processes. Since the sizes and van der Waals FSI intermolecular interactions of [EMIm$^+$], [MPyr$^+$], [TFSI$^-$], and [BF$_4$$^-$] were all unique, each ion system exhibited different electrosorption densities. Furthermore, although the model could not simulate ion mobilities, strong ion-surface interactions and dense ion layers at interfaces likely influenced ion impedance and rate handling properties. Finally, although the MD simulation did not incorporate quantum capacitance contributions, examined GNP and CB electrode particle model systems were sufficiently thick (more than 4 stacked layers) to negate noticeable effects of this parameter.

4.3.3. Capacitance and Electrochemical Stability in Long Pores

Electrochemical tests on non-porous materials demonstrated that, although influences of surface chemical groups and graphitic defects were fundamentally similar to those of internal surfaces, their practical effects on capacitance drastically changed when ion confinement disappeared. Furthermore, differences in rate handling abilities and charging dynamics between similarly functionalized nanoporous microparticles and nanoparticles (section **4.1**) underscored the additional significance of the pore length (particle diameter)

parameter. To obtain a more comprehensive understanding of the influence of surface defects on confined ions, very large CDCs (75 μm diameter and 250 μm diameter) with finely tuned porosities were synthesized from TiC at 800 ℃. Vacuum annealing at 1,400 ℃ (for 11 hours) of the 75 μm diameter sized CDC particles defunctionalized and graphitized them, and vacuum annealing at 800 ℃ (for 48 hours) of the 250 μm-sized CDCs yielded a defunctionalized version of them. Since the pore lengths in these particles were significantly larger than the pore diameters, the external surface areas of these electrodes (fraction of total area in direct contact with the bulk electrolyte) could be discounted as negligible. Subsequently, all ions could be assumed to be confined in pores. This approach directly contrasted with the external surface GNPs and CBs.

4.3.3.1. Structure and Surface Chemistry of Long Pores

The starting pore structure of 75 μm and 250 μm diameter CDC particles resembled the typical PSDs of TiC-CDC microparticles and nanoparticles that had been synthesized at 800 ℃ before. Structural characterization of the coarse-grained powders is shown in **Fig. 4.54**. SANS data (**Fig. 4.54(d)**) showed similar Q vs. I(Q) trends in the "flat" Guinier region ($0.15 \text{ Å}^{-1} < Q < 0.5 \text{ Å}^{-1}$) for CDCs synthesized at 800 ℃ from differently sized carbide precursors and reinforced the similarities in pore size distributions and their predominant dependence on Cl_2 treatment temperature.[128,176] The Q vs. I(Q) slopes diverged in the Porod region ($0.01 \text{ Å}^{-1} < Q < 0.03 \text{Å}^{-1}$) and suggested differences in scattering from surface and mass fractals. Structural transformations, which were induced by high-temperature (1,400 ℃) annealing of 75 μm-sized particles, paralleled those of micropowders and nanopowders (section **4.1.1**).
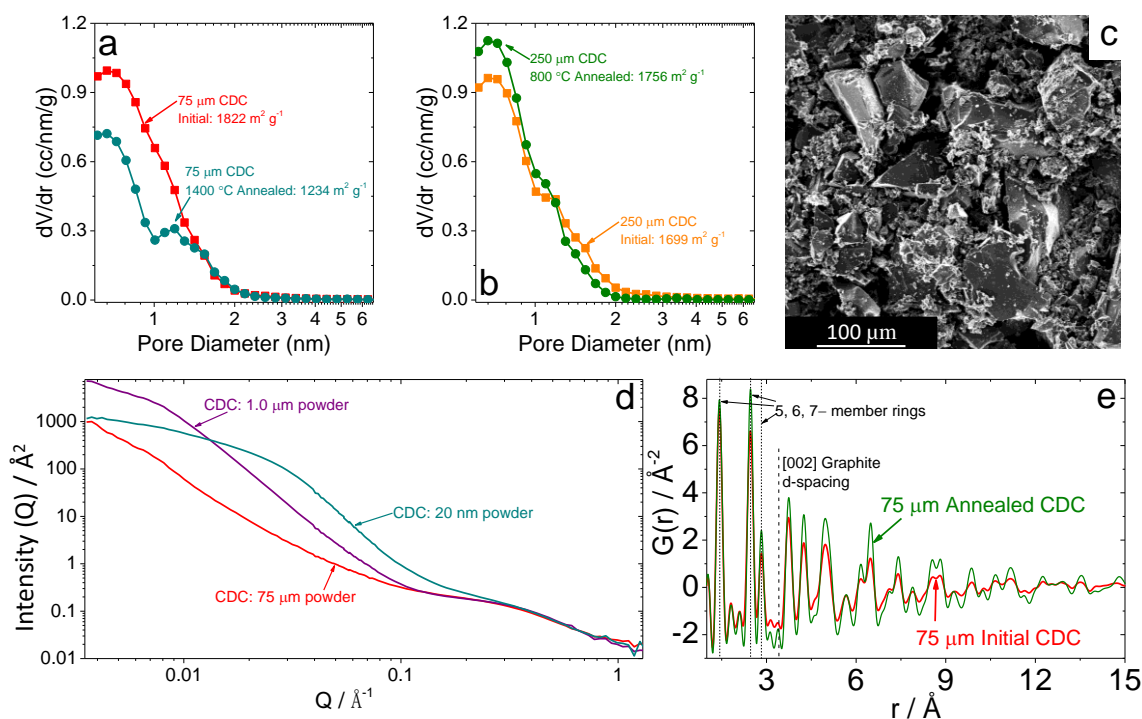
Figure 4.54. PSDs for a) 75 µm-diameter CDCs before and after 1,400 ºC annealing, and for b) 250 µm-diameter CDCs before and after 800 ºC annealing. c) SEM image of 250 µm-diameter CDCs. d) Small-angle neutron scattering (SANS) comparison of coarse-grained CDC, micron-sized particles, and nanopowders synthesized from TiC at 800 ºC. e) X-ray PDF analysis of 75 µm diameter CDCs before and after 1,400 ºC annealing.

Coarse-grained CDCs exhibited robust and heterogeneous surface chemistries in their initial states. **Table 4.9** summarizes EDS- and TGA-derived surface chemistry compositions. As shown by the porosity analysis in **Fig. 4.54(a)**, 800 ºC annealing process removed all functional groups from the 250 µm-size CDC without graphitizing the structure. The 1,400 ºC annealing process yielded defunctionalized and graphitized CDCs with 75 µm long pores. The initial CDC compositions did not exhibit singular predominant surface defects on their pore walls, and the post-Cl_2 H_2 anneal of each CDC at 600 ºC likely introduced significant amounts of hydrogen functionalities onto CDC surfaces.

Table 4.9. Elemental composition of coarse-grained CDCs before and after annealing.

Element	75 µm diameter CDC		250 µm diameter CDC
	Initial	1,400 ºC annealed	Initial
Carbon (at. %)	93.6	97.7	98.5
Nitrogen (at. %)	1.9	0.0	0.0
Oxygen (at. %)	3.9	2.2	2.0
Sulfur (at. %)	0.0	0.00	1.1
Chlorine (at. %)	0.5	0.02	0.8
Iron (at. %)	0.5	0.03	0.3
TGA-derived functional group content	3.64%	1.45%	4.66%

4.3.3.2. Influence of Surface Defects on Capacitance of Long Pores

Initial and annealed 75 µm diameter sized CDCs were cycled in 1.5 M [NEt$_4^+$][BF$_4^-$] acetonitrile-solvated organic electrolyte and [EMIm$^+$][TFSI$^-$] neat RTIL. The results are shown in **Fig. 4.55**. Despite a large decrease in film resistivity (5.27 Ω cm), annealed CDC showed 38% lower capacitance in 1.5 M [NEt$_4^+$][BF$_4^-$]/CH$_3$CN and 55% lower capacitance in [EMIm$^+$][TFSI$^-$]. Although the cyclic rectangular nature of CVs in organic electrolyte was unaffected for coarse-grained CDC after annealing, the defect-free porous materials show greater evidence of ion sieving and resistance (corroborated by the Nyquist plot in **4.55(c)**) for the RTIL electrolyte.
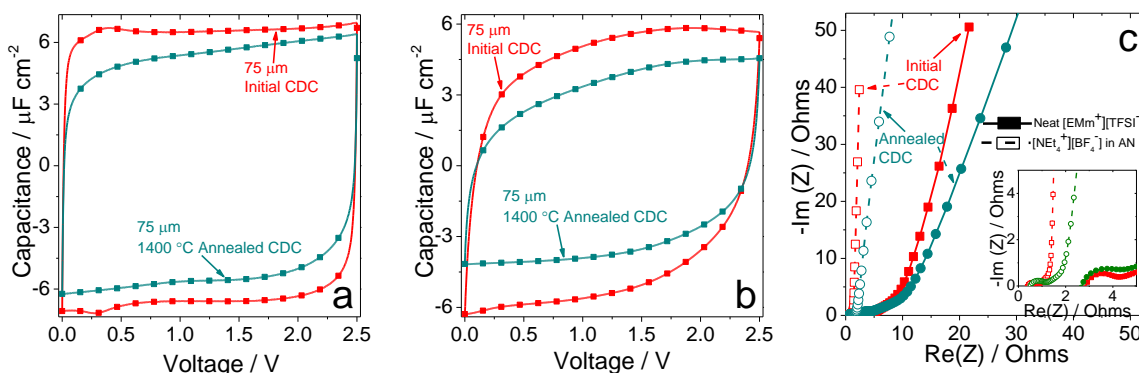
Figure 4.55. a) CVs measured at 20 mV s^{-1} in a) 1.5 M [NEt$_4^+$][BF$_4^-$]/acetonitrile and b) neat [EMIm$^+$][TFSI$^-$] electrolytes compared electrochemical performance of initial 75 µm diameter CDC and after vacuum annealing. c) Nyquist plots derived from impedance spectroscopy to compare the initial and annealed CDCs in the same two electrolytes.

The observed behavior more closely resembles similar comparisons for micron-sized TiC-CDCs than that of SiC-CDC nanoparticles (section **4.1.3-4.1.4**). Subsequently, surface defect removal impeded ion mobility and reduced capacitance, and this effect became more amplified in longer pore lengths. It was even more pronounced for the 250-µm diameter sized CDCs, where chemical functionalization (and no re-graphitization) alone significantly hurt the capacitance of annealed CDCs in [EMIm$^+$][TFSI$^-$] (**Fig. 4.56**). In particular, although initial CDCs allowed relatively acceptable mobilities of ions through surface pores enriched with functional groups, defunctionalized ion interfaces were highly resistive to ion dynamics during charging and discharging processes.
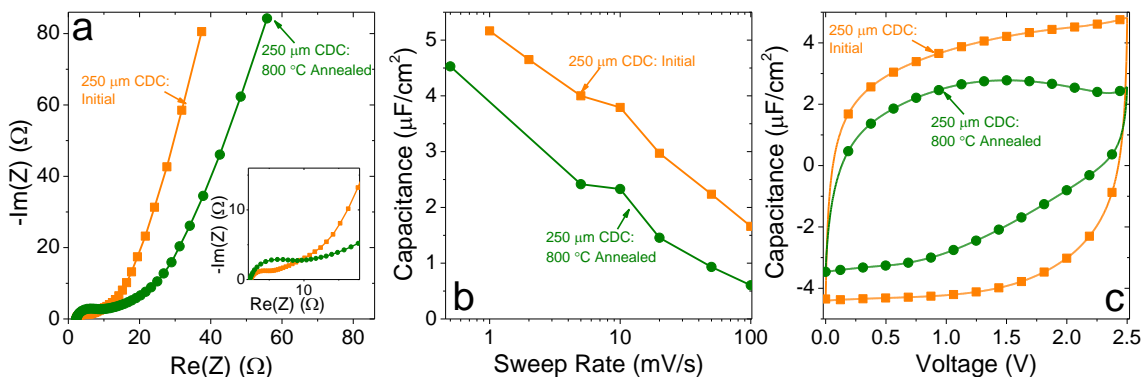
Figure 4.56. a) Nyquist impedance, b) Rate handling comparison, and c) 5 mV s^{-1} comparison of 250 µm diameter CDCs before and after 800 ºC vacuum annealing in neat [EMIm$^+$][TFSI$^-$] electrolyte.

4.3.3.3. Electrochemical Stability and Voltage Window of Coarse-Grained CDCs

The 75 μm diameter particles were also cycled in voltage windows that exceeded the traditional $0 \leftrightarrow 2.5$ V limit to determine the influence of ion confinement on electrochemical stability. CV sweeps at 2 mV s^{-1} in $0 \leftrightarrow 3.5$ V voltage windows (0.1 V step increments) evaluated coulombic efficiency and irreversible reactions. Square wave CA measurements identified residual, parasitic currents at each potential step.

Cyclic voltammograms, coulombic efficiencies, and parasitic current analyses are shown in **Fig. 4.57**. Even though the initial CDC surface included numerous chemical functionalities, the material maintained good electrochemical stability up to 3.1 V and demonstrated minimal potential-induced breakdown throughout the entire tested voltage range. The leakage current of the laboratory-assembled pouch cell at 3.3 V was lower than the specification listed for a commercial supercapacitor (rated to 2.7 V and 350 F).[252] Cyclic voltammograms did not show distinct inflection points at high potentials during charge profiles and, subsequently, allowed reversible ion electrosorption in an extended voltage window. After 10,000 cycles in a $0 \leftrightarrow +2.5$ V voltage window, the initial CDC retained most of its capacitance and only lost 6.7% of its initial C_{sp}.
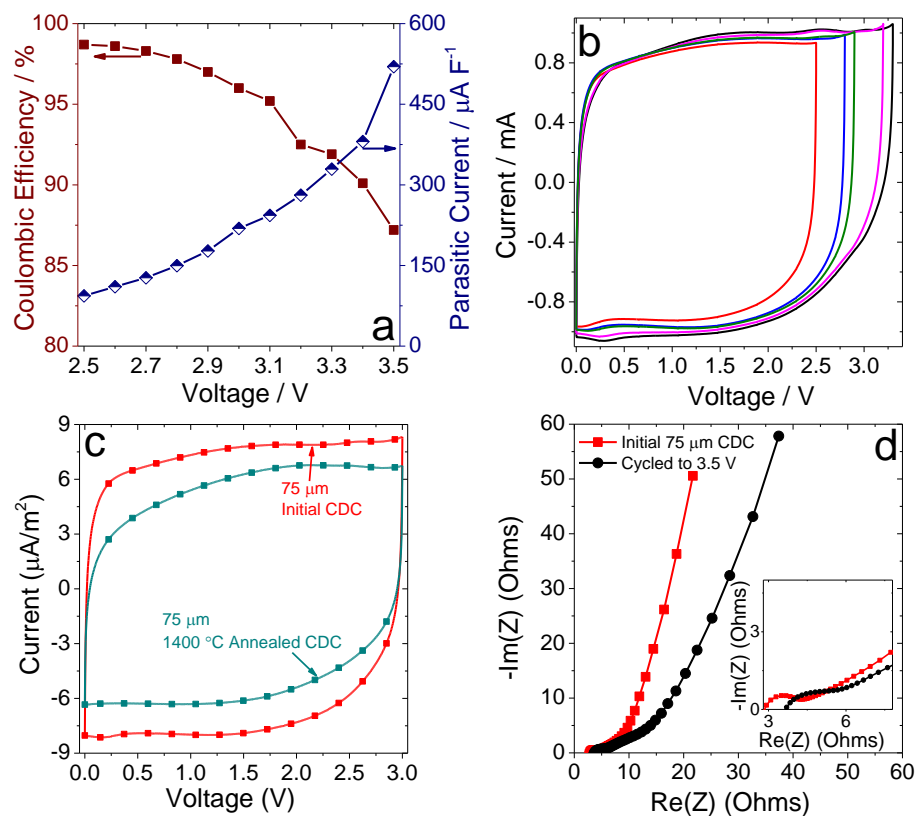
Figure 4.57. a) Comparison of coulombic efficiency (from 2 mV s^{-1} CVs) and steady-state current measurements (60-minute CA) in the 2.5 ↔ 3.5 V window. b) CVs comparing initial CDC and milled CDC cycled in neat [EMIm$^+$][TFSI$^-$] electrolyte at 2 mV s^{-1} in the 0.0 ↔ 3.4 V window. c) Comparison of 2 mV s^{-1} CV sweeps for initial and defunctionalized/graphitized coarse-grained CDCs. d) Nyquist impedance comparison of initial CDC before start of cycling and after extending its voltage window to 3.5 V.

Although annealed, coarse-grained CDCs featured significantly fewer electrochemically unstable functional groups (including hydrogen, oxygen, nitrogen, and chlorine) and graphitic defects on its pore surfaces, their electrochemical stability did not exceed the one demonstrated by their defect-rich initial CDC counterparts. Furthermore, electrochemical impedance analysis of the material before and after cycling did not detect increased charge transfer resistance (semi-circular mid-frequency region). Subsequently, electrochemical decomposition likely occurred inside the pore channels (impeding ion transport) rather than outside the particles (between the electrode and the current collector). Coarse-grained CDCs have a large internal surface, with the ratio of ions

confined in pores vs. those electrosorbed on the outside of particles significantly greater than for micro- and nano- sized CDCs,[85] carbon onions,[27] carbon nanotubes,[253] and graphene.[124] Since the fundamental reactivities, densities, and ion-surface interactions of electrolytes fundamentally transformed during confinement in narrow pores, rates and prevalence of irreversible electrochemical breakdown (such as ion-surface reactions or catalyzed dimerization[154]) may had drastically changed. Subsequently, relative influence of ion confinement could overshadow the effects of the structural/chemical composition of pore interfaces on electrochemical stability.

4.3.4. Summary of Pore Size and Confinement Effects

Several porous and non-porous electrode systems demonstrated significant convolution of ion confinement effects with influences of surface composition and defects at electrode-electrolyte interfaces. Fundamentally, ionophilic surfaces identically affected ions in internal and external environments: they drew the ions closer to surfaces and reduced densities in the bulk electrolyte environments. However, while this behavior allowed ions to efficiently move alongside surfaces in narrow (pore $d_{av} \approx$ ion d_{av}) confinement and improved capacitance of CDCs, it minimized charge densities on planar and spherical particles and hurt capacitance of CBs and GNPs.
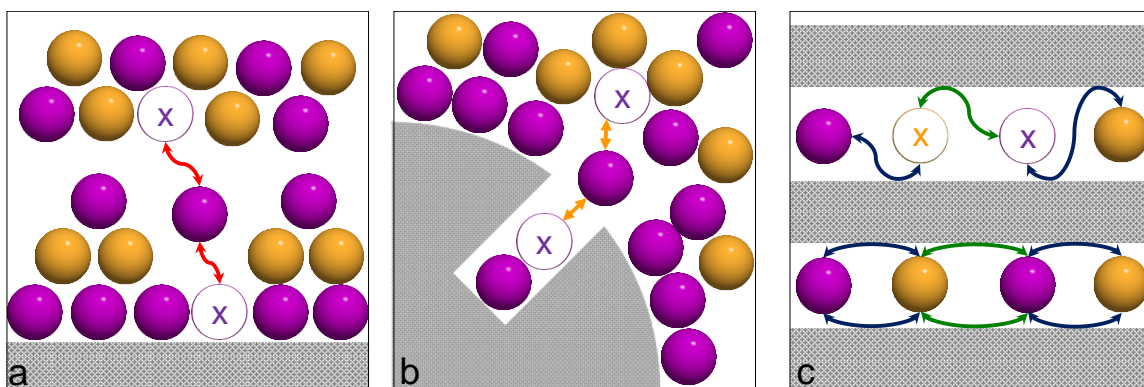
Figure 4.58. Exaggerated schematics of a) ion adsorption from bulk onto external electrode surface, b) Ion insertion into confined pores, and c) Localized ion exchange in pores. "X"s denote different states of ions in bulk electrolytes, electrosorbed on surfaces, or confined pores.

Depending on the structure of the electrode and the specific electrochemical process, ions interacted with surfaces during three distinct processes: 1) separation of ion from the bulk electrolyte and its electrosorption on a charged electrode surface; 2) insertion of ion from bulk/dense electrosorbed layers outside the particles into confined pores; and 3) localized ion exchange to fill pores with co-ions and expel counterions. These processes are shown in **Fig. 4.58**. The energies associated with each process are unique; whereas process 1 requires only singular contact with the surface, process 3 surrounds both ions with ionophilic or ionophobic interfaces. Defect-rich, disordered, ionophilic interfaces of long pores favored quicker and more efficient ion transport, and near-infinite pore lengths of coarse-grained powders noticeably amplified this effect.

Studies of differently functionalized electrodes with diverse pore sizes and lengths further underscored the localized nature of the ion exchange processes. Most co-ion electrosorption/counter-ion expulsion processes likely involved short-range (1-2 molecular lengths) interactions. Although surface defects have significant influences over these processes, the net effect of all forces on the ions, and the resulting electrochemical

behavior of supercapacitors, predominantly depends on the electrode particles' geometries. Co-ion filling (and counterion defilling), for instance, may be construed as a thermodynamic phase change and resemble intercalation processes.[254] These forces require additional follow-up computational and experimental investigations.

4.4. Applied Supercapacitor Characterization and Energy Storage Materials

The findings from sections **4.1**, **4.2**, and **4.3** provided insights into important electrosorption mechanisms and the fundamental processes that occur at the heterogeneous electrode-electrolyte interface. Although electrochemical measurements, neutron scattering, and MD simulations provided descriptions of charge/discharge mechanisms for carbons with different structures and pore wall compositions, several outstanding charging mechanisms required novel, *in situ* characterization approaches. Furthermore, important findings about the CDC structure and influence of pore size could be integrated into novel electrode material design and applied in commercially critical high-performance energy storage devices. Section **4.4.1** describes an FTIR-based spectroelectrochemistry method that was used to evaluate charging dynamics in porous and non-porous carbons. Section **4.4.2** describes a novel hybrid porous particle structure that relied on a microporous core and a mesoporous shell to maximize capacitance and rate handling abilities. Section **4.4.3** describes the coarse-grained CDCs (from section **4.3.3**) and their advantage in low-cost, high-capacitive supercapacitors. Finally, section **4.4.4** addresses the broader sustainability aspect of supercapacitors and proposes an EDLC design that included only environmentally benign materials.

4.4.1 *In situ* FTIR Spectroelectrochemistry

If classical supercapacitor double layer theory was applied to the 75-250 µm diameter internal surface electrodes with semi-infinite pore lengths (from section **4.3.3**), it would predict total pore defilling and a subsequent pore filling during charge/discharge processes. Such a process would require very long charge times, operate highly inefficiently, and render these coarse-grained electrodes useless. These findings, along with behaviors of ions at differently functionalized external surface interfaces, suggested that the electrosorption process was localized in nature and mostly composed of short-range ion exchanges at short time scales. However, verification of this proposed charging/discharging mechanisms of ILs in porous CDC and non-porous OLC particles required molecular-level *in situ* experimental techniques. Unfortunately, there are only a few *in situ* experimental techniques that are capable of measuring ion dynamics in carbon electrodes of EDLCs, including NMR spectroscopy[255] and electrochemical quartz crystal microbalance.[256] To date, they have not properly studied IL electrolyte electrosorption processes.

An *in situ* infrared spectroelectrochemical technique, which had been previously developed to investigate [EMIm$^+$][Tf$^-$] in RuO$_2$ actuators,[257] was adapted to investigate IL-filled electrodes.[258] The method compared electrosorption in TiC-CDC internal surface nanoparticles (800 ºC Cl$_2$: 1310 m^2 g^{-1} SSA, 20 nm diameter particles, pore d_{av} = 1.01 nm), or OLC external surface nanoparticles (1,800 ºC anneal: 370 m^2 g^{-1} SSA, 5 nm diameter particles, pore d_{av} = 0.86 nm). The *in situ* FTIR approach coupled chemical changes with electrical inputs/outputs.[259] The setup, which is shown in **Fig. 4.59**, used 75 µm-thick electrodes (same preparation method as described in section **3.7**)

and tracked the relative intensities of IR absorbance bands that represented chemical bonds in the cation (1575 cm^{-1}; C=C stretch) and the anion (1070 cm^{-1}; SO$_2$ stretch).
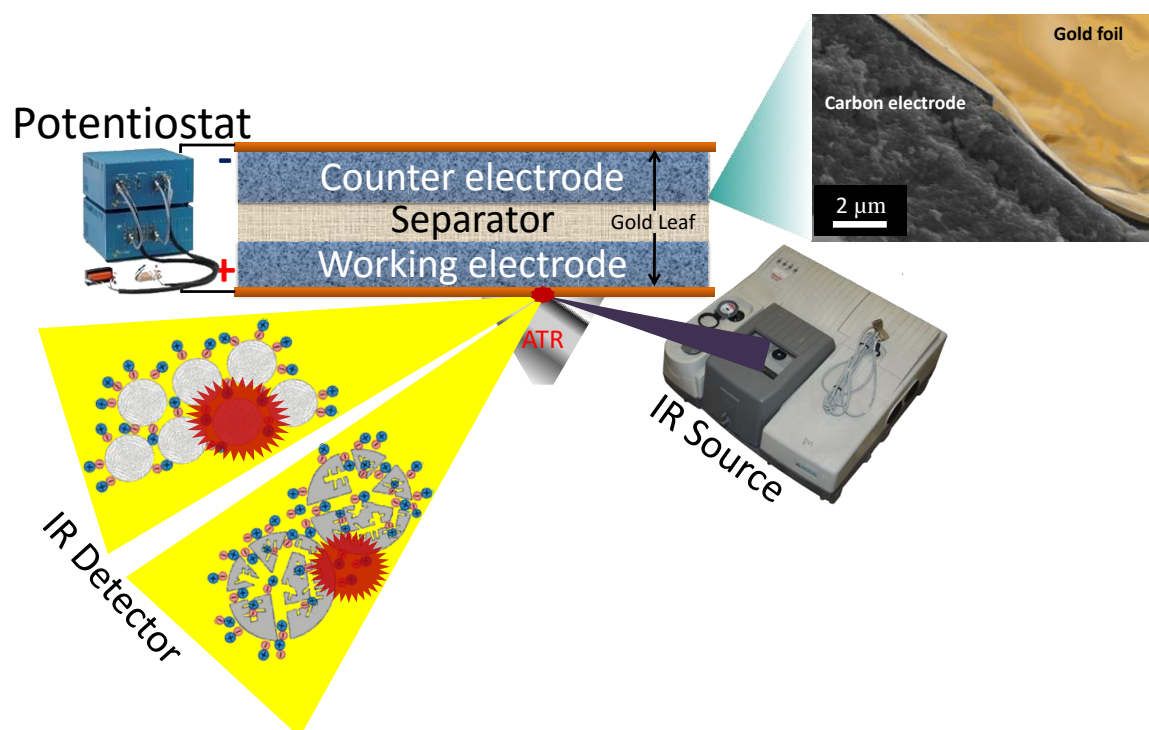
Figure 4.59. Schematic of the *in situ* FTIR spectroelectrochemical setup. The instrument used Attenuated Total Reflection (ATR) setup and operated the instrument in a grazing angle mode. Electrode films were mounted on 50-nm thick gold current collector foils, which were transparent to the IR signal. The electrode was compressed with an anvil onto the diamond ATR crystal, and leads from the films connected the electrochemical cell with a potentiostat.

Fig. 4.60 shows time-resolved infrared spectra of [EMIm$^+$][TFSI$^-$] in the CDC electrode in response to dynamic charging/discharging. IR spectra showed highest intensity at ~0.0 V and decreased as the voltage moved in the positive or negative direction. Subsequently, changes in IL absorbance band intensities stemmed from filling/defilling of ions from the CDC pores during a CV experiment from -1.5 V to +1.5 V. Ions inside of CDC pores were no longer detected due to high IR signal absorbance by the black CDC pore walls. Therefore, the technique measured absorbance decreased during charging (ions fill pores) and increases during discharging (ions leave pores). In

Fig. 4.60(a)-(b), IR representing both the cation and anion of [EMIm$^+$][TFSI$^-$] increased or decreased simultaneously with changes in voltage. Electrosorption resembled chain-like aggregate ion transfer and was in agreement with findings in section **4.2.4** and recent MD simulations that had shown interlinked cation and anion dynamics.[260]
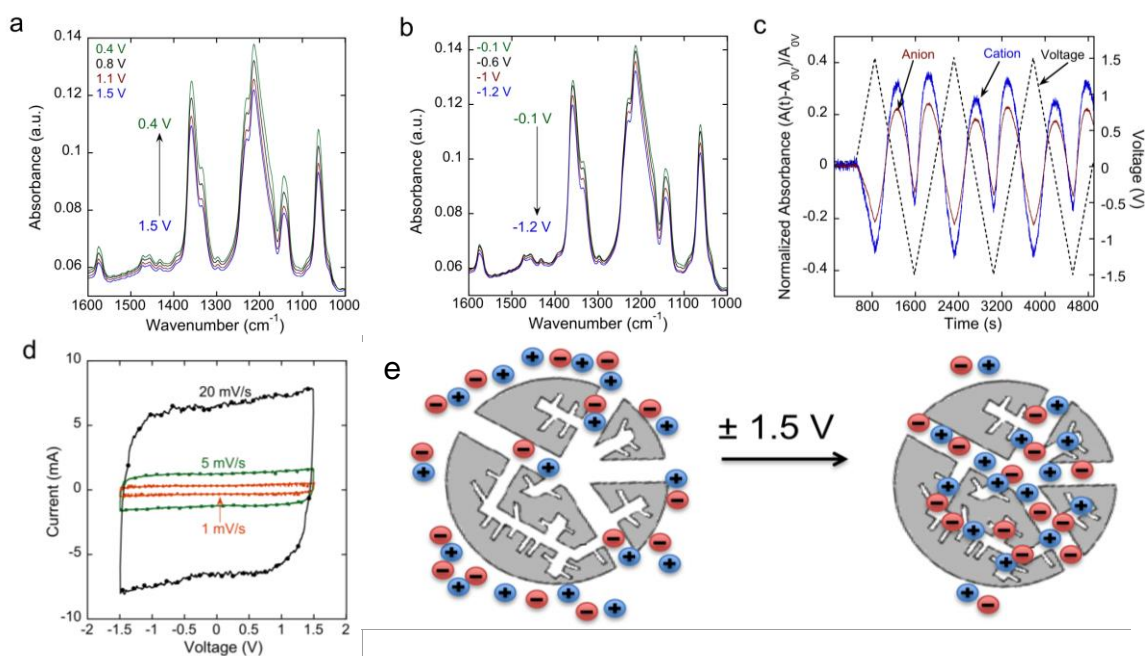
Figure 4.60. Results for CDC electrodes: Time-resolved infrared spectra corresponding to a) positive and b) negative voltages during a CV scan from -1.5 V ↔ +1.5 V. c) Normalized absorbance of IR bands of the cation and anion as a function of time during three CV cycles from -1.5 V to +1.5 V at 5 mV s^{-1}; d) Corresponding CVs at 1, 5, and 20 mV s^{-1} sweep rates; e) Schematic of ion dynamics within pores of CDCs. Although some ions are drawn into pores *via* capillary action under neutral potentials, most ion filling occurred under an applied electromotive driving force.

Non-porous OLC electrodes were cycled using the same approach to compare ion electrosorption in external surface carbons. The results are shown in **Fig. 4.61**. The spectra of [EMIm$^+$][TFSI$^-$] in the electrodes in the charged state (± 1 V) and uncharged state (0 V) were nearly identical. In other words, the concentration of ions detected by the spectrometer was not affected by charge/discharge processes of non-porous OLCs. Additionally, none of the IR peaks shifted during charging. Subsequently, the

environment that had surrounded the ions did not significantly change. This result noticeably contrasted with results for porous CDCs, which highlighted differences in the spectra of the charged and uncharged electrodes. The plot of normalized absorbance of cations and anions vs. time (**Fig. 4.61(b)**) showed absorbance changes within the noise of the data and demonstrated no statistically significant changes. Normalized absorbance difference between the [EMIm$^+$] cation and [TFSI$^-$] anion was less than 10% of their absorbance change in CDC electrodes. This agreed with *in situ* electrochemical dilatometry results, which showed lower swelling of OLC electrodes than CDCs.[261]
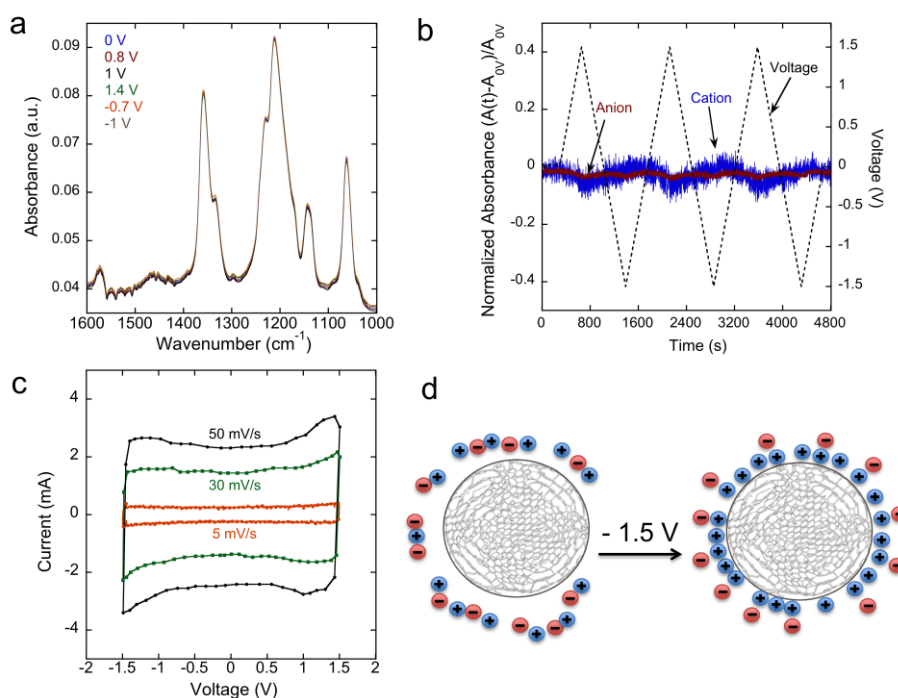
Figure 4.61. a) Time-resolved IR spectra that correlated with -1.5 V ↔ +1.5 V cycling of OLC electrodes. b) Normalized time-resolved absorbance of IR bands of ions during 3 CV cycles at 5 mV s^{-1}. c) Corresponding CVs at 3 different scan rates. d) Schematic of ion dynamics on non-porous spherical OLCs.

These results suggested that the majority of both cations and anions entered and exited CDC pores during electrosorption. Results also demonstrated rapid charging and discharging of non-porous OLCs with only small bulk electrolyte concentration changes.

The ions effectively reorganized into layers on the surface and did not require diffusion-limited long-range mass transport from oppositely charged electrodes. Subsequently, all interactions involved short-range interactions (within the ~30 nm IR beam size). The *in situ* FTIR spectroelectrochemistry technique showed exceptional promise beyond supercapacitors and is highly usable in efforts to investigate fundamental charge storage mechanisms in systems such as Li-ion batteries, fuel cells, pseudocapacitors, and many other electrochemical systems.

4.4.2. Core-shell Porous CDCs

All comparisons between internal surface and external surface carbon structures, as well as microporous and mesoporous CDCs, demonstrated superior rate handling abilities of larger-pore electrodes. Although ions achieved optimal desolvation and packing densities in systems with matching ion-pore diameters,[77] microporous electrodes inhibited ion transport and reduced rapid electrosorption dynamics.[262] On the other hand, mesoporous materials, which facilitated greater ion mobilities than microporous carbons, typically exhibited lower SSAs (100-500 m^2 g^{-1}, as opposed to $1,000 - 2,500$ m^2 g^{-1} in microporous CDCs) and, subsequently, limited C_{sp}.[17] Therefore, hierarchically structured hybrid microporous-mesoporous materials may provide an optimal balance between the two extremes with: 1) prevalence of micropores to maintain high capacitance, 2) network of mesopores to facilitate rapid ion transport, and 3) graphitized external morphology that improves particle-to-particle electron transport.

To find a proper trade-off between these three objectives, a novel synthesis methodology modified the traditional horizontal steady CDC synthesis (described in

section **3.1.1**) to produce hybrid particle with mesoporous/graphitic shells (for fast ion transport and high electric conductivity) that enveloped microporous cores (with high specific surface areas).[263] The schematic of this core-shell particle structure is illustrated in **Fig. 4.62(a)**. The synthesis procedure relied on two-stage Cl_2 etching of TiC-CDC microparticles in a vertical furnace (**Fig. 4.63(b)**). The first approach partially converted outer TiC layers to mesoporous CDCs at 1,200 ℃ (for 15 minutes). Following an Ar gas flushing step, the remaining carbide (**Fig. 4.63(c)**) was converted at 800 ℃ (for 150 minutes) to form the microporous core. This method featured a sharp transition between the two stages (hereafter labeled as CDC-STEP). The second route implemented a constant 10 °C min⁻¹ temperature ramp-down from 1,200 to 800 ℃ and yielded a gradual porosity change and graphitization (CDC-GRADUAL). Reference TiC-CDC samples were also synthesized using isothermal 800 ℃ (CDC-800) and 1,200 ℃ (CDC-1200) in a horizontal furnace.
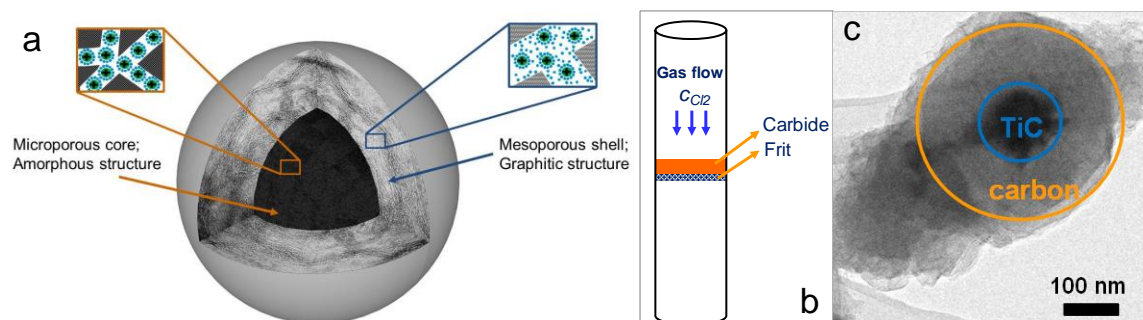
Figure 4.62. a) Schematic of the core-shell porous particle. b) A flow-through carbide bed vertical set-up. c) TEM image of CDC shell on carbide core (before secondary treatment).

The characteristics of the resulting structures are shown in **Fig. 4.63**. As expected, carbons with greater mesoporosity (CDC-STEP, CDC-GRADUAL, and CDC-1200) were more graphitized. Electrodes fabricated from both novel core-shell materials showed comparably high conductivities of 2.60 and 1.50 S cm⁻¹ for CDC-STEP and CDC-

GRADUAL, respectively (0.15 S cm^{-1} for CDC-800 and 2.72 S cm^{-1} for CDC-1200). Analysis of dTG peaks suggested that the shell structure constituted 35% of the CDC-STEP particles. This material exhibited a bimodal pore structure as a mixture of the 800 °C and 1200 °C pore size distributions (**Fig. 4.63(b)**). Although CDC-GRADUAL demonstrated a mixed porosity and graphitic microstructure, its boundary between the core and shell phases was less distinct. Despite the pronounced mesoporosity of the core-shell hybrid materials, their SSA values matched the ~1500 m^2 g^{-1} benchmark of the purely microporous CDC-800 particles. The conversion process successfully removed all metal carbides.
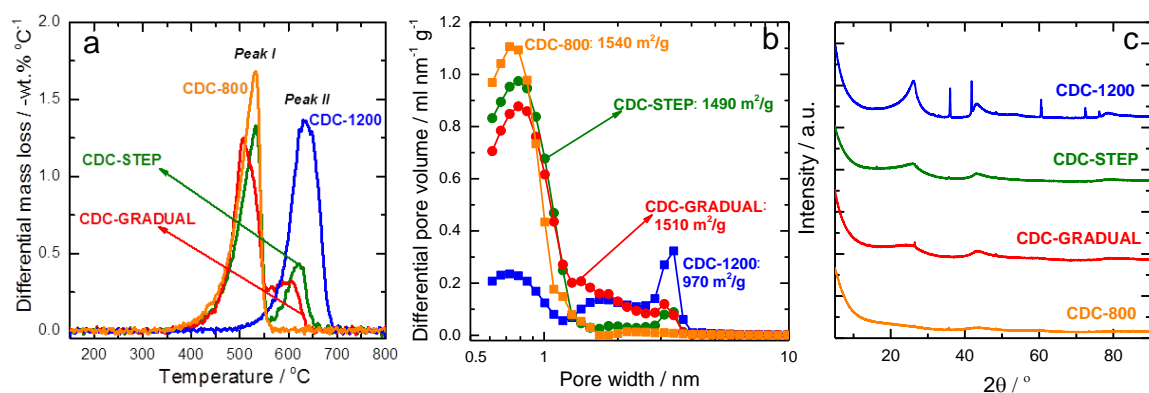
Figure 4.63. a) Differential mass loss (dTG) during temperature-programmed oxidation (TGA). b) PSDs for the different TiC-CDC structures. c) XRD analysis of the CDCs.

Electrochemical measurements were conducted with 1.5 M [NEt$_4^+$][BF$_4^-$]/CH$_3$CN electrolyte. The results are shown in **Fig. 4.64**. Charge/discharge profiles for all samples at 10 mV s^{-1} yielded rectangular CVs and showed no mass transfer limitations. At the high 500 mV s^{-1} sweep rate, mass transfer limitations noticeably distorted the CV curves of microporous CDC-800, and its capacitance decreased by 45%. However, core-shell pore structured materials exhibited minimal mass transfer limitations: their capacitance decay did not exceed 20%. While CDC-800 shows significant diffusion limitations (RS =

0.836), both core-shell materials exhibit a near-ideal capacitive behaviors with RS coefficients approaching 0.920. Capacitance and rate handling abilities (**Fig. 4.64(c)**) exceeded the capabilities of the low-SSA mesoporous (and ionophobic) CDC-1200. EIS comparisons (**Fig. 4.64(d)**) highlighted CDC-GRADUAL's minimal ionic impedance behavior at low frequencies. Bode impedance analysis arranged the relative capacitance order as: CDC-1200 > CDC-GRADUAL ≈ CDC-STEP > CDC-800, which corroborated the rate handling results. The small relaxation time constant (2 s) of the core-shell materials showed their fast charge-discharge response.
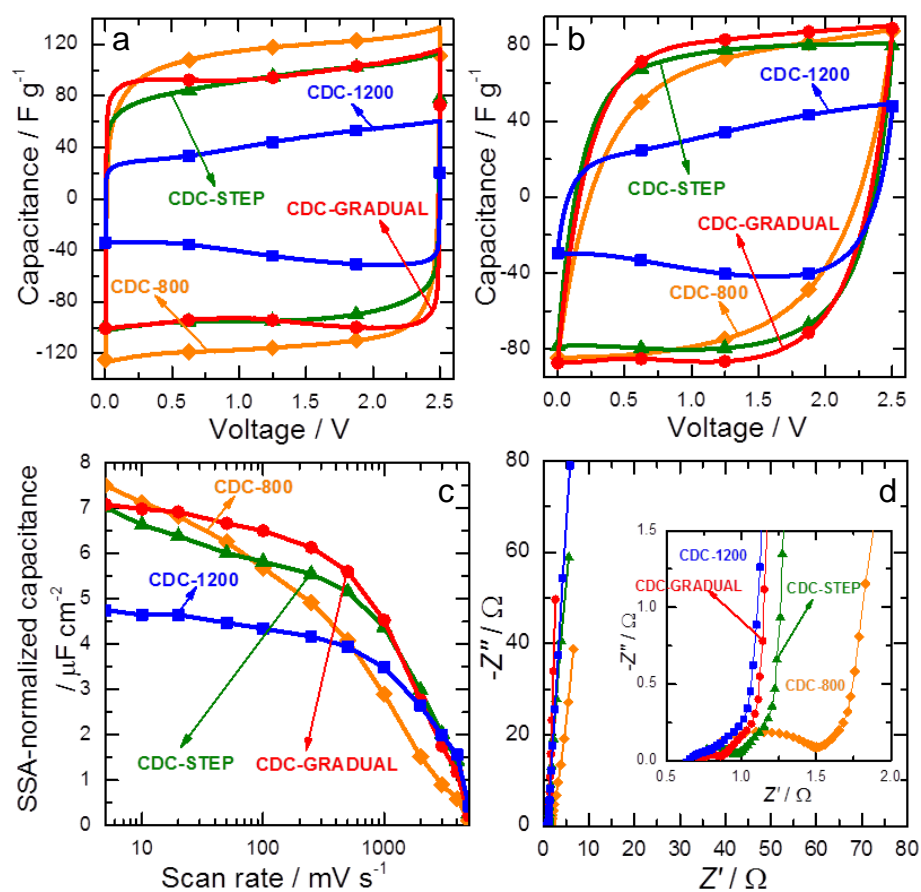
Figure 4.64. CV measurement at a) 10 and b) and 500 mV s^{-1}. c) Capacitance normalized by SSA. d) Nyquist plots (the inset: the high-frequency region).

This novel synthesis approach demonstrated high temperature-dependent tunability of the shell thickness and graphitic composition of these core-shell CDCs. As a

supercapacitor electrode, this novel electrode material showcased an optimal combination of specific surface area, electric conductivity, and mesoporosity that provided critical performance advantages. The core-shell structures yielded higher capacitance retention (only 6% capacitance drop associated with a tenfold sweep rate increase), which exceeded the 13 - 27% capacitance decay that had been the recorded performance ceiling in hierarchical porous materials.[264-266] The core-shell supercapacitor electrodes showcased 27 Wh kg^{-1} energy densities and 40 kW kg^{-1} power densities. Beyond energy storage systems, this nanostructured material is applicable in applications such as electrocatalysis, water or fuel sorption, and thermal catalysis.

4.4.3. Coarse-grained Porous Carbon Electrodes

Results from section **4.3.3**, which analyzed influence of surface defects in long pores, and section **4.4.1**, which confirmed the localized nature of most electrosorption interactions and ion exchange processes, allowed a comprehensive re-thinking of the key macroscale supercapacitor parameters. Most commercial supercapacitors use porous carbons with the particle size of a few microns. In the case of CDCs, the precursor carbides undergo a conformal transformation during synthesis [83] and yield porous particles with unchanged diameters (1-5 μm diameters). Other previously reported supercapacitors, which were composed of nanosized CDC electrode particles,[85] had relied on high-energy plasma synthesis of 20 nm TiC precursor nanopowders.[86] However, these processes have not been sufficiently cost-effective for CDCs to become economically competitive with activated carbon. Prolonged milling and sieving, which is required to produce micron-sized TiC powders, significantly amplifies the raw material

costs. If electrodes were to successfully implement large-diameter CDCs (from coarse-grained abrasive carbides), supercapacitors would become much more economically viable.

Synthesis of coarse-grained 75-250 μm diameter CDCs can effectively use the same Cl_2 furnace synthesis procedure that had been successfully implemented for micropowder and nanopowder CDCs.[267] As shown in section **4.3.3**, coarse-grained TiC fully converted to porous carbon with no Cl_2 or $TiCl_4$ transport limitations. XRD, TGA, and elemental analysis of the resulting coarse-grained powders found, respectively, no TiC/TiO2 peaks, < 2 wt. % ash content, and < 1 wt. % of metallic impurities. As shown in **Fig. 4.65**, the 75 μm diameter CDCs offered high capacitances and rate handling abilities in 1.5 M $[NEt_4^+][BF_4^-]/CH_3CN$ organic electrolyte. Charge/discharge experiments conducted current-voltage sweeps in the $0 \leftrightarrow +2.5$ V window for YP50 (baseline activated carbon) electrodes (4.0 mg cm^{-2} loading) and CDC films (6.2 mg cm^{-2} mass loading) with identical 85 μm film thicknesses. This dimension suggested that coarse-grained CDC films often contained single carbon particles across entire electrodes. From CVs and rate handling analysis, 75 μm diameter CDCs demonstrated very high capacitance throughout the entire 2 mV s^{-1} – 1 V s^{-1} sweep range. Cyclic voltammograms yielded C_{sp} values as high as 134 F g^{-1} (at 2 mV s^{-1}) and 100 F g^{-1} (at 250 mV s^{-1}). The material retained 44% of its capacitance during 1 V s^{-1} cycling. The material consistently demonstrated significantly higher charge storage density capabilities than fine-grained activated carbon (YP50) electrode tested under identical conditions. Capacitance of coarse-grained CDC was 31% higher than YP50, and the 75 μm diameter particles demonstrated superior rate handling ability.
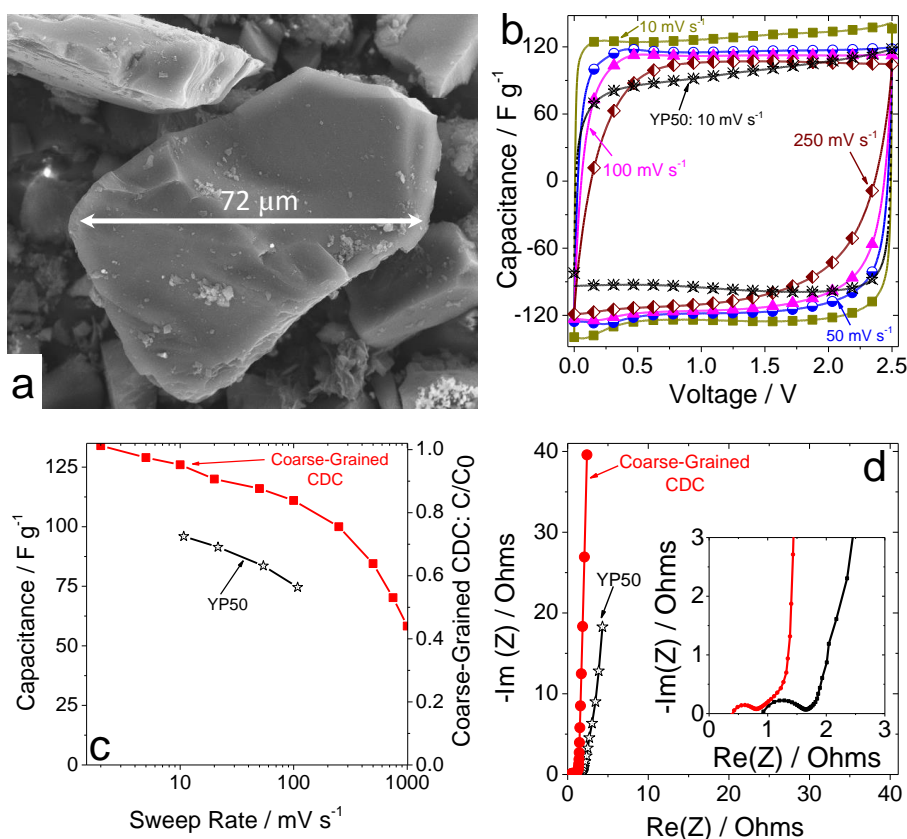
Figure 4.65. a) SEM image of coarse-grained CDC. b) Cyclic voltammograms showing charge/discharge behavior of coarse-grained CDC at 10, 50, 100, and 200 mV s^{-1} in organic electrolyte, and YP50 activated carbon cycled at 10 mV s^{-1}. c) Comparison of rate handling ability and capacitance retention of CDC and YP50. d) Nyquist plots comparing electronic and ionic resistance of coarse-grained CDC and YP50.

The same electrode fabrication process successfully increased film thickness from 85 μm to 250-1000 μm to maximize their mass loading. These electrodes retained the same bulk densities and linearly maximized their areal densities to 21.9 mg cm^{-2} (for 250 μm thick films) and 81.2 mg cm^{-2} (for 1 mm thick films). As shown in **Fig. 4.66**, the areal capacitance of thicker films improved by 1.8-5.5 times. Although thicker electrodes showed some ion transport limitations (exhibited by increases in impedance and slightly lower capacitance retention),[228] the material still maintained high capacitance and near-rectangular cyclic voltammograms. RS coefficient calculations showed values above 0.9 for all films (indicating near-ideal capacitive behavior with minimal diffusion

limitation) that did not degrade for thicker films.[268] Impedance comparisons (**Fig. 4.66(c)**) showed greater contact resistance (high-frequency region) and lower capacitance (low-frequency region) of 250-1000 µm thick films compared to the 90 µm thick ones and demonstrated the need for different binders, processing/rolling techniques, and other electrode design that is accessible in an industrial setting. Subsequently, these coarse-grained CDCs offer a promising approach that maximizes gravimetric and volumetric energy densities without sacrificing rate handling ability or cycling efficiencies at high sweep rates.
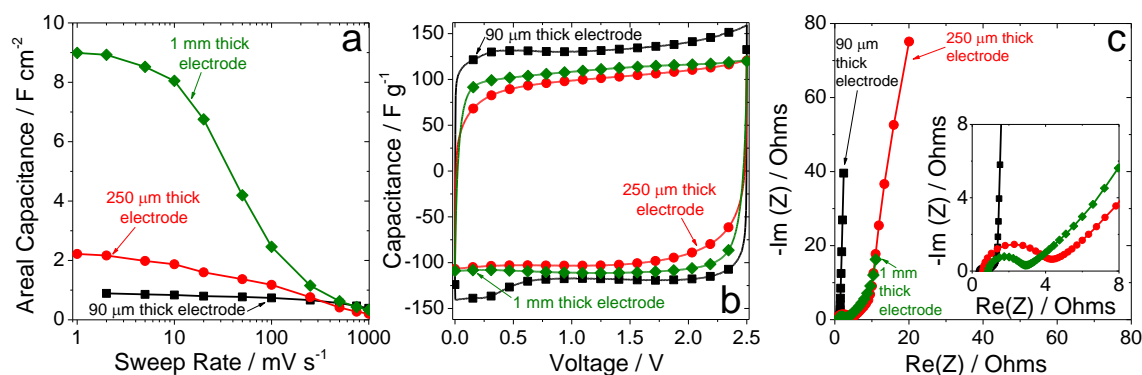
Figure 4.66. Rate handling comparison of 90 µm, 250 µm, and 1 mm thick coarse-grained CDC electrode films normalized by a) mass loading per unit area. b) Cyclic voltammograms comparing 10 mV s^{-1} cycling of films with different thicknesses in 1.5 M [NEt$_4^+$][BF$_4^-$]/acetonitrile electrolyte and c) EIS-derived Nyquist plots for these films.

Some of the 75 µm diameter CDCs were mechanically milled down to a 5-20 µm size to determine the influence of particle diameter. Although the resulting electrodes featured the same 85 µm thickness and similar mass loading (initial CDC: 6.2 mg cm^{-2}, milled CDC: 6.1 mg cm^{-2}), the coarse-grained films exhibited lower resistivity (9.77 Ω cm) compared to those composed of smaller, milled particles (13.60 Ω cm). This can be explained by a smaller number of interparticle contacts in the films cross-section. The performance of CDC electrodes in 1.5 M [NEt$_4^+$][BF$_4^-$]/ CH$_3$CN was unaffected by diameter of powders in the electrodes (**Fig. 4.67(a)**). Both materials exhibited very high

capacitance and rate handling ability. When the materials were tested in a more viscous, solvent-free [EMIm$^+$][TFSI$^-$] electrolyte, electrodes with smaller CDC particle diameter performed better at higher charge/discharge rates (as shown in **Fig. 4.67(b)**, 71 F g^{-1} for initial CDC vs. 117 F g^{-1} for milled CDC at 2.0 A g^{-1}). The materials demonstrated high ionic transport and low impedance, regardless of particle size for acetonitrile-solvated [EMIm$^+$][TFSI$^-$] electrolyte (**Fig. 4.67(c)**).
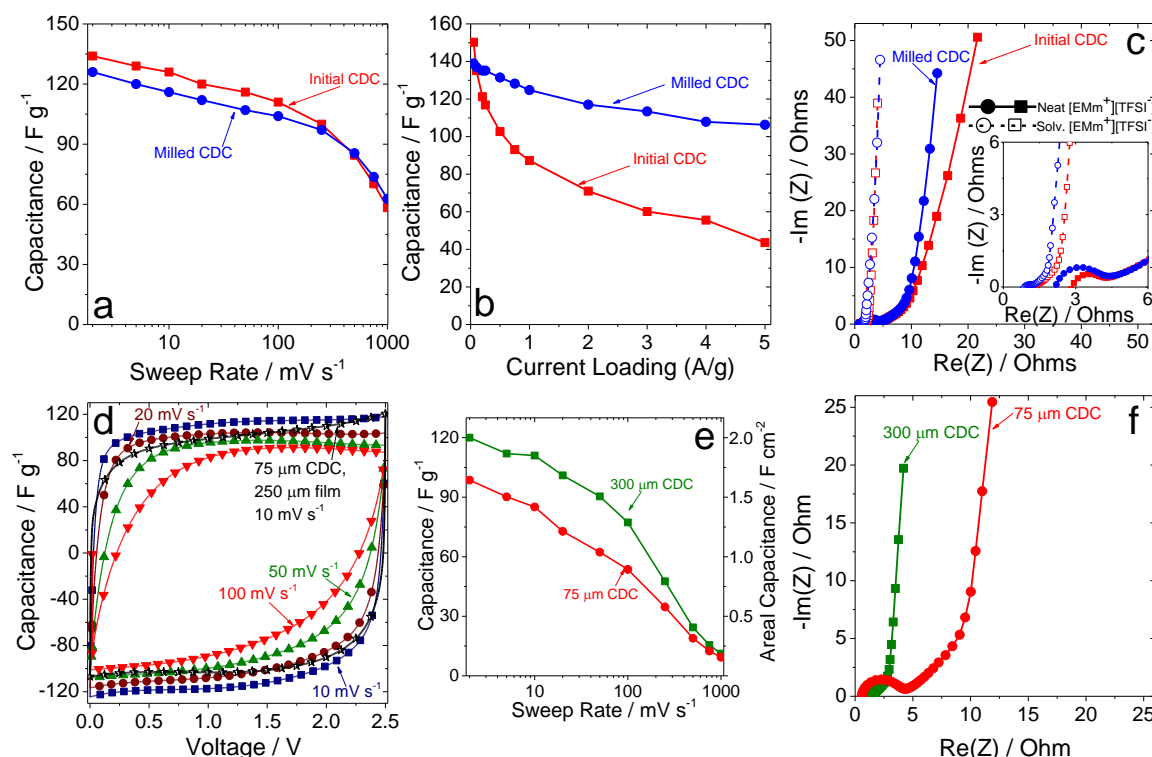
Figure 4.67. a) Rate handling and capacitance retention comparison of initial coarse-grained CDCs and an electrode composed of those particles after milling and particle diameter reduction. Tests were conducted in 1.5 M [NEt$_4^+$][BF$_4^-$]/acetonitrile electrolyte. b) Current loading comparison (from galvanostatic cycling) for initial and milled CDCs in neat (solvent-free) [EMIm$^+$][TFSI$^-$] ionic liquid electrolyte. c) Nyquist plot comparison of initial and milled CDCs in neat and solvated (50 wt.% solution in acetonitrile) [EMIm$^+$][TFSI$^-$] electrolyte. d) Cyclic voltammograms of TiC-CDC films composed of 250 μm diameter particles at 10 mV s^{-1}, 20 mV s^{-1}, 50 mV s^{-1}, and 100 mV s^{-1}. Data is shown for 1.5 M [NEt$_4^+$][BF$_4^-$]/acetonitrile. e) Rate handling ability and f) Nyquist impedance plot of larger CDC electrodes in organic electrolyte. For comparison, performance for a similarly thick (250 μm) electrode composed of 75 μm diameter TiC-CDCs is included in d), e), and f). The time constant for the 250 μm CDC film was 12.6 s, versus 10.4 s for a similarly thick film composed of 75 μm particles.

250 μm diameter CDCs also demonstrated high capacitance in organic electrolyte (**Fig. 4.67(d-f)**). CVs, rate handling analyses, and Nyquist plots (**Fig. 4.67(f)**) also include results from 280 μm thick films composed of 75 μm diameter particles – the closest electrode comparison. The larger particles demonstrate equally high capacitance and are capable of delivering over 110 F g^{-1} at 10 mV s^{-1}. Across the 2 – 200 mV s^{-1} sweep range, C_{sp} for large CDCs was 20-30 F g^{-1} larger than that for 75 μm ones (**Fig. 4.67(e)**. Although 75 μm diameter CDCs are more cost-effective than micropowder and nanopowder CDCs, 250 μm diameter CDCs are less expensive than all other alternatives. To date, no electrodes with comparable thickness and adequate performance have been reported in the literature.

Aside from offering significant production cost and mass loading advantages, these results further advanced a fundamentally different view of electrosorption. Coarse-grained CDC films offered higher specific surface areas, greater mass loading, and improved electrolyte accessibility. Larger carbon structures with high conductivity may provide better electrostatic screening of ions and counterions in narrow pores, allow greater charge packing density in pores, and, subsequently, maximize capacitance. The fundamental mechanism of localized ion exchange in near-infinite pore lengths and co-ion filling/counter-ion defilling must be explored in the future, as its significance extends into slurry-based flow systems[62] for grid storage solutions.

4.4.4. Environmentally Sustainable Supercapacitor

One of the broader goals of high-performance electrical energy storage solutions, such as EDLCs, is to improve overall energy sustainability and increase use of renewable fuel sources. However, the rising numbers of electrical energy storage devices underscore

the problem of exponentially increasing the mass of spent batteries and supercapacitors that must be subsequently processed to avoid a detrimental impact on the environment. Over 8 billion batteries annually enter the U.S. and European markets, with 3 billion of just alkaline units discarded each year in North America alone.[269] Moreover, although supercapacitors have long cycle lifetimes, they are likely to be discarded together when the devices relying on them are retired. The acetonitrile and fluorine-containing organic electrolytes,[270] and PTFE-based carbon particle binders[271] and separators [272] are likely to generate volatile fluorocarbons during traditional incineration. The [TFSI$^-$] anion has been shown to inhibit cellular respiration.[38] While aqueous electrolytes (Li_2SO_4 or Na_2SO_4) are mostly benign,[22] they still emit SO_2, which contributes to acid rain if released into the environment during incineration.[273] Subsequently, spent commercial supercapacitors require expensive hazardous waste processing rather than incineration and landfill storage.[274] Although supercapacitors rarely contain no noble or heavy metals, current collectors and packaging materials, such as steel and aluminum, are incombustible and cannot be fully burned without leaving ash residue.

To address these issues, key supercapacitor device components were critically evaluated, and a holistic overhaul of the design selected material alternatives that yielded environmentally friendly, fully combustible devices.[275] The approach relied on activated carbon electrodes, which are typically synthesized using coconut shells,[276] corn biomass,[277] or seaweed[278] precursors and pose minimal environmental concern.[159] Key traditional components and proposed substitutes are shown in **Fig. 4.68**. "Green" alternatives were carbon-based, lightweight, and simple/inexpensive to synthesize. Device components, which aimed to meet or exceed performance metrics of

traditional materials, were combined into operating prototypes (**Fig. 4.68(b)**) with same

manufacturing methods and operational standards as commercial supercapacitor devices.
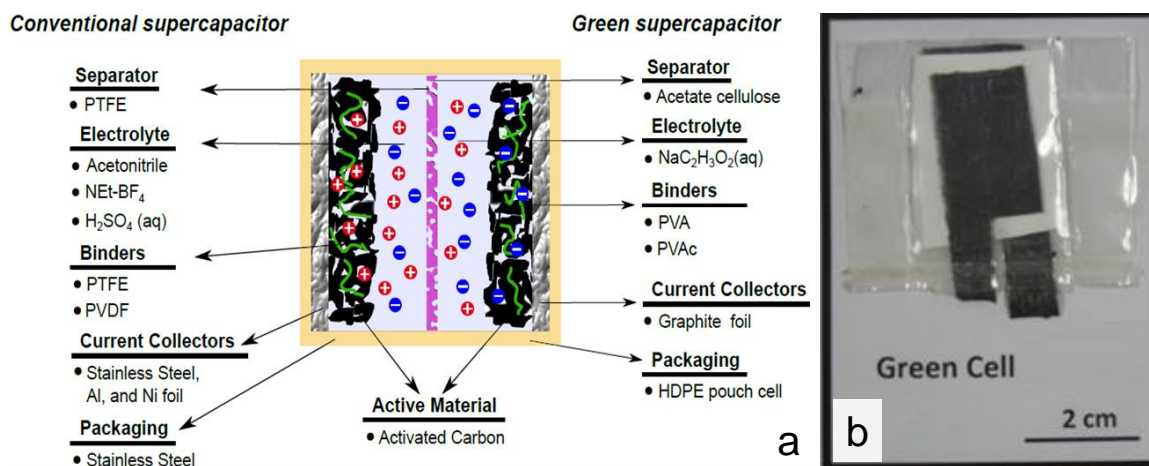
Figure 4.68. a) Cross-sectional schematic of a typical supercapacitor, traditional materials, and developed environmentally benign alternatives. b) Assembled pouch cells that contained solely "green" components.

A carbon-based alternative to metallic current collectors implemented graphite foil sheets (**Fig. 4.69(a)**), which were flexible sheets of stacked graphite layers. These materials were used for contact angle measurements (section **4.2.2**). The surface resembles lightly crumpled vertically stacked graphene sheets. Sandpaper roughening treatment introduced macroscopic defects in the form of protruding sheets, and the SSA of the foil remained at approximately 17 m^2 g^{-1} (**Fig. 4.69(b)**). Compared to steel coated with carbon paint (72 F g^{-1}), capacitance of cells with mechanically roughened graphite foil current collectors increased by 14% to reach 81 F g^{-1} at 10 mV s^{-1} scan rates. No expensive modifications (carbon-coated graphite foil, etc.) were needed for high performance, and the safe, combustible material required minimal treatment procedures to demonstrate high capacitance and low resistance.

As sulfur-free alternatives to sodium sulfate (Na_2SO_4), sodium acetate ($NaC_2H_3O_2$) and sodium formate (NaHCOO) aqueous electrolytes we examined with the graphite foil

current collector swapped into the system. Sodium acetate (99 F g^{-1}) showed an 18 F g^{-1} C_{sp} increase over the sodium sulfate counterpart (81 F g^{-1}) and maintained high rate handling abilities in the 10-100 mV s^{-1} sweep rate range (**Fig. 4.69(c)**). NaC$_2$H$_3$O$_2$ is as safe as household vinegar, and the 1.0 M electrolyte concentration demonstrated minimal ionic impedance and good electrochemical stability in the $0.0 \leftrightarrow 1.0$ V window.

As an alternative to fluorinated or sulfonated porous separator membranes (manufactured by W.L. Gore® or Celgard®), filter paper membranes provided more "green" alternatives. Overall, more open (cast or inter-woven textile) structures (such as acetate cellulose esters, paper, and nitrocellulose) had greater porosities and yielded better mobility than track-edged membranes with narrow channels (polyester, polycarbonate). Electrochemical performance of supercapacitor cells (implementing 1.0 M NaC$_2$H$_3$O$_2$ electrolyte and graphite foil current collectors) indicated that nitrate or acetate cellulose esters, polyethersulfonate, and nylon separators performed similarly to the standard PTFE material (**Fig. 4.69(d)**). Acetate cellulose posed least risk of offgassing sulfur or nitrogen compounds (cyanide) during combustion and was selected as the environmentally friendly alternative.
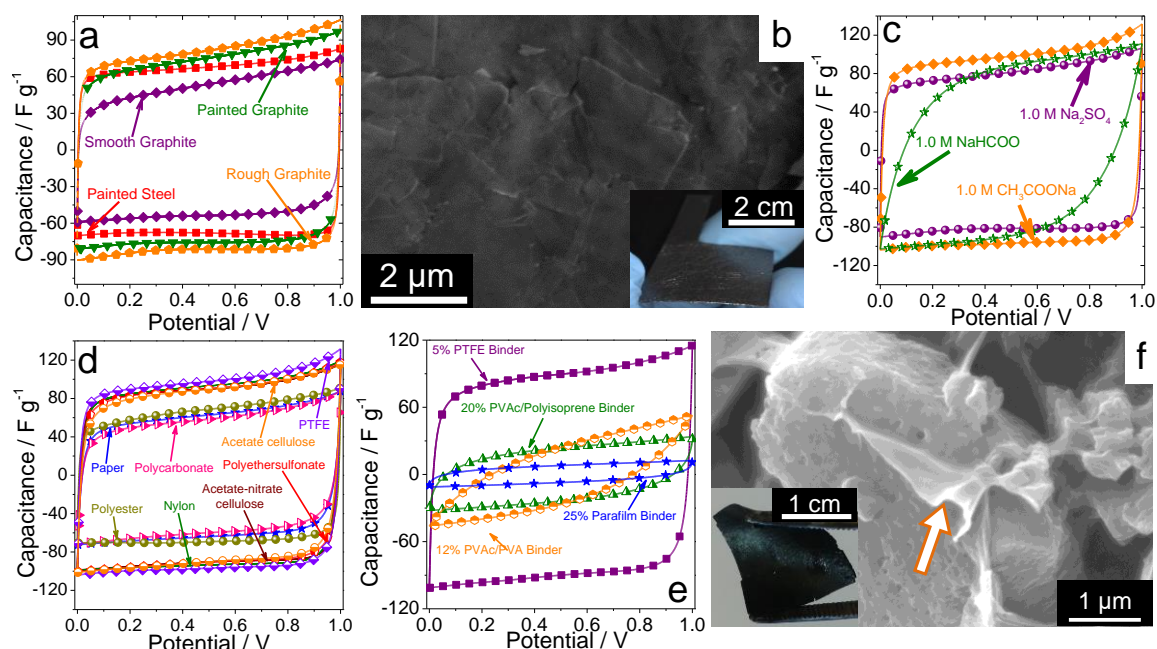
Figure 4.69. a) 10 mV s^{-1} sweeps that compared stainless steel current collector (72 F g^{-1}) with untreated graphite foil (53 F g^{-1}), painted graphite foil (75 F g^{-1}), and roughened graphite foil (82 F g^{-1}). b) Mechanically roughened graphite current collector, with photograph in insert. c) CVs that compared performances of 3 different environmentally benign electrolytes at 10 mV s^{-1}. d) CVs conducted at 10 mV s^{-1} to compare baseline PTFE separator (98 F g^{-1}) with "greener" alternatives. Acetate cellulose offered 90 F g^{-1}. e) 10 mV s^{-1} CVs that compare different YP50 particle binders. f) SEM image of polyvinyl alcohol polymer binder structures attached to carbon surfaces. Photographic inset shows image of macroscopic film produced with this binder.

A variety of long-chain polymers were mixed with YP50 particles in a variety of solvents and using different mass proportions in an effort to develop flexible, freestanding films with controllable thicknesses. The majority of tested alternatives to PTFE – C$_{100}$ hydrocarbons, polyisoprene, egg white protein – failed to exhibit the necessary elasticity, molecular mass (chain length), and cross-linking ability to yield coherent, dense, electrically conductive electrodes. The most promising approach used 95% hydrolyzed polyvinyl alcohol or a blend of polyvinyl alcohol and polyvinyl acetate. They were dispersed in a 12 wt. % ratio with carbon particles in H$_2$O, with the resulting slurry subsequently cured *via* cross-linking of hydroxyl groups with BO$_4^-$ ions using a

sodium borate solution (**Fig. 4.69(e-f)**). The approach reduced electrode SSA to 30% of its initial value, and future solutions will require finely tuned cross-linking polymers with well-defined molecular weights for high-performing "green," fluorine-free binders.

To assess the environmental impact of disposal of this design, the fully packaged device was incinerated at 1,000 ºC. The "green" supercapacitor retained only ~2% of its initial mass, indicating a burn-off of most of the system and minimal ash content. Elemental analysis of the burn-off residue indicated sodium salts (from both the electrolyte and the cross-linking of PVA binders), oxygen, and trace amounts of benign metals from component impurities. Chromatographic analysis of the gaseous products revealed no fluorine or sulfur-containing compounds, as well as an absence of dioxins, phenols, or benzyl groups. The most common organic compound products were 9-eicosene, 1-dodecanol, 1-heptadecanol, and other similar large-chain alcohols. None of those compounds pose significant environmental risks.

The results found environmentally benign to all key supercapacitor components and relied on simple "green" chemistry for final materials selection. A wide array of possible alternatives for several components (such as electrolyte and separator) makes this approach applicable for electrochemical capacitors and batteries. This low-cost, conceptual design, as well as the criteria that were used to evaluate its environmental impact, will aid the holistic design of energy storage solutions in automotive, personal electronics, and grid-storage applications.

CHAPTER 5: CONCLUSIONS

This work addressed the influence of heterogeneity and disorder at the electrode-electrolyte interfaces of carbon electrodes on capacitance, electrosorption mechanisms, and electrochemical stability. Thermal and chemical treatments modified the surface chemistry and structural ordering of carbon model systems with internal and external surfaces to decouple functional groups, graphitization, and ion confinement effects. The results led to the following key conclusions:

1. Vacuum annealing of CDC microparticles and nanoparticles at 700 – 1,800 ºC effectively controlled their structure and surface composition. The materials maintained ordered PSDs with 0.61 nm $< d_{av} <$ 0.85 nm and 1,400 – 2,100 m^2 g^{-1} SSAs. Low annealing temperatures ($<$ 1,200 ºC) removed weakly bonded groups and increased accessible surface areas; higher annealing temperatures eventually collapsed microporosities. Freestanding carbon sheets were restacked into more periodic phases, and ordered domains grew in both the [002] and [100] directions. Graphitization made 6–membered graphene rings more prevalent in the CDC structure, at the expense of 5– and 7– membered ones. Annealing yielded atomically corrugated CDC surfaces, transformed mixed sp^2/sp^3 bonding to sp^2-dominant, and increased electric conductivities of annealed CDC particles. Annealing removed functional groups (–H, –Cl, –OH, –NH$_x$) from surfaces and made them more hydrophobic. Chemical treatments, such as hydrogenation, amination, and air oxidation deposited desired functional groups and did not alter the ordered porosities of porous and non-porous electrode model systems.

2. Contrary to initial expectations, defect-free pore surfaces decreased capacitances by up to 30% compared to initial, untreated porous carbons. Although this effect was

consistently observed for microparticles and nanoparticles, the influence of defunctionalization on charge transport was convoluted with pore length and internal surface: external surface ratio. Although annealing improved ion mobilities and rate handling in 20 nm diameter CDCs, similar defect-free pore surfaces increased ionic impedance in 1-250 μm diameter CDCs. CDCs synthesized at 600 ℃, 800 ℃, and 1,000 ℃ showed similar responses to surface defunctionalization and graphitization in aqueous Na_2SO_4, $[NEt_4^+][BF_4^-]/CH_3CN$ organic electrolytes, and $[EMIm^+][TFSI^-]$ ionic liquids. Comparable microporous activated carbons also corroborated this behavior and confirmed the negative influence of defect-free surfaces on capacitance. Since NMR $\Delta\delta$ measurements quantified similar pore filling densities in defect-rich and defect-free pores, quantum capacitance changes likely significantly influenced C_{sp}.

3. Although defunctionalized pores improved electrochemical stabilities and Q_{eff} by 4-10% in 3.25 V electrochemical cycling windows, they did not completely preclude electrochemical breakdown of $[EMIm^+][TFSI^-]$ electrolytes. Different irreversible mechanisms, including reactions with surface impurities or catalyzed dimerization of ions, limit the theoretical 4.0+ V operating window of RTILs in carbon electrodes to 2.5-3.5 V.

4. While hydrogenated surfaces improved capacitance and dynamics of $[EMIm^+][TFSI^-]$ in narrow pores, aminated pore walls impeded ion mobilities despite greater pore hydrophilicities. Neutron scattering measurements showed the strongest intermolecular interactions between –H terminated pore walls and electrolyte molecules. In addition to increasing C_{sp} by >10 F g^{-1} and lowering ionic impedance by 3.5 Ω, this favorable surface chemistry improved cyclability and reduced C_{sp} degradation by 15%.

5. Oxygen-rich CDC pore surfaces demonstrated high IL ionophilicities, and the favorable electrode-electrolyte interface more than doubled the diffusion coefficients and jump lengths of electrolytes. [EMIm$^+$][TFSI$^-$] benefitted from greater mobility and demonstrated 0.7 – 3.2 µF cm^{-2} higher C_{sp} in dynamic potential experiments. Although static charge accumulation showed faster ion saturation of oxidized pores, total filling of defunctionalized pores met or exceeded equilibrium charge densities of oxygen-rich pores. MD simulations and neutron scattering experiments showed 20% lower ion densities in oxidized pores and we attributed the changes to surface-dependent ion orientations in pores. Oxygen groups drew ions closer to surfaces and facilitated charge transport through narrow pores, but defunctionalized pores packed ions denser into pore centers.

6. Electrodes with larger pore diameters transformed the overall effect of surface oxidation from being beneficial to ion electrosorption in narrow channels to reducing total capacitance in bulk-like states. Lack of ion confinement in large pores and on external surfaces lowered areal charge accumulation densities, and oxidized graphene nanoplatelets and carbon black electrodes demonstrated lower C_{sp} values in static and dynamic electrochemical measurements than their defunctionalized counterparts.

7. Influence of surface oxygen groups on electrochemical stabilities was strongly convoluted with ion confinement and external: internal surface area aspect ratios. Although oxidized 1 µm diameter CDCs demonstrated lower Q_{eff} values than defunctionalized porous particles, oxidized carbon black and carbon onion particles were more electrochemically stable at 3.25 V potentials in [EMIm$^+$][TFSI$^-$]. On the other hand,

coarse-grained CDCs with near-infinite pore lengths demonstrated high stabilities up to 3.1 V regardless of surface defect composition.

8.   In situ FTIR spectroelectrochemistry experiments confirmed the localized nature of most ion charging/discharging processes in supercapacitors. This finding was applied to redesign CDC particles into hybrid core-shell structures, with outer graphitic mesoporous shells and inner microporous cores for, respectively, greater power and energy densities. Furthermore, coarse-grained CDC particles, which yielded 80 mg cm^{-2} electrode loading, showcased 100 F g^{-1} at 250 mV s^{-1} sweep rates and demonstrated a significantly less expensive implementation pathway for supercapacitors aimed at large-volume grid and transportation storage applications. In a broader approach, the entire construction of supercapacitor devices was overhauled to introduce environmentally benign alternatives for all key materials and components.

CHAPTER 6: OUTLOOK AND FUTURE WORK

Although this work provided important fundamental insights into the role that surface defects play during electrosorption, it raised several important issues that must be addressed in future research efforts. From a performance-oriented perspective, the results have not yet identified specific surface functional groups or graphitic defects that maximize capacitance and yield 50-75 µF cm^{-2} C_{sp} values (estimated theoretical threshold) for porous carbons. Furthermore, irreversible breakdown occurs in all electrode systems, regardless of surface composition, in 2.5 – 3.1 V operating voltage windows, and the full energy density potential of high-performance ionic liquids remains underutilized. However, the results from this dissertation identified several promising pathways and demonstrated their viabilities in several applied deliverables. The following research avenues are likely to advance understanding and capabilities of EDLCs:

1. <u>Effects of hydrogen on carbon surfaces</u>. MD simulations of planar graphene electrodes and electrochemical tests of untreated CDCs suggest –H terminated surfaces as the best surface functionalization option for achieving high capacitance. Coincidentally, all CDCs with high C_{sp} values that had been reported in the literature were hydrogenated during synthesis. However, the standalone effect of hydrogen on surfaces remains unexplored because of materials synthesis (difficult to deposit only hydrogen adatoms) and characterization (difficult to quantify). Approaches such as ion sputtering and dielectric barrier discharge plasma should be explored for homogenous hydrogenation, and neutron activation and spectroscopy may more precisely correlate surface compositions with electrochemistry.

2. <u>Comprehensive structural modeling of CDCs</u>. Extensive materials characterization revealed the heterogeneity of structural features in CDCs. A comprehensive computational model will facilitate predictive chemistry and provide relative prevalence and effects of 5–/6–/7–member rings, graphene sheet vacancies, pore wall thicknesses, atomic corrugation, sp^2/sp^3 bonding, defined functional groups, etc. Future efforts must combine MD simulations with reverse Monte Carlo simulations of structures from experimental characterization of well-defined CDCs.

3. <u>Significance of quantum capacitance</u>. Quantum capacitance contributions have only been inferred for experimental CDCs, and no technique has effectively measured this parameter for porous carbons. Modeling efforts will need to quantify interpore layer thicknesses, and characterization efforts must provide detailed descriptions of surface curvatures and structure-dependent pore shapes. Sensitive microelectrode experiments, neutron scattering characterization, and DFT modeling will correlate defect concentration with voltage-dependent Fermi energy levels and resulting capacitance changes.

4. <u>Charging and ion correlation in coarse-grained CDCs</u>. Although particles with semi-infinite pore lengths and high internal-to-external surface ratios exhibited unexpectedly high capacitances and electrochemical stabilities, the specific charge mechanisms remain unclear. Future experiments must rely on computational simulations and novel characterization methods to determine ion transport through long pores and pore filling/defilling, which may require a novel thermodynamics-based approach and examination of ion solvation/desolvation from a phase transformation perspective.

5. <u>Novel *in situ* characterization.</u> To verify the influence of ionophilic functionalities (such as oxygen) on charge mobilities and accumulation densities, *in situ* experiments

must combine electrochemical testing with real-time ion dynamics measurements. QENS experiments may measure ion dynamics at different applied potentials and provide key initial findings. X-ray and neutron reflectometry measurements on simplified planar model systems, such as functionalized/defective graphene with well-defined functionalities, will provide important insights into electrosorption mechanisms. Furthermore, *in situ* spectroscopy experiments must accompany electrochemical stability measurements to identify breakdown mechanisms and suggest surface adatoms that inhibit irreversible reactions. FTIR, XPS, and GC/MS techniques must be combined with novel chemical treatments and matching electrolytes.

The supercapacitor research field is gaining increasing appreciation of reversible redox contributions from metal oxides, quinones, and organic surface groups. Researchers and commercial entities are gradually moving towards incorporating pseudocapacitance for greater energy densities.[34,279] Research efforts must also take advantage of high energy densities that intercalation processes may offer (up to 120 mAh h^{-1} for anion insertion into graphite),[280] which, arguably, offer the greatest energy storage densities for carbon electrodes. Finally, asymmetric approaches, including different carbons electrodes optimized for negative and positive ions,[204] Li-ion capacitors,[281] and battery/supercapacitor hybrids may expand energy densities and voltage windows. These solutions will feature even more complex electrode-electrolyte interfaces, and this dissertation's theme of heterogeneity and disorder will be highly relevant for such energy storage systems.

LIST OF REFERENCES

[1]   September 2015 - Monthly Energy Review. (Department of Energy, Washington, DC, 2015).

[2]   Larcher, D. & Tarascon, J. M. Towards greener and more sustainable batteries for electrical energy storage. *Nat Chem* **7**, 19-29, (2015).

[3]   Operational Energy Strategy: Implementation Plan. (Department of Defense, Washington, DC, 2011).

[4]   Dunn, B., Kamath, H. & Tarascon, J.-M. Electrical Energy Storage for the Grid: A Battery of Choices. *Science* **334**, 928-935, (2011).

[5]   Simon, P. & Gogotsi, Y. Materials for electrochemical capacitors. *Nature Materials* **7**, 845 - 854, (2008).

[6]   Mahlia, T. M. I., Saktisahdan, T. J., Jannifar, A., Hasan, M. H. & Matseelar, H. S. C. A review of available methods and development on energy storage; technology update. *Renewable and Sustainable Energy Reviews* **33**, 532-545, (2014).

[7]   Zhang, S. & Pan, N. Supercapacitors Performance Evaluation. *Advanced Energy Materials* **5**, (2015).

[8]   Pandolfo, A. G. & Hollenkamp, A. F. Carbon properties and their role in supercapacitors. *Journal of Power Sources* **157**, 11-27, (2006).

[9]   World Ultracapacitor Market. (Frost & Sullivan, 2009).

[10]   Zhai, Y., Dou, Y., Zhao, D., Fulvio, P. F., Mayes, R. T. & Dai, S. Carbon Materials for Chemical Capacitive Energy Storage. *Advanced Materials* **23**, 4828–4850, (2011).

[11]   Tanimura, A., Kovalenko, A. & Hirata, F. Molecular theory of an electrochemical double layer in a nanoporous carbon supercapacitor. *Chemical Physics Letters* **378**, 638–646, (2003).

[12]   Pilon, L., Wang, H. & d'Entremont, A. Recent Advances in Continuum Modeling of Interfacial and Transport Phenomena in Electric Double Layer Capacitors. *Journal of the Electrochemical Society* **162**, A5158-A5178, (2015).

[13]   Merlet, C., Rotenberg, B., Madden, P. A., Taberna, P.-L., Simon, P., Gogotsi, Y. & Salanne, M. On the molecular origin of supercapacitance in nanoporous carbon electrodes. *Nature Materials* **11**, 306-312, (2012).

[14]   Conway, B. E. *Electrochemical Supercapacitors: Scientific Fundamentals and Technological Applications*. (Springer, 1999).

[15]   Rodriguez, R. C., Moncada, A. B., Acevedo, D. F., Planes, G. A., Miras, M. C. & Barbero, C. A. Electroanalysis using modified hierarchical nanoporous carbon materials. *Faraday Discussions* **164**, 147-173, (2013).

[16]   Conway, B. E. & Pell, W. G. Power limitations of supercapacitor operation associated with resistance and capacitance distribution in porous electrode devices. *Journal of Power Sources* **105**, 169-181, (2002).

[17]   Béguin, F., Presser, V., Balducci, A. & Frackowiak, E. Carbons and Electrolytes for Advanced Supercapacitors. *Advanced Materials* **26**, 2219–2251, (2014).

[18]   Laforgue, A. & Robitaille, L. Electrochemical Testing of Ultraporous Membranes as Separators in Mild Aqueous Supercapacitors. *Journal of the Electrochemical Society* **159**, A929-A936, (2012).

[19]   Portet, C., Taberna, P. L., Simon, P. & Laberty-Robert, C. Modification of Al current collector surface by sol–gel deposit for carbon–carbon supercapacitor applications. *Electrochimica Acta* **49**, 905-912, (2004).

[20]   Jost, K., Stenger, D., Perez, C. R., McDonough, J. K., Lian, K., Gogotsi, Y. & Dion, G. Knitted and screen printed carbon-fiber supercapacitors for applications in wearable electronics. *Energy & Environmental Science* **6**, 2698-2705, (2013).

[21]   Meng, C., Liu, C., Chen, L., Hu, C. & Fan, S. Highly Flexible and All-Solid-State Paperlike Polymer Supercapacitors. *Nano Letters* **10**, 4025-4031, (2010).

[22]   Fic, K., Lota, G., Meller, M. & Frackowiak, E. Novel insight into neutral medium as electrolyte for high-voltage supercapacitors. *Energy & Environmental Science* **5**, 5842-5850, (2012).

[23]   O'Mahony, A. M., Silvester, D. S., Aldous, L., Hardacre, C. & Compton, R. G. Effect of Water on the Electrochemical Window and Potential Limits of Room-Temperature Ionic Liquids. *Journal of Chemical & Engineering Data* **53**, 2884–2891, (2008).

[24]   Chmiola, J., Largeot, C., Taberna, P.-L., Simon, P. & Gogotsi, Y. Desolvation of Ions in Subnanometer Pores and Its Effect on Capacitance and Double-Layer Theory. *Angewandte Chemie* **120**, 3440-3443, (2008).

[25]   Kurzweil, P. & Chwistek, M. Electrochemical stability of organic electrolytes in supercapacitors: Spectroscopy and gas analysis of decomposition products. *Journal of Power Sources* **176**, 555–567, (2008).

[26] Jänes, A., Eskusson, J., Thomberg, T. & Lust, E. Electrochemical Double Layer Capacitors Based on Propylene Carbonate Solution Operating from −45°C to 100°C. *Journal of the Electrochemical Society* **161**, A712-A717, (2014).

[27] Aken, K. L. V., McDonough, J. K., Li, S., Feng, G., Chathoth, S. M., Mamontov, E., Fulvio, P. F., Cummings, P. T., Dai, S. & Gogotsi, Y. Effect of cation on diffusion coefficient of ionic liquids at onion-like carbon electrodes. *Journal of Physics: Condensed Matter* **26**, 284104, (2014).

[28] Frolov, A. I., Kirchner, K., Kirchner, T. & Fedorov, M. V. Molecular-scale insights into the mechanisms of ionic liquids interactions with carbon nanotubes. *Faraday Discussions* **154**, 235-247, (2012).

[29] Lin, R., Taberna, P.-L., Fantini, S., Presser, V., Perez, C. R., Malbosc, F., Rupesinghe, N. L., Teo, K. B. K., Gogotsi, Y. & Simon, P. Capacitive Energy Storage from −50 to 100 °C Using an Ionic Liquid Electrolyte. *The Journal of Physical Chemistry Letters* **2**, 2396–2401, (2011).

[30] Tsai, W.-Y., Lin, R., Murali, S., Zhang, L. L., McDonough, J. K., Ruoff, R. S., Taberna, P.-L., Gogotsi, Y. & Simon, P. Outstanding performance of activated graphene based supercapacitors in ionic liquid electrolyte from −50 to 80 °C. *Nano Energy*, in press, (2012).

[31] Fedorov, M. V. & Kornyshev, A. A. Ionic Liquids at Electrified Interfaces. *Chemical Reviews* **114**, 2978-3036, (2014).

[32] Schmuelling, G., Placke, T., Kloepsch, R., Fromm, O., Meyer, H.-W., Passerini, S. & Winter, M. X-ray diffraction studies of the electrochemical intercalation of bis(trifluoromethanesulfonyl)imide anions into graphite for dual-ion cells. *Journal of Power Sources* **239**, 563-571, (2013).

[33] Reddy, M. V., Subba Rao, G. V. & Chowdari, B. V. R. Metal Oxides and Oxysalts as Anode Materials for Li Ion Batteries. *Chemical Reviews* **113**, 5364-5457, (2013).

[34] Simon, P., Gogotsi, Y. & Dunn, B. Where Do Batteries End and Supercapacitors Begin? *Science* **343**, 1210-1211, (2014).

[35] Simon, P. & Gogotsi, Y. Charge storage mechanism in nanoporous carbons and its consequence for electrical double layer capacitors. *Philosophical Transactions of the Royal Society A* **368**, 3457–3467, (2010).

[36] Yan, J., Wei, T., Shao, B., Ma, F., Fan, Z., Zhang, M., Zheng, C., Shang, Y., Qian, W. & Wei, F. Electrochemical properties of graphene nanosheet/carbon black composites as electrodes for supercapacitors. *Carbon* **48**, 1731-1737, (2010).

[37]   Archuleta, M. M. Toxicity of materials used in the manufacture of lithium batteries. *Journal of Power Sources* **54**, 138-142, (1995).

[38]   Couling, D. J., Bernot, R. J., Docherty, K. M., Dixon, J. K. & Maginn, E. J. Assessing the factors responsible for ionic liquid toxicity to aquatic organisms via quantitative structure-property relationship modeling. *Green Chemistry* **8**, 82-90, (2006).

[39]   Novoselov, K. S., Geim, A. K., Morozov, S. V., Jiang, D., Zhang, Y., Dubonos, S. V., Grigorieva, I. V. & Firsov, A. A. Electric Field Effect in Atomically Thin Carbon Films. *Science* **306**, 666-669, (2004).

[40]   Terrones, M., Botello-Méndez, A. R., Campos-Delgado, J., López-Urías, F., Vega-Cantú, Y. I., Rodríguez-Macías, F. J., Elías, A. L., Muñoz-Sandoval, E., Cano-Márquez, A. G., Charlier, J.-C. & Terrones, H. Graphene and graphite nanoribbons: Morphology, properties, synthesis, defects and applications. *Nano Today* **5**, 351-372, (2010).

[41]   Stoller, M. D., Magnuson, C. W., Zhu, Y., Murali, S., Suk, J. W., Piner, R. & Ruoff, R. S. Interfacial capacitance of single layer graphene. *Energy & Environmental Science* **4**, 4685-4689, (2011).

[42]   Hughes, Z. E. & Walsh, T. R. Computational chemistry for graphene-based energy applications: progress and challenges. *Nanoscale* **7**, 6883-6908, (2015).

[43]   Yoo, J. J., Balakrishnan, K., Huang, J., Meunier, V., Sumpter, B. G., Srivastava, A., Conway, M., Leela, A., Reddy, M., Yu, J., Vajtai, R. & Ajayan, P. M. Ultrathin Planar Graphene Supercapacitors. *Nano Letters* **11**, 1423–1427, (2011).

[44]   Stankovich, S., Dikin, D. A., Piner, R. D., Kohlhaas, K. A., Kleinhammes, A., Jia, Y., Wu, Y., Nguyen, S. T. & Ruoff, R. S. Synthesis of graphene-based nanosheets via chemical reduction of exfoliated graphite oxide. *Carbon* **45**, 1558–1565, (2007).

[45]   Zhu, Y., Murali, S., Stoller, M. D., Velamakanni, A., Piner, R. D. & Ruoff, R. S. Microwave assisted exfoliation and reduction of graphite oxide for ultracapacitors. *Carbon* **48**, 2106 –2122, (2010).

[46]   Zhu, Y., Murali, S., Stoller, M. D., Ganesh, K. J., Cai, W., Ferreira, P. J., Pirkle, A., Wallace, R. M., Cychosz, K. A., Thommes, M., Su, D., Stach, E. A. & Ruoff, R. S. Carbon-Based Supercapacitors Produced by Activation of Graphene. *Science* **332**, 1537-1541, (2011).

[47]   Portet, C., Taberna, P. L., Simon, P., Flahaut, E. & Laberty-Robert, C. High power density electrodes for Carbon supercapacitor applications. *Electrochimica Acta* **50**, 4174-4181, (2005).

[48]   Huang, J., Sumpter, B. G., Meunier, V., Yushin, G., Portet, C. & Gogotsi, Y. Curvature effects in carbon nanomaterials: Exohedral versus endohedral supercapacitors. *Journal of Materials Research Society* **25**, 1525-1531, (2010).

[49]   Huang, L.-L., Zhang, L.-Z., Shao, Q., Wang, J., Lu, L.-H., Lu, X.-H., Jiang, S.-Y. & Shen, W.-F. Molecular Dynamics Simulation Study of the Structural Characteristics of Water Molecules Confined in Functionalized Carbon Nanotubes. *The Journal of Physical Chemistry B* **110**, 25761-25768, (2006).

[50]   de las Casas, C. & Li, W. A review of application of carbon nanotubes for lithium ion battery anode material. *Journal of Power Sources* **208**, 74-85, (2012).

[51]   Yang, C.-M., Kim, Y.-J., Miyawaki, J., Kim, Y. A., Yudasaka, M., Iijima, S. & Kaneko, K. Effect of the Size and Position of Ion-Accessible Nanoholes on the Specific Capacitance of Single-Walled Carbon Nanohorns for Supercapacitor Applications. *The Journal of Physical Chemistry C* **119**, 2935-2940, (2015).

[52]   Toupin, M., Belanger, D., Hill, I. R. & Quinn, D. Performance of experimental carbon blacks in aqueous supercapacitors. *Journal of Power Sources* **140**, 203–210, (2005).

[53]   Pech, D., Brunet, M., Durou, H., Huang, P., Mochalin, V., Gogotsi, Y., Taberna, P.-L. & Simon, P. Ultrahigh-power micrometre-sized supercapacitors based on onion-like carbon. *Nature Nanotechnology* **5**, 651–654, (2010).

[54]   McDonough, J., Frolov, A., Presser, V., Niu, J., Miller, C., Ubieto, T., Fedorov, M. & Gogotsi, Y. Influence of the structure of carbon onions on their electrochemical performance in supercapacitor electrodes. *Carbon* **50**, 3298-3309, (2012).

[55]   Sing, K. S. W. in *Pure and Applied Chemistry* Vol. 57   603 (1985).

[56]   Ferrari, A. C. & Robertson, J. Interpretation of Raman spectra of disordered and amorphous carbon. *Physical Review B* **61**, 1495-14107, (2000).

[57]   Zhang, L. L., Gu, Y. & Zhao, X. S. Advanced porous carbon electrodes for electrochemical capacitors. *Journal of Materials Chemistry A* **1**, 9395-9408, (2013).

[58]   Osswald, S., Portet, C., Gogotsi, Y., Laudisio, G., Singer, J. P., Fischer, J. E., Sokolov, V. V., Kukushkina, J. A. & Kravchik, A. E. Porosity control in nanoporous carbide-derived carbon by oxidation in air and carbon dioxide. *Journal of Solid State Chemistry* **182**, 1733-1741, (2009).

[59]   Moreno-Castilla, C., López-Ramón, M. V. & Carrasco-Marín, F. Changes in surface chemistry of activated carbons by wet oxidation. *Carbon* **38**, 1995-2001, (2000).

[60]   Fuertes, A. B., Lota, G., Centeno, T. A. & Frackowiak, E. Templated mesoporous carbons for supercapacitor application. *Electrochimica Acta* **50**, 2799-2805, (2005).

[61]   Gogotsi, Y. & Presser, V. *Carbon nanomaterials*. 2nd edn, (CRC Press, 2013).

[62]   Presser, V., Dennison, C. R., Campos, J., Knehr, K. W., Kumbur, E. C. & Gogotsi, Y. The Electrochemical Flow Capacitor: A New Concept for Rapid Energy Storage and Recovery. *Advanced Energy Materials* **2**, 895-902, (2012).

[63]   Jost, K., Dion, G. & Gogotsi, Y. Textile energy storage in perspective. *Journal of Materials Chemistry A* **2**, 10776-10787, (2014).

[64]   Gogotsi, Y. & Simon, P. True Performance Metrics in Electrochemical Energy Storage. *Science* **334**, 917-918, (2011).

[65]   Feng, G., Jiang, D.-e. & Cummings, P. T. Curvature Effect on the Capacitance of Electric Double Layers at Ionic Liquid/Onion-Like Carbon Interfaces. *Journal of Chemical Theory and Computation* **8**, 1058-1063, (2012).

[66]   Vatamanu, J., Hu, Z., Bedrov, D., Perez, C. & Gogotsi, Y. Increasing Energy Storage in Electrochemical Capacitors with Ionic Liquid Electrolytes and Nanostructured Carbon Electrodes. *The Journal of Physical Chemistry Letters* **4**, 2829-2837, (2013).

[67]   Presser, V., Heon, M. & Gogotsi, Y. Carbide-Derived Carbons - From Porous Networks to Nanotubes and Graphene. *Advanced Functional Materials* **21**, 810-833, (2011).

[68]   Dash, R. K., Yushin, G. & Gogotsi, Y. Synthesis, structure and porosity analysis of microporous and mesoporous carbon derived from zirconium carbide. *Microporous and Mesoporous Materials* **86**, 50-57, (2005).

[69]   Hoffman, E. N., Yushin, G., El-Raghy, T., Gogotsi, Y. & Barsoum, M. W. Micro and mesoporosity of carbon derived from ternary and binary metal carbides. *Microporous and Mesoporous Materials* **112**, 526–532, (2008).

[70]   Janes, A., Thomberg, T., Kurig, H. & Lust, E. Nanoscale fine-tuning of porosity of carbide-derived carbon prepared from molybdenum carbide. *Carbon* **47**, 23-29, (2009).

[71]   Kim, H. S., Singer, J. P., Gogotsi, Y. & Fischer, J. E. Molybdenum carbide-derived carbon for hydrogen storage. *Microporous and Mesoporous Materials* **120**, 267-271, (2009).

[72]   Jänes, A., Thomberg, T. & Lust, E. Synthesis and characterisation of nanoporous carbide-derived carbon by chlorination of vanadium carbide. *Carbon* **45**, 2717-2722, (2007).

[73]   Chmiola, J., Yushin, G., Dash, R. & Gogotsi, Y. Effect of pore size and surface area of carbide derived carbons on specific capacitance. *Journal of Power Sources* **158**, 765–772, (2006).

[74]   Gu, Y., Chen, L., Qian, Y., Zhang, W. & Ma, J. Synthesis of Nanocrystalline Boron Carbide via a Solvothermal Reduction of CCl4 in the Presence of Amorphous Boron Powder. *Journal of the American Ceramic Society* **88**, 225-227, (2005).

[75]   Wang, H. & Gao, Q. Synthesis, characterization and energy-related applications of carbide-derived carbons obtained by the chlorination of boron carbide. *Carbon* **47**, 820-828, (2009).

[76]   Palmer, J. C., Llobet, A., Yeon, S. H., Fischer, J. E., Shi, Y., Gogotsi, Y. & Gubbins, K. E. Modeling the structural evolution of carbide-derived carbons using quenched molecular dynamics. *Carbon* **48**, 1116-1123, (2010).

[77]   Chmiola, J., Yushin, G., Gogotsi, Y., Portet, C., Simon, P. & Taberna, P. L. Anomalous Increase in Carbon Capacitance at Pore Sizes Less Than 1 Nanometer. *Science* **313**, 1760-1763, (2006).

[78]   Urbonaite, S., Halldahl, L. & Svensson, G. Raman spectroscopy studies of carbide derived carbons. *Carbon* **46**, 1942-1947, (2008).

[79]   Vora, P. M., Gopu, P., Rosario-Canales, M., Perez, C. R., Gogotsi, Y., Santiago-Aviles, J. J. & Kikkawa, J. M. Correlating magnetotransport and diamagnetism of sp2-bonded carbon networks through the metal-insulator transition. *Physical Review B* **84**, 155114, (2011).

[80]   Efros, A. L. High volumetric capacitance near the insulator-metal percolation transition. *Physical Review B* **84**, 155134-155137, (2011).

[81]   Portet, C., Kazachkin, D., Osswald, S., Gogotsi, Y. & Borguet, E. Impact of synthesis conditions on surface chemistry and structure of carbide-derived carbons. *Thermochimica Acta* **497**, 137–142, (2010).

[82]   Stein, A., Wang, Z. & Fierke, M. A. Functionalization of Porous Carbon Materials with Designed Pore Architecture. *Advanced Materials* **21**, 265-293, (2009).

[83] Gogotsi, Y., Nikitin, A., Ye, H., Zhou, W., Fischer, J. E., Yi, B., Foley, H. C. & Barsoum, M. W. Nanoporous carbide-derived carbon with tunable pore size. *Nature Materials* **2**, 591-594, (2003).

[84] Portet, C., Yushin, G. & Gogotsi, Y. Effect of Carbon Particle Size on Electrochemical Performance of EDLC. *Journal of the Electrochemical Society* **155**, A531-A536, (2008).

[85] Perez, C. R., Yeon, S.-H., Segalini, J., Presser, V., Taberna, P.-L., Simon, P. & Gogotsi, Y. Structure and Electrochemical Performance of Carbide-Derived Carbon Nanopowders. *Advanced Functional Materials* **23**, 1081–1089, (2013).

[86] Tong, L. & Reddy, R. G. Synthesis of titanium carbide nano-powders by thermal plasma. *Scripta Materialia* **52**, 1253-1258, (2005).

[87] Kondrat, S. & Kornyshev, A. A. Pressing a spring: what does it take to maximize the energy storage in nanoporous supercapacitors? *Nanoscale Horizons*, (2016).

[88] Jian, J., Dapeng, C., De-en, J. & Jianzhong, W. Time-dependent density functional theory for ion diffusion in electrochemical systems. *Journal of Physics: Condensed Matter* **26**, 284102, (2014).

[89] Yachamaneni, S., Yushin, G., Yeon, S.-H., Gogotsi, Y., Howell, C., Sandeman, S., Phillips, G. & Mikhalovsky, S. V. Mesoporous carbide-derived carbon for cytokine removal from blood plasma. *Biomaterials* **31**, 4789-4795, (2010).

[90] Yushin, G., Hoffman, E. N., Barsoum, M. W., Gogotsi, Y., Howell, C. A., Sandeman, S. R., Phillips, G. J., Lloyd, A. W. & Mikhalovsky, S. V. Mesoporous carbide-derived carbon with porosity tuned for efficient adsorption of cytokines. *Biomaterials* **27**, (2006).

[91] Porada, S., Weinstein, L., Dash, R., Wal, A. v. d., Bryjak, M., Gogotsi, Y. & Biesheuvel, P. M. Water Desalination Using Capacitive Deionization with Microporous Carbon Electrodes. *ACS Applied Materials & Interfaces* **4**, 1194–1199, (2012).

[92] Carroll, B., Gogotsi, Y., Kovalchenko, A., Erdemir, A. & McNallan, M. J. Effect of Humidity on the Tribological Properties of Carbide-Derived Carbon (CDC) Films on Silicon Carbide. *Tribology Letters* **15**, 51-55, (2003).

[93] Lin, R., Taberna, P. L., Chmiola, J., Guay, D., Gogotsi, Y. & Simon, P. Microelectrode Study of Pore Size, Ion Size, and Solvent Effects on the Charge/Discharge Behavior of Microporous Carbons for Electrical Double-Layer Capacitors. *Journal of The Electrochemical Society* **156**, A7-A12, (2009).

[94] Jiang, D.-e., Jin, Z. & Wu, J. Oscillation of Capacitance inside Nanopores. *Nano Letters* **11**, 5373-5377, (2011).

[95] Feng, G. & Cummings, P. T. Supercapacitor Capacitance Exhibits Oscillatory Behavior as a Function of Nanopore Size. *The Journal of Physical Chemistry Letters* **22**, 2859–2864, (2011).

[96] Largeot, C., Portet, C., Chmiola, J., Taberna, P.-L., Gogotsi, Y. & Simon, P. Relation between the Ion Size and Pore Size for an Electric Double-Layer Capacitor. *Journal of the American Chemical Society* **130**, 2730–2731, (2008).

[97] Kondrat, S., Georgi, N., Fedorov, M. V. & Kornyshev, A. A. A superionic state in nano-porous double-layer capacitors: insights from Monte Carlo simulations. *Physical Chemistry Chemical Physics* **13**, 11359-11366, (2011).

[98] Kondrat, S. & Kornyshev, A. Superionic state in double-layer capacitors with nanoporous electrodes. *Journal of Physics: Condensed Matter* **23**, 022201, (2011).

[99] Kondrat, S., Perez, C. R., Presser, V., Gogotsi, Y. & Kornyshev, A. A. Effect of pore size and its dispersity on the energy storage in nanoporous supercapacitors *Energy & Environmental Science* **5**, 6474-6479, (2012).

[100] Forse, A. C., Griffin, J. M., Presser, V., Gogotsi, Y. & Grey, C. P. Ring Current Effects: Factors Affecting the NMR Chemical Shift of Molecules Adsorbed on Porous Carbons. *The Journal of Physical Chemistry C* **118**, 7508-7514, (2014).

[101] Boukhalfa, S., Gordon, D., He, L., Melnichenko, Y. B., Nitta, N., Magasinski, A. & Yushin, G. In-Situ Small Angle Neutron Scattering Revealing Ion Sorption in Microporous Carbon Electrical Double Layer Capacitors. *ACS Nano* **8**, 2495–2503, (2014).

[102] Weingarth, D., Zeiger, M., Jäckel, N., Aslan, M., Feng, G. & Presser, V. Graphitization as a Universal Tool to Tailor the Potential-Dependent Capacitance of Carbon Supercapacitors. *Advanced Energy Materials* **4**, (2014).

[103] Kimizuka, O., Tanaike, O., Yamashita, J., Hiraoka, T., Futaba, D. N., Hata, K., Machida, K., Suematsu, S., Tamamitsu, K., Saeki, S., Yamada, Y. & Hatori, H. Electrochemical doping of pure single-walled carbon nanotubes used as supercapacitor electrodes. *Carbon* **46**, 1999-2001, (2008).

[104] Al-zubaidi, A., Inoue, T., Matsushita, T., Ishii, Y., Hashimoto, T. & Kawasaki, S. Cyclic Voltammogram Profile of Single-Walled Carbon Nanotube Electric Double-Layer Capacitor Electrode Reveals Dumbbell Shape. *The Journal of Physical Chemistry C* **116**, 7681-7686, (2012).

[105] Zang, J., Cao, C., Feng, Y., Liu, J. & Zhao, X. Stretchable and High-Performance Supercapacitors with Crumpled Graphene Papers. *Scientific Reports* **4**, 6492, (2014).

[106] Kornyshev, A. A. The simplest model of charge storage in single file metallic nanopores. *Faraday Discussions* **164**, 117-133, (2013).

[107] He, L., Chathoth, S. M., Melnichenko, Y. B., Presser, V., McDonough, J. & Gogotsi, Y. Small-angle neutron scattering characterization of the structure of nanoporous carbons for energy-related applications. *Microporous and Mesoporous Materials* **149**, 46–54, (2012).

[108] Rajput, N. N., Monk, J., Singh, R. & Hung, F. R. On the Influence of Pore Size and Pore Loading on Structural and Dynamical Heterogeneities of an Ionic Liquid Confined in a Slit Nanopore. *The Journal of Physical Chemistry C* **116**, 5169-5181, (2012).

[109] Monk, J., Singh, R. & Hung, F. R. Effects of Pore Size and Pore Loading on the Properties of Ionic Liquids Confined Inside Nanoporous CMK-3 Carbon Materials. *The Journal of Physical Chemistry C* **115**, 3034-3042, (2011).

[110] Bañuelos, J. L., Feng, G., Fulvio, P. F., Li, S., Rother, G., Dai, S., Cummings, P. T. & Wesolowski, D. J. Densification of Ionic Liquid Molecules within a Hierarchical Nanoporous Carbon Structure Revealed by Small-Angle Scattering and Molecular Dynamics Simulation. *Chemistry of Materials* **26**, 1144-1153, (2014).

[111] Bañuelos, J. L., Feng, G., Fulvio, P. F., Li, S., Rother, G., Arend, N., Faraone, A., Dai, S., Cummings, P. T. & Wesolowski, D. J. The influence of a hierarchical porous carbon network on the coherent dynamics of a nanoconfined room temperature ionic liquid: A neutron spin echo and atomistic simulation investigation. *Carbon* **78**, 415-427, (2014).

[112] Lee, A. A. & Kornyshev, S. K. A. A. Single-File Charge Storage in Conducting Nanopores. *Physical Review Letters* **113**, 048701, (2014).

[113] Joseph, S., Mashl, R. J., Jakobsson, E. & Aluru, N. R. Electrolytic Transport in Modified Carbon Nanotubes. *Nano Letters* **3**, 1399-1403, (2003).

[114] Baldelli, S. Surface Structure at the Ionic Liquid−Electrified Metal Interface. *Accounts of Chemical Research* **41**, 421-431, (2008).

[115] Ohba, T., Kojima, N., Kanoh, H. & Kaneko, K. Unique Hydrogen-Bonded Structure of Water around Ca Ions Confined in Carbon Slit Pores. *The Journal of Physical Chemistry C* **113**, 12622-12624, (2009).

[116] Richey, F. W., Tran, C., Kalra, V. & Elabd, Y. A. Ionic Liquid Dynamics in Nanoporous Carbon Nanofibers in Supercapacitors Measured with in Operando Infrared Spectroelectrochemistry. *The Journal of Physical Chemistry C* **118**, 21846-21855, (2014).

[117] Canongia Lopes, J. N. A. & Pádua, A. A. H. Nanostructural Organization in Ionic Liquids. *The Journal of Physical Chemistry B* **110**, 3330-3335, (2006).

[118] Wang, S., Li, S., Cao, Z. & Yan, T. Molecular Dynamic Simulations of Ionic Liquids at Graphite Surface. *The Journal of Physical Chemistry C* **114**, 990-995, (2010).

[119] Vatamanu, J. & Bedrov, D. Capacitive Energy Storage: Current and Future Challenges. *The Journal of Physical Chemistry Letters*, 3594-3609, (2015).

[120] Cambaz, Z. G., Yushin, G., Osswald, S., Mochalin, V. & Gogotsi, Y. Noncatalytic synthesis of carbon nanotubes, graphene and graphite on SiC. *Carbon* **46**, 841-849, (2008).

[121] Stoner, B. R., Raut, A. S., Brown, B., Parker, C. B. & Glass, J. T. Graphenated carbon nanotubes for enhanced electrochemical double layer capacitor performance. *Applied Physics Letters* **99**, 183104, (2011).

[122] Wood, B. C., Ogitsu, T., Otani, M. & Biener, J. First-Principles-Inspired Design Strategies for Graphene-Based Supercapacitor Electrodes. *The Journal of Physical Chemistry C* **118**, 4-15, (2014).

[123] Xia, J., Chen, F., Li, J. & Tao, N. Measurement of the quantum capacitance of graphene. *Nature Nanotechnology* **4**, 505-509, (2009).

[124] Ji, H., Zhao, X., Qiao, Z., Jung, J., Zhu, Y., Lu, Y., Zhang, L. L., MacDonald, A. H. & Ruoff, R. S. Capacitance of carbon-based electrical double-layer capacitors. *Nature Communications* **5**, 3317, (2014).

[125] Fang, T., Konar, A., Xing, H. & Jena, D. Carrier statistics and quantum capacitance of graphene sheets and ribbons. *Applied Physics Letters* **91**, 092109, (2007).

[126] Uesugi, E., Goto, H., Eguchi, R., Fujiwara, A. & Kubozono, Y. Electric double-layer capacitance between an ionic liquid and few-layer graphene. *Sci. Rep.* **3**, 1595, (2013).

[127] Zhan, C., Neal, J., Wu, J. & Jiang, D.-e. Quantum Effects on the Capacitance of Graphene-Based Electrodes. *The Journal of Physical Chemistry C* **119**, 22297–22303, (2015).

[128] Faber, K., Badaczewski, F., Oschatz, M., Mondin, G., Nickel, W., Kaskel, S. & Smarsly, B. M. In-Depth Investigation of the Carbon Microstructure of Silicon Carbide-Derived Carbons by Wide-Angle X-ray Scattering. *The Journal of Physical Chemistry C* **118**, 15705-15715, (2014).

[129] Vatamanu, J., Cao, L., Borodin, O., Bedrov, D. & Smith, G. D. On the Influence of Surface Topography on the Electric Double Layer Structure and Differential Capacitance of Graphite/Ionic Liquid Interfaces. *The Journal of Physical Chemistry Letters* **2**, 2267-2272, (2011).

[130] Kondrat, S., Wu, P., Qiao, R. & Kornyshev, A. A. Accelerating charging dynamics in subnanometre pores. *Nat Mater* **13**, 387-393, (2014).

[131] Feng, G., Li, S., Zhao, W. & Cummings, P. T. Microstructure of room temperature ionic liquids at stepped graphite electrodes. *AIChE Journal* **61**, 3022-3028, (2015).

[132] Shen, W., Li, Z. & Liu, Y. Surface Chemical Functional Groups Modification of Porous Carbon. *Recent Patents on Chemical Engineering* **1**, 27-40, (2008).

[133] Seredych, M., Hulicova-Jurcakova, D., Lu, G. Q. & Bandosz, T. J. Surface functional groups of carbons and the effects of their chemical character, density and accessibility to ions on electrochemical performance. *Carbon* **46**, 1475-1488, (2008).

[134] Kim, P., Zheng, Y. & Agnihotri, S. Adsorption Equilibrium and Kinetics of Water Vapor in Carbon Nanotubes and Its Comparison with Activated Carbon. *Industrial & Engineering Chemistry Research* **47**, 3170–3178, (2008).

[135] Zhou, H., Ganesh, P., Presser, V., Wander, M. C. F., Fenter, P., Kent, P. R. C., Jiang, D.-e., Chialvo, A. A., McDonough, J., Shuford, K. L. & Gogotsi, Y. Understanding controls on interfacial wetting at epitaxial graphene: Experiment and theory. *Physical Review B* **85**, 035406, (2012).

[136] Montes-Moran, M. A., Suarez, D., Menendez, J. A. & Fuente, E. On the nature of basic sites on carbon surfaces: an overview. *Carbon* **42**, 1219–1225, (2003).

[137] Xu, K., Ji, X., Chen, C., Wan, H., Miao, L. & Jiang, J. Electrochemical double layer near polar reduced graphene oxide electrode: Insights from molecular dynamic study. *Electrochimica Acta* **166**, 142-149, (2015).

[138] Kerisit, S., Schwenzer, B. & Vijayakumar, M. Effects of Oxygen-Containing Functional Groups on Supercapacitor Performance. *The Journal of Physical Chemistry Letters* **5**, 2330-2334, (2014).

[139] DeYoung, A. D., Park, S.-W., Dhumal, N. R., Shim, Y., Jung, Y. & Kim, H. J. Graphene Oxide Supercapacitors: A Computer Simulation Study. *The Journal of Physical Chemistry C* **118**, 18472-18480, (2014).

[140] Fornasiero, F., In, J. B., Kim, S., Park, H. G., Wang, Y., Grigoropoulos, C. P., Noy, A. & Bakajin, O. pH-Tunable Ion Selectivity in Carbon Nanotube Pores. *Langmuir* **26**, 14848-14853, (2010).

[141] Black, J. M., Baris Okatan, M., Feng, G., Cummings, P. T., Kalinin, S. V. & Balke, N. Topological defects in electric double layers of ionic liquids at carbon interfaces. *Nano Energy* **15**, 737-745, (2015).

[142] Kondrat, S. & Kornyshev, A. Charging Dynamics and Optimization of Nanoporous Supercapacitors. *The Journal of Physical Chemistry C* **117**, 12399-12406, (2013).

[143] Lee, A. A., Kondrat, S., Vella, D. & Goriely, A. Dynamics of Ion Transport in Ionic Liquids. *Physical Review Letters* **115**, 106101, (2015).

[144] Alpha, A. L., Svyatoslav, K., Gleb, O. & Alexei, A. K. Charging dynamics of supercapacitors with narrow cylindrical nanopores. *Nanotechnology* **25**, 315401, (2014).

[145] G. Lota, B. G., Machnikowska, H., Machnikowski, J. & Frackowiak, E. Effect of nitrogen in carbon electrode on the supercapacitor performance. *Chemical Physics Letters* **404**, 53–58, (2005).

[146] Hulicova-Jurcakova, D., Seredych, M., Lu, G. Q. & Bandosz, T. J. Combined Effect of Nitrogen- and Oxygen-Containing Functional Groups of Microporous Activated Carbon on its Electrochemical Performance in Supercapacitors. *Advanced Functional Materials* **19**, 438–447, (2009).

[147] McCann, R., Roya, S. S., Papakonstantinou, P., Bain, M. F., Gamble, H. S. & McLaughlin, J. A. Chemical bonding modifications of tetrahedral amorphous carbon and nitrogenated tetrahedral amorphous carbon films induced by rapid thermal annealing. *Thin Solid Films* **482**, 34-40, (2005).

[148] Szymanski, G. S., Grzybek, T. & Papp, H. Influence of nitrogen surface functionalities on the catalytic activity of activated carbon in low temperature SCR of NOx with NH3. *Catalysis Today* **90**, 51–59, (2004).

[149] Zhao, L., Fan, L.-Z., Zhou, M.-Q., Guan, H., Qiao, S., Antonietti, M. & Titirici, M.-M. Nitrogen-Containing Hydrothermal Carbons with Superior Performance in Supercapacitors. *Advanced Materials* **22**, 5202–5206, (2010).

[150] Frackowiak, E., Lota, G., Machnikowski, J., Vix-Guterl, C. & Beguin, F. Optimisation of supercapacitors using carbons with controlled nanotexture and nitrogen content. *Electrochimica Acta* **51**, 2209–2214, (2006).

[151] Azais, P., Duclaux, L., Florian, P., Massiot, D., Lillo-Rodenas, M.-A., Linares-Solano, A., Peres, J.-P., Jehoulet, C. & Beguin, F. Causes of supercapacitors ageing in organic electrolyte. *Journal of Power Sources* **171**, 1046-1053, (2007).

[152] Borodin, O., Behl, W. & Jow, T. R. Oxidative Stability and Initial Decomposition Reactions of Carbonate, Sulfone, and Alkyl Phosphate-Based Electrolytes. *The Journal of Physical Chemistry C* **117**, 8661-8682, (2013).

[153] Profatilova, I. A., Choi, N.-S., Roh, S. W. & Kim, S. S. Electrochemical and thermal properties of graphite electrodes with imidazolium- and piperidinium-based ionic liquids. *Journal of Power Sources* **192**, 636-643, (2009).

[154] Romann, T., Oll, O., Pikma, P., Tamme, H. & Lust, E. Surface chemistry of carbon electrodes in 1-ethyl-3-methylimidazolium tetrafluoroborate ionic liquid – an in situ infrared study. *Electrochimica Acta* **125**, 183–190, (2014).

[155] Kostecki, R., Richardson, T., Boesenberg, U., Pollak, E. & Lux, S. Modified carbon black materials for lithium-ion batteries. United States Patent patent (2014).

[156] Mochalin, V. N., Shenderova, O., Ho, D. & Gogotsi, Y. The properties and applications of nanodiamonds. *Nat Nano* **7**, 11-23, (2012).

[157] Osswald, S., Havel, M. & Gogotsi, Y. Monitoring oxidation of multiwalled carbon nanotubes by Raman spectroscopy. *Journal of Raman Spectroscopy* **38**, 728-736, (2007).

[158] Wan, L., Wang, J., Xie, L., Sun, Y. & Li, K. Nitrogen-Enriched Hierarchically Porous Carbons Prepared from Polybenzoxazine for High-Performance Supercapacitors. *ACS Applied Materials & Interfaces* **6**, 15583-15596, (2014).

[159] Noked, M., Soffer, A. & Aurbach, D. The electrochemistry of activated carbonaceous materials: past, present, and future. *Journal of Solid State Electrochemistry* **15**, 1563-1578, (2011).

[160] Ros, T. G., Dillen, A. J. v., Geus, J. W. & Koningsberger, D. C. Surface Oxidation of Carbon Nanofibres. *Chemistry - A European Journal* **8**, 1151–1162, (2002).

[161] Xie, Z. W., Wang, L. P., Wang, X. F., Huang, L., Lu, Y. & Yan, J. C. Influence of high temperature annealing on the structure, hardness and tribological properties of diamond-like carbon and TiAlSiCN nanocomposite coatings. *Applied Surface Science* **258**, 1206-1211, (2011).

[162] Frisk, K. A revised thermodynamic description of the Ti-C system. *Calphad Computer Coupling Of Phase Diagrams And Thermochemistry* **27**, 367–373, (2003).

[163] Allen, L., Ranyi, Z. & McNallan, M. Kinetics of conversion of silicon carbide to carbide derived carbon. *Journal of Physics: Condensed Matter* **18**, S1763, (2006).

[164] Dash, R., Chmiola, J., Yushin, G., Gogotsi, Y., Laudisio, G., Singer, J., Fischer, J. & Kucheyev, S. Titanium carbide derived nanoporous carbon for energy-related applications. *Carbon* **44**, 2489-2497, (2006).

[165] Hendricks, T. R., Lu, J., Drzal, L. T. & Lee, I. Intact pattern transfer of conductive exfoliated graphite nanoplatelet composite films to polyelectrolyte multilayer platforms. *Advanced Materials* **20**, 2008-2012, (2008).

[166] Shao, Y., Zhang, S., Wang, C., Nie, Z., Liu, J., Wang, Y. & Lin, Y. Highly durable graphene nanoplatelets supported Pt nanocatalysts for oxygen reduction. *Journal of Power Sources* **195**, 4600-4605, (2010).

[167] Chmiola, J., Osswald, S. & Gogotsi, Y. Structural Evolution of Carbide-Derived Carbons upon Vacuum Annealing. *Carbon* **50**, 4880-4886, (2012).

[168] Ros, T. G., van Dillen, A. J., Geus, J. W. & Koningsberger, D. C. Surface Oxidation of Carbon Nanofibres. *Chemistry – A European Journal* **8**, 1151-1162, (2002).

[169] Lowell, S. & Shields, J. E. *Powder surface area and porosity*. Vol. 2 (Springer Science & Business Media, 2013).

[170] Brunauer, S., Emmett, P. H. & Teller, E. Adsorption of Gases in Multimolecular Layers. *Journal of the American Chemical Society* **60**, 309-319, (1938).

[171] Gor, G. Y., Thommes, M., Cychosz, K. A. & Neimark, A. V. Quenched solid density functional theory method for characterization of mesoporous carbons by nitrogen adsorption. *Carbon* **50**, 1583 –1590, (2012).

[172] Caguiat, J. N., Kirk, D. W. & Jia, C. Q. Uncertainties in characterization of nanoporous carbons using density functional theory-based gas physisorption. *Carbon* **72**, 47-56, (2014).

[173] Zhao, J., Gao, C. Y. & Liu, D. The extended Q-range small-angle neutron scattering diffractometer at the SNS. *Journal of Applied Crystallography* **43**, 1068-1077, (2010).

[174] Arnold, O., Bilheux, J. C., Borreguero, J. M., Buts, A., Campbell, S. I., Chapon, L., Doucet, M., Draper, N., Ferraz Leal, R., Gigg, M. A., Lynch, V. E.,

Markvardsen, A., Mikkelson, D. J., Mikkelson, R. L., Miller, R., Palmen, K., Parker, P., Passos, G., Perring, T. G., Peterson, P. F., Ren, S., Reuter, M. A., Savici, A. T., Taylor, J. W., Taylor, R. J., Tolchenov, R., Zhou, W. & Zikovsky, J. Mantid—Data analysis and visualization package for neutron scattering and SR experiments. *Nuclear Instruments and Methods in Physics Research Section A: Accelerators, Spectrometers, Detectors and Associated Equipment* **764**, 156-166, (2014).

[175] Etzold, B. J. M., Neitzel, I., Kett, M., Strobl, F., Mochalin, V. N. & Gogotsi, Y. Layer-by-Layer Oxidation for Decreasing the Size of Detonation Nanodiamond. *Chemistry of Materials* **26**, 3479-3484, (2014).

[176] Laudisio, G., Dash, R. K., Singer, J. P., Yushin, G., Gogotsi, Y. & Fischer, J. E. Carbide-Derived Carbons: A Comparative Study of Porosity Based on Small-Angle Scattering and Adsorption Isotherms. *Langmuir* **22**, 8945-8950, (2006).

[177] Engel, M., Stuhn, B., Schneider, J. J., Cornelius, T. & Naumann, M. Small-angle X-ray scattering (SAXS) off parallel, cylindrical, well-defined nanopores: from random pore distribution to highly ordered samples. *Applied Physics B* **97**, 99-108, (2009).

[178] Dillon, R. O. & Woollam, J. A. Use of Raman scattering to investigate disorder and crystallite formation in as-deposited and annealed carbon films *Physical Review B* **29**, 3482-3489, (1984).

[179] Petkov, V., Ren, Y., Kabekkodu, S. & Murphy, D. Atomic pair distribution functions analysis of disordered low-Z materials. *Physical Chemistry Chemical Physics* **15**, 8544-8554, (2013).

[180] Smith, M. A., Foley, H. C. & Lobo, R. F. A simple model describes the PDF of a non-graphitizing carbon. *Carbon* **42**, 2041-2048, (2004).

[181] Neuefeind, J., Feygenson, M., Carruth, J., Hoffmann, R. & Chipley, K. K. The Nanoscale Ordered MAterials Diffractometer NOMAD at the Spallation Neutron Source SNS. *Nuclear Instruments and Methods in Physics Research Section B: Beam Interactions with Materials and Atoms* **287**, 68-75, (2012).

[182] Mochalin, V. N., Neitzel, I., Etzold, B. J. M., Peterson, A., Palmese, G. & Gogotsi, Y. Covalent Incorporation of Aminated Nanodiamond into an Epoxy Polymer Network. *ACS Nano* **5**, 7494-7502, (2011).

[183] Urbonaite, S., Wachtmeister, S., Mirguet, C., Coronel, E., Zou, W., Csillag, S. & Svensson, G. EELS studies of carbide derived carbons. *Carbon* **45**, 2047-2053, (2007).

[184] Muller, D. A., Tzou, Y., Raj, R. & Silcox, J. Mapping sp2 and sp3 states of carbon at sub-nanometre spatial resolution. *Nature* **366**, 725-727, (1993).

[185] Papworth, A. J., Kiely, C. J., Burden, A. P., Silva, S. R. P. & Amaratunga, G. A. J. Electron-energy-loss spectroscopy characterization of the sp2 bonding fraction within carbon thin films. *Physical Review B* **62**, 12628-12631, (2000).

[186] Lotfi, M., Nejib, M. & Naceur, M. *Cell Adhesion to Biomaterials: Concept of Biocompatibility*. (2013).

[187] Embs, J. P., Burankova, T., Reichert, E. & Hempelmann, R. Cation Dynamics in the Pyridinium Based Ionic Liquid 1-N-Butylpyridinium Bis((trifluoromethyl)sulfonyl) As Seen by Quasielastic Neutron Scattering. *The Journal of Physical Chemistry B* **116**, 13265-13271, (2012).

[188] Chathoth, S. M., Mamontov, E., Kolesnikov, A. I., Gogotsi, Y. & Wesolowski, D. J. Quasielastic neutron scattering study of water confined in carbon nanopores. *Europhysics Letters* **95**, 56001, (2011).

[189] Mamontov, E. & Herwig, K. W. A time-of-flight backscattering spectrometer at the Spallation Neutron Source, BASIS. *Review of Scientific Instruments* **82**, 085109, (2011).

[190] Cole, K. S. & Cole, R. H. Dispersion and Absorption in Dielectrics I. Alternating Current Characteristics. *The Journal of Chemical Physics* **9**, 341-351, (1941).

[191] Seeger, P. A., Daemen, L. L. & Larese, J. Z. Resolution of VISION, a crystal-analyzer spectrometer. *Nuclear Instruments and Methods in Physics Research Section A: Accelerators, Spectrometers, Detectors and Associated Equipment* **604**, 719-728, (2009).

[192] Sears, V. F. Neutron scattering lengths and cross sections. *Neutron news* **3**, 26-37, (1992).

[193] Forse, A. C., Griffin, J. M., Wang, H., Trease, N. M., Presser, V., Gogotsi, Y., Simon, P. & Grey, C. P. Nuclear magnetic resonance study of ion adsorption on microporous carbide-derived carbon. *Physical Chemistry Chemical Physics* **15**, 7722-7730, (2013).

[194] Forse, A. C., Merlet, C., Allan, P. K., Humphreys, E. K., Griffin, J. M., Aslan, M., Zeiger, M., Presser, V., Gogotsi, Y. & Grey, C. P. New Insights into the Structure of Nanoporous Carbons from NMR, Raman, and Pair Distribution Function Analysis. *Chemistry of Materials* **27**, 6848-6857, (2015).

[195] Hess, B., Kutzner, C., Van Der Spoel, D. & Lindahl, E. GROMACS 4: Algorithms for highly efficient, load-balanced, and scalable molecular simulation. *Journal of chemical theory and computation* **4**, 435-447, (2008).

[196] Canongia Lopes, J. N. & Pádua, A. A. H. Molecular Force Field for Ionic Liquids Composed of Triflate or Bistriflylimide Anions. *The Journal of Physical Chemistry B* **108**, 16893-16898, (2004).

[197] Canongia Lopes, J. N., Deschamps, J. & Pádua, A. A. H. Modeling Ionic Liquids Using a Systematic All-Atom Force Field. *The Journal of Physical Chemistry B* **108**, 2038-2047, (2004).

[198] Cornell, W. D., Cieplak, P., Bayly, C. I., Gould, I. R., Merz, K. M., Ferguson, D. M., Spellmeyer, D. C., Fox, T., Caldwell, J. W. & Kollman, P. A. A Second Generation Force Field for the Simulation of Proteins, Nucleic Acids, and Organic Molecules. *Journal of the American Chemical Society* **117**, 5179-5197, (1995).

[199] Yan, J.-A. & Chou, M. Y. Oxidation functional groups on graphene: Structural and electronic properties. *Physical Review B* **82**, 125403, (2010).

[200] Hoover, W. G. Canonical dynamics: Equilibrium phase-space distributions. *Physical Review A* **31**, 1695-1697, (1985).

[201] Yeh, I.-C. & Berkowitz, M. L. Ewald summation for systems with slab geometry. *The Journal of Chemical Physics* **111**, 3155-3162, (1999).

[202] Darden, T., York, D. & Pedersen, L. Particle mesh Ewald: An N·log(N) method for Ewald sums in large systems. *The Journal of Chemical Physics* **98**, 10089-10092, (1993).

[203] Cao, W. J., Shih, J., Zheng, J. P. & Doung, T. Development and characterization of Li-ion capacitor pouch cells. *Journal of Power Sources* **257**, 388-393, (2014).

[204] Van Aken, K. L., Beidaghi, M. & Gogotsi, Y. Formulation of Ionic-Liquid Electrolyte to Expand the Voltage Window of Supercapacitors. *Angewandte Chemie International Edition* **54**, 4806-4809, (2015).

[205] Stoller, M. D. & Ruoff, R. S. Best practice methods for determining an electrode material's performance for ultracapacitors. *Energy & Environmental Science* **3**, 1294-1301, (2010).

[206] Gau, V., Ma, S.-C., Wang, H., Tsukuda, J., Kibler, J. & Haake, D. A. Electrochemical molecular analysis without nucleic acid amplification. *Methods* **37**, 73-83, (2005).

[207] McEwen, A. B., Ngo, H. L., LeCompte, K. & Goldman, J. L. Electrochemical Properties of Imidazolium Salt Electrolytes for Electrochemical Capacitor Applications. *Journal of the Electrochemical Society* **146**, 1687-1695, (1999).

[208] Taberna, P. L., Portet, C. & Simon, P. Electrode surface treatment and electrochemical impedance spectroscopy study on carbon/carbon supercapacitors. *Applied Physics A* **82**, 639-646, (2006).

[209] Taberna, P. L., Simon, P. & Fauvarque, J. F. Electrochemical Characteristics and Impedance Spectroscopy Studies of Carbon-Carbon Supercapacitors. *Journal of the Electrochemical Society* **150**, A292-A300, (2003).

[210] Dyatkin, B. & Gogotsi, Y. Effects of Structural Disorder and Surface Chemistry on Electric Conductivity and Capacitance of Porous Carbon Electrodes. *Faraday Discussions* **172**, 139-162, (2014).

[211] Wang, Y. & Xia, Y. Recent Progress in Supercapacitors: From Materials Design to System Construction. *Advanced Materials* **25**, 5336-5342, (2013).

[212] Ganesh, P., Kent, P. & Mochalin, V. Formation, characterization, and dynamics of onion-like carbon structures for electrical energy storage from nanodiamonds using reactive force fields. *Journal of Applied Physics* **110**, 073506, (2011).

[213] Sánchez-González, J., Macías-García, A., Alexandre-Franco, M. F. & Gómez-Serrano, V. Electrical conductivity of carbon blacks under compression. *Carbon* **43**, 741-747, (2005).

[214] Zhang, L. L., Zhao, X., Stoller, M. D., Zhu, Y., Ji, H., Murali, S., Wu, Y., Perales, S., Clevenger, B. & Ruoff, R. S. Highly Conductive and Porous Activated Reduced Graphene Oxide Films for High-Power Supercapacitors. *Nano Letters* **12**, 1806-1812, (2012).

[215] Singh, D. K., Iyer, P. K. & Giri, P. K. Diameter dependence of oxidative stability in multiwalled carbon nanotubes: Role of defects and effect of vacuum annealing. *Journal of Applied Physics* **108**, 084313, (2010).

[216] Van Duin, A. C., Dasgupta, S., Lorant, F. & Goddard, W. A. ReaxFF: a reactive force field for hydrocarbons. *The Journal of Physical Chemistry A* **105**, 9396-9409, (2001).

[217] Aktulga, H. M., Fogarty, J. C., Pandit, S. A. & Grama, A. Y. Parallel reactive molecular dynamics: Numerical methods and algorithmic techniques. *Parallel Computing* **38**, 245-259, (2012).

[218] Plimpton, S. Fast Parallel Algorithms for Short-Range Molecular Dynamics. *Journal of Computational Physics* **117**, 1-19, (1995).

[219] Srinivasan, S. G., van Duin, A. C. T. & Ganesh, P. Development of a ReaxFF Potential for Carbon Condensed Phases and Its Application to the Thermal Fragmentation of a Large Fullerene. *The Journal of Physical Chemistry A* **119**, 571-580, (2015).

[220] Rappe, A. K. & Goddard, W. A. Charge equilibration for molecular dynamics simulations. *The Journal of Physical Chemistry* **95**, 3358-3363, (1991).

[221] Nakano, A. Parallel multilevel preconditioned conjugate-gradient approach to variable-charge molecular dynamics. *Computer Physics Communications* **104**, 59-69, (1997).

[222] Sun, L., Li, Q., Ren, H., Su, H., Shi, Q. & Yang, J. Strain effect on electronic structures of graphene nanoribbons: A first-principles study. *The Journal of Chemical Physics* **129**, 074704, (2008).

[223] Tallo, I., Thomberg, T., Kontturi, K., Jänes, A. & Lust, E. Nanostructured carbide-derived carbon synthesized by chlorination of tungsten carbide. *Carbon* **49**, 4427-4433, (2011).

[224] Weisbecker, P., Leyssale, J.-M., Fischer, H. E., Honkimäki, V., Lalanne, M. & Vignoles, G. L. Microstructure of pyrocarbons from pair distribution function analysis using neutron diffraction. *Carbon* **50**, 1563-1573, (2012).

[225] Pinkert, K., Oschatz, M., Borchardt, L., Klose, M., Zier, M., Nickel, W., Giebeler, L., Oswald, S., Kaskel, S. & Eckert, J. Role of Surface Functional Groups in Ordered Mesoporous Carbide-Derived Carbon/Ionic Liquid Electrolyte Double-Layer Capacitor Interfaces. *ACS Applied Materials & Interfaces* **6**, 2922-2928, (2014).

[226] Lemus, J., Palomar, J., Heras, F., Gilarranz, M. A. & Rodriguez, J. J. Developing criteria for the recovery of ionic liquids from aqueous phase by adsorption with activated carbon. *Separation and Purification Technology* **97**, 11-19, (2012).

[227] Balducci, A., Dugas, R., Taberna, P. L., Simon, P., Plée, D., Mastragostino, M. & Passerini, S. High temperature carbon–carbon supercapacitor using ionic liquid as electrolyte. *Journal of Power Sources* **165**, 922-927, (2007).

[228] Segalini, J., Daffos, B., Taberna, P. L., Gogotsi, Y. & Simon, P. Qualitative Electrochemical Impedance Spectroscopy study of ion transport into sub-nanometer carbon pores in Electrochemical Double Layer Capacitor electrodes. *Electrochimica Acta* **55**, 7489–7494, (2010).

[229] Liu, X.-m., Zhang, R., Zhan, L., Long, D.-h., Qiao, W.-m., Yang, J.-h. & Ling, L.-c. Impedance of carbon aerogel/activated carbon composites as electrodes of

electrochemical capacitors in aprotic electrolyte. *New Carbon Materials* **22**, 153-158, (2007).

[230] Prabaharan, S., Vimala, R. & Zainal, Z. Nanostructured mesoporous carbon as electrodes for supercapacitors. *Journal of Power Sources* **161**, 730-736, (2006).

[231] Mysyk, R., Raymundo-Piñero, E. & Béguin, F. Saturation of subnanometer pores in an electric double-layer capacitor. *Electrochemistry Communications* **11**, 554-556, (2009).

[232] Dyatkin, B., Mamontov, E., Cook, K. C. & Gogotsi, Y. Capacitance, Charge Dynamics, and Electrolyte-Surface Interactions in Functionalized Carbide-Derived Carbon Electrodes. *Progress in Natural Science - Materials International*, (2015).

[233] Kosmulski, M., Gustafsson, J. & Rosenholm, J. B. Thermal stability of low temperature ionic liquids revisited. *Thermochimica Acta* **412**, 47-53, (2004).

[234] Hueso, J. L., Espinós, J. P., Caballero, A., Cotrino, J. & González-Elipe, A. R. XPS investigation of the reaction of carbon with NO, O2, N2 and H2O plasmas. *Carbon* **45**, 89-96, (2007).

[235] Zhang, L., Zhang, F., Yang, X., Long, G., Wu, Y., Zhang, T., Leng, K., Huang, Y., Ma, Y., Yu, A. & Chen, Y. Porous 3D graphene-based bulk materials with exceptional high surface area and excellent conductivity for supercapacitors. *Scientific Reports* **3**, 1408, (2013).

[236] Kim, K.-S. & Park, S.-J. Synthesis and high electrochemical capacitance of N-doped microporous carbon/carbon nanotubes for supercapacitor. *Journal of Electroanalytical Chemistry* **673**, 58-64, (2012).

[237] Chu, X.-q., Gajapathy, M., Weiss, K. L., Mamontov, E., Ng, J. D. & Coates, L. Dynamic Behavior of Oligomeric Inorganic Pyrophosphatase Explored by Quasielastic Neutron Scattering. *The Journal of Physical Chemistry B* **116**, 9917-9921, (2012).

[238] Chu, X.-q., Lagi, M., Mamontov, E., Fratini, E., Baglioni, P. & Chen, S.-H. Experimental evidence of logarithmic relaxation in single-particle dynamics of hydrated protein molecules. *Soft Matter* **6**, 2623-2627, (2010).

[239] Chu, X.-q., Mamontov, E., O'Neill, H. & Zhang, Q. Temperature Dependence of Logarithmic-like Relaxational Dynamics of Hydrated tRNA. *The Journal of Physical Chemistry Letters* **4**, 936-942, (2013).

[240] Ewert, J. K., Weingarth, D., Denner, C., Friedrich, M., Zeiger, M., Schreiber, A., Jackel, N., Presser, V. & Kempe, R. Enhanced capacitance of nitrogen-doped

hierarchically porous carbide-derived carbon in matched ionic liquids. *Journal of Materials Chemistry A* **3**, 18906-18912, (2015).

[241] Lin, R., Huang, P., Ségalini, J., Largeot, C., Taberna, P. L., Chmiola, J., Gogotsi, Y. & Simon, P. Solvent effect on the ion adsorption from ionic liquid electrolyte into sub-nanometer carbon pores. *Electrochimica Acta* **54**, 7025-7032, (2009).

[242] Ratajczak, P., Jurewicz, K., Skowron, P., Abbas, Q. & Béguin, F. Effect of accelerated ageing on the performance of high voltage carbon/carbon electrochemical capacitors in salt aqueous electrolyte. *Electrochimica Acta* **130**, 344-350, (2014).

[243] Dementev, N., Osswald, S., Gogotsi, Y. & Borguet, E. Purification of carbon nanotubes by dynamic oxidation in air. *Journal of Materials Chemistry* **19**, 7904-7908, (2009).

[244] Lassègues, J. C., Grondin, J., Holomb, R. & Johansson, P. Raman and ab initio study of the conformational isomerism in the 1-ethyl-3-methyl-imidazolium bis(trifluoromethanesulfonyl)imide ionic liquid. *Journal of Raman Spectroscopy* **38**, 551-558, (2007).

[245] Umebayashi, Y., Fujimori, T., Sukizaki, T., Asada, M., Fujii, K., Kanzaki, R. & Ishiguro, S.-i. Evidence of Conformational Equilibrium of 1-Ethyl-3-methylimidazolium in Its Ionic Liquid Salts: Raman Spectroscopic Study and Quantum Chemical Calculations. *The Journal of Physical Chemistry A* **109**, 8976-8982, (2005).

[246] Hayes, R., Warr, G. G. & Atkin, R. Structure and Nanostructure in Ionic Liquids. *Chemical Reviews* **115**, 6357-6426, (2015).

[247] Debye, P., Anderson, H. R. & Brumberger, H. Scattering by an Inhomogeneous Solid. II. The Correlation Function and Its Application. *Journal of Applied Physics* **28**, 679-683, (1957).

[248] Firsich, D. W. Carbon supercapacitor electrode materials. United States Patent patent (1997).

[249] Tran, C., Kafle, J., Yang, X.-Q. & Qu, D. Increased discharge capacity of a Li-air activated carbon cathode produced by preventing carbon surface passivation. *Carbon* **49**, 1266-1271, (2011).

[250] Hu, Z., Vatamanu, J., Borodin, O. & Bedrov, D. A molecular dynamics simulation study of the electric double layer and capacitance of [BMIM][PF6] and [BMIM][BF4] room temperature ionic liquids near charged surfaces. *Physical Chemistry Chemical Physics* **15**, 14234-14247, (2013).

[251] Xing, L., Vatamanu, J., Borodin, O. & Bedrov, D. On the Atomistic Nature of Capacitance Enhancement Generated by Ionic Liquid Electrolyte Confined in Subnanometer Pores. *The Journal of Physical Chemistry Letters* **4**, 132-140, (2013).

[252] BC Series Ultracapacitor Datasheet. 1-5 (2013).

[253] Portet, C., Yushin, G. & Gogotsi, Y. Electrochemical performance of carbon onions, nanodiamonds, carbon black and multiwalled nanotubes in electrical double layer capacitors. *Carbon* **45**, 2511–2518, (2007).

[254] Jiang, D.-e. & Wu, J. Microscopic Insights into the Electrochemical Behavior of Nonaqueous Electrolytes in Electric Double-Layer Capacitors. *The Journal of Physical Chemistry Letters* **4**, 1260-1267, (2013).

[255] Wang, H., Koster, T. K. J., Trease, N. M., Segalini, J., Taberna, P. L., Simon, P., Gogotsi, Y. & Grey, C. P. Real-Time NMR Studies of Electrochemical Double-Layer Capacitors. *Journal of the American Chemical Society* **133**, 19270-19273, (2011).

[256] Levi, M. D., Salitra, G., Levy, N., Aurbach, D. & Maier, J. Application of a quartz-crystal microbalance to measure ionic fluxes in microporous carbons for energy storage. *Nature Materials* **8**, 872-875, (2009).

[257] Richey, F. W. & Elabd, Y. A. In Situ Molecular Level Measurements of Ion Dynamics in an Electrochemical Capacitor. *The Journal of Physical Chemistry Letters* **3**, 3297-3301, (2012).

[258] Richey, F. W., Dyatkin, B., Gogotsi, Y. & Elabd, Y. A. Ion Dynamics in Porous Carbon Electrodes in Supercapacitors Using in situ Infrared Spectroelectrochemistry. *Journal of the American Chemical Society* **135**, 12818–12826, (2013).

[259] Li, J. T., Zhou, Z. Y., Broadwell, I. & Sun, S. G. In-Situ Infrared Spectroscopic Studies of Electrochemical Energy Conversion and Storage. *Accounts of Chemical Research* **45**, 485-494, (2012).

[260] Merlet, C., Rotenberg, B., Madden, P. A., Taberna, P. L., Simon, P., Gogotsi, Y. & Salanne, M. On the molecular origin of supercapacitance in nanoporous carbon electrodes. *Nature Materials* **11**, 306-310, (2012).

[261] Hantel, M. M., Presser, V., Kötz, R. & Gogotsi, Y. In situ electrochemical dilatometry of carbide-derived carbons. *Electrochemistry Communications* **13**, 1221-1224, (2011).

[262] Yang, K. L., Yiacoumi, S. & Tsouris, C. Electrosorption capacitance of nanostructured carbon aerogel obtained by cyclic voltammetry. *J. Electroanal. Chem.* **540**, 159-167, (2003).

[263] Ariyanto, T., Dyatkin, B., Zhang, G.-R., Kern, A., Gogotsi, Y. & Etzold, B. J. M. Synthesis of carbon core–shell pore structures and their performance as supercapacitors. *Microporous and Mesoporous Materials* **218**, 130-136, (2015).

[264] Zheng, Z. J. & Gao, Q. M. Hierarchical porous carbons prepared by an easy one-step carbonization and activation of phenol-formaldehyde resins with high performance for supercapacitors. *J. Power Sources* **196**, 1615-1619, (2011).

[265] Xia, K. S., Gao, Q. M., Jiang, J. H. & Hu, J. Hierarchical porous carbons with controlled micropores and mesopores for supercapacitor electrode materials. *Carbon* **46**, 1718-1726, (2008).

[266] Li, F. J., Morris, M. & Chan, K. Y. Electrochemical capacitance and ionic transport in the mesoporous shell of a hierarchical porous core-shell carbon structure. *J. Mater. Chem.* **21**, 8880-8886, (2011).

[267] Dyatkin, B., Gogotsi, O., Malinovskiy, B., Zozulya, Y., Simon, P. & Gogotsi, Y. High Capacitance of Coarse-Grained Carbide Derived Carbon Electrodes. *Journal of Power Sources*, 32-41, (2016).

[268] Lim, J., Malati, P., Bonet, F. & Dunn, B. Nanostructured Sol-Gel Electrodes for Biofuel Cells. *Journal of the Electrochemical Society* **154**, A140-A145, (2007).

[269] Krekeler, M. P. S., Barrett, H. A., Davis, R., Burnette, C., Doran, T., Ferraro, A. & Meyer, A. An investigation of mass and brand diversity in a spent battery recycling collection with an emphasis on spent alkaline batteries: Implications for waste management and future policy concerns. *Journal of Power Sources* **203**, 222-226, (2012).

[270] McEwen, A. B., McDevitt, S. F. & Koch, V. R. Nonaqueous Electrolytes for Electrochemical Capacitors: Imidazolium Cations and Inorganic Fluorides with Organic Carbonates. *Journal of the Electrochemical Society* **144**, L84-L86, (1997).

[271] Beck, F. & Dolata, M. Fluorine-free binders for carbon black based electrochemical supercapacitors. *Journal of Applied Electrochemistry* **31**, 517-521, (2001).

[272] Karabelli, D., Lepretre, J.-C., Alloin, F. & Sanchez, J.-Y. Poly(vinylidene fluoride)-based macroporous separators for supercapacitors. *Electrochimica Acta* **57**, 98-103, (2011).

[273] Lin, C.-Y. & Pan, J.-Y. The effects of sodium sulfate on the emissions characteristics of an emulsified marine diesel oil-fired furnace. *Ocean Engineering* **28**, 347-360, (2001).

[274] Bernardes, A. M., Espinosa, D. C. R. & Tenório, J. A. S. Recycling of batteries: a review of current processes and technologies. *Journal of Power Sources* **130**, 291-298, (2004).

[275] Dyatkin, B., Presser, V., Heon, M., Lukatskaya, M. R., Beidaghi, M. & Gogotsi, Y. Development of a Green Supercapacitor Composed Entirely of Environmentally Friendly Materials. *ChemSusChem* **6**, 2269–2280, (2013).

[276] Lane, J. & Yunes, S. Effect of the Preparation method on the Pore Size Distribution of Activated Carbon rom the Coconut Shell. *Carbon* **30**, 601-604, (1992).

[277] Wang, L., Mu, G., Tian, C., Sun, L., Zhou, W., Yu, P., Yin, J. & Fu, H. Porous Graphitic Carbon Nanosheets Derived from Cornstalk Biomass for Advanced Supercapacitors. *ChemSusChem* **6**, 880-889, (2013).

[278] Raymundo-PiCero, E., Cadek, M., Wachtler, M. & Beguin, F. Carbon Nanotubes as Nanotexturing Agents for High Power Supercapacitors Based on Seaweed Carbons. *ChemSusChem* **4**, 943-949, (2011).

[279] Gogotsi, Y. Not just graphene: The wonderful world of carbon and related nanomaterials. *MRS Bulletin* **40**, 1110-1121, (2015).

[280] Read, J. A. In-Situ Studies on the Electrochemical Intercalation of Hexafluorophosphate Anion in Graphite with Selective Cointercalation of Solvent. *The Journal of Physical Chemistry C* **119**, 8438-8446, (2015).

[281] Cao, W., Li, Y., Fitch, B., Shih, J., Doung, T. & Zheng, J. Strategies to optimize lithium-ion supercapacitors achieving high-performance: Cathode configurations, lithium loadings on anode, and types of separator. *Journal of Power Sources* **268**, 841-847, (2014).

APPENDIX A: LIST OF ABBREVIATIONS AND SYMBOLS

Symbol or Abbreviation	Description
EDLC	Electric double layer capacitor
C	Capacitance (F or µC)
A	Area of capacitor ($m^2\ g^{-1}$)
ε	Electric permittivity of medium
Q	Charge (C or µC)
V	Voltage (V)
SSA	Specific surface area ($m^2\ g^{-1}$)
FSI	Fluid-solid interface
WE	Working electrode
CE	Counter electrode
E	Energy ($Wh\ kg^{-1}$)
P	Power($kW\ kg^{-1}$)
R	Resistance (Ω)
τ	Time constant (s)
RTIL/IL	Room temperature ionic liquid/ionic liquid
C_{sp}	Normalized specific capacitance ($F\ g^{-1}$, $F\ cm^{-3}$, or $µF\ cm^{-2}$)
MD	Molecular dynamics
DFT	Density functional theory
CB	Carbon black
OLC	Onion-like carbon
CDC	Carbide-derived carbon
GNP	Graphene nanoplatelets
d_{av}	Average pore diameter (nm)
AC	Activated carbon
MC	Metal carbide (TiC, SiC, Mo_2C, etc.)
SANS/SAXS	Small-angle neutron scattering/small-angle X-ray scattering
C_Q	Quantum capacitance

TGA	Thermogravimetric analysis
BET	Brunauer-Emmett-Teller (SSA calculation)
P/P_0	Partial pressure of a gas $(0-1)$
FWHM/HWHM	Full width at half maxima/half width at half maxima
S(Q)	Structure factor
PDF	Probability distribution function
Q	Momentum transfer coefficient (Å^{-1})
σ	Electric conductivity (S cm^{-1})
I	Current (mA)
FTIR	Fourier transform IR spectroscopy
XPS	X-ray photoelectron spectroscopy
DVS	Dynamic water vapor sorption
EELS	Electron energy loss spectroscopy
QENS	Quasi-elastic neutron scattering
Γ	Lorentzian fit of energy transfer (meV)
D_{coeff}	Diffusion coefficient ($\text{m}^2\ \text{s}^{-1}$)
L	Jump diffusion length (Å)
NMR	Nuclear magnetic resonance
$^{dV}/_{dt}$	Sweep rate (mV s^{-1})
V_W	Voltage window (V)
Q_{eff}	Coulombic efficiency (%)
CA	Chronoamperometry
CV	Cyclic voltammetry
EIS	Electrochemical impedance spectroscopy
RS	Randles-Sevcik coefficient
Re(Z)	Real component of impedance (Ohms)
Im(Z)	Imaginary component of impedance (Ohms)
R_g	Radius of gyration (Å)
R_s	Series resistance (Ω)

APPENDIX B: MODELING ION-ION CORRELATIONS IN PORES

In addition to exploring the dynamics and charge densities of [EMIm+][TFSI-] ions in defunctionalized and oxidized SiC-CDC pores (section **4.2.2**), X-Ray PDF analysis and MD simulations aimed to assess short-range and long-range ion-ion correlations.[1] Simulations predict a 15-20 Å limit to long-range charge ordering in pores (2-3 layers) and negligible contributions of ions outside of this threshold to the overall capacitance of the system.[1,2] Surface defects that alter this parameter likely influence C_{sp}.

MD computational analyses of ionic liquid electrolytes inside of CDC pores were performed at Sorbonne University (Paris, France). Simulations were performed using the molecular dynamics package GROMACS. The ionic liquid electrolyte and CDC pore force fields were provided, respectively from [3] and [4]. The simulation was equilibrated in the 2D-periodic NVT ensemble. The temperature was maintained at 298 K with the Nose-Hoover thermostat.[5] Electrostatic calculations used particle mesh Ewald summations, with a long range cut-off distance of 1.2 nm for electrostatic and van der Waals interactions. The initial simulation placed an equilibrated box of 216 ion pairs next to the CDC pore in the non-periodic direction and was capped by a wall of immobile carbon atoms at the simulation boundary (**Fig. B1**). To facilitate pore filling, carbon walls incrementally and periodically shifted closer towards pores as a quasi-manual piston.

Once the pore filling was completed fully, the position of the carbon walls was shifted away from the pore and the system was allowed to relax for 10^{-9} seconds until the correct density of ions in the pore was reached. Following this, all the excess ions outside the pore and the carbon walls were removed leaving 72 ion pairs, with a concentration of 1.6 mmol g^{-1} carbon inside the pore. The simulation switched to the 3D periodic NVT

ensemble and re-equilibrated for 550 ps. A $5 \cdot 10^{-9}$ second production run was performed with snapshots taken every 5 ps. From the production run data, radial distribution functions (RDFs) were calculated for all possible atom combinations and included intramolecular combinations. The RDF information was then used to calculate the PDF for the total system. The PDF was also computed for an empty CDC pore and the pure ionic liquid and compared to X-Ray PDF data obtained from IL-filled CDC samples.
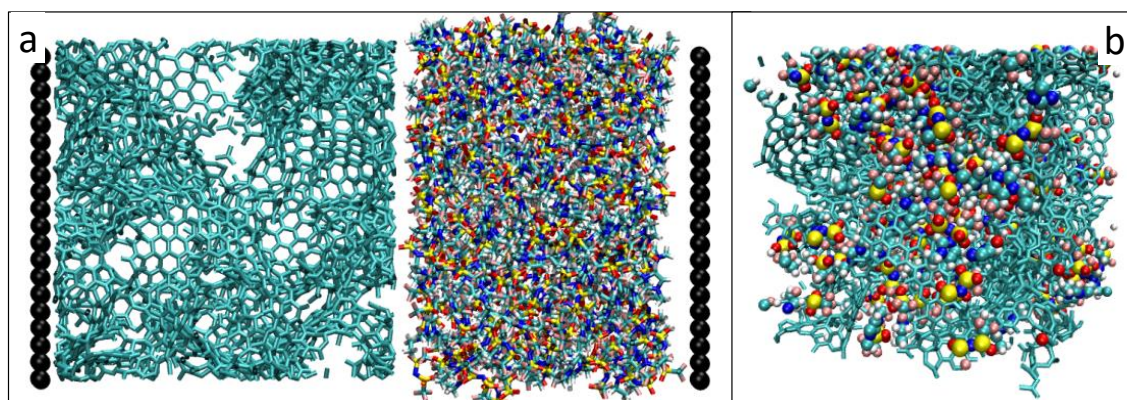

Figure B1. a) Simulation snapshot during equilibration before pore filling. Empty CDC is displayed on the left, and pressurized ionic liquid on the right. The simulation was capped by immobile wall atoms in the non-periodic dimension. b) 3D periodic filled CDC pore used for MD production runs.

The results of the bulk RTIL simulation are in very good agreement with experimental results due to the all-atom model used capturing key molecular properties.[3] The pure CDC and RTIL+CDC simulation results are in qualitative agreement with experimental PDF: although the relative intensities of peaks cannot be scaled to the same intensities, the relative peak positions are the same (**Fig. B2**). The short-range bond correlations, which are dominated by intra-molecular and first-neighbor contributions, are almost identical for bulk and confined RTIL. Some changes arise at medium-range (3 to 12 Å), which can be attributed to the excluded volume and affects data normalization. The comparison between the two structures shows more differences

when comparing the partial RDFs. The positions of the peaks are clearly the same, i.e. the short range structure is not affected.
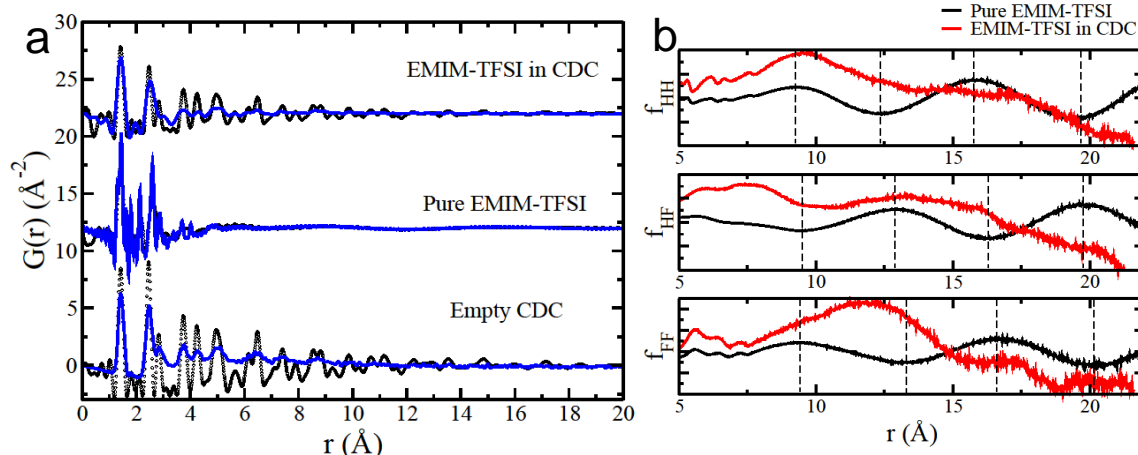

Figure B2. a) r vs. G(r) pair distribution function of the data comparing the experimental results (black) and corresponding model (blue). b) MD-derived radial distribution function modeling of PDF data (r^3*[g(r)-1]) to account for H-H (cation-cation), HF (cation-anion), and FF (anion-anion) interactions. Vertical dashed lines show the points of maxima and minima for the pure EMIM-TFSI partials.

The most important changes are seen at medium and long ranges. The structure in ionic liquids is characterized by a (very) long-range charge ordering: previous simulations have predicted interactions lengths of 6 Å ([EMIm$^+$]···[TFSI$^-$]), 9 Å ([EMIm$^+$]···[EMIm$^+$]), and 15 Å (second neighbor [EMIm$^+$]···[TFSI$^-$]). This ordering is completely lost for the ionic liquid inside the CDC at r=15 Å. Therefore, the short-range confined RTIL structure was not affected, but the disordered structure of the carbon r the long-range ordering of the IL and coordination beyond one cation-anion pair.

This further reinforced several important fundamental differences in behavior and interactions of experimentally measured IL confined in pores (**Fig. B3**). The X-ray PDF measurements somewhat lacked atomic resolution and could not properly discern between IL and CDC atoms. Future experiments must rely on neutron scattering.
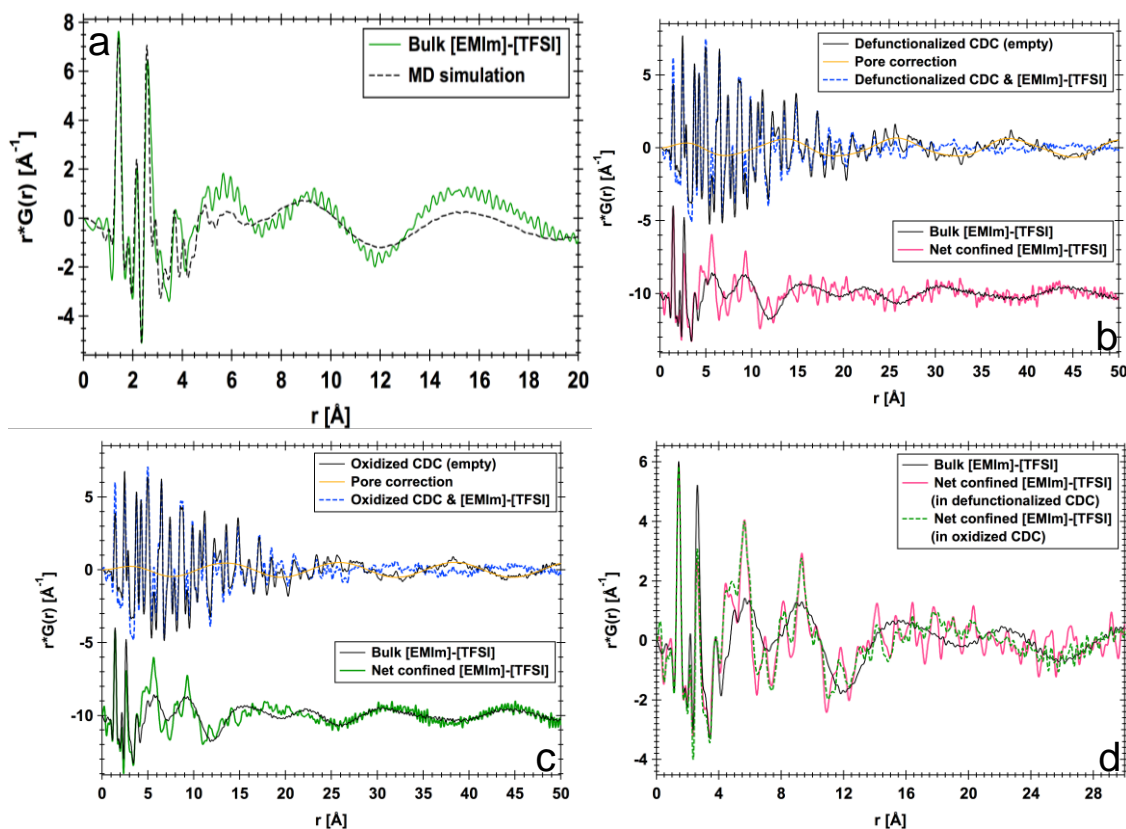
Figure B3. a) Comparison of IL PDF data derived with X-Ray scattering and similar parameters calculated with DISCUS program. X-Ray PDFs are shown for IL confined in b) Defunctionalized CDCs and c) Oxidized CDCs. d) PDF of net IL subtracted from the CDC structure in differently functionalized pores and in its bulk state. Correction factor for different scattering contrasts = $FT[S(Q),Q_{min}=0.5] – FT[S(Q), Q_{min}=1.1]$

[1]   Wang, S., Li, S., Cao, Z. & Yan, T. Molecular Dynamic Simulations of Ionic Liquids at Graphite Surface. *The Journal of Physical Chemistry C* **114**, 990-995, (2010).

[2]   Vatamanu, J. & Bedrov, D. Capacitive Energy Storage: Current and Future Challenges. *The Journal of Physical Chemistry Letters*, 3594-3609, (2015).

[3]   Köddermann, T., Paschek, D. & Ludwig, R. Molecular Dynamic Simulations of Ionic Liquids: A Reliable Description of Structure, Thermodynamics and Dynamics. *ChemPhysChem* **8**, 2464-2470, (2007).

[4]   Palmer, J. C. et al. Modeling the structural evolution of carbide-derived carbons using quenched molecular dynamics. *Carbon* **48**, 1116-1123, (2010).

[5]   Hoover, W. G. Canonical dynamics: Equilibrium phase-space distributions. *Phys. Rev. A* **31**, 1695-1697, (1985).

APPENDIX C: CHARGING OF IONOPHOBIC/IONOPHILIC PORES

The objective of the work in this section was to provide experimental confirmation of recent modeling efforts by Kondrat and Kornyshev (described in section **1.6**). Their findings concluded that ionophobic pores, which repelled ions under no applied potentials and initially remained under vacuum, would charge faster (with only co-ions) than ionophilic pores (which would slow down pore saturation by counterion de-filling).[1] Additionally, the simulations equated ionophobic pores to stiff springs and predicted that, in cases of unfavorable ($\Delta G > 0$) pore filling thermodynamic conditions, the (eventually) filled pores would store greater amounts of energies.[2]

The first attempt to experimentally replicate this behavior relied on SiC-CDC nanoparticles (same as those in section **4.1**). After 800 ℃ Cl_2 synthesis, they were defunctionalized at 1,400 ℃ (annealed), treated in dry air at 400 ℃ for 5 hours (oxidized), and treated with H_2 (g) at 600 ℃ (post-oxidation) for 10 hours (hydrogenated). The resulting materials were tested with 1-butyl-3-methylimidazolim hexafluorophosphate ([$BMIm^+$][PF_6^-]). Based on contact angle measurements, annealed were most ionophobic ($\theta = 77.0 \pm 0.8°$); oxidized were more ionophilic ($\theta = 55.1 \pm 0.8°$); and hydrogenated were most ionophilic ($\theta = 44.7 \pm 0.1°$).

Cells were cycled in dynamic modes (EIS and CVs) and static modes (CA). The results are shown in **Fig. C1**. As shown from the Nyquist plot, hydrogenated pores demonstrated lowest ionic impedance at low frequencies. Functionalized CDCs exhibited high charge transfer resistance at high frequencies: it could stem from their reduced electrical conductivities (0.63 S cm^{-1} for hydrogenated and 1.21 S cm^{-1} for oxidized films, compared to 2.18 S cm^{-1} for annealed CDCs). The dynamic cycling results closely

resembled the findings for similarly functionalized planar electrodes (section 4.3.2), which agreed with the short pore lengths and aspect ratios of the nanoparticles. Furthermore, static charging experiments did not show faster charge accumulation in ionophobic pores or any evidence of ion defilling in ionophilic pores.
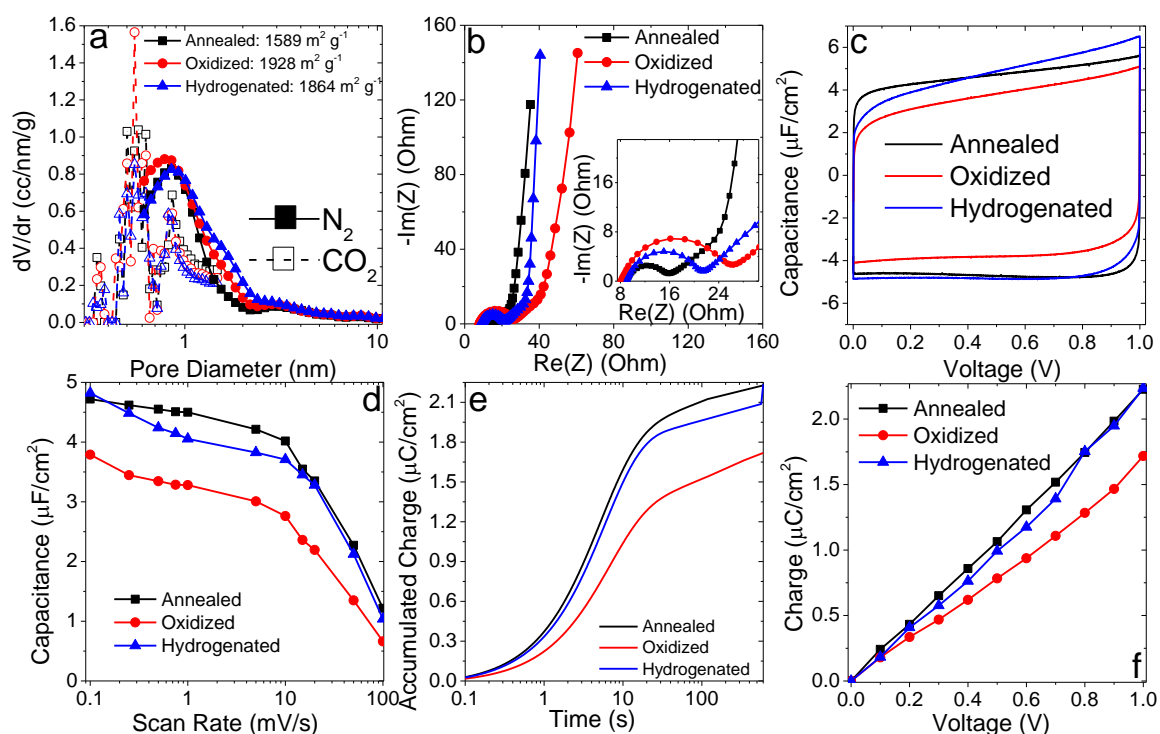

Figure C1. a) PSDs of differently functionalized SiC-CDC nanoparticles. b) Nyquist plot, c) 0.1 mV s^{-1} CV, and d) CV-derived rate handling comparison of annealed, oxidized, and hydrogenated CDCs in [BMIm$^+$][PF$_6^-$]. e) Square wave charge accumulation from 0.0 to 1.0 V. f) Cumulative accumulated charge at each 0.1 V step in the 0.0 ↔ 1.0 V window using static charge accumulation.

The experimental results did not agree with the conclusions of continuum modeling for several reasons. The model assumed that ionophobic pores would be empty (under vacuum), whereas experimental cells pre-cycled cells to obtain reliable results. Furthermore, [BMIm$^+$][PF$_6^-$] was a very viscous electrolyte and included a large cation, whereas the model simplified both ions to point charges. Finally, the surface functionalization may have been insufficient to generate significant pore ionophobicity.

In an alternative approach, coarse-grained 250 µm diameter CDCs (same as in section

4.3.4) was annealed at 800 ºC for 48 hours to completely strip away all functional groups.

Its pores were filled with cyclohexane, which is a very hydrophobic solvent. This system

used both the pore surface and pore void space to create initially ionophobic conditions.

They were tested using the square wave approach and compared against similar cells with

pores that had initially been filled with the electrolyte (ionophilic). The cells were not

precycled and the 1st and 2nd cycles were recorded to assess initial and filled pore states.
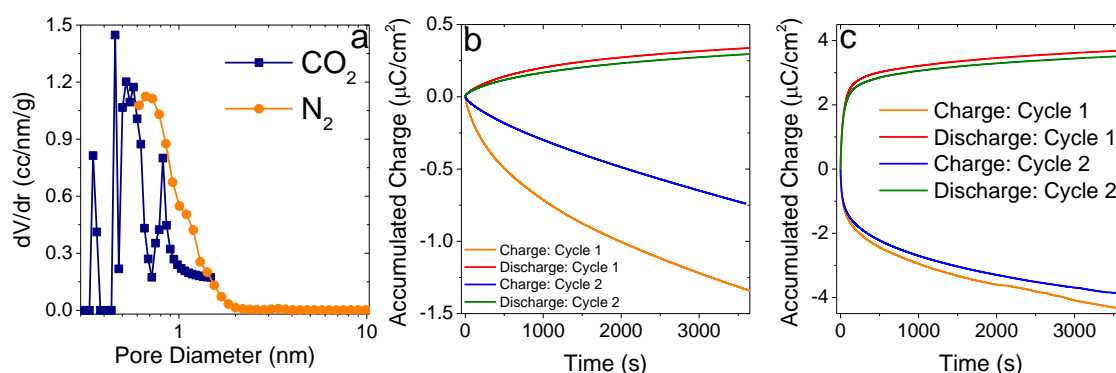

Figure C2. a) Pore structure of CDC. Charging dynamics in the $0 \leftrightarrow \pm 1.0$ V windows are shown for a) initially ionophobic pores and c) initially ionophilic pores.

The ionophobic pores were highly resistive and did not allow ions to displace solvent

molecules under applied potentials. It is possible that the thermodynamics of the system

would make ion adsorption more favorable at higher potentials, but such experiments

could have initiated electrochemical breakdown in cells. In order to properly replicate the

continuum modeling conditions, future efforts will need to assess the free energies of

specific solvents in pores and electrolyte-specific ion adsorption energies.

[1] Alpha, A. L., Svyatoslav, K., Gleb, O. & Alexei, A. K. Charging dynamics of supercapacitors with narrow cylindrical nanopores. *Nanotechnology* **25**, 315401, (2014).

[2] Kondrat, S. & Kornyshev, A. A. Pressing a spring: what does it take to maximize the energy storage in nanoporous supercapacitors? *Nanoscale Horizons*, (2016).

VITA

Boris Dyatkin
Email: BorisDyatkin@gmail.com • Phone: (267) 481-3367

Education
- **Drexel University**, Philadelphia, PA, USA
  Degree: PhD, Materials Science and Engineering, *January 2016*
  Advisor: Professor Yury Gogotsi
- **University of Pennsylvania**, Philadelphia, PA, USA
  Degree: B.S.E., Materials Science and Engineering, *May 2009*
  Advisor: Professor Dawn A. Bonnell

Work and Research Experience
- Graduate Research Assistant, Drexel University, Philadelphia, PA (*03/11 – 01/16*)
- Research Fellow, Oak Ridge National Laboratory, Oak Ridge, TN (*03/15– 08/15*)
- Visiting Researcher, Dalian University of Technology, Dalian, China (*08/14– 10/14*)
- Visiting Researcher, Army Research Laboratory, Adelphi , MD *(06/14-08/14)*
- Materials Chemist, AlumiFuel Power, Inc., Philadelphia, PA *(11/08-02/11)*

Selected Publications (17 total in press)
- **B. Dyatkin**, O. Gogotsi, B. Malinovskiy, Y. Zozulya, P. Simon, Y. Gogotsi. High Capacitance of Coarse-Grained Carbide-Derived Carbon Electrodes. *Journal of Power Sources* **306**, 32-41 (2016).
- **B. Dyatkin**, E. Mamontov, K.M. Cook, Y. Gogotsi. Capacitance, Charge Dynamics, and Electrolyte-Surface Interactions in Functionalized Carbide-Derived Carbon Electrodes. *Progress in Natural Science – Materials International. In Press (*2015*).*
- **B. Dyatkin**, Y. Gogotsi. Effects of Structural Disorder and Surface Chemistry on Electric Conductivity and Capacitance of Porous Carbon Electrodes. *Faraday Discussions* **172 (1)**, 139-162 (2014).
- **B. Dyatkin**, V. Presser, M.R. Lukatskaya, M. Beidaghi, Y. Gogotsi. Development of a Green Supercapacitor Composed Entirely of Environmentally Friendly Materials. *ChemSusChem* **6 (12)**, 2269-2280 (2013).
- T. Ariyanto, **B. Dyatkin**, G.R. Zhang, A. Kern, Y. Gogotsi, B. Etzold. Synthesis of carbon core–shell pore structures and their performance as supercapacitors. *Microporous and Mesoporous Materials* **218**, 130-136 (2015).
- F.W. Richey, **B. Dyatkin**, Y. Elabd, Y. Gogotsi. Ion Dynamics in Porous Carbon Electrodes in Supercapacitors Using *in Situ* Infrared Spectroelectrochemistry. *Journal of the American Chemical Society* **135 (34)**, 12818-12826 (2013).

Honors and Awards
- EFRC PI Meeting Graduate Student Competition Winner, *October 2015*
- Alpha Sigma Mu Honor Society Inductee, *August 2015*
- National Academy of Science Research Associateship, *July 2015*
- DOE Graduate Student Research Program Fellowship, *December 2014*
- ACS Ciba Travel Award in Green Chemistry, *November 2014*
- Drexel COE Leroy M. Resser Endowed Fellowship, *April 2014*
- ICMR International Research Fellowship, *December 2013*